Department of Chemistry

Structural and Photophysical Investigation of Lanthanoid β-Triketonates

Brodie Lionel Reid

This thesis is presented for the Degree of
Doctor of Philosophy
of
Curtin University

October 2015

Declaration

To the best of my knowledge and belief this thesis contains no material previously published by any other person except where due acknowledgement has been made. This thesis contains no material which has been accepted for the award of any other degree or diploma in any university.

Signature: 

Date: 28/10/2015

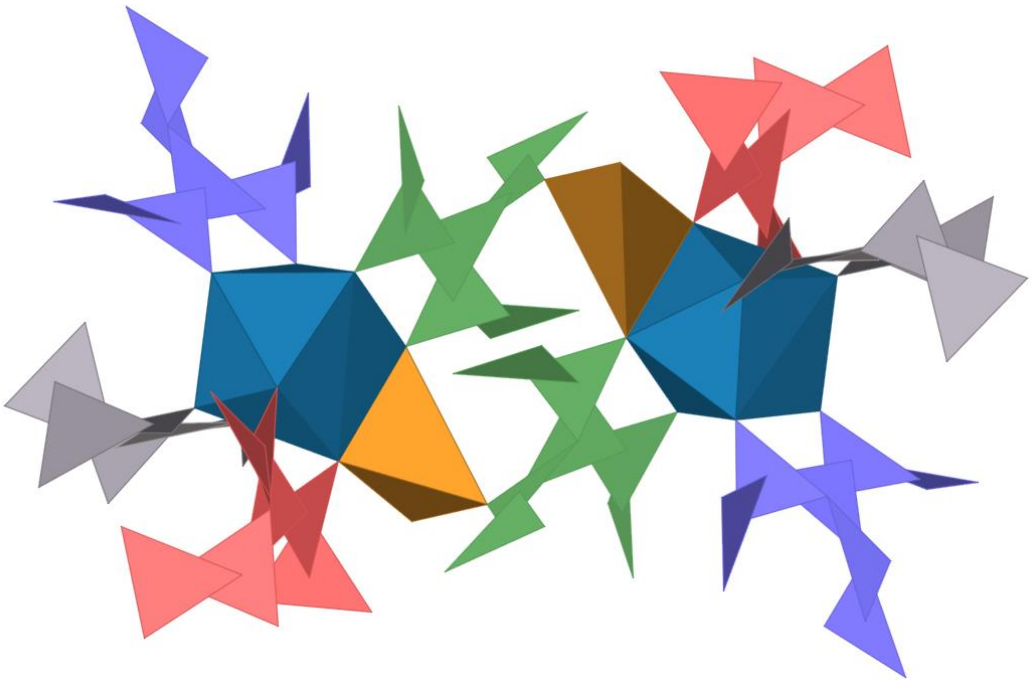

“Give light, and the darkness will disappear of itself.” – Desiderius Erasmus

Abstract

The first part of this thesis aimed to explore the coordination chemistry of the β-triketonate class of ligands, with the initial structural characterisation of 23 new lanthanoid β-triketonate species, using the tribenzoylmethane ligand (2-benzoyl-1,3-phenyl-1,3-propandione, **L1**H). The β-triketonate supports the crystallisation of mononuclear lanthanoid complexes when made to react in the presence of an organic base. The reaction of **L1**H with lanthanoid cations in the presence of alkali metals resulted in the formation of structurally unique Ln^{3+}/Ae^{+} (Ln^{3+} = Eu^{3+}, Gd^{3+}, Tb^{3+}, Dy^{3+}, Ho^{3+}, Er^{3+}, Yb^{3+}; Ae^{+} = Na^{+}, K^{+}, Rb^{+}) tetranuclear assemblies of the general formula $[Ln(Ae{\cdot}HOEt)(\mathbf{L1})_4]_2$.

The photophysical properties of the assemblies were assessed in the solid state and after dissolution in ethanol, revealing bright visible and NIR emission with respect to lanthanoid complexes bearing β-diketonate ligands. In fact, for the NIR emitting species, the excited state lifetimes and intrinsic quantum yields were found to be among the longest-lived in the literature for this class, even including those which are perfluorinated to minimise quenching.

An Yb^{3+} species was trialled as a precursor for the fabrication of NIR-OLEDs by sublimation of the solid samples, revealing a device with a performance which is among the best of all previously reported NIR-OLEDs where Ln^{3+} have been used in the emissive layer.

The second part of this work aimed to extend the substitution of the classic β-diketonate molecule at the α-C position with a nitrile substituent. This type of substitution allowed the crystallisation of a one-dimensional Eu^{3+} coordination polymer assisted by the linear coordination mode of the –CN substituent. An investigation of the metal-centred emission of the polymer, both in the solid state and solution, revealed red emission characterised by relatively long-lived excited state lifetimes and high intrinsic quantum yields. However, analysis of the overall quantum yield and sensitisation efficiency revealed that ultrafast processes in the ligand potentially inhibit Eu^{3+} sensitisation. Further investigations into these processes using transient absorption spectroscopy suggested that nitrile substitution at the α-C position may significantly decrease sensitisation *via* the antenna effect.

Acknowledgements

There are a number of people without whom this thesis would not have been possible.

First and foremost, I thank my PhD supervisors Dr. Massimiliano Massi and Prof. Mark I. Ogden for imparting their knowledge, and providing me with a platform to develop professionally in Australia and Overseas. They have allowed me to create my own directions for the work, whilst keeping me on track and within useful boundaries. I am grateful for the help and teachings, and I am sure that this thesis would not be possible without their guidance.

My stay of research in Montréal would not have been possible without the supervision of Prof. Garry S. Hanan, and support from the Université de Montréal. I also thank Assoc. Prof. Frank Schaper and Mr. Thierry Maris for teaching me X-ray diffraction and how to resolve some of the crystal structures presented in this thesis.

The Transient Absorption measurements presented in this work could not have been achieved without the knowledge and supervision of Dr. Evan G. Moore in my stay of research at the University of Queensland. However, I also thank Dr. Evan Moore for his useful discussions, from which I gained invaluable knowledge of the lanthanoid elements.

I thank Prof. Brian Skelton and Dr. Alexandre Sobolev from the University of Western Australia for their help with final crystal structure resolutions. Whilst Dr. Stefano Stagni, Dr. Massimo Cocchi, and Dr. Joanna M. Malicka are thanked for fabrication of the OLED presented in this work.

I am thankful to all of my colleagues from Curtin University and the Université de Montréal for their useful conversations. Although mostly light-hearted, the work in this thesis was built on the humorous daily interactions in the lab, as well as relaxed scientific discussions.

I thank my friends and family for their encouragement throughout all of my study to date. Finishing this work would have been much more challenging without the stable foundation of my family. Finally, to Elodie, I thank you for your love and support. Meeting you has been the highlight of these four years.

Table of Contents

Symbols and Abbreviations

Δ	change
δ	chemical shift
ε	Molar absorptivity
η	refractive index
λ_{em}	emission wavelength
λ_{ex}	excitation wavelength
ν	frequency
τ_{obs}	observed lifetime
τ_R	radiative lifetime
Φ_{Ln}^{L}	overall quantum yield
Φ_{Ln}^{Ln}	intrinsic quantum yield
Φ_{sens}	sensitisation efficiency
χ^2	goodness of fit
acacCN	2-cyano-1,3-methyl-1,3-propandione
AAS	Atomic Absorption Spectroscopy
Ae	alkali element
ATR	Attenuated total reflectance
Bath	bathophenanthroline
BET	back energy transfer
Bipy	2,2'-bipyridine
Bta	benzoyltrifluoroacetone
Btfax	1,1'-(4,4'-(2,2bis((4-(4,4,4-trifluoro-3-oxobutanoyl)phenoxy)methyl)propane-1,3-diyl)bis(oxy)bis(4,4,4-trifluorobutane-1,3-dione).
BuOH	*n*-butanol
Bzac	1-phenyl-1,3-butanedione
Calcd	Calculated
CCD	Charge-coupled device
CCDC	Cambridge Crystallographic Data Centre
COSY	Homonuclear correlation spectroscopy
c.p.s.	counts per second
CSD	Cambridge Structural Database
CShM	Continuous Shape Measures
CT	charge transfer
dec.	decomposition
DEPT-Q	Distortionless enhancement by polarisation transfer including detection by quaternary nuclei
Dmh	2,6-dimethyl-3,5-heptanedione
DMSO	dimethylsulfoxide
ED	electric dipole
EDFA	erbium doped fibre amplifier
EL	electroluminescence
EML	emissive layer
EMR	electromagnetic radiation
ET	energy transfer
ETL	electron transporting layer
EtOH	ethanol
Fod	6,6,7,7,8,8,8-heptafluoro-2,2-dimethyl-3,5-octadionate
FRET	Förster resonance energy transfer
FT-IR	Fourier transform infrared
FWHM	full-width at half-maximum
GS	ground state
h	2,4-hexanedionate
Hfa	hexafluoroacetylacetone
HOMO	highest occupied molecular orbital

HMBC	heteronuclear multiple bond correlation spectroscopy
HSQC	heteronuclear single-quantum correlation spectroscopy
HTL	hole transporting layer
IC	internal conversion
IR	infrared
IRF	Instrumental response function
ISC	intersystem crossing
ITO	Indium tin oxide
k_{nr}	non-radiative rate constant
k_r	radiative rate constant
L1H	2-benzoyl-1,3-phenyl-1,3-propandione
L2H	2-cyano-1,3-phenyl-1,3-propandione
L3H	2-(4-methoxybenzoyl)-1,3-phenyl-1,3-propandione
L4H	2-(4-methoxybenzoyl)-1-(4-methoxyphenyl)-3-phenyl-1,3-propandione
L5H	2-(4-methoxybenzoyl)-1,3-(4-methoxyphenyl)-1,3-propandione
LC	ligand-centred
LED	light emitting device
LEIP	lowest energy interconversion pathway
lit.	literature
LMCT	ligand-to-metal charge transfer
Ln	lanthanoid
LUMO	lowest unoccupied molecular orbital
MC	metal-centred
mCP	1,3-bis(*N*-carbazoyl)benzene
Me	methyl
MD	magnetic dipole
Mdbm	1-(4-methoxyphenyl)-3-phenyl-1,3-propandione
MLCT	metal-to-ligand charge transfer
Mfa	1-(2-furanyl)-3-(4-methoxyphenyl)-1,3-propanedione
m.p.	melting point
NIR	near-infrared
NMR	nuclear magnetic resonance
$5NO_2$phen	5-nitro-1,10-phenanthroline
OD	optical density
OLED	organic light emitting device
Phen	1,10-phenanthroline
RT	room temperature
S_1	first singlet excited state
S_2	second singlet excited state
SAF	solid angle factor
T_1	triplet excited state
TA	transient absorption
Tfnb	4,4,4-trifluoro-1-(2-napthyl)-1,3-butanedione
TGA	thermal gravimetric analysis
THF	tetrahydrofuran
TPBi	1,3,5-tris(*N*-phenyl-benzimidazol-2-yl)benzene
Tta	thenoyltrifluoroacetone
UV	ultraviolet

List of Compounds

Abbreviation	*Compound*
	Ligands
L1H	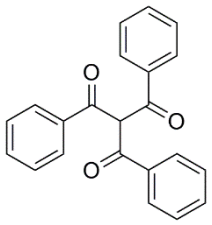
L2H	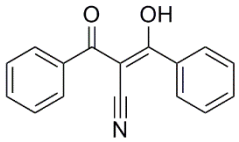
L3H	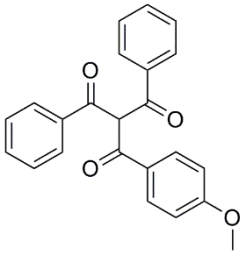
L4H	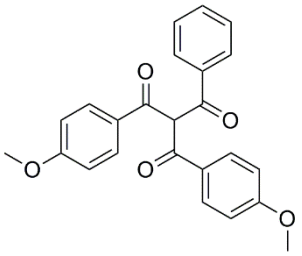
L5H	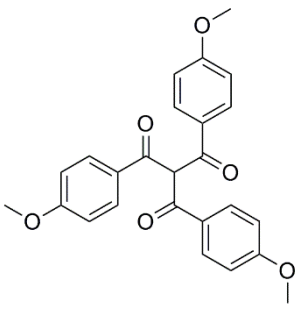

Mononuclear Species and Coordination Polymers

$[Ce(acacCN)_3(H_2O)_2]$

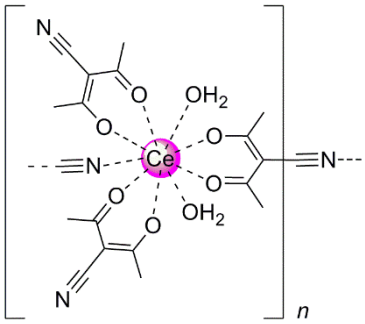

$[Cs(\mathbf{L1})]_n$

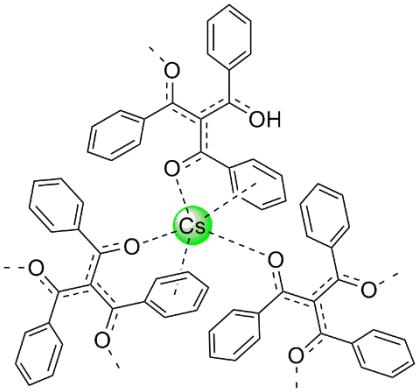

$[Eu(Phen)(\mathbf{L1})_3]$

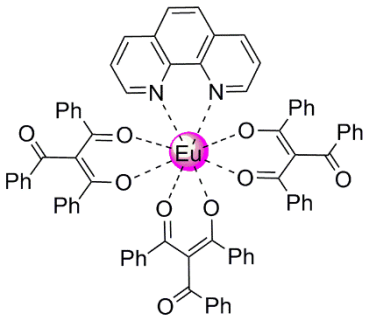

$[Eu(Phen)(\mathbf{L2})_3]_n$

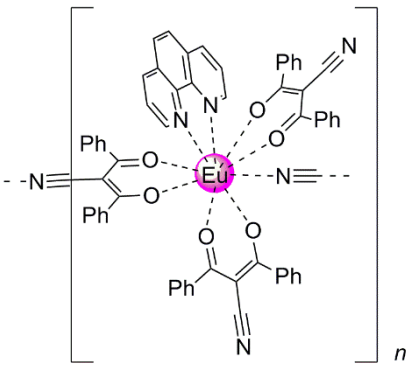

$[Ho(\mathbf{L1})_3(EtOH)(H_2O)]$

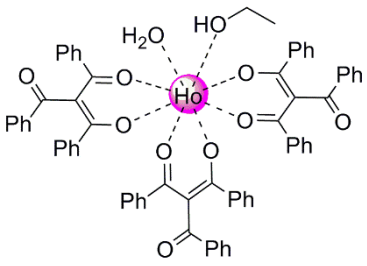

Tetranuclear Assemblies

$\{Dy_2K_2\}^{II/IV}$

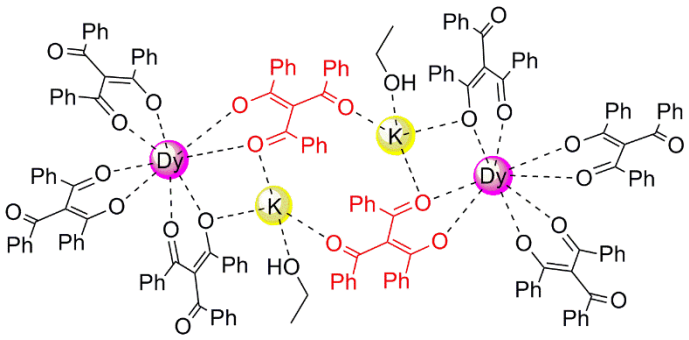

$\{Dy_2Rb_2\}^{IV}$

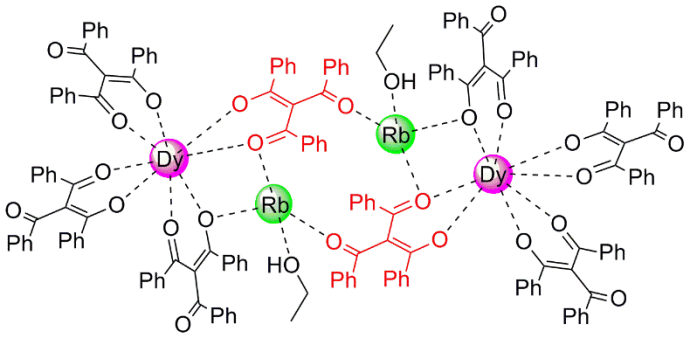

$\{Er_2K_2\}^{III}$

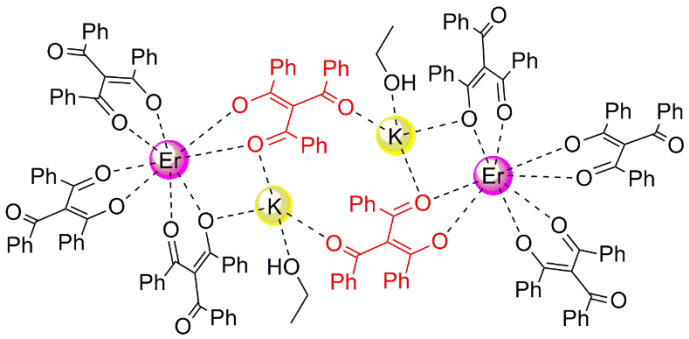

$\{Er_2Na_2\}^{I}$

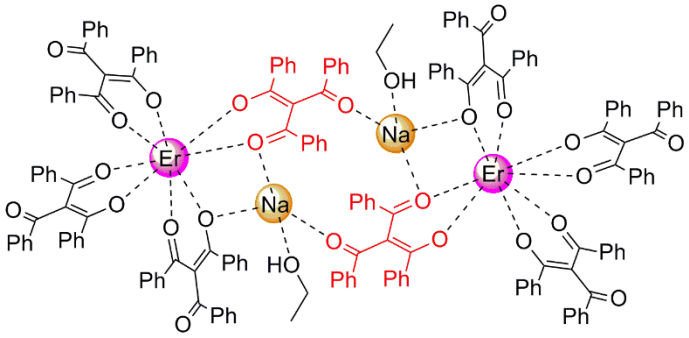

$\{Er_2Rb_2\}^{II}$

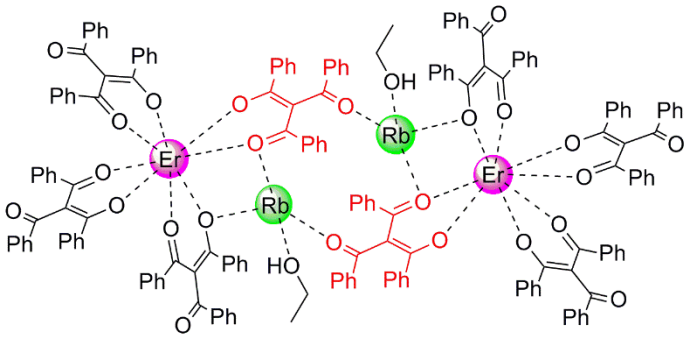

$\{Eu_2K_2\}^{IV}$

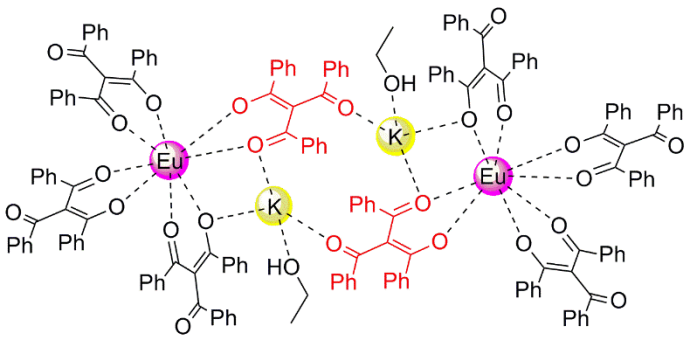

$\{Eu_2K_2\text{-}BuOH\}^{III}$

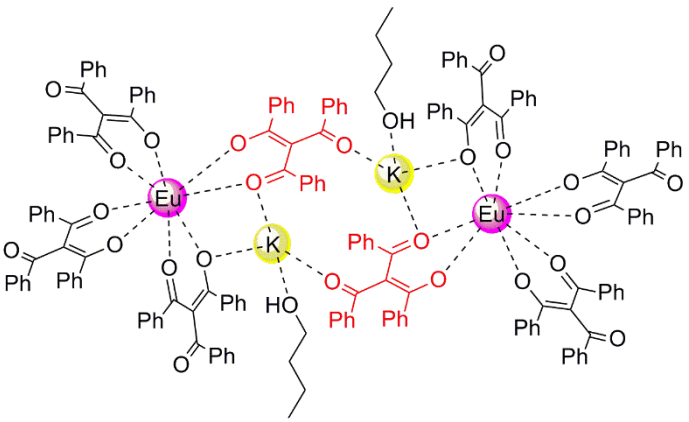

$\{Eu_2Na_2\}^{I}$

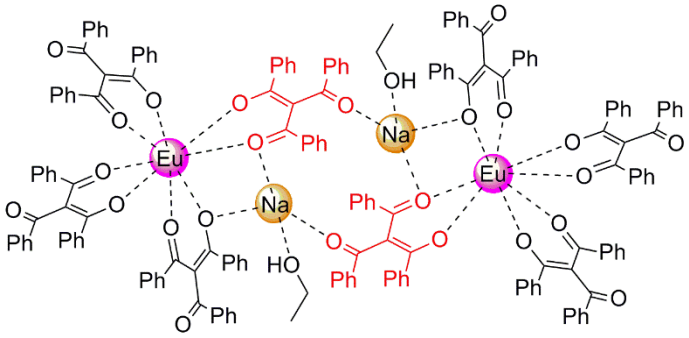

$\{Eu_2Rb_2\}^{IV}$

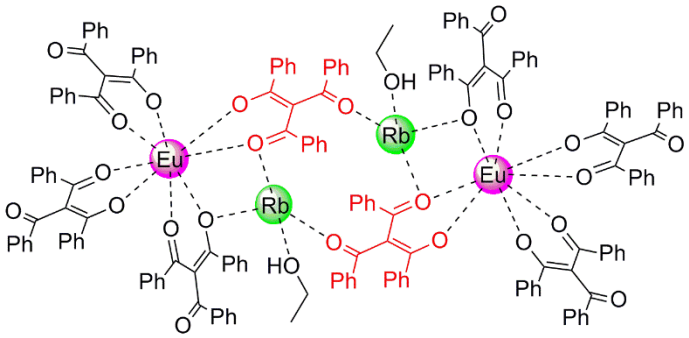

$\{Gd_2K_2\}^{IV}$

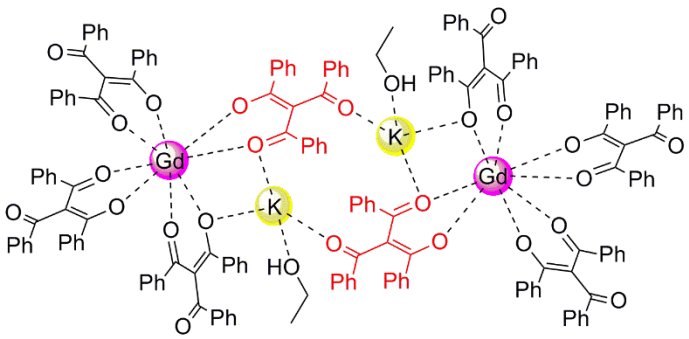

$\{Gd_2Rb_2\}^{IV}$

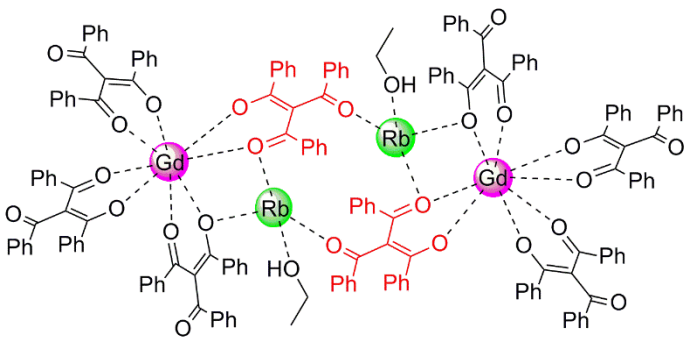

$\{Ho_2K_2\}^{II}$

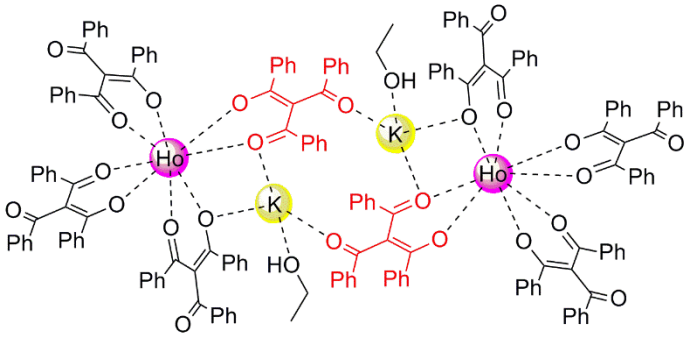

$\{Ho_2Rb_2\}^{IV}$

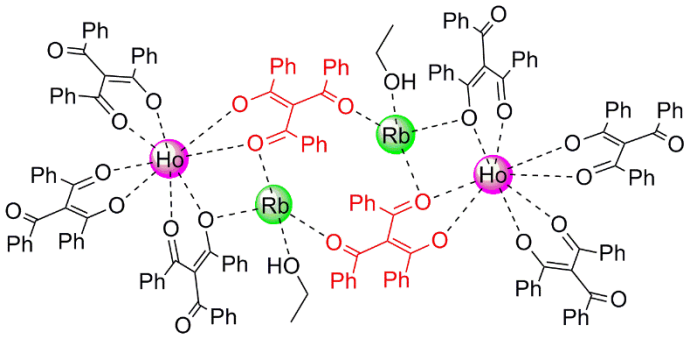

$\{Tb_2K_2\}^{II}$

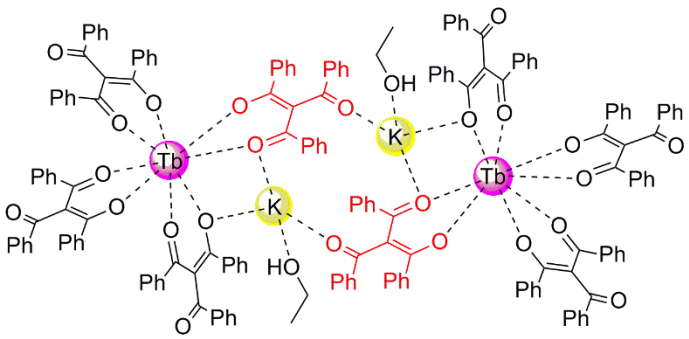

$\{Tb_2Na_2\}^{I}$

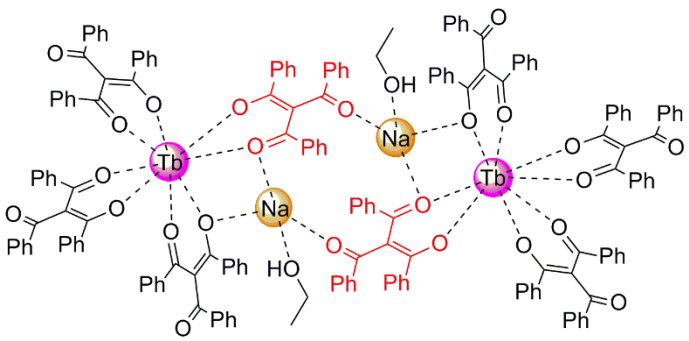

$\{Tb_2Rb_2\}^{IV}$

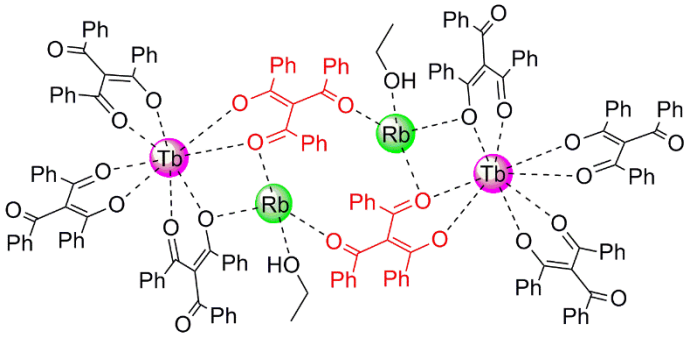

$\{Yb_2K_2\}^{II/III}$

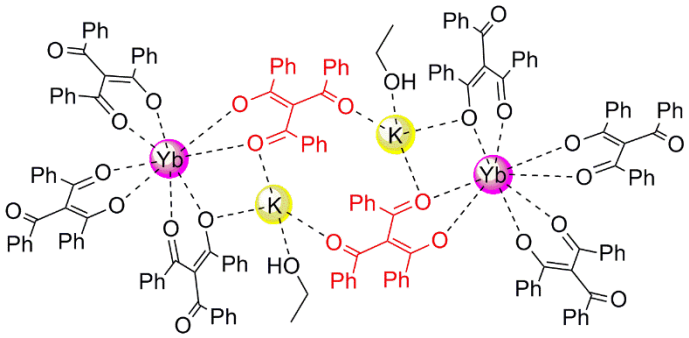

$\{Yb_2Na_2\}^{I}$

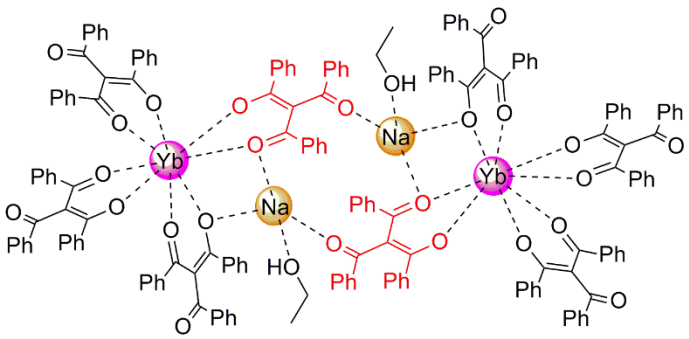

$\{Yb_2Rb_2\}^{II}$

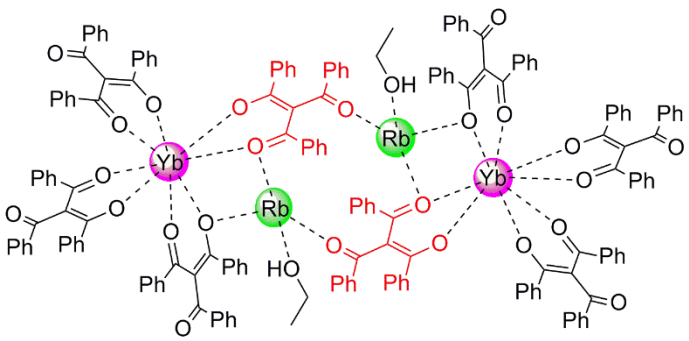

1 Introductory Remarks

Sensitised lanthanoid emission by an organic molecule was first discovered by Weissman in 1942,[1] and later coined *the antenna effect* by Sabbatini and Lehn.[2,3] Since this discovery, lanthanoid chemists have utilised the bright and pure colours provided by the sensitised lanthanoids for a vast variety of applications.[4] These emissions span the visible and near infrared (NIR) spectral regions depending on the trivalent lanthanoid of choice.

Visible emitters such as Eu^{3+} (red), Tb^{3+} (green), Sm^{3+} (orange), and Dy^{3+} (yellow) are finding application as the emissive species in light emitting devices (LEDs), and organic light emitting devices (OLEDs), needed in LED and OLED televisions, as well as the LEDs present in smart devices including smartphones and tablets.[5–9] Visible emitters are used in bioimaging applications,[10–13] solar energy conversion,[7,14,15] anti-counterfeit banknotes,[9,16] and hybrid materials.[17–21]

Lanthanoid complexes which exhibit emission in the NIR region have been highly sought after in the biomedical area,[6,7,10,12,13,22] as NIR photons offer deeper tissue penetration and are less affected by scattering.[23] However such emissions also find use in telecommunications, optical signalling, and night vision technology.[7,24]

Sensitised lanthanoid emission from the bis-chelating class of β-diketonate ligands is a field which has received much interest since the early 1960s,[25–30] shortly after the findings of Weissman. The β-diketonate allows sensitisation of a range of lanthanoid emission, and can also support the formation of larger

multinuclear lanthanoid cluster motifs. Work in this field continues to grow due to the absolute versatility of the ligand.[31–35]

In stark contrast, the β-triketonate class of ligand is relatively unexplored, with no structural characterisation of a lanthanoid β-triketonate ever reported prior to work described here. This is remarkable given that the molecule should be a very straightforward extension to the classic β-diketone molecule. Furthermore, the β-triketone might allow the formation of novel lanthanoid coordination compounds due to the extra ketone coordinating site.

The underlying aim of the research presented in this thesis, was to uncover the structural characteristics of lanthanoid β-triketonates, such as the coordinating modes of this new class of ligands and the novel lanthanoid structures which may form. Furthermore the β-triketone molecule presents a viable alternative to the β-diketone for emissive lanthanoid species, as a key CH quenching vibration is removed from the α-C position. Chapter 3 will cover the initial synthesis of the β-triketone molecule used in majority of the work as well as the initial investigation of structurally unique lanthanoid β-triketonate complexes and tetranuclear assemblies. These assemblies are the cornerstone of the work presented in this thesis.

Chapter 4 will present the solid state photophysical examination of the lanthanoid species spanning the visible (Eu^{3+}) and NIR (Er^{3+}, Yb^{3+}) emitting lanthanoids. This chapter also covers the initial application of the emissive tetranuclear assemblies to the field of NIR-OLEDs, with the fabrication of a working device achieved, and a focus on thermal stability of the complexes in the solid state.

Chapter 5 will focus on the stability of the studied complexes after dissolution, as an alternate method to the fabrication of OLEDs. The emission structure, excited state lifetimes, and emission in deuterated solvents were used to decipher the solution chemistry of these species.

Chapter 6 will cover the extension of the work to an α-substituted –CN β-diketonate ligand, and the initial coordination studies with Eu^{3+} and photophysical analysis of the complex. This discussion is aided by Transient

Absorption (TA) spectroscopy, to highlight the ultrafast processes occurring in the sensitising ligand.

To finish, Chapter 7 will present the beginning of future work in the direction of new lanthanoid β-triketonates, and the initial results highlighting the similarities and differences in the β-triketonates by progressive functionalisation.

Before the results of the work can be presented, it is necessary that the fundamental electronic properties, and coordination chemistry of the lanthanoids be discussed, in addition to the inherent properties and process of lanthanoid sensitisation *via* the antenna effect. Furthermore, the necessary lanthanoid β-diketonate chemistry will be reviewed. Thus, what follows in the next Chapter is the theoretical and literature recount of relevant lanthanoid chemistry.

2 Lanthanoid Luminescence

2.1 Electronic Configuration and Oxidation States

The lanthanoids are the fifteen elements commencing the fourth period of the periodic table, and have the atomic numbers of 57-71. The typical electronic configuration for the lanthanoids is [Xe]$4f^n6s^2$, with the exceptions of lanthanum, cerium, gadolinium, and lutetium which follow the electronic configuration of [Xe]$4f^{n-1}5d^16s^2$.[36,37] The most stable, and hence predominant, oxidation state of the lanthanoids is the trivalent state in which the typical electronic configuration follows [Xe]$4f^n$ (n = 0-14). However, other oxidation states can be attained, and in fact Sm^{2+}, Eu^{2+}, and Yb^{2+} are notable exceptions,[38–41] as well as Ce^{4+}.[42–44] While the valence orbitals are of 4*f* nature, they are effectively shielded from the ligand field by the more radially expanded 5*s* and 5*p* orbitals.[37]

For this reason, the 4*f* orbitals of the lanthanoids are called *inner core*, and are protected from interaction with the ligand field. This phenomenon governs the *lanthanide contraction*, which describes the gradual decrease in ionic radius as the lanthanoid period is traversed.[36,45] This is a result of poor screening of the 4*f* electrons by the [Xe] core.

2.2 The 4*f* Electrons

Pauli's Exclusion Principle states: in any atom, no two electrons can be described by the same set of four quantum numbers. Thus, an electron can be uniquely described by their quantum numbers, n, l, m_l, and m_s.[42]

The principle quantum number, n, details the size of the orbital which holds the electron and the distance from the nucleus. For the lanthanoids, $n = 4$, as we are dealing with the 4*f* electrons. The azimuthal quantum number, l, describes the relative shape of an orbital and can have values of $0 \ldots n-1$. In this case, the value of $l = 3$ describes the *f* orbitals. The magnetic quantum number, m_l, describes the orientation in space of the angular momentum and follows the rule: $m_l = -l, -l+1 \ldots l$. A 4*f* electron will therefore be defined inherently by one of the magnetic quantum numbers, $m_l = -3, -2, -1, 0- 1, 2, 3$. Finally, the orientation of electron spin is given by the spin quantum number, m_s, and can be one of the values, $\pm 1/2$, corresponding to the two possible spin states.[46]

2.3 Energies of the 4*f* Electrons and the Ground Term

The Ln^{3+} ground electronic configuration of $[Xe]4f^n$ is energetically well separated from the $[Xe]4f^{n-1}5d^1$ configuration (e.g. $\Delta E = 32{,}000\ cm^{-1}$).[47] Although the 4*f* electrons are *inner core*, their energies are not degenerate due to electronic repulsion, spin-orbit coupling, and small influences from the ligand field (Figure 2.1).

The strongest interaction which affects the degeneracy of the 4*f* energy states is electronic repulsion, and is responsible for the separation in terms in the order of $10^4\ cm^{-1}$.[37,48] This electronic repulsion splits the 4*f* electronic states into $2S+1$ states, which is known as spin multiplicity where S is the total spin number. The total orbital angular momentum number L, represented by the letters S, P, D, F, G, H *etc*. in lieu of $L = 0, 1, 2, 3, 4, 5$ *etc*. Thus the overall electronic configuration can be defined by a term symbol, $^{(2S+1)}L$.

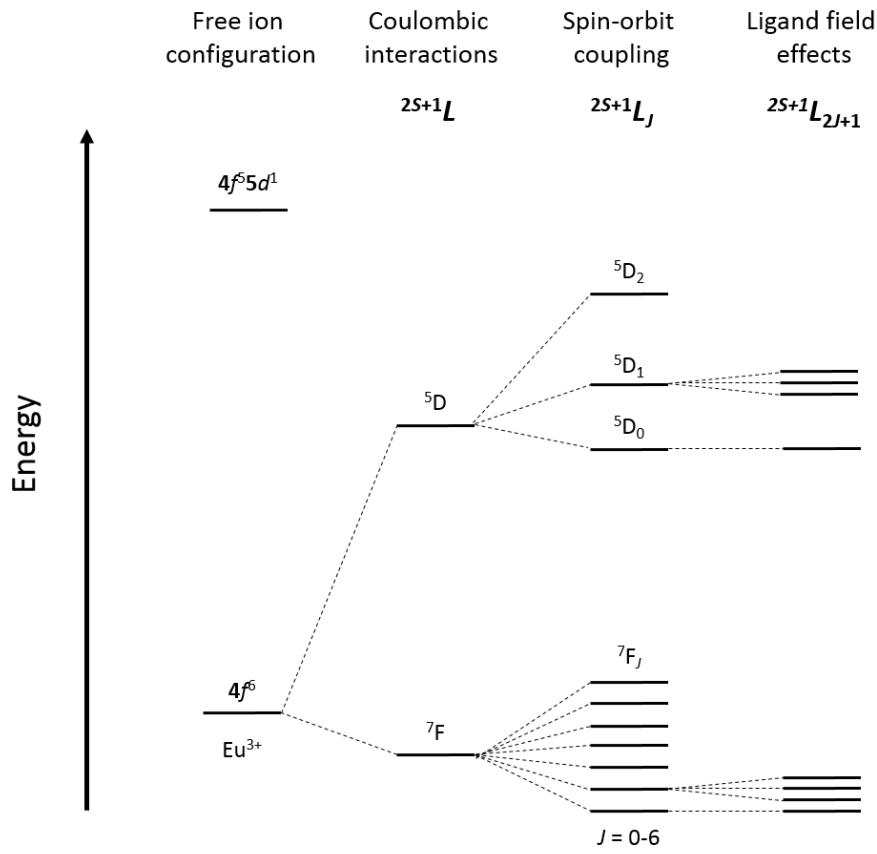

Figure 2.1 – Splitting of the 4*f* energy states in Eu^{3+}.

Generally, the term representing the lowest energy state, called the ground term, can be determined following Hund's rules:[45]

1. The largest value of spin multiplicity is the lowest in energy.
2. Of the given spin multiplicity in rule 1, the largest value of total angular momentum is the lowest in energy.

Therefore, using Eu^{3+} ($4f^6$) as an example, we find after following Hund's rules that $S = 3$ and $L = 3$. This equates to $2S+1 = 7$, while L will be represented by the letter F. Hence, the ground term for the Eu^{3+} ground electronic configuration is ^7F, as is represented in Figure 2.1.

The total angular spin number (J) is the contribution of spin-orbit coupling. Spin-orbit coupling is the interaction of the sum of orbital momenta with the sum of spin momenta. The new quantum number J, can be introduced and can have the

values: $J = \left| L\text{-}S \right| \ldots L\text{+}S$,[45–47] split in the region of 10^3 cm^{-1}.[48] As such, the ground term can now be represented by, $^{(2S+1)}L_J$. In addition, the J value corresponding to the lowest energy will be governed by another of Hund's rules:[45,49]

3. The largest value of J when the number of f-electrons > $(2l+1)$, or the smallest value of J when the number of f-electrons < $(2l+1)$.

Continuing with Eu^{3+} as an example, the ground state J values would be evaluated as $J = 6, 5, 4, 3, 2, 1$, and 0; where according to Hund's third rule $J = 0$ would be the state the lowest in energy. This equates to a ground term of $^7F_0$ for Eu^{3+}.

The interaction of the 4f electrons with the surrounding ligand field influences the spherical nature of the orbitals, and thus splits these Stark components into $2J+1$ states. This effect will be referred to as J-splitting. This is a weaker interaction, and thus causes splitting in the order of 10^2 cm^{-1}.[37,48]

In the late 1960s, Carnell reported a series of papers regarding the spectral intensities and electronic energy states of a lanthanoid aquo series,[50–54] which was followed in 1989 with a similar investigation of lanthanoids doped in LaF_3.[55] Figure 2.2 illustrates the relative energy levels of the Ln^{3+} ions, as reported by Carnell, with lowest energy ground states and emissive excited states highlighted in blue.

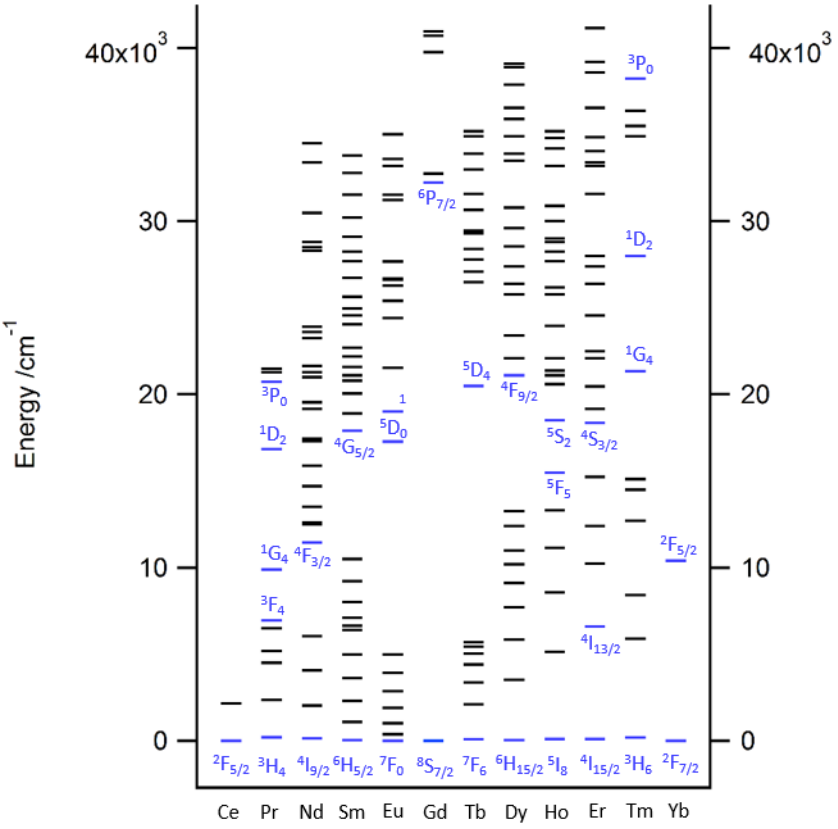

Figure 2.2 – Energy levels of the lanthanoids illustrating the ground and emitting excited states (blue). Energy values taken from Carnall *et al.*[51–54]

2.4 Fundamentals of Photophysics

Before dealing with the complexity of the nature of lanthanoid emissions, it is important to first cover the fundamentals of the interaction of light and matter. This section will discuss the process of harnessing light energy, for emission at very specific wavelengths.

2.4.1 Absorption of Light

The interaction of light and matter can be classed into three main interactions: reflection, transmission, and absorption.

The reflection of light simply describes the process of light hitting a sample surface and rebounding without penetration of the sample. This interaction occurs without a transfer of energy. In contrast, transmission also results in no transfer of energy, however presents a case in which the light is not at all reflected or refracted by the sample. In fact, transmittance of light means that the light will travel directly through a sample.

In contrast, when light hits a sample and the intensity dissipates, this is called absorption. As absorption of light is directly proportional to concentration, absorption is not defined as the inverse log of transmittance. Therefore it is useful to quantify absorbance in relation to relative concentration of chromophore using the Beer-Lambert law (Eqn 2.1).[56]

$$A = log\frac{I_0}{I} = \varepsilon bc \qquad \text{Eqn 2.1}$$

The term $log\frac{I_0}{I}$ describes absorbance and can be shortened to the term, A. In the Beer-Lambert law, ε is the molar absorptivity, b is the pathlength, and c is the concentration.[46] The molar absorptivity presents a quantitative approach to the inherent ability of the chromophore to absorb light, and is dependent on the concentration of the sample.

The absorption of light at specific frequencies from a molecule results in the molecule going from a low energy ground state, to a state of higher energy, often referred to as an excited state.

In conjugated organic chromophores, absorption of light can lead to electronic transitions with high molar absorptivities. Transitions involving excitation of electrons in a σ-bond (σ-σ*, n-σ*) require a very high energy input, whereas transitions of electrons in a conjugated π-system (π-π* or n-π*) are inherently lower in energy according to classic molecular orbital theory. A π-π* transition is typically the excitation of an electron in a conjugated bonding π-system to the antibonding π* orbitals. In contrast, an n-π* transition is usually of lower energy, and involves

the transition of an electron from a functional group bearing lone pair electrons to antibonding π* orbitals.[56]

2.4.2 The Fate of Excited States

The absorption of light by a molecule can lead to excitation to a higher electronic state. According to the Born-Oppenheimer approximation,[57] electronic transitions will occur so fast that the nuclear framework can be assumed to be stationary. Thus, it is assumed that the most probable electronic transitions will be between vibrational wavefunctions which have the greatest overlap, an approximation which is known as the Franck-Condon principle, after their published works in 1926 on the subject.[58,59] At this stage, the molecule is in a state of higher energy and will find a process to remove this energy.

In the excited state, the molecule can use this energy to react with surrounding molecules (photochemistry), or return to its electronic ground state *via* radiative and non-radiative relaxation pathways (photophysics).

Non-radiative relaxations include all pathways which do not result in emission of light. Figure 2.3 illustrates that the excitation of the molecule from the ground state (GS) has led to the population of a higher excited state of the same multiplicity (GS→S_2). This type of transition could refer to, for example, a π-π* transition in conjugated organic molecules. From here, the molecule can relax *via* molecular vibrations (v_r), to eventually occupy the lowest vibrational state (v_0) of the S_2 electronic excited state. Typically, energy lost by vibrational relaxation is given off as heat. This type non-radiative process occurs very rapidly, and as such, it is assumed that a system will undergo vibrational deactivation to a v_0 state.

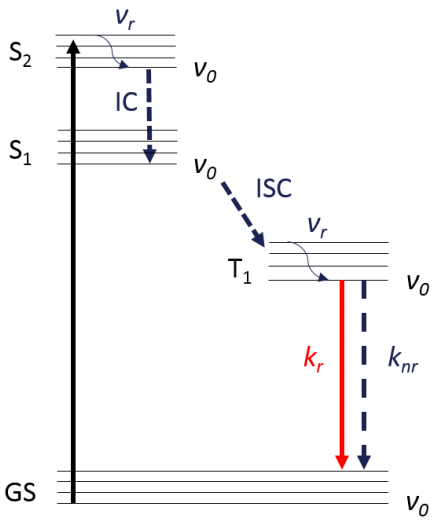

Figure 2.3 – Jabloński diagram illustrating common radiative and non-radiative decay pathways. The symbol *k* denotes the rate constant of radiative (*r*) and non-radiative (*nr*) processes.

Relaxation from an electronic excited state to a lower energy electronic state of the same spin multiplicity is a process known as internal conversion (IC).[60] This is typically the process which describes the relaxation from $S_1 \leftarrow\!\!- S_2$. In contrast, the relaxation from $T_1 \leftarrow\!\!- S_1$ is known as intersystem crossing (ISC), and instead involves a change in the spin multiplicity.

Although these are the classic processes of non-radiative relaxation, an electronic excited state can also be deactivated through collisions of molecules, known as collisional or concentration quenching. A non-radiative relaxation rate constant (k_{nr}) is used to denote the non-radiative processes occurring. The non-radiative process from $GS \leftarrow\!\!- S_1$, or $GS \leftarrow\!\!- T_1$ can be a contribution of more than one of the examples described above. The other process of relaxation is of course radiative relaxation denoted by a radiative decay constant (k_r).

Radiative decay is the decay which is accompanied by emission of light in the form of luminescence. It is assumed that radiative decay will most likely occur from the lowest excited state. This is known as Kasha's rule defined by Michael Kasha in 1950, stating that:

"The emitting electronic level of a given multiplicity is the lowest excited level of that multiplicity".[60]

Kasha's rule explains the common observation of an emission spectrum being of lower energy than an absorption spectrum, of which the difference in wavelength is commonly referred to as the Stokes shift. For example, Figure 2.4 illustrates this process. Using light (*hv*), excitation occurs from the GS to a variety of vibrational levels of the S2 excited state. Kasha's rule is valid after rapid vibrational relaxation and IC to the v_0 vibrational level of the S_1 excited state. Emission from this excited state to the vibrational levels of GS results in an overall emission of a lower energy than the original excitation. The 0-phonon transition is defined as the electronic transition from $v_0 \leftarrow\!\!- v_0$ vibrational states (Figure 2.4). The energy of this transition can be estimated at the highest energy band of vibrational progression in the emission spectrum.

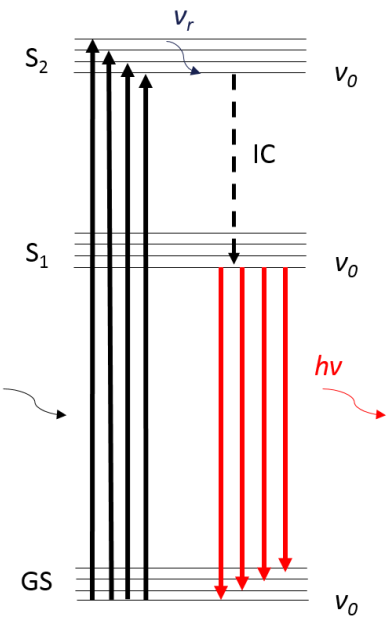

Figure 2.4 – Generalised absorption (black) and emission (red) highlighting Kasha's rule.

Before the properties of light emission are discussed in depth, it is necessary to define the probability of an electronic transition occurring. Electronic transitions

are subject to some quantum mechanical selection rules which govern the probability of an electronic transition taking place.

2.4.3 Selection Rules

For simplicity, the discussion throughout this chapter will focus on three selection rules, including the spin selection rule, the Laporte selection rule, and the orbital angular momentum selection rule.

The spin selection rule states that electronic transitions which involve a change in the spin multiplicity (e.g. ISC) are forbidden.

Rule: $\Delta S = 0$

The Laporte selection rule states that an allowed electronic transition should be accompanied by a change in parity. The symmetry of atomic orbitals can be described as gerade (*g*), for *s* and *d* orbitals, and ungerade (*u*), for *p* and *f* orbitals. These terms describe whether the orbitals *are* or *are not* defined by a centre of inversion respectively. Thus, transitions which are Laporte allowed follow, $l = \pm 1$. Intrashell transitions therefore do not change parity and hence the transition dipole moment and transition probability will be zero.

Rule: $l = \pm 1$

As the quantum number *J* describes angular spin momentum, its selection rule will be governed by both S and *L* quantum numbers. As a photon is a boson with $S = 1$, *L* must also change by 1 as angular momentum couples with spin. This means that $\Delta L = 0, \pm 1$, and in turn $\Delta J = 0, \pm 1$.

If the starting *J* state is zero, this would mean that the system would not have any momentum. Furthermore, if in both involved states $J = 0$, the transition would not have any momentum, and so the transition probability would be strictly zero. Therefore, any $J_0 \rightarrow J_0$' transitions are strictly forbidden by the law of conservation of momentum.

Rule: $\Delta L = 0, \pm 1$ $\Delta J = 0, \pm 1$ $J_0 \rightarrow J_0$' is forbidden

The spin selection rule can be relaxed through spin-orbit coupling. This is typical in species containing heavy atoms (those with many electrons), and is a common hypothesis for the relaxation of some spin-forbidden electronic transitions.[46] In theory *f-f* transitions are forbidden by parity. However, the Laporte selection rule can be relaxed through vibrational distortions of the wavefunction which temporarily change the parity of the wavefunction, or make the parity no longer well-defined. In these cases, transitions such as *f-f* become slightly allowed, as parity may not be defined as purely $u \rightarrow u$.

2.4.4 Luminescence

The term *luminescenz* was first introduced in 1888 by the great German physicist Eilhardt Weidemann, to describe the light which is not conditioned by a rise in temperature, *viz.* incandescence.[61,62] In general, luminescence is a term which can be used to describe the processes of phosphorescence and fluorescence.

Since the middle ages, the term *phosphor*, derived from the Greek word 'phosphoros' meaning 'light-bringer', has been used to describe materials which glow-in-the-dark after excitation with light. In fact, in the later part of the 1600s, a German alchemist, Henning Brandt, assigned the same name to the element phosphorus, after he noticed that it burns brightly when exposed to air.[62] Although this technically was not phosphorescence, but rather chemiluminescence, the term phosphorescence was thereafter used to describe emission of light.

Nowadays, after much deliberation over the exact electronic mechanism of phosphorescence,[63–65] the word *phosphorescence* has come to describe the emission of light from an electronic transition which is forbidden by the spin selection rule.[66] In this thesis, phosphorescence will be dealt with in ligand-centred singlet⟵triplet emissions ($^1\pi\pi \longleftarrow {}^3\pi\pi^*$), as well as some typical long-lived lanthanoid metal-centred emissions (Eu^{3+}, $^7F_2 \longleftarrow {}^5D_0$).

It was later in 1852, that Sir George G. Stokes coined the term *fluorescence* to describe the observation of dispersive reflexion from fluorspar.[62,67,68] On halting the excitation source, Stokes observed an immediate cessation in the 'epipolism'

(now obsolete term for fluorescence), and deemed this phenomenon to be different to the longer-lived phosphorescence. Stokes reported that fluorspar was able to transform UV light to blue visible light. This red shift in emission compared to absorption is now known as the aforementioned Stokes shift.

To follow IUPAC naming rules, fluorescence is the radiative emission of light from a spin-allowed transition.[66] Its spin-allowed nature makes fluorescence a bright and efficient emission characterised by short-lived excited states. This type of radiative emission is typical of short-lived ligand-centred singlet←singlet emission ($^1\pi\pi \leftarrow\!\!- {}^1\pi\pi^*$), and even some lanthanoid metal-centred emission (Yb^{3+}, $^2F_{7/2} \leftarrow\!\!- {}^2F_{5/2}$).

2.5 Absorption of the Lanthanoids

The lanthanoids can absorb light resulting in metal-centred 4*f*-5*d* transitions or 4*f*-4*f* transitions. This thesis will focus on the 4*f*-4*f* transitions.

2.5.1 Intraconfigurational *f-f* Transitions

The 4*f*-4*f* electronic transitions are forbidden, however in a ligand field, the Laporte selection rule is somewhat relaxed. Therefore, it is sometimes possible to observe these intraconfigurational *f-f* transitions, appearing as line-like absorptions, as the *f*-orbitals are well protected from the ligand field.

Some of these induced electric dipole (ED) transitions are highly sensitive to the coordination environment, whereby intensity is affected as the mixing of electronic states with those of the ligand field. This phenomenon was coined the *nephelauxetic effect* (cloud-expanding) by Schäffer and Jørgensen in 1958, citing the term construction to Prof. Kaj Barr.[69] The effect itself describes the cloud expanding nature of the *f*-orbitals as an effect of the electron cloud of the ligand field, which promotes overlap of metal and ligand orbitals thus relaxing the Laporte selection rule.[70,71]

The *f-f* electronic transitions directly affected by the nephelauxetic effect are called *hypersensitive* transitions, and are observed in lanthanoid absorptions and emissions. It was Judd[72] and Ofelt[73] who independently, but simultaneously, reported expressions to explain the relative and differing intensities of the *f-f*

transitions. Since their reports presented very similar results, their theory became known as the Judd-Ofelt theory.[74]

These intraconfigurational transitions are characterised by very small absorption cross-sections. Thus, it is necessary to excite the lanthanoids in a more efficient way.

2.6 The Antenna Effect

With a need for an efficient pathway to the excitation of the lanthanoids, Weissman in 1942 reported the first ever description of lanthanoid sensitisation by intermolecular energy transfer from an organic fluorophore.[1] Although thereafter Crosby solidified findings on the subject,[25,26,75] the effect was named in the later 1980s as the *antenna effect* by Sabbatini and Lehn.[2,3] The effect simply describes the process of using a sensitising molecule, which has a greater capacity for absorption of light, that can transfer the energy to the lanthanoid resulting in metal-centred emission as represented in Figure 2.5.[9] The sensitising molecule is generally based upon an organic framework,[9,76–79] however it is not uncommon to sensitise lanthanoid emission *via d*-metals,[80–86] or other lanthanoids.[87,88]

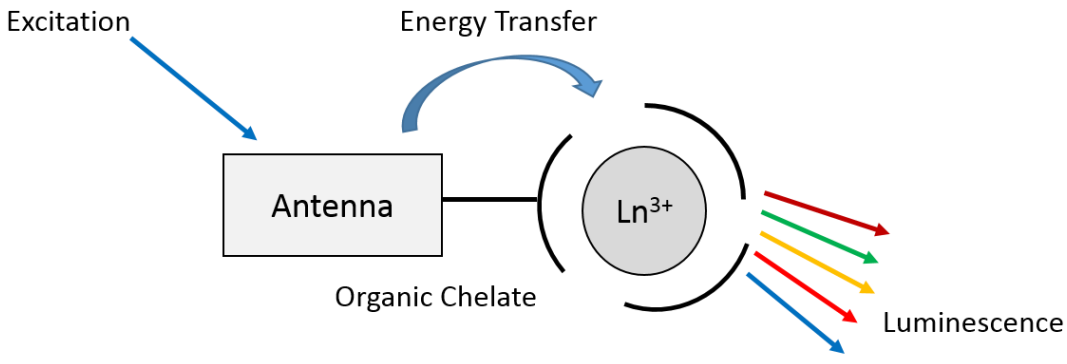

Figure 2.5 – A pictorial representation of the transfer of energy in the antenna effect.

The antenna effect involves the absorption of light from the antenna molecule. This transition is illustrated in the Jabloński diagram in Figure 2.6 as excitation

from the ground state of the ligand (GS) to the excited state. Decay pathways in Figure 2.6 are denoted by their rate constants (k). The S_2 state can decay to the S_1 state *via* IC, which can then deactivate non-radiatively (k_{nr}^{fl}), or radiatively by fluorescence (k_r^{fl}). In the presence of the lanthanoid, the singlet and triplet states can alternatively undergo aspin-forbidden ISC, to populate a lower energy T_1 state. Similarly the T_1 state can decay non-radiatively (k_{nr}^{ph}) or radiatively by phosphorescence (k_r^{ph}). From the T_1 state, there can also be an energy transfer (ET) to the lanthanoid, which itself can decay non-radiatively (k_{nr}^{Ln}) or radiatively by luminescence (k_r^{Ln}). Each of these decay rates mentioned are affected by the nature of the ligand and/or lanthanoid cation, and this section will describe some of these key influences and the optimisation of the antenna effect.

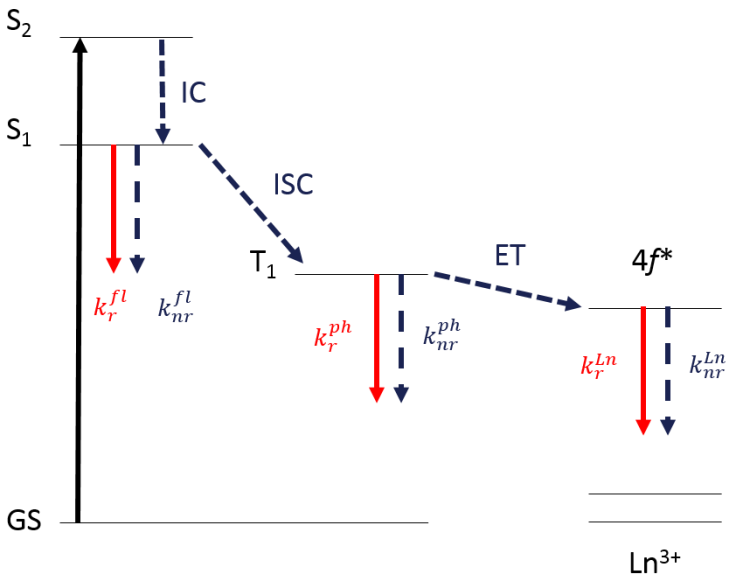

Figure 2.6 – Jabloński diagram illustrating the energy states as well as radiative and non-radiative pathways associated with the antenna effect.

2.6.1 The Heavy Atom Effect

The enhancement of the rate of a spin-forbidden process due to the presence of a heavy atom is called the heavy atom effect. This effect enhances the rate of singlet

to triplet processes such as the aforementioned ISC, as well as triplet to singlet processes such as phosphorescence.[46] The presence of a heavy atom increases the spin-orbit coupling within the atom itself as well as surrounding atoms, enhancing the mixing of singlet and triplet states, thus relaxing the spin selection rule. The effect is not only seen in the presence of the lanthanoids but also other heavy metals, or even in solvent systems whereby a heavy atom such as bromine is found.[89]

In the case of the antenna effect, the heavy atom effect can be referred to as the *external heavy atom effect* as the electron affected is that of the surrounding ligands. This effect results in the ISC mechanism being enhanced. It has been reported that for an efficient ISC the $\Delta E(^1\pi\pi^*\text{-}^3\pi\pi^*)$ should be greater than 5,000 cm^{-1}.[90]

Furthermore, the heavy atom effect extends to the populated triplet state, in which k^{ph} will increase due to the relaxation in the spin-selection rule. In the antenna effect, this emission is not the goal, with the energy transfer from this state to the lanthanoid the preferred pathway.

2.6.2 The Role of the Triplet State

The triplet state of the sensitising ligand plays a vital role in the antenna effect, however it is believed that energy transfer to the lanthanoid is also possible from the singlet state.[91,92] Although energy transfer to the lanthanoid occurs very rapidly, the triplet state will typically give rise to the more appreciable yield of ET to the lanthanoids given its excited state is longer-lived than the singlet state. Therefore, the relative energy of this level is very important in respect to the excited state energies of the lanthanoids.

For example, if the triplet state energy is lower than the lanthanoid emissive states, it is very unlikely that energy will be transferred to the lanthanoid excited state which is higher in energy. In addition, if the triplet state energy is much too high compared with an accepting excited state of the lanthanoid, this too will result in a very inefficient energy transfer.

In fact, it has been reported that the optimal energy difference for efficient energy transfer is a triplet state which lies ~3,500 cm^{-1} above the accepting lanthanoid excited state.[90] In the case of Eu^{3+}, energy transfer will usually occur to the $^5D_0$ (17,200 cm^{-1}) or $^5D_1$ (19,000 cm^{-1}) states. However, Sato and Wada have

reported that for efficient funnelling of the energy to the $^5D_1$ state, an energy difference of 1,500 cm^{-1} is sufficient.[93]

As the triplet state of the sensitising ligand is the most important factor in transferring energy to the lanthanoid, it is important that the quenching of this state in inhibited. The triplet state is long-lived in comparison to the singlet state, and hence can be effectively quenched by ground state triplet oxygen by triplet-triplet annihilation. In fact, there are many reports of oxygen quenching of lanthanoid emission *via* the triplet state.[64,94–97]

This mechanism is a collision based quenching process which involves an electron transfer between the excited triplet state ligand and the ground state triplet oxygen, resulting in the ligand returning to its ground singlet state and the oxygen excited to its singlet state. This type of quenching is plausible, but is usually curtailed if the energy transfer from ligand triplet state to the lanthanoid is relatively fast and efficient. However, if triplet oxygen quenching is affecting the ligand triplet state, removal of oxygen from the environment would evidently inhibit this quenching process.

It is possible to estimate the relative singlet and triplet state energies of organic molecules experimentally. The method is to measure the emission of the organic molecule in a solvent at a low temperature, in order to estimate the 0-phonon transition from a triplet state emission. At ambient temperature, triplet state emission might not be observed as the triplet excited state is quenched much faster than the radiative decay. However, at low temperature quenching is relatively reduced, due to the slower diffusion of oxygen, and it is possible to observe emission from the triplet state.

This triplet state emission can be improved by improving ISC *via* use of a solvent containing heavy atoms. Furthermore, the addition of a Gd^{3+} source can further improve the ISC by the heavy atom effect. Energy transfer in this case will most likely not occur from ligand to Gd^{3+}, as its lowest excited state ($^6P_{7/2}$) is far too high in energy (32,500 cm^{-1})[54] to be populated by the antenna effect.

Another option is the use of molecules containing lone-pair electrons, as El-Sayed's rule states that the spin selection rule is slightly relaxed if the ISC

involves a change of orbital type.[98] For example, the ISC will occur faster if the transition is from $^1n\pi^*$ to $^3\pi\pi^*$, rather than $^1\pi\pi^*$ to $^3\pi\pi^*$.

The singlet and triplet state energies can be estimated by assuming the 0-phonon transitions, at the highest energy vibronic progression band of the singlet or triplet emission spectrum. This simple experiment provides an insight into the expected efficiency of energy transfer from antenna to different lanthanoids.

2.6.3 Energy and Charge Transfer Mechanisms

Once the triplet state of the sensitiser is populated, the next step is the transfer of this energy to excite the lanthanoid species. The transfer of energy from sensitiser to lanthanoid can occur *via* a formal energy transfer (ET) mechanism, or aided by a less common ligand-to-metal charge transfer (LMCT) mechanism.

2.6.3.1 Energy Transfer

The antenna effect relies upon the energy transfer from ligand to lanthanoid, which may occur by various mechanisms including, Förster resonance energy transfer (FRET), Dexter electron transfer, or the lesser known dipole-multipole mechanism. For the simplicity of discussion, this thesis will focus on the FRET and Dexter mechanisms, however, it should be noted that the dipole-multipole mechanism may also contribute greatly to the energy transfer process.[9,91]

The mechanism of FRET was reported by Förster in 1948,[99] in which he described the transfer of energy *via* a virtual photon (Figure 2.7). In general, the donor molecule in its excited state (D*) can decay *via* two pathways: to its ground state releasing a virtual photon which excites the accepting molecule (A), or *via* a non-radiative/radiative decay. The release of a virtual photon leaves the donor in its ground state (D) and the acceptor in its excited state (A*). The energy transfer process does not include the transfer of electrons, rather the transfer of energy *via* a resonance type energy transfer. Moreover, it is not necessary that the donor and acceptor be in contact, they need only be within a sufficient distance for exchange of energy.

On the other hand, Dexter electron transfer, discovered by Dexter in 1953,[100] involves the movement of electrons rather a virtual photon (Figure 2.7). For

example, the excited donor molecule (D*) transfers an excited electron to the accepting molecule (A), which simultaneously transfers a ground state electron to the donor. This results with the acceptor in its excited state (A*) while the donor finds itself in its ground state (D).

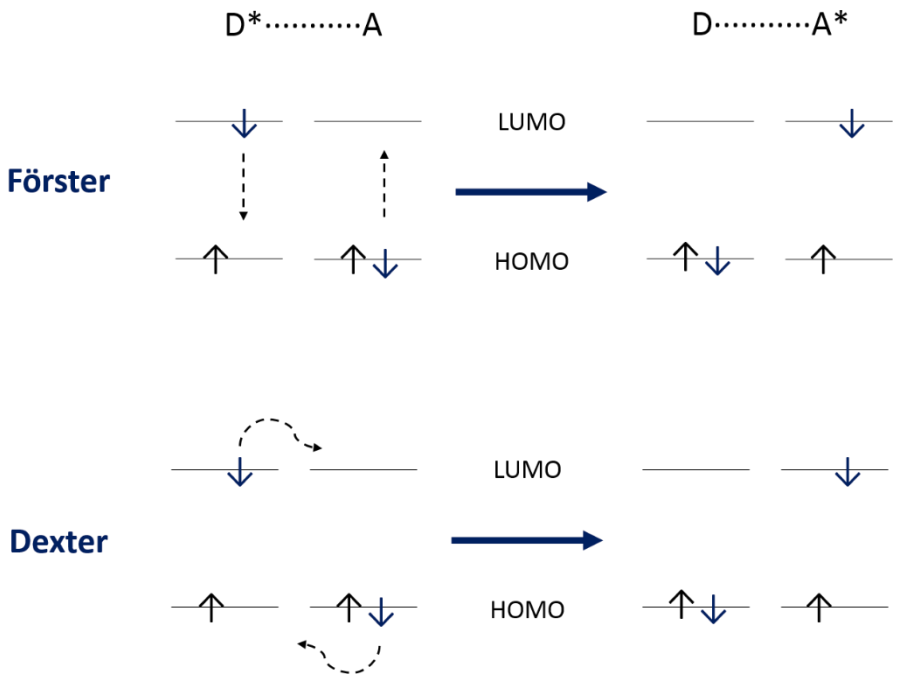

Figure 2.7 – Förster (top) vs. Dexter (bottom) energy transfer mechanisms.

The exact mechanism of energy transfer from ligand to lanthanoid is largely assumed throughout the literature to be a mixture of the two mechanisms.[37,49]

2.6.3.2 **Ligand-to-Metal Charge Transfer**

While traditional energy transfer mechanisms have been discussed above, a LMCT mechanism has also been identified for some trivalent lanthanoids. A LMCT is the oxidation of a ligand and concurrent reduction of a metal as a consequence of photoabsorption. In particular Eu^{3+} and Yb^{3+} are somewhat prone to LMCT, as they are more readily reduced in comparison to other trivalent lanthanoids.[36] The energy of the LMCT state will vary depending on the character of the ligand.

In the case of Eu^{3+}, the LMCT state is usually a dark state and finds an efficient non-radiative decay to the ground state Eu^{3+} ion.[101–104]

In comparison, the LMCT to Yb^{3+} is relatively less explored, and in fact the exact mechanism is still not known. The first report of an Yb^{3+} emission supported by an initial LMCT mechanism was reported by Horrocks.[105] with an Yb^{3+}-tryptophan complex. It is possible that the strong reducing potential of the ligand in this case was a key to the reduction of Yb^{3+} to Yb^{2+}. There have been some reports thereafter hypothesising the LMCT mechanism.[106–109]

2.6.4 Quenching of Lanthanoid Excited States

Once the lanthanoid excited state has been populated, the lanthanoid can decay radiatively with its characteristic line-like emission, or alternatively decay non-radiatively. The main causes of quenching include back energy transfer (BET) to the ligand triplet state, lanthanoid-lanthanoid cross-relaxation, or by multiphonon relaxation with molecular vibrations in the coordinating ligand or solvent molecules. All of these processes will lead to an increase in non-radiative decay in each emissive lanthanoid.

2.6.4.1 Back Energy Transfer

The optimal energy difference between ligand triplet state and lanthanoid excited state takes into account the possibility of BET from lanthanoid to ligand. If the triplet state and lanthanoid excited states lie too close in energy, it is possible that the lanthanoid will transfer that energy back to ligand in a similar fashion. In this case, the energy could then be lost through triplet state emission, or non-radiative decay from the ligand triplet state. Thus, the tuning of a ligand triplet state is very important. In fact, the optimal ΔE between triplet and lanthanoid excited state has been reported to be >3,500 cm^{-1} for irreversible and efficient sensitisation.[90]

2.6.4.2 **Lanthanoid-Lanthanoid Cross Relaxation**

Lanthanoid-lanthanoid cross relaxation quenching is possible if the lanthanoid ions in a system are very close in distance (<8.0 Å).[110] In this case, an excited lanthanoid is capable of transferring the energy to a ground state lanthanoid in close proximity, by either a FRET or Dexter energy transfer mechanism. This type of quenching can also occur at distances longer than 8.0 Å, particularly where the energy transfer can be ligand mediated.[111]

2.6.4.3 **Multiphonon Relaxation**

The more common type of lanthanoid quenching is due to multiphonon relaxation with common molecular vibrations found in surrounding ligands or solvent molecules. In general, the lanthanoids are more easily quenched with a smaller energy gap between lowest energy excited state and highest energy ground state.[37] This is because it takes less vibrational quanta to accept that energy. In 1975, Stein and Würzberg reported this effect to be a *modified energy gap law*.[112]

A typical example of multiphonon relaxation is the quenching of Eu^{3+} by OH and OD stretching vibrations (Figure 2.8). The ΔE between the $^7F_6$ and $^5D_0$ states is ~12,297 cm^{-1},[51] and thus the $^5D_0$ state can be effectively quenched by the third harmonic (ν_3) of the OH stretching vibration (water, ν_1 = 3,657 cm^{-1}).[113]

The quenching of the Eu^{3+} excited state by OH is typically reduced by deuteration strategies as the OD stretching vibration is of lower frequency (D_2O, 2,621 cm^{-1})[113] and thus it takes four vibrational quanta for efficient quenching. Therefore, it is evident that solvent molecules such as water and alcohols should not be close to a Eu^{3+} metal centre if the aim is a highly emissive Eu^{3+} species.

Generally, Eu^{3+} and Tb^{3+} [$\Delta E(^7F_0\text{-}^5D_4)$ = 14,800 cm^{-1})][52] are characterised by longer-lived excited states than other visible emitting lanthanoids such as Dy^{3+} [$\Delta E(^6F_{3/2}\text{-}^4F_{9/2})$ = 7,850 cm^{-1}][53] and Sm^{3+} [$\Delta E(^6F_{11/2}\text{-}^4G_{5/2})$ = 7,400 cm^{-1}][53] as a consequence of this energy gap law, and the more proficient quenching of the Dy^{3+} and Sm^{3+} excited states.[37]

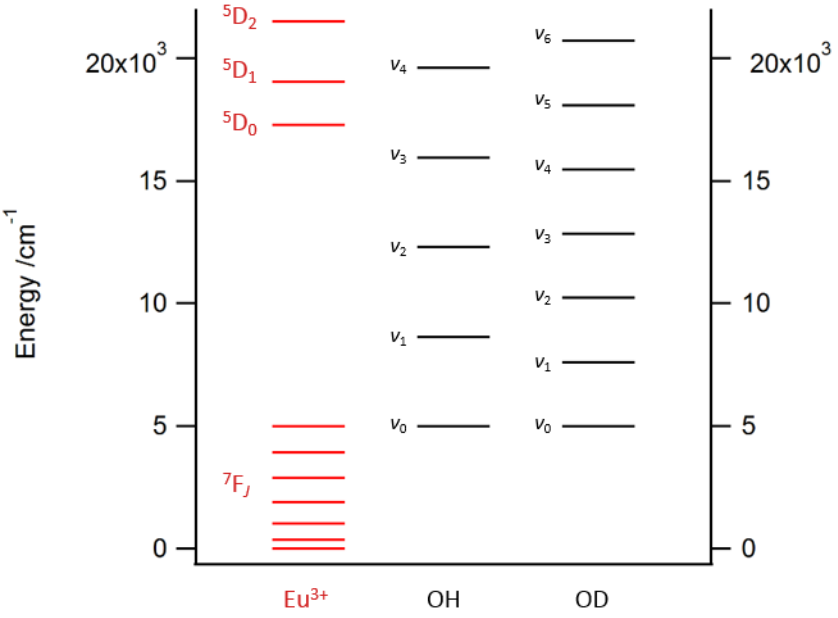

Figure 2.8 – Quenching of Eu^{3+} $^5D_0$ excited state through OH and OD vibrations.

At the end of the 1970's, Horrocks and Sudnik discovered that the different quenching efficiencies could be used to evaluate the number of coordinated water molecules in a Eu^{3+} or Tb^{3+} complex.[114,115] The report analysed the excited state lifetimes of the various species of known formulation in both H_2O and D_2O solvent systems. Remarkably the reciprocal of the difference in the lifetimes for each complex, in milliseconds (ms), was found to be directly proportional to the known number of coordinated H_2O molecules (w, ± 0.5). Thus resulted in a linear regression described in Eqn 2.2.

$$w = a \times ({\tau_{H_2O}}^{-1} - {\tau_{D_2O}}^{-1}) \qquad \text{Eqn 2.2}$$

Taking the slope of the regression leads to the evaluation of the constant a (where a = 1.05, 4.20 for Eu^{3+} and Tb^{3+}, respectively). Although there are reports considering outer sphere quenching oscillators,[116–118] the Horrocks model is still a very good estimation of the degree of coordinated water.

Soon thereafter, Horrocks extended the investigation to methanol, realising that the effect of quenching should be consistent, with the assumption methanol would act as half a water molecule.[119] Another useful expression was discovered (Eqn 2.3) for the number of coordinated methanol molecules. In the equation, *m*, refers to the number of coordinated methanol molecules (± 0.5), and again *a* is a constant (*a* = 2.1, 8.4 for Eu^{3+} and Tb^{3+}, respectively).[48]

$$m = a \times ({\tau_{CH_3OH}}^{-1} - {\tau_{CD_3OD}}^{-1}) \qquad \text{Eqn 2.3}$$

The NIR emitting lanthanoids such as Nd^{3+}, Er^{3+}, and Yb^{3+} are also significantly quenched by multiphonon relaxation with vibrations of OH, but also CH, and NH. In fact, lifetime and quantum yield measurements indicate that the NIR emitters are usually significantly less intense than the brighter Eu^{3+}/Tb^{3+}, which is in agreement with the aforementioned modified energy gap law. These quenching bonds are common in organic antennae and so they are obviously a problem in obtaining NIR emission from the lanthanoids. An example of the quenching of Yb^{3+} by different organic bonds is presented in Figure 2.9.

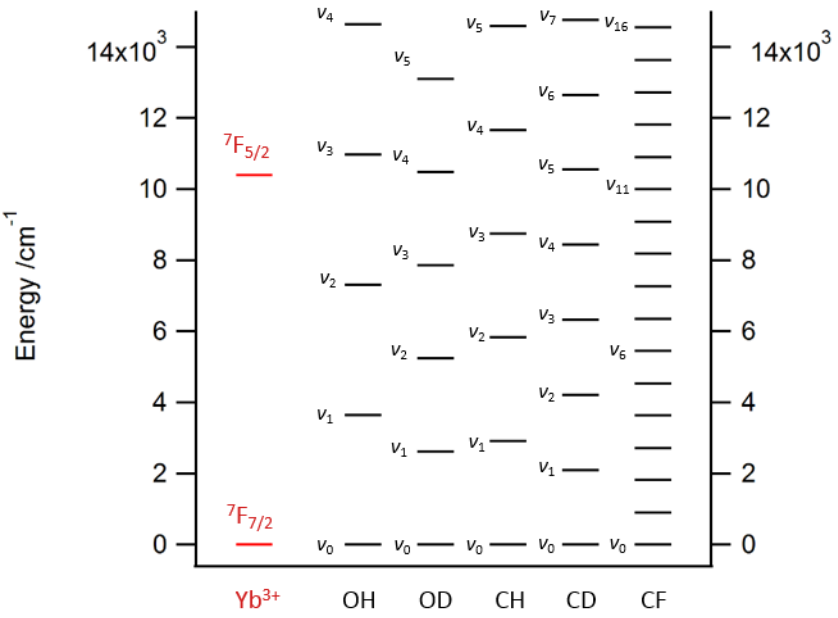

Figure 2.9 – Relative energies of OH, OD, CH, CD, and CF vibrations[113] with respect to the Yb^{3+} excited state.

A common practice to remove this type of quenching is again to deuterate (i.e. OD, CD),[120,121] or even perfluorinate (i.e. CF).

Perfluorination of organic ligands is clearly the most efficient inhibitor of multiphonon relaxation for the NIR emitters, with the CF vibration being of very low frequency (CF_4, 909 cm^{-1}).[113] It is therefore not surprising that this substitution is a very common method of improving the efficiency of NIR emission in the lanthanoids.[122] Although deuteration and perfluorination strategies are efficient in reducing quenching *via* multiphonon relaxation, they are often synthetically challenging or not readily available in synthetic labs.

The number of H_2O/CH_3OH molecules coordinated to Yb^{3+} has also been investigated in a similar fashion to the work of Horrocks. Faulkner presented a modified equation for the Yb^{3+} ion, which includes the contribution of outer sphere oscillators to the quenching by the coefficient *C* (Eqns 2.4-2.5, *C* = 0.2 and 0.1 for H_2O and CH_3OH, respectively).[117,123,124]

$$w = \left({\tau_{H_2O}}^{-1} - {\tau_{D_2O}}^{-1}\right) - C \qquad \text{Eqn 2.4}$$

$$m = 2 \times \left({\tau_{CH_3OH}}^{-1} - {\tau_{CD_3OD}}^{-1}\right) - C \qquad \text{Eqn 2.5}$$

This type of vibrational deactivation of lanthanoid excited states is temperature dependent, and therefore the effect of multiphonon relaxation can be effectively reduced at low temperature.[37] Generally, if there is little change in the value of excited state lifetime (τ_{obs}) with varying temperatures, this suggests that multiphonon relaxation is not a major contributor to the quenching of the lanthanoid.

2.6.5 Quantifying the Efficiency of the Antenna Effect

In general, the efficiency of the antenna effect is considered by overall quantum yield measurements (Φ_{Ln}^{L}), described in Eqn 2.6. The quantum yield describes the

efficiency of the entire process from absorption of the antenna to emission of the lanthanoid.

$$\Phi_{\mathrm{Ln}}^{\mathrm{L}} = \frac{no.of\ photons\ emitted}{no.photons\ absorbed} \qquad \text{Eqn 2.6}$$

Regarding the sensitising ligand, the efficiency of absorption to energy transfer is known as the sensitisation efficiency (Φ_{sens}), and is formulated by the relative efficiencies of the ISC (Φ_{ISC}) and energy transfer (Φ_{ET}) mechanisms (Eqn 2.7).[37]

$$\Phi_{\mathrm{sens}} = \Phi_{\mathrm{ISC}} \times \Phi_{\mathrm{ET}} \qquad \text{Eqn 2.7}$$

The intrinsic quantum yield ($\Phi_{\mathrm{Ln}}^{\mathrm{Ln}}$) describes the relative contribution of radiative decay from the lanthanoid excited state compared to non-radiative decay. This can be expressed in terms of the radiative (k_r) and non-radiative (k_{nr}) rate constants in Eqn 2.8.[125]

$$\Phi_{\mathrm{Ln}}^{\mathrm{Ln}} = \frac{k_r}{k_r + k_{nr}} \qquad \text{Eqn 2.8}$$

In the case of the antenna effect, the overall quantum yield is dependent on the sensitisation efficiency (Φ_{sens}) of the coordinated ligand, and the relative intrinsic quantum yield ($\Phi_{\mathrm{Ln}}^{\mathrm{Ln}}$) of the lanthanoid excited state (Eqn 2.9).[9]

$$\Phi_{\mathrm{Ln}}^{\mathrm{L}} = \Phi_{\mathrm{sens}} \times \Phi_{\mathrm{Ln}}^{\mathrm{Ln}} \qquad \text{Eqn 2.9}$$

While the overall quantum yield can be determined experimentally,[126] the sensitisation efficiency and intrinsic quantum yield values can be more difficult to estimate.

The observed lifetime (τ_{obs}), describes the time taken for the lanthanoid excited state to reduce to 1/e of its original value.[66] Eqn 2.10 describes the observed lifetime in terms of radiative (k_r) and non-radiative decay (k_{nr}) constants.[125]

$$\tau_{obs} = \frac{1}{k_r + k_{nr}} \qquad \text{Eqn 2.10}$$

In contrast, the radiative lifetime (τ_R) describes the lifetime of a lanthanoid excited state in the absence of non-radiative decay pathways (Eqn 2.11).[125]

$$\tau_R = \frac{1}{k_r} \qquad \text{Eqn 2.11}$$

Determining the radiative lifetime experimentally is much more difficult, however has been achieved for some lanthanoid excited states.[49,125]

Finally, the sensitisation efficiency (Φ_{sens}) can be determined experimentally by the use of Eqn 2.12.

$$\Phi_{Ln}^{L} = \Phi_{sens} \times \frac{\tau_{obs}}{\tau_R} \qquad \text{Eqn 2.12}$$

2.7 Characteristic Lanthanoid Emission

Each of the lanthanoids has a characteristic emission due to their unique *f*-electronic configurations. However, small interactions of the *f*-orbitals and orbitals of the ligand field will influence the structure of the emission bands, and can provide insight into the coordination geometry. The emission spectra of the visible emitting Eu^{3+} and the NIR emitting Er^{3+} and Yb^{3+} will be discussed, as these lanthanoids are the focus in this work.

2.7.1 Europium

The first observation of the classic line-like emission from Eu^{3+} was reported in 1906 by French chemist, Georges Urbain, after he discovered the intense red emission from a sample of yttrium oxide doped with europium.[127,128] From the

discovery in Urbain's work, the field of Eu^{3+} emission in inorganic phosphors has grown rapidly.[71]

The emission spectrum of europium is useful as a probe to identify coordination geometry, and whether geometry is unique within a sample. Although europium emission from higher excited states such as the $^5D_1$ is known,[129] the most structural information comes from emission from the $^5D_0$ excited state. The $^5D_0$ state does not split in the ligand field as $2J+1 = 1$, and therefore splitting patterns in the emission peaks are intrinsic to the splitting of the ^7F_J states. The main seven emission bands correspond to $^7F_J \leftarrow ^5D_0$ where J = 0-6, and usually appear at 580, 590, 615, 650, 720, 750, and 820 nm respectively (Figure 2.10).

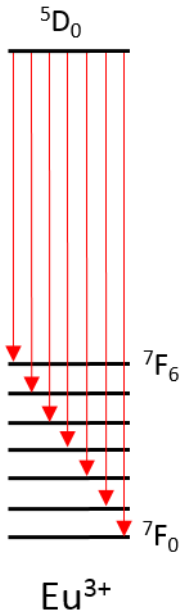

Figure 2.10 – Jabloński diagram of the radiative excited state emission, $^7F_J \leftarrow ^5D_0$.

2.7.1.1 **The Magnetic Dipole Allowed Transition**

An emission band which makes the Eu^{3+} spectrum unique, is the $^7F_1 \leftarrow ^5D_0$ band as this is the only transition in the lanthanoid series which is *solely* allowed by magnetic dipole (MD) selection rules.

As the transition is only MD allowed, the intensity of the transition is completely unaffected by the ligand field, and so the intensity should be identically comparable between all emissive Eu^{3+} complexes. As the integrated intensity of the MD transition should be independent of ligand field, it can therefore be compared to those transitions that are influenced by the ligand field to make useful comparisons of the deviation from centrosymmetric systems.

The common comparison is achieved using Eqn 2.13, where I_{rel} is the ratio of the integrated intensity of a transition $^7F_J \leftarrow {}^5D_0$ (J = 0, 2, 3, 4, 5, or 6) and the MD allowed transition $^7F_1 \leftarrow {}^5D_0$. When comparing the $^7F_2 \leftarrow {}^5D_0$ transition intensity, the higher the value of I_{rel}, generally the greater the deviation from a centrosymmetric ligand field.[130,131]

$$I_{rel} = \frac{I(\,^7F_J \leftarrow {}^5D_0)}{I(\,^7F_1 \leftarrow {}^5D_0)} \qquad \text{Eqn 2.13}$$

The radiative Eu^{3+} lifetime (τ_R) can be determined experimentally by the integrations of the $^7F_1 \leftarrow {}^5D_0$ MD allowed transition and the entire emission spectrum following Eqn 2.14 proposed by Werts,[125]

$$\frac{1}{\tau_R} = 14.65\ s^{-1}.\eta^3.\frac{I(\,^7F_J \leftarrow {}^5D_0)}{I(\,^7F_1 \leftarrow {}^5D_0)} \qquad \text{Eqn 2.14}$$

where 14.65 s^{-1} is the spontaneous emission probability of the $^7F_1 \leftarrow {}^5D_0$ transition reported previously[132] and η is the refractive index of the solvent (~1.5 for the solid state).[133,134]

2.7.1.2 **Probing Coordination Geometry**

A Eu^{3+} emission spectrum also has transitions in which their relative intensities change with the change in the ligand field.

The $^7F_2 \leftarrow {}^5D_0$ emission band at 612 nm is known as a hypersensitive band, and is usually the most intense emission peak in the Eu^{3+} emission spectrum. This effect is primarily caused by the nephelauxetic effect. This of course increases the overlap of the *f*-orbitals with orbitals of the ligand field, further relaxing the Laporte

selection rule, generally for the transitions involving $^7F_{2,4,6}$.[71,135] Not only is the $^7F_2 \leftarrow ^5D_0$ the most intense of the three transitions, but also the $^7F_2$ state can gain magnetic dipole allowed character as mixing of the *J*-states increases due to the non-centrosymmetric ligand field and couples the $^7F_1$ and $^7F_2$ states. Therefore the $^7F_2$ state also gains some MD allowed character, further increasing its intensity in a non-centrosymmetric ligand field.

Another transition sensitive to the ligand field is the $^7F_4 \leftarrow ^5D_0$ transition, and should usually be compared to the intensity of the $^7F_1 \leftarrow ^5D_0$ transition. The transition is generally less sensitive to the environment than the $^7F_2 \leftarrow ^5D_0$ transition, however, in some cases it has been reported to be as intensely emissive as the $^7F_2 \leftarrow ^5D_0$ state.[71,136]

The $^7F_0 \leftarrow ^5D_0$ at 580 nm is a J_0-J_0' transition and hence is strictly forbidden by the aforementioned selection rules. It is therefore not surprising that emission caused by this transition is sometimes not observed. However, *J*-splitting caused by interaction of the ligand field coordination in a non-centrosymmetric environment can give the transition some MD allowed character by mixing with the $^7F_1$ state. As the extent of this mixing is unique for each ligand field, emission from this state is also unique for each coordination geometry making it a useful probe for multiple geometries in a sample.

Experimentally it has been reported that for a single unique coordination site in a sample, the full-width at half-maximum (FWHM) of the emission band should generally be less than 40 cm^{-1}.[137,138] This value can be a good indicator as to whether there are multiple coordination geometries in a given sample.

The $^7F_3 \leftarrow ^5D_0$ electronic transition is forbidden by selection rules and usually results in very weak emission. The band is usually observed in non-centrosymmetric coordination geometries due to *J*-mixing with the hypersensitive $^7F_2$ state, however very rarely is its emission band very intense. However, there are rare cases where the emission to this state is astoundingly efficient.[139]

There are many reports using the splitting patterns observed in Eu^{3+} spectra to determine the relative ligand field geometry and symmetry present.[36,37,49] The

analysis of each band in the Eu^{3+} emission spectrum the emission, makes it a key tool for coordination sphere information

2.7.2 NIR Emitters

The NIR emitting lanthanoids Er^{3+} and Yb^{3+} are generally characterised by short-lived excited states, given that their emissions are spin-allowed transitions, and are prone to quenching.

The main emission band of interest for Er^{3+} is observed at 1540 nm and is attributed to the fluorescence from the $^4I_{15/2} \leftarrow\!\!- {}^4I_{13/2}$ electronic transition. This emission is of particular interest as it coincides with the wavelength needed for telecommunication amplification. As such, Er^{3+} emission finds application in erbium doped fibre amplifiers (EDFA).[7] Acquiring emission from this transition is quite elusive given that the Er^{3+} excited state is prone to quenching by multiphonon relaxation from common molecular vibrations in coordinated ligands, but also because the direct excitation of Er^{3+} ions is particularly inefficient.[49]

Emission from Yb^{3+} is centred 980 nm and is attributed to the $^2F_{7/2} \leftarrow\!\!- {}^2F_{5/2}$ electronic transition.[49] It is interesting to note that Yb^{3+} has only one excited state, as its 4*f*-orbitals contain 13 electrons. This excited state has an energy lying at ~10,400 cm^{-1} and hence can be easily accessed *via* the antenna effect, but also easily quenched through multiphonon relaxation with common molecular vibrations.

2.8 Luminescent Lanthanoid Complexes

As the antenna effect presents a logical and efficient approach to the acquisition of lanthanoid emission, the systematic design and application of ligand systems has been thoroughly explored. These range from simple coordinating molecules,[30,140,141] to larger organic chelates,[79,117,123,142] and coordinating macrocycles (Figure 2.11).[20,21,90,101,102,143–146]

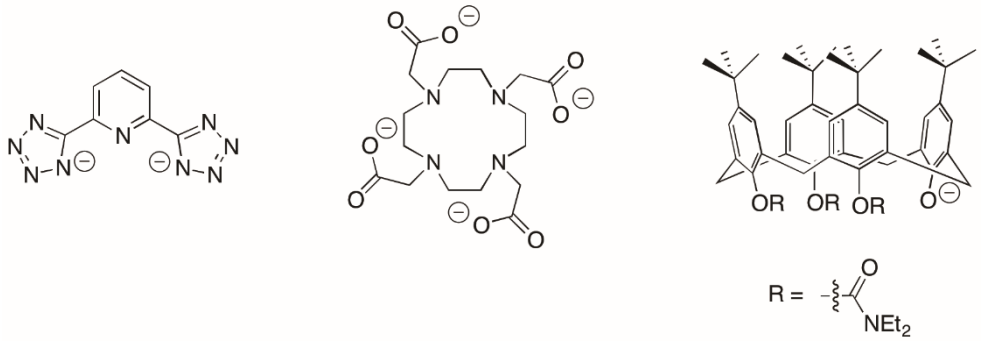

Figure 2.11 – Examples of organic antennae for lanthanoid coordination and sensitisation.[21,141,142]

More recently the sensitisation pathway has even been extended to *d*-metal sensitisation *via* metal-to-ligand charge-transfers (MLCT),[80–86] or even metal-centred sensitisation by auxiliary *f*-metal complexes, such as mixed Yb^{3+}/Er^{3+} complexes.[87,88]

Furthermore, lanthanoid complexation with sensitising ligands can lead to a range of structurally unique metal complexes ranging from simple mononuclear complexes,[141] to more elaborate lanthanoid clusters,[147–153] or even multimetallic complexes[84,85,110,154] and coordination polymers.[154–158]

Structurally, the β-diketonate ligand has produced a large variety of lanthanoid metal structures,[32–35,159–165] with the ability to sensitise lanthanoid emission.[130,166] The section will take a look at the different sensitising ligands capable of coordinating the lanthanoids, as well as the unique metal structures which can be identified after complexation.

2.8.1 Coordination Chemistry of the Trivalent Lanthanoids

Due to the inner core nature of the *f*-orbitals, the lanthanoids are generally assumed to coordinate organic ligands in an electrostatic fashion, with very little overlap in molecular orbitals. As such, the lanthanoids find a variety of coordination numbers generally ranging from 7-12.[36,45] This is of course reliant on solid angle factors (SAF) of the coordinating ligands, whereby the lanthanoid will tend towards completely filling its coordination sphere.[36] The size of the lanthanoid plays its role, where the larger ions will have a greater surface area for coordination. For example lanthanum, the largest of the trivalent lanthanoids, generally has a

coordination number of 9-12,[133,167] whereas for lutetium it is more common to find a coordination number of 7-9.[36] Another factor is the nature of the coordinating ligand. The bulkier the ligand, the higher the coverage of lanthanoid surface area upon coordination.

The electrostatic nature of lanthanoid-ligand bonding, gives preference to lanthanoid coordination with ligands bearing electronegative atoms or negatively charged donors. Thus, the lanthanoids are generally oxophilic, given the Lewis acid nature of the lanthanoid cations. Although neutral nitrogen donors have generated much interest in the field of sensitisation,[76,77,140,168] clearly the stronger interaction is that of oxygen donors. Since the work of Crosby in the 1960s,[25,26,75] the application of β-diketonate ligands as ligands and sensitisers of lanthanoid emission has grown immensely.[30]

2.8.2 β-Diketonates

The 1,3-diketone class of molecule was first synthesised by Claisen in 1896[169] and generally can be referred to as a β-diketone. The β-diketone molecule typically exhibits keto-enol tautomerism. In solution the tautomerism is present in equilibrium, usually highly influenced by the nature of the solvent (Figure 2.12).[29]

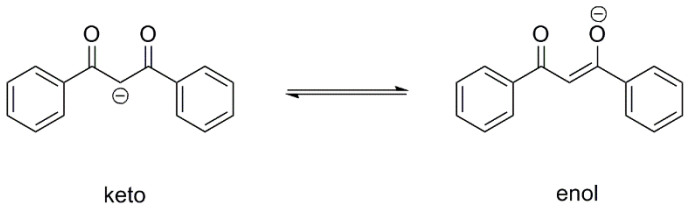

Figure 2.12 – keto and enol tautomers of deprotonated β-diketone, dibenzoylmethane.

The β-diketonate is a bis-chelating ligand, with relatively acidic protons on the α-C. Upon deprotonation, the negative charge is delocalised over the conjugated chelating part of the molecule (Figure 2.13).

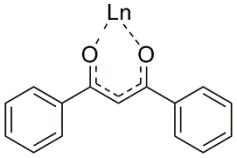

Ln(DBM)

Figure 2.13 – Typical bis-chelating mode of the β-diketonate ligand.

Structural investigations of lanthanoid β-diketonates have surged in recent times,[29,30,32,34,155,160,162,170] with interests focussed on the structural versatility of lanthanoid complexes when varying the substituents at the 1,3- positions on the β-diketonate backbone.[163] Such studies have deduced that changes in relative size of the substituents can affect the nature of the lanthanoid species formed, with structures obtained ranging from one metal centre to much larger multinuclear lanthanoid clusters (Figure 2.14).[33,171] These clusters are also known to be emissive, despite multiphonon relaxation with OH vibrations in the cluster core.[35,130,166,172]

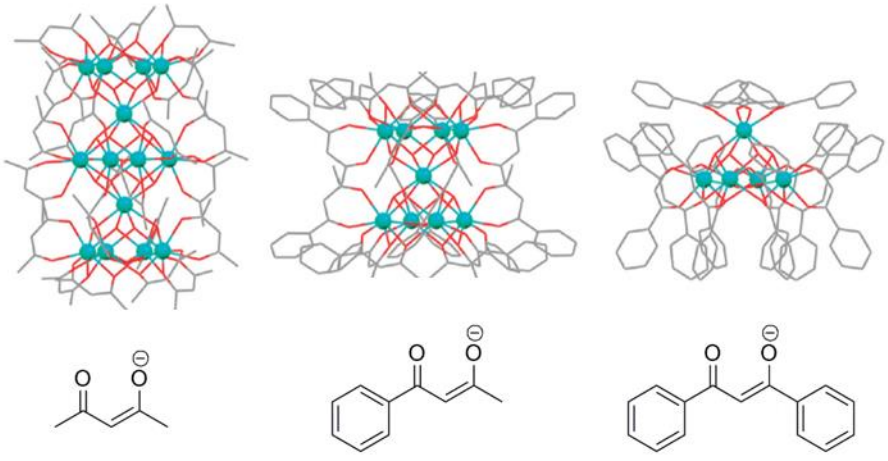

Figure 2.14 – Example lanthanoid cluster structures by varying the steric bulk at the 1,3-positions of the β-diketonate ligand adapted from Andrews *et al*.[33] The metal centre is Dy^{3+} in each case.

In the field of mononuclear lanthanoid β-diketonates, most work has focussed on the electrically neutral tris(β-diketonate) lanthanoid complexes. However, the six coordination sites filled by the ligand do not complete the lanthanoid coordination sphere, and so solvent molecules would typically complete the coordination.[163,173,174] This of course causes issues of multiphonon relaxation for photophysical applications, and hence there are many reports completing the coordination sphere with either another anionic β-diketonate,[28,175,176] or a neutral *N*-donor such as 1,10-phenanthroline (Phen) or 2,2'-bipyridine (Bipy).[92,177–180]

From a photophysical perspective, the substituents at the 1,3- positions of the β-diketonate backbone have often been perfluorinated to reduce the extent of multiphonon relaxation for NIR emitting lanthanoid species.[122,181–184] These are still not as efficient as an inorganic β-diphosphinate such as perfluorinated iminodiphosphinates (Figure 2.15),[185,186] which can yield Yb^{3+} metal-centred emissions with lifetimes up to 60 times longer than Yb^{3+} species with perfluorinated β-diketonate ligands. This is most likely an effect of the removal of the proton at the α-C position which would typically quench NIR emission, in conjunction with complete perfluorination of the ligand to remove aromatic CH quenchers.

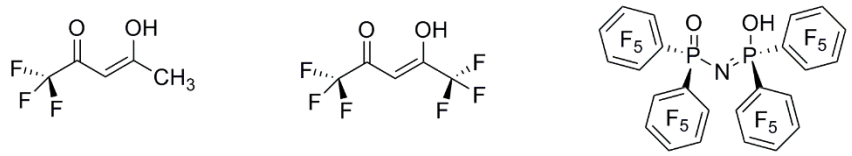

Figure 2.15 – Typical perfluorinated β-diketones (left[183] and middle[182]), and perfluorinated iminodiphosphinates.[185]

2.8.3 β-Triketonates

Lanthanoid complexes bearing β-diketonate ligands substituted at the 2- (or α-) position are rarer in the literature, with typical examples using a deuterium atom in the α-position for the abovementioned photophysical considerations.[182,187] However, there are examples of other more bulky α-substituted β-diketonate complexes, such as α-substituted allyl[188], phenyl[189], or nitrile[190] β-diketonates,

and moreover acetato-dehydroacetato ligands,[191] and 2-benzoylcyclopentanone derivatives (Figure 2.16).[192]

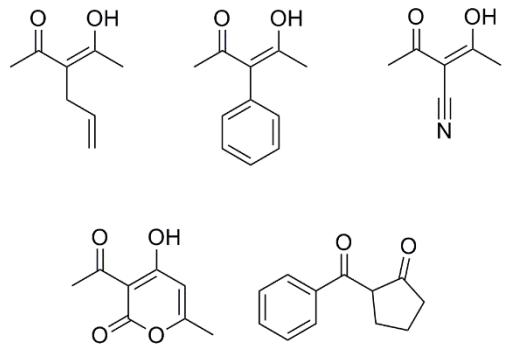

Figure 2.16 – Various literature α-substituted β-diketones used for lanthanoid coordination.[188–192]

Substitution at this position is particularly advantageous to the NIR emitting lanthanoids, as the high frequency CH oscillator is replaced by a CD or CC ($\nu_1 = 995$ cm^{-1})[113] bond, which is less likely to quench the lanthanoid excited states.

Given the interest in the classic β-diketonate ligand in the field of lanthanoid coordination chemistry, it is surprising that the simple extension of this molecule to β-triketonates, such as tribenzoylmethane (**L1**H) in Figure 2.17,[193,194] has been relatively unexplored. In fact, since the first example of a lanthanoid β-triketonate interaction was reported in 1960[26] there have only been two further reports of lanthanoid β-triketonate complexes.[25,26] Moreover, in no case there was any structural characterisation of a lanthanoid β-triketonate complex. Indeed, a search of the Cambridge Structural Database (CSD)[195] indicates that no metal complex of tribenzoylmethanide or triacetylmethanide had ever been structurally characterised prior to the work reported herein, despite these ligands being a seemingly obvious extension of the classic β-diketonate motif.

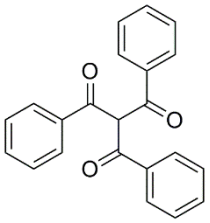

L1H

Figure 2.17 – Structure of the tribenzoylmethane molecule (**L1**H).

The work of Crosby focussed on the relative triplet state energy of β-triketonate ligands in the presence of the range of lanthanoids. This was followed some years later with a report from Ismail focussing on the β-triketonate sensitised emission of Eu^{3+} in a complex with an assumed formulation of [Eu(**L1**)$_3$(EtOH)(H_2O)], where **L1**- is the tribenzoylmethanide ligand (**L1**H is shown in Figure 2.17).[196] After this report, there has been no further interest in the coordination or sensitising ability of this new class of ligand.

From a photophysical perspective, the β-triketonate class of ligand provides an example whereby the CH vibration of the α-C is removed in lieu of a much lower frequency CC vibration, thus decreasing the metal-centred quenching by the ligand. This, in theory, should improve the efficiency in emission from the lanthanoids such as Er^{3+} and Yb^{3+}. Furthermore, the β-triketonate gives access to a further coordination site which could lead to the discovering of novel coordination modes and coordination complexes. In fact, in the absence of crystallographic characterisation, the exact coordination mode of the β-triketonate was not clearly characterised prior to the work reported here.

2.9 Applications of Lanthanoid Emission

Lanthanoid visible and NIR emission are applicable to many fields, due to the bright and pure colours emitted. Visible emitters find viable application in hybrid materials,[20,21,166] OLEDs, as well as biological imaging.[10–12] The application of

lanthanoid NIR emission is also far-reaching, touching fields of optical amplification, night vision technology, and NIR-OLEDs.[7] In this section the application of visible and NIR emissions in OLEDs will be briefly illustrated, as well as the application of NIR emission to optical amplification.

2.9.1 Organic Light Emitting Devices

An Organic Light Emitting Device (OLED) is a light source achieving emission from an organic emissive layer through electroluminescence (EL). Figure 2.18 illustrates the composition of a typical OLED. There is a sequence of organic layers lying between a anode (top) and cathode (bottom). The cathode allows a transfer of electrons through the electron transporting layer (ETL), while the anode causes the transport of holes through the hole transporting layer (HTL). The recombination of these charges in the emissive layer (EML) creates excitons which can excite the species in the EML resulting in the emission of light.[8]

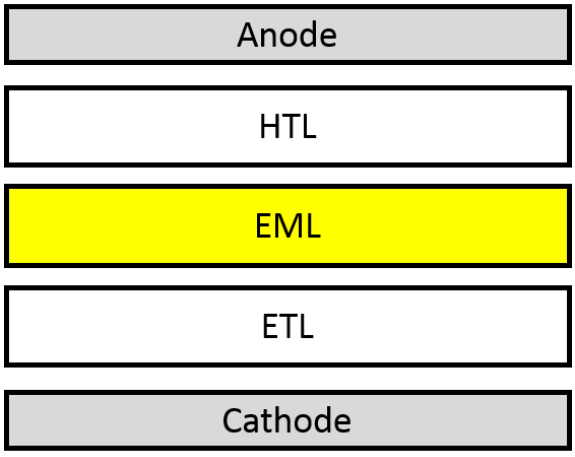

Figure 2.18 – Typical composition of an OLED.

The use of rare earths as the emissive species in the fabrication of OLEDs is a growing field with typical examples using visible emitting Eu^{3+} and Tb^{3+} species to create visible OLEDs.[197–199] However there has been recent interest in the development of NIR-OLEDs containing Nd^{3+}, Er^{3+}, and Yb^{3+},[200–206] in the EML.

2.9.2 Optical Amplification

Fibre optic communication is the transfer of information by electromagnetic radiation (EMR) through silica fibres at 1540 nm.[24] As EMR at 1540 nm travels along the optical fibre (Figure 2.19), its intensity diminishes, and thus it is necessary to amplify the signal at distance intervals.

Amplification of the EMR in the silica fibres is generally achieved *via* the emission of Er^{3+} in EDFAs. The emission of Er^{3+} at 1540 nm interferes with the attenuated signal and hence amplifies the EMR in optical fibres. In an EDFA unit, a laser periodically illuminates (980 nm) Er^{3+} to its $^4I_{11/2}$ state, from which it undergoes IC to its $^4I_{15/2}$ state and emits at 1540 nm.

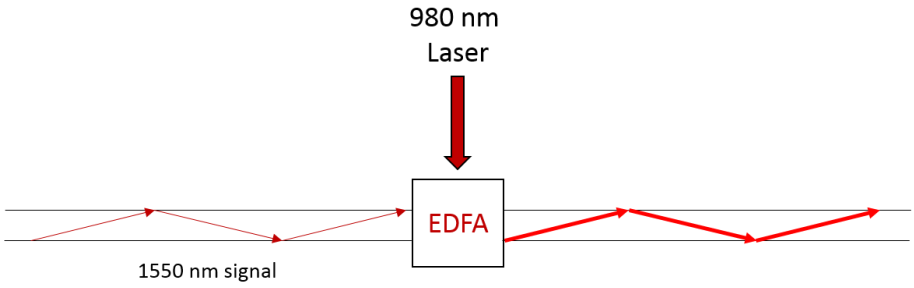

Figure 2.19 – Representation of the amplification of 1550 nm signal by EDFAs.

A pitfall with the EDFA process is that the antenna effect is not used and so the overall excitation efficiency is quite poor. In contrast, Er^{3+} has often been excited through sensitisation *via* Yb^{3+}.[24] However, there is still a key need for efficient sensitisation of Er^{3+} for this application.

2.10 Outlook

The work described in this thesis will start its focus on the first structural characterisation of lanthanoid complexes bearing β-triketonate ligands, in particular the tribenzoylmethane ligand shown in Figure 2.17.

The major component of the research seeks to investigate the sensitisation pathways and efficacy of the β-triketonate ligand, as well as the resulting

photophysical properties of the lanthanoid complexes. The emissive properties of the lanthanoid complexes will be studied in the solid state, as well as solution to observe the stability of the lanthanoid β-triketonates in solution.

For emissive lanthanoids, the solid state emission will be extended to the fabrication of visible and NIR-OLEDs for potential application as optical amplifiers, or OLEDs for smart devices or night vision technologies.

Finally this thesis will cover the extension to new β-triketonate functionalities, and the effect on structural and photophysical properties.

3 Preparation of Lanthanoid β-Triketonates

Some of the work presented in this chapter has been published in peer reviewed journals which are cited below:

B. L. Reid, S. Stagni, J. M. Malicka, M. Cocchi, G. S. Hanan, M. I. Ogden, M. Massi, *Chem. Commun.* **2014**, *50*, 11580–11582. doi: 10.1039/C4CC04961F

B. L. Reid, S. Stagni, J. M. Malicka, M. Cocchi, A. N. Sobolev, B. W. Skelton, E. G. Moore, G. S. Hanan, M. I. Ogden, M. Massi, *Chem. Eur. J.* **2015**, *21(50)*, 18354-18363. doi: 10.1002/chem.201502536

3.1 Introduction

This chapter will focus on the synthesis of a scarcely reported β-triketone molecule and the initial X-ray crystallographic characterisation of its lanthanoid complexes. The synthesis of the tribenzoylmethane ligand (2-benzoyl-1,3-diphenyl-1,3-propandione, **L1**H in Figure 3.1) and the characterisation of the β-triketone in comparison to β-diketones using techniques including Nuclear Magnetic Resonance (NMR), infrared (IR), and melting point (m.p.) will be discussed.

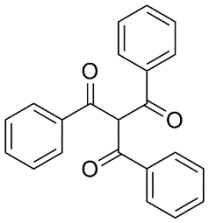

L1H

Figure 3.1 – Structure of the tribenzoylmethane molecule (**L1**H).

The coordination chemistry of the $\mathbf{L1}^-$ ligand was investigated with a variety of lanthanoid cations and in the presence of different bases (Figure 3.2). Coordination of the β-triketonate resulted in the crystallisation of a library of novel eight-coordinate lanthanoid β-triketonate species ranging from mononuclear complexes to multinuclear lanthanoid assemblies which were identified by single crystal X-ray diffraction. This chapter will present 23 new crystal structures and an in depth analysis of their similarities and differences, as well as details on the lanthanoid coordination geometries. One of the aims was to assess the variations of coordination geometry to provide insight into subtle changes in photophysical properties of the complexes, which will be encountered in Chapter 4.

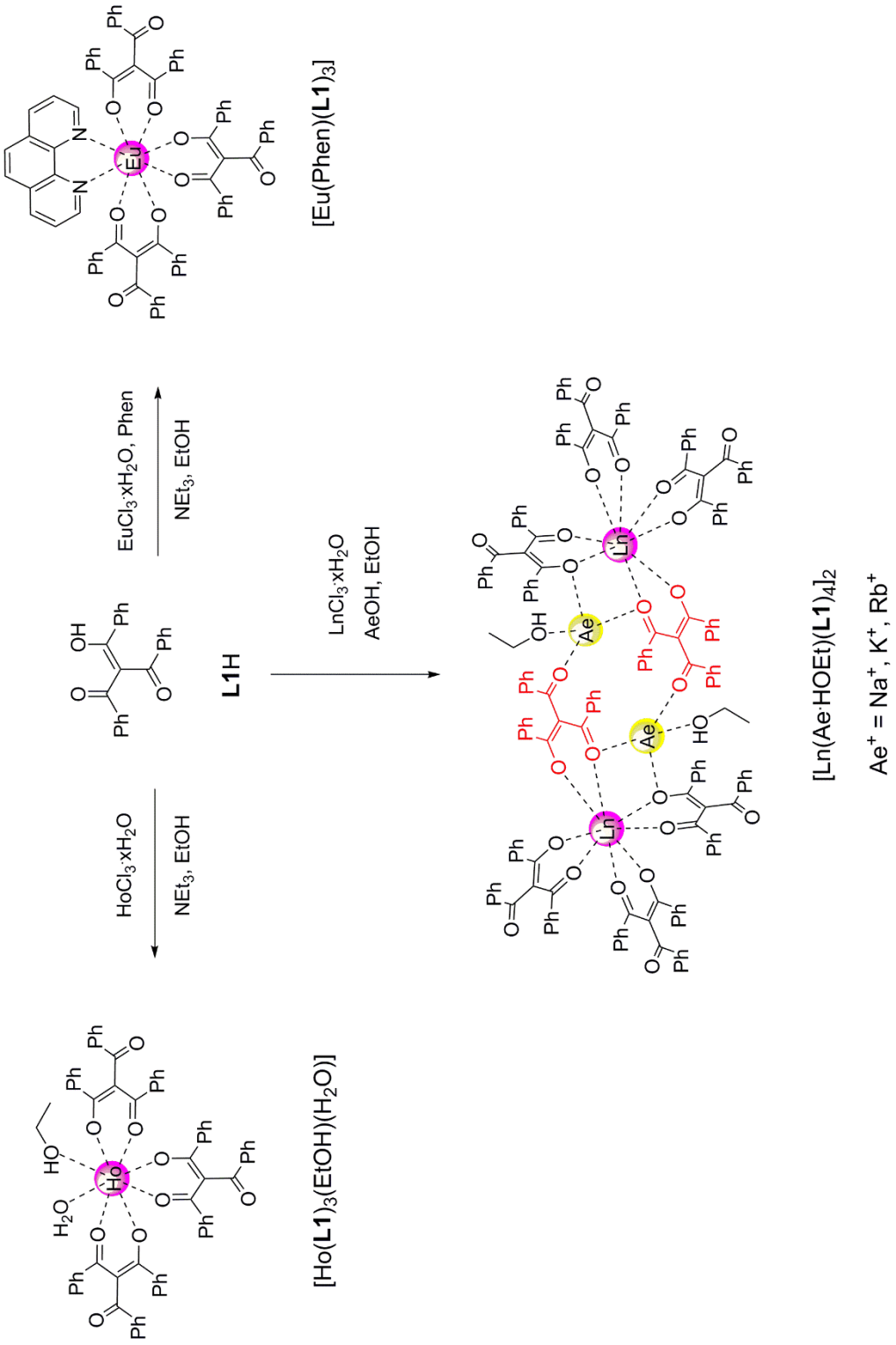

Figure 3.2 – Summary of lanthanoid β-triketonate structures presented in this chapter.

3.2 The Tribenzoylmethane Ligand

As a starting point for an investigation into lanthanoid β-triketonate chemistry, **L1**H was chosen as a suitable candidate for lanthanoid coordination. The **L1**H molecule provides a good starting point for lanthanoid complexation as it bears unsubstituted phenyl groups which is relatively simple from a synthetic viewpoint.

The presence of the third benzoyl substituent can provide rigidity, and a certain coordination directionality, which might lead to novel coordination modes. Furthermore, the three phenyl groups form a hydrophobic environment around the lanthanoid which can favour the absence of water molecules in the first coordination sphere, thus elongating emission lifetimes and improving luminescence properties.

Although the **L1**H molecule has been synthesised previously,[193] its characterisation was not reported in detail, and this was the initial aim of the work presented in this chapter.

3.2.1 Synthesis of β-Diketones and β-Triketones

The synthesis of β-diketones is well known in the literature, whilst the preparation of β-triketones should be a simple extension to the classic β-diketone synthesis. Characterisation of β-diketones can be somewhat challenging due to the presence of keto-enol tautomerism,[29] which is also possible in β-triketones (Figure 3.3).

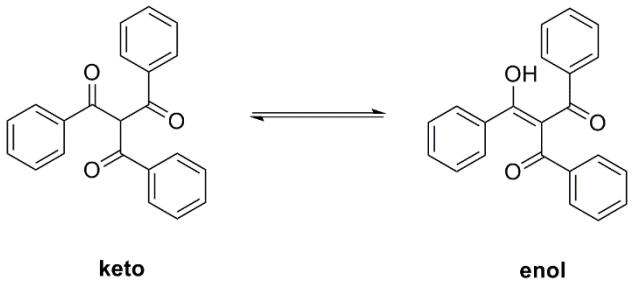

Figure 3.3 – The keto-enol tautomerism in β-triketones.

The synthesis of β-diketones can be achieved by the crossed Claisen condensation of a ketone and an ester, first reported by Claisen at the end of the 19th century,[169] and has been the classic method for β-diketone preparation for over one hundred years.[30,163,207–209] This simple reaction scheme can be extended to prepare functionalised β-diketones, as represented in Figure 3.4.

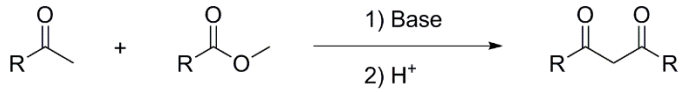

Figure 3.4 – Generalised synthetic scheme for the preparation of functionalised β-diketones.

For the preparation of β-triketones, the same crossed Claisen condensation can be used. In fact, the **L1**H molecule has been previously synthesised in a ~10% yield by Guthrie and Rabjon[193] *via* reaction of dibenzoylmethane and benzoyl chloride in the presence of metallic sodium in tetrahydrofuran (THF). For this work, the procedure was modified so that the dibenzoylmethane was reacted with benzoyl chloride and NaH in diethyl ether for 24 hours at ambient temperature (Figure 3.5). The reaction proceeds in a very high and reproducible yield (85%). The isolation procedure involved reprotonation of the β-triketone in an aqueous solution to force a reprecipitation of the keto tautomer.

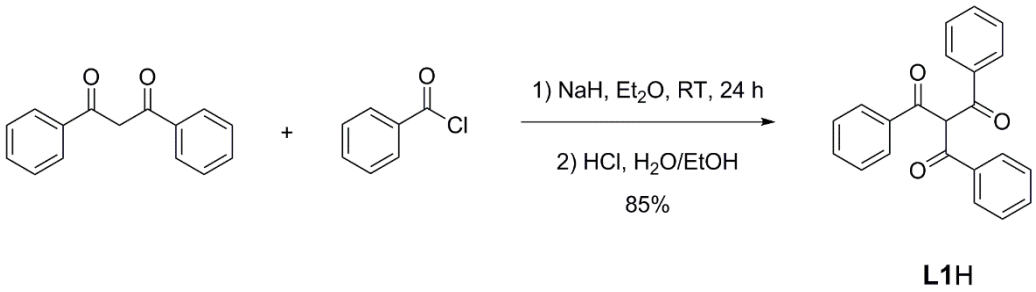

Figure 3.5 – Synthetic scheme for the preparation of **L1**H.

The m.p. of the **L1**H product matches acceptably with that reported in the literature, melting within the range of 221-223 ºC (lit. 226-231 ºC).[193]

Furthermore, the m.p. lies more than 100 ºC higher than that of the precursor dibenzoylmethane (76-78 ºC),[210] providing evidence that a new species had formed.

Analysis of the solid state product by FT-IR reveals a carbonyl stretch at 1666 cm^{-1}, which has shifted in comparison to the dibenzoylmethane precursor (1500-1600 cm^{-1}).[211] Furthermore, the product was also characterised by elemental analysis (see page 168).

3.2.2 Characterisation by NMR Spectrometry

The product was characterised by ^{1}H NMR experiments in DMSO-d_6, which revealed four peaks in the aromatic region of the spectrum between 7.50 ppm and 8.20 ppm (Figure 3.6). The assignment of these peaks was aided by a 2D COSY experiment (see Appendix). A singlet, labelled *a* in Figure 3.6, with a relative integration of 1 at 8.11 ppm, is attributed to the proton situated at the α-C position. This proton does not couple to any other protons in the molecule, and also lies at a higher chemical shift value compared to its β-diketone precursor (6.90 ppm) as an effect of the three closely bound electron withdrawing carbonyl groups. The presence of this peak suggests that, in this solvent system, the keto tautomer is the major species present, as this peak would not be present in the case of an enol tautomer.

With a relative integration of ~6, the doublet centred on 8.02 ppm is attributed to the two protons on the phenyl ring in the *ortho* position. The apparent triplet peak with a relative integration of ~3, centred on 7.70 ppm, is attributed to the phenyl proton in the *para* position to the *ipso* substituted carbonyl group. Finally, the apparent triplet peak with a relative integration of ~6, centred on 7.57 ppm, is attributed to the remaining protons in the *meso* position of the phenyl group, labelled *d* in Figure 3.6.

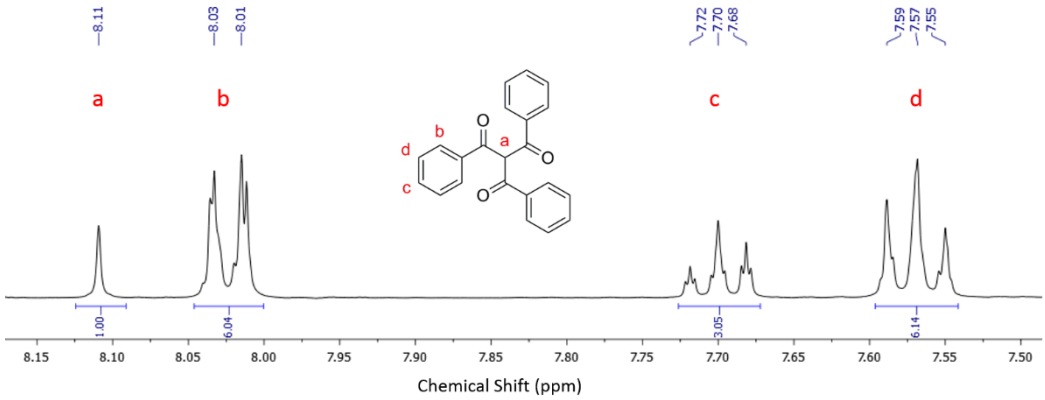

Figure 3.6 – A portion of the ^{1}H NMR spectrum of **L1**H in DMSO-d_6.

The **L1**H molecule was also characterised by a DEPT-Q ^{13}C NMR experiment (Figure 3.7), with attributions aided by 2D HMBC and HSQC experiments (see Appendix). There is one quaternary carbon peak at 193.7 ppm corresponding to the carbonyl carbon. The other quaternary carbon is that of the phenyl ring and has a peak at 135.4 ppm. Phenyl carbon peaks bearing protons are present in the aromatic region of the spectrum (120-140 ppm), while the α-C peak is present at 65.0 ppm. It is interesting to note that the α-C is not identified as quaternary by DEPT-Q ^{13}C NMR, providing further evidence that the major species present is not the enol tautomer.

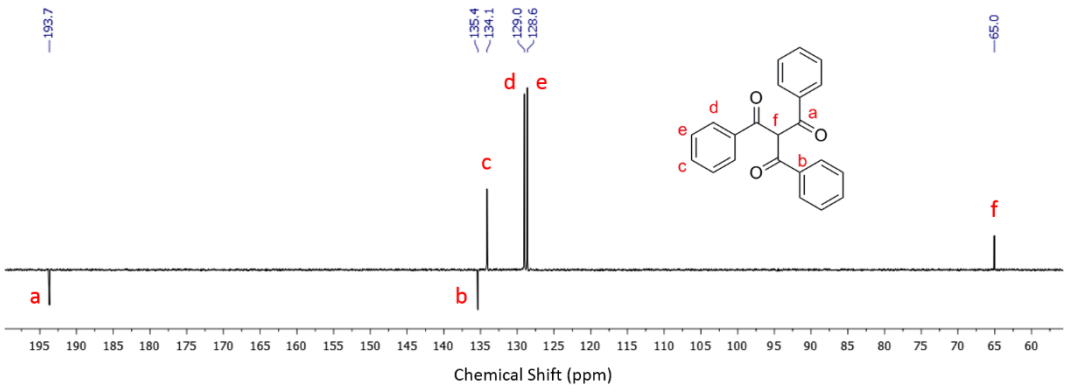

Figure 3.7 – A portion of the DEPT-Q ^{13}C NMR spectrum of **L1**H in DMSO-d_6.

In summary, the β-triketone can be synthesised by a straightforward crossed Claisen condensation reaction akin to that used for the precursor β-diketone. Furthermore, the β-triketone can be identified from the precursor β-diketone *via* characterisation techniques including IR and m.p. The **L1**H molecule was found to be present as its keto tautomer in a DMSO-d_6 solvent system *via* ^{1}H and ^{13}C NMR experiments. However, it should be noted that the keto-enol tautomerism is an equilibrium which will be affected by the nature of the solvent and β-triketone substituents.

3.3 Mononuclear Lanthanoid β-Triketonate Complexes

The coordinating nature of the β-triketonate molecule is largely unknown, and a search of the CSD[195] at the commencement of the project indicated that no metal complex of tribenzoylmethanide (**L1**$^{-}$) or triacetylmethanide had ever been structurally characterised. Thus, the initial aim was to crystallise a lanthanoid complex bearing the **L1**$^{-}$ ligand to examine its coordinating nature.

The first report of the formulation of a lanthanoid β-triketonate complex was the mononuclear [Eu(**L1**)$_3$(EtOH)(H$_2$O)] complex by Ismail, formulated from elemental and thermal analyses.[196] This complex was precipitated from a reaction of **L1**H with europium nitrate and NaOH in warm ethanol.

With the aim to grow single crystals of a lanthanoid complex bound to **L1**$^{-}$, hydrated HoCl$_3$ was reacted with three equivalents of **L1**H and triethylamine in hot ethanol (Figure 3.8). Slow evaporation of the solvent over several days resulted in the formation of yellow single crystals. Analysis of the product by X-ray diffraction revealed a structure of [Ho(**L1**)$_3$(EtOH)(H$_2$O)]·EtOH (Figure 3.9), a formulation similar to that proposed by Ismail.[196]

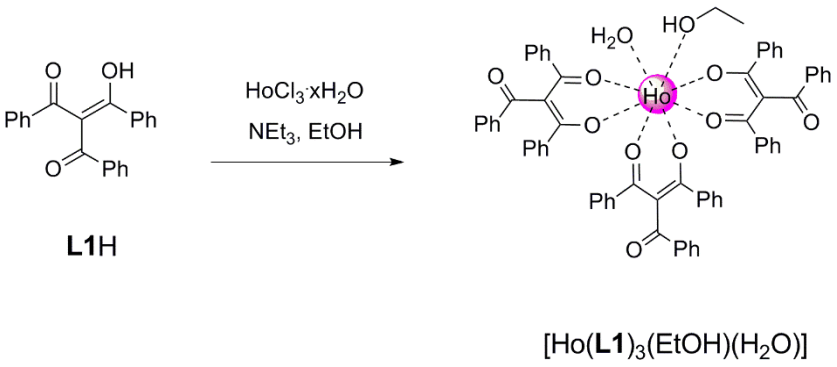

Figure 3.8 – Synthetic pathway to the crystallised [Ho(**L1**)$_3$(EtOH)(H$_2$O)] complex.

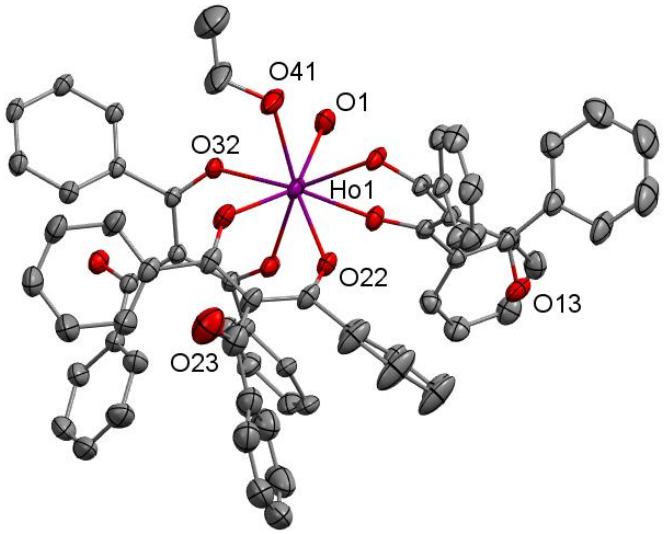

Figure 3.9 – Molecular plot of the [Ho(**L1**)$_3$(EtOH)(H$_2$O)]·EtOH complex. Displacement ellipsoids are shown at the 50% probability level. Hydrogen atoms and solvent molecules are omitted for clarity.

Notably, the X-ray crystal structure reveals that the β-triketonate ligand has a similar coordination mode to the classic chelating nature of β-diketonates. The ligand is bis-chelating using two of the three available O atoms, whilst the third ketone arm is non-coordinating and lies at the tail of the molecule. This is not surprising as the deprotonated α-C is sp^2 hybridised, and so the three carbonyl C atoms become trigonal planar in geometry around the α-C atom. The

β-triketonate, likely in its enolate form, localises the negative charge on two carbonyl groups and becomes a bis-chelating ligand.

The [Ho(**L1**)$_3$(EtOH)(H$_2$O)]·EtOH complex crystallised as a triclinic $P\bar{1}$ structure. The Ho^{3+} cation is eight-coordinate with six O atoms from three bidentate **L1**$^-$ ligands, an O atom from a coordinated water molecule, and another O atom from a coordinated ethanol molecule. The coordination geometry is best described as a distorted square antiprism, with one square face consisting of two O atoms from one ligand, and one oxygen atom from a second ligand plus the ethanol molecule, while the other face is similar bearing a water molecule in place of the ethanol.

There are interesting intermolecular hydrogen bonding which characterise the complex. The OH group of the coordinated ethanol molecule interacts with the O atom of a co-crystallised solvent ethanol. This in turn hydrogen bonds to a third keto O atom of another complex (Figure 3.10). This occurs in both complexes to form a hydrogen bonded pair with a Ho···Ho distance of 7.93 Å. As well as this interaction, the bound water molecule in each complex binds with a third keto O atom of a β-triketonate bound of a different complex, forming a distinct hydrogen bonded pair with a Ho···Ho distance of 8.42 Å. The result is a one-dimensional polymer of hydrogen-bond linked coordination complexes.

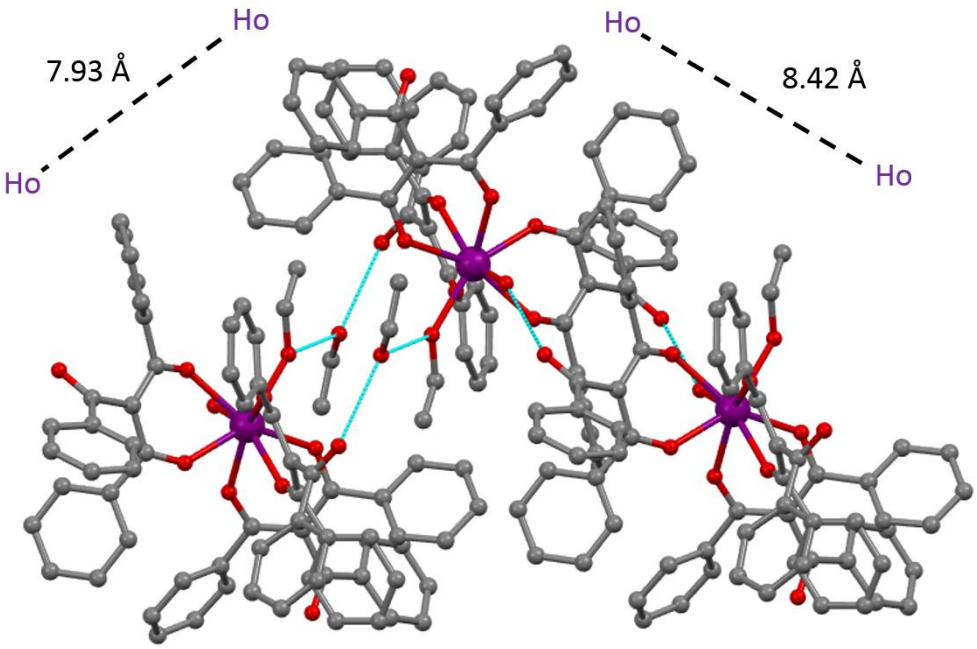

Figure 3.10 – Ball and stick representation of the [Ho(**L1**)$_3$(EtOH)(H$_2$O)]·EtOH complex, with blue dashed lines showing the intermolecular hydrogen bonding interactions. Hydrogen atoms are removed for clarity.

The bound ethanol and water molecules in the Ho^{3+} complex would result in strong vibronic deactivation in emissive lanthanoids, thus this type of structure is not the best target for a luminescent lanthanoid complex. This problem is regularly overcome in lanthanoid β-diketonate complexes by occupying the remaining two coordination sites with neutral bis-chelating *N*-donors such as Phen or Bipy,[178,183,212] in place of solvent molecules.

Following this precedence, another mononuclear complex was prepared by the reaction of one equivalent of Phen and hydrated $EuCl_3$, with three equivalents of **L1**H and triethylamine in ethanol (Figure 3.11). Slow evaporation of the solvent over several days resulted in the deposition of large yellow single crystals. X-ray diffraction studies revealed a complex of the formulation [Eu(Phen)(**L1**)$_3$] (Figure 3.12).

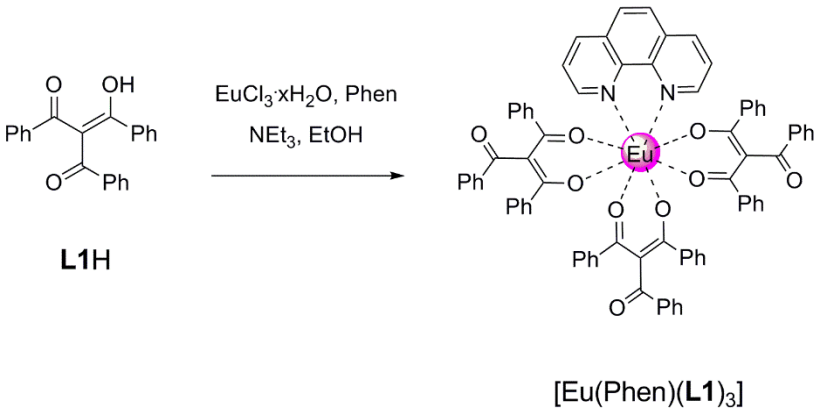

Figure 3.11 – Synthetic scheme to the crystallisation of the [Eu(Phen)(**L1**)$_3$] complex.

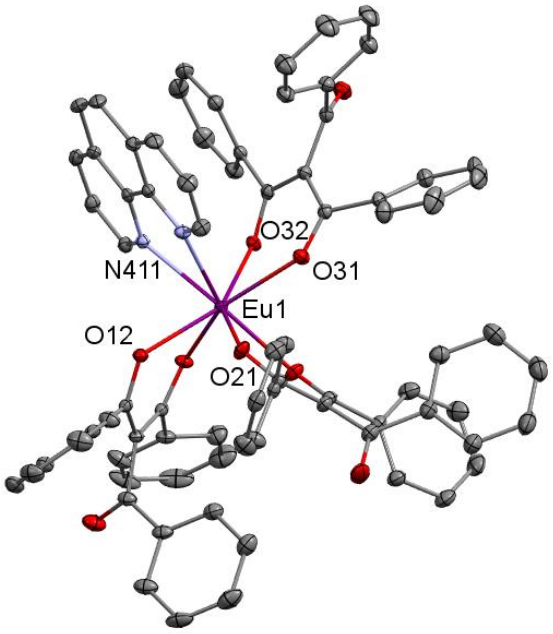

Figure 3.12 – Molecular plot of [Eu(Phen)(**L1**)$_3$], with displacement ellipsoids drawn at the 50% probability level. Hydrogen atoms have been omitted for clarity.

The [Eu(Phen)(**L1**)$_3$] complex crystallised as a triclinic structure in the $P\bar{1}$ space group. The Eu^{3+} cation is eight-coordinate, in this case by six O atoms from three **L1**$^-$ ligands and two N atoms from the coordinated Phen molecule. This coordination geometry is again best described as a distorted square antiprism. A pair is formed through π-stacking[213] of Phen ligands of two complexes (Figure 3.13),

with a distance of 3.26 Å between the π-stacked planes of Phen ligands. There is also intramolecular π-stacking between the Phen ligand and a phenyl substituent of a bound β-triketonate, with a distance of 3.36 Å between the π-stacked planes. These interactions result in a Eu···Eu distance of 9.25 Å.

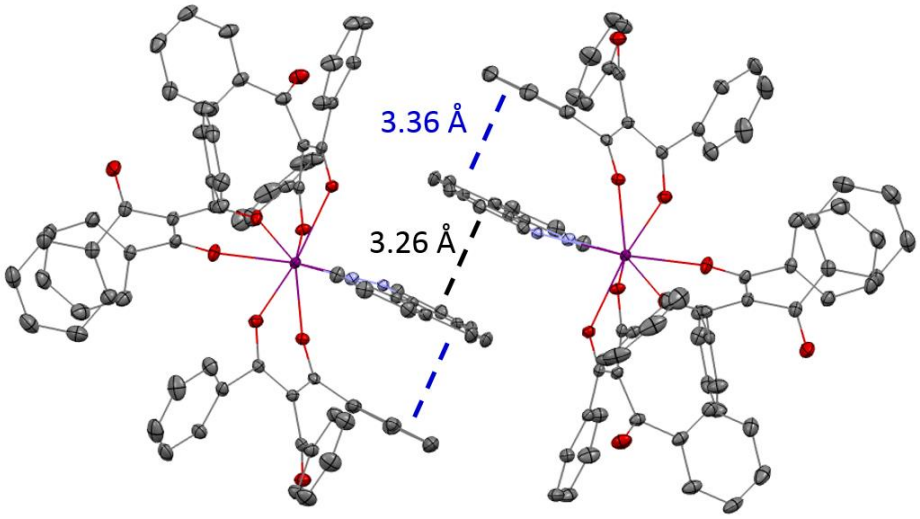

Figure 3.13 – Molecular plot of the [Eu(Phen)(**L1**)$_3$] complex, with displacement ellipsoids shown at the 50% probability level, highlighting the π-stacking of the Phen ligands and phenyl substituents. Hydrogen atoms have been omitted for clarity.

The [Eu(Phen)(**L1**)$_3$] complex is a lanthanoid β-triketonate species which is completely devoid of closely bound high frequency oscillators, and should result in highly efficient metal-centred emission from the Eu^{3+} cation.

Although these mononuclear complexes present the first metal β-triketonate crystal structures reported, their formulations are very similar to those observed previously with β-diketonate ligands.

3.4 Discrete Tetranuclear Assemblies

To further explore the coordination chemistry of the β-triketonate ligand with lanthanoids, the base in the reaction was changed from triethylamine to NaOH, to

follow the work of Ismail. Surprisingly, it was found that the change in the base had a profound effect on the structure of the crystallised lanthanoid complex.

3.4.1 Crystallisation of Lanthanoid/Alkali Metal Assemblies

To emulate the conditions used by Ismail, the first set of conditions trialled was the reaction of three equivalents of **L1**H and NaOH with one equivalent of hydrated $EuCl_3$ in ethanol (Figure 3.14). In contrast to the literature, this reaction resulted in the unexpected crystallisation of a discrete Eu^{3+}/Na^+ tetranuclear assembly of the formulation $[Eu(Na{\cdot}HOEt)(\mathbf{L1})_4]_2$ (Figure 3.15), which was characterised by single crystal X-ray diffraction. The reaction conditions were then adjusted according to the correct stoichiometric ratio, and the reaction repeated by addition of four equivalents of **L1**H and NaOH to one equivalent of hydrated $EuCl_3$ in ethanol. After slow evaporation of the solvent, large yellow crystals deposited again.

The $[Eu(Na{\cdot}HOEt)(\mathbf{L1})_4]_2$ assembly crystallised as a triclinic structure and comprises of an overall neutral and discrete species whereby the eight positive charge of the two Eu^{3+} and two Na^+ ions is counterbalanced by eight negatively charged $\mathbf{L1}^-$ ligands. The complex can be viewed as a dimer disposed about a centre of symmetry. Each Eu^{3+} is eight-coordinate, binding four $\mathbf{L1}^-$ ligands in its bis-chelating mode, and adopts a geometry best described as a distorted square antiprism. The third keto O atoms on three of these ligands are not involved in any close contacts, while the fourth bridges to form the dimer, linking to a centrosymmetrically related Na^+ ion. The remainder of the coordination sphere of the Na^+ cation comprises of two μ-O atoms bridging to the Eu^{3+} cation and an ethanol O atom.

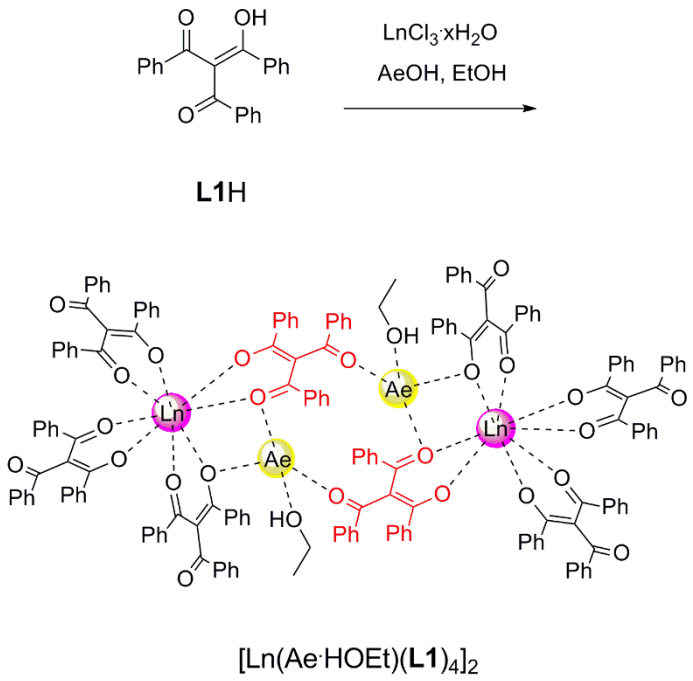

Figure 3.14 – Synthetic pathway for the crystallisation of $[Ln(Ae{\cdot}HOEt)(\mathbf{L1})_4]_2$ tetranuclear assemblies.

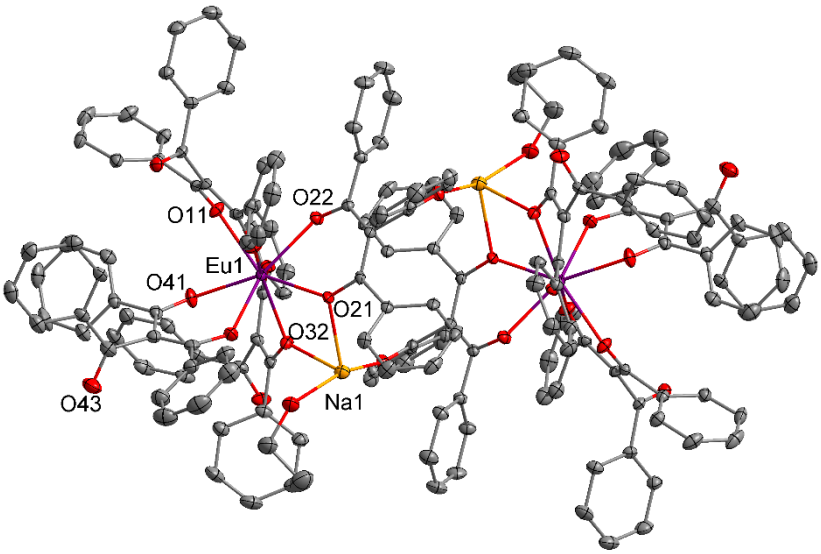

Figure 3.15 – Molecular plot of the $[Eu(Na{\cdot}HOEt)(\mathbf{L1})_4]_2$ assembly with displacement ellipsoids shown at the 50% probability level. Hydrogen atoms have been omitted for clarity.

The synthesis of the $[Eu(Na{\cdot}HOEt)(\mathbf{L1})_4]_2$ tetranuclear assembly, using NaOH as the base in the reaction, was extended to a variety of lanthanoids. Under the same conditions, the $[Ln(Na{\cdot}HOEt)(\mathbf{L1})_4]_2$ assemblies, where Ln^{3+} = Eu^{3+}, Tb^{3+}, Er^{3+}, Yb^{3+}, were prepared. As well as changing the lanthanoid in the reaction, the base could be extended to KOH and RbOH. For each Ln^{3+}/Ae^{+} combination (Ln^{3+} = Eu^{3+}, Gd^{3+}, Tb^{3+}, Dy^{3+}, Ho^{3+}, Er^{3+}, and Yb^{3+}; Ae^{+} = K^{+}, Rb^{+}), structural investigation by X-ray diffraction revealed the targeted $[Ln(Ae{\cdot}HOEt)(\mathbf{L1})_4]_2$ assembly (for molecular plots of these crystal structures, see Appendix).

The same reaction was trialled for lanthanoids larger than Eu^{3+}, such as Nd^{3+} and Sm^{3+}, however crystals were not deposited. Using CsOH as the base did not form a crystalline product, and using Cs_2CO_3 resulted in the crystallisation of a $[Cs(\mathbf{L1})]_n$ coordination network regardless of the lanthanoid ion present (see Appendix). These results may indicate that the Eu^{3+} and Rb^{+} ions are the larger limit for the crystallisation of the family of tetranuclear assemblies.

Changing the solvent from ethanol to *n*-butanol (BuOH) was also trialled using Eu^{3+} and K^{+}, which yielded the analogous $[Eu(K{\cdot}HOBu)(\mathbf{L1})_4]_2$ assembly (Figure 3.16). The resulting tetranuclear core is featured again, with a BuOH molecule coordinated to the K^{+} ion in place of ethanol. The longer BuOH molecule chain 'wraps' around the assembly rather than points out of the assembly, as in the case of the shorter ethanol molecule. This is likely due to packing effects in the crystal.

Based on these results, this family of tetranuclear assemblies is remarkably robust, with the observed structure being maintained while systematically changing the lanthanoid, the alkali metal, or the alcoholic solvent.

Although each of the successfully isolated $[Ln(Ae{\cdot}HOEt)(\mathbf{L1})_4]_2$ assemblies are analogous in structure, it was determined that, in addition to unsolvated structures, the assemblies can also crystallise as different solvates including $[Ln(Ae{\cdot}HOEt)(\mathbf{L1})_4]_2{\cdot}2(EtOH)$ and $[Ln(Ae{\cdot}HOEt)(\mathbf{L1})_4]_2{\cdot}2(H_2O)(EtOH)$. In fact, for the $[Dy(K{\cdot}HOEt)(\mathbf{L1})_4]_2$ and $[Yb(K{\cdot}HOEt)(\mathbf{L1})_4]_2$ assemblies, both unsolvated and solvated structures were identified by single crystal X-ray diffraction from the same crystallisation vial. Table 3.1 presents each crystallised assembly according to the crystallised solvate, whilst for the unsolvated assemblies, two different classes have been identified distinguishable between either a Na^{+} ion or a K^{+}/Rb^{+}

ion. This division of assemblies into classes (I, II, III, and IV) due to solvate or alkali metal was used due to structural variations in the crystallised species, which will be discussed in this chapter (for a comparison of solvate structures, see Figure 3.17).

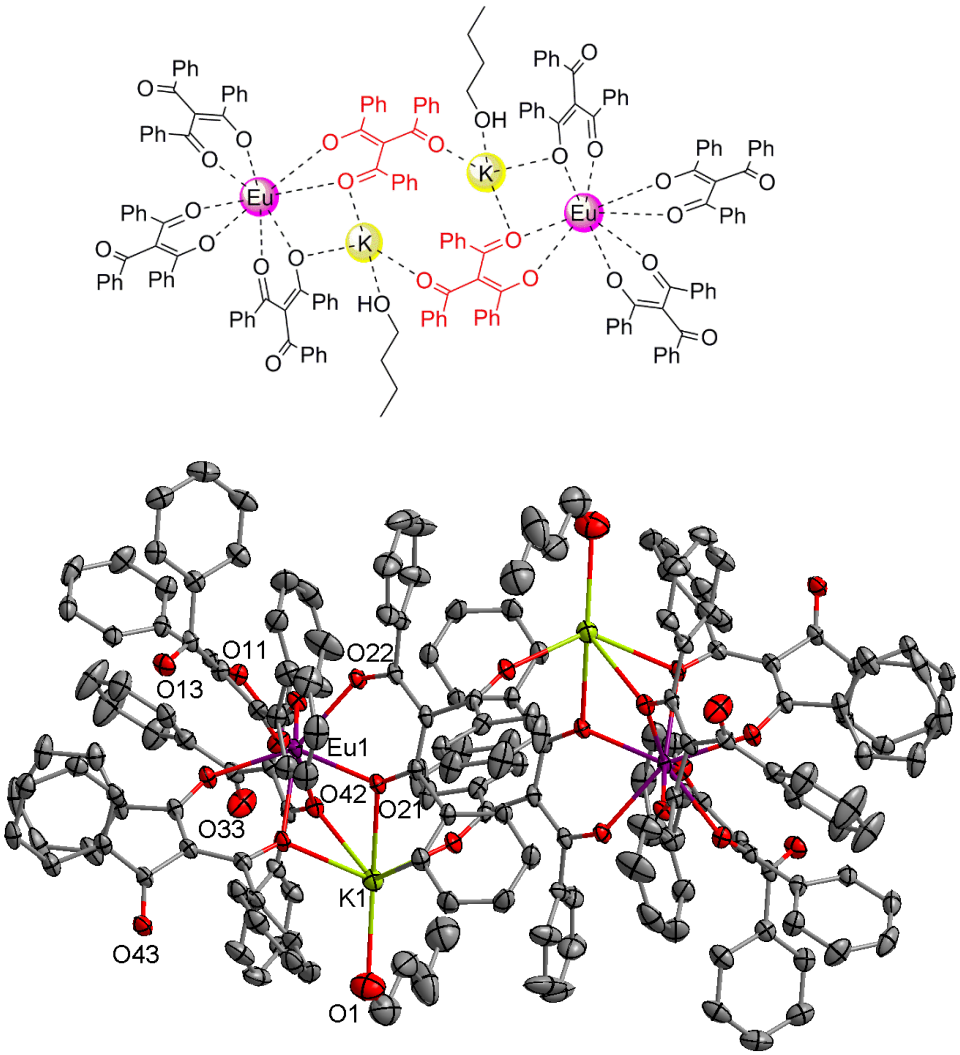

Figure 3.16 – Top: Simplified pictorial representation of the [Eu(K·HOBu)(**L1**)$_4$]$_2$ assembly. Bottom: Molecular plot of the [Eu(K·HOBu)(**L1**)$_4$]$_2$ assembly with displacement ellipsoids shown at the 50% probability level. Hydrogen atoms and solvent molecules have been omitted for clarity.

The [Eu(K·HOBu)(**L1**)$_4$]$_2$ assembly crystallised as a solvate of formula [Eu(K·HOBu)(**L1**)$_4$]$_2$·2(H_2O)(BuOH), but the core structure of the assembly does not seem to be strongly influenced by the change in the coordinated alcohol molecules.

For simplicity of discussion, from this point forward the $[Ln(Ae{\cdot}HOEt)(\mathbf{L1})_4]_2$ assemblies will be represented by $\{Ln_2Ae_2\}^{class}$, where Ln^{3+} = Eu^{3+}, Gd^{3+}, Tb^{3+}, Dy^{3+}, Ho^{3+}, Er^{3+}, and Yb^{3+}; Ae^+ = Na^+, K^+, Rb^+; *class* = the value I, II, III, or IV as presented in Table 3.1.

Table 3.1 - Tetranuclear assemblies sorted by their crystallised structure.

Class	Formulation	$\{Ln_2Ae_2\}$ Assemblies
I	$[Ln(Na{\cdot}HOEt)(\mathbf{L1})_4]_2$	$\{Eu_2Na_2\}^{I}$, $\{Tb_2Na_2\}^{I}$, $\{Er_2Na_2\}^{I}$, $\{Yb_2Na_2\}^{I}$
II	$[Ln(K/Rb{\cdot}HOEt)(\mathbf{L1})_4]_2$	$\{Tb_2K_2\}^{II}$,$\{Dy_2K_2\}^{II}$, $\{Ho_2K_2\}^{II}$, $\{Er_2Rb_2\}^{II}$, $\{Yb_2K_2\}^{II}$, $\{Yb_2Rb_2\}^{II}$
III	$[Ln(Ae{\cdot}HOEt)(\mathbf{L1})_4]_2{\cdot}2(H_2O)(EtOH)$	$\{Er_2K_2\}^{III}$, $\{Yb_2K_2\}^{III}$, $\{Eu_2K_2\text{-}BuOH\}^{III}$
IV	$[Ln(Ae{\cdot}HOEt)(\mathbf{L1})_4]_2{\cdot}2EtOH$	$\{Eu_2K_2\}^{IV}$, $\{Eu_2Rb_2\}^{IV}$, $\{Tb_2Rb_2\}^{IV}$, $\{Gd_2K_2\}^{IV}$, $\{Gd_2Rb_2\}^{IV}$, $\{Dy_2K_2\}^{IV}$, $\{Dy_2Rb_2\}^{IV}$, $\{Ho_2Rb_2\}^{IV}$

In the case of $[Yb(K{\cdot}HOEt)(\mathbf{L1})_4]_2$, where two structures have been identified, the crystal class number II or III will be used to identify the referred crystal structure. The $[Eu(K{\cdot}HOBu)(\mathbf{L1})_4]_2{\cdot}2(H_2O)(BuOH)$ assembly will be abbreviated $\{Eu_2K_2\text{-}BuOH\}^{III}$, as it crystallised similarly to the solvate III assemblies containing two ethanol molecules.

Figure 3.17 shows a comparison of the structures of the four crystal solvates in Table 3.1. The image portrays the robustness of the tetranuclear core, with the major change in the structure being the position of the coordinated ethanol molecule. In the class I assemblies, the Na^+ ion is small enough to only bind to two μ-O atoms while bridging to the Ln^{3+} cation, and has a coordination mode best described by a four-coordinate saddle geometry. In all other assemblies, the larger K^+ and Rb^+ ions bind to three μ-O bridged atoms, which results in these cations being five-coordinate. This effect is important as the Na^+ ion is small enough to allow the ethanol OH to hydrogen bond the third μ-O atom, while the K^+ and Rb^+ complexes effectively disallow this interaction (Figure 3.17).

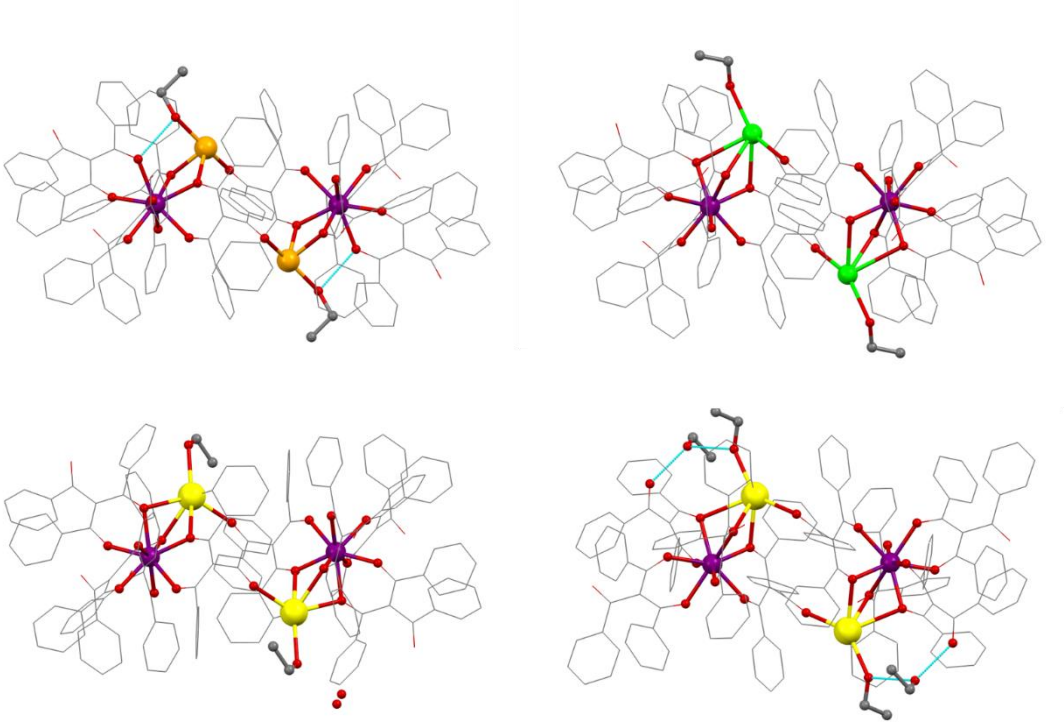

Figure 3.17 - X-ray crystal structures of $\{Er_2Na_2\}^{I}$ (top left), $\{Er_2Rb_2\}^{II}$ (top right), $\{Er_2K_2\}^{III}$ (bottom left), and $\{Eu_2K_2\}^{IV}$ (bottom right); where Ln = purple, Na = orange, K = yellow, and Rb = green. Hydrogen bonds are represented by blue dashed lines. Hydrogen atoms are omitted for clarity.

Analysis of the Hirshfield surfaces[214] of the ethanol molecules in the two unsolvated structures (class I and II) enabled a more detailed understanding of the intramolecular interactions occurring (Figure 3.18). The $\{Yb_2Na_2\}^{I}$ and $\{Yb_2K_2\}^{II}$ crystal structures were used as a representative exemplar for each unsolvated structure. This analysis revealed that the OH···O interaction found in the $\{Yb_2Na_2\}^{I}$ assembly is replaced by an OH···π interaction in the $\{Yb_2K_2\}^{II}$ assembly. The red colouration is indicative of a close approach to atoms outside of the surface. The strongest interaction in both cases is the coordination to the Ae^{+} cation, with an additional OH···H interaction indicated in class I, and an OH···π interaction indicated in class II.

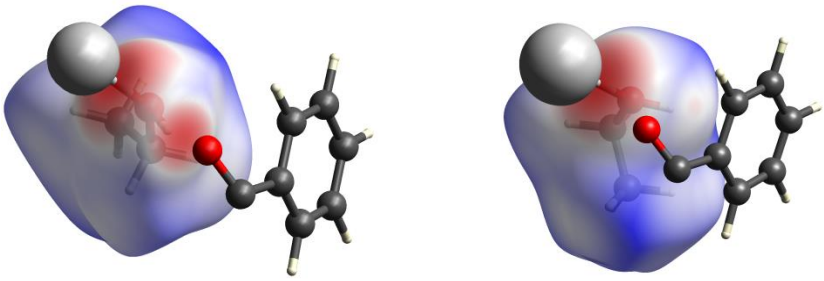

Figure 3.18 - Hirshfield surfaces[214] of the ethanol molecule in class I (left), and in class II (right).

Furthermore, in the class III assemblies the bound ethanol OH has a weak hydrogen bond to a co-crystallised water molecule, and in the class IV assemblies the coordinated ethanol OH hydrogen binds to a lattice ethanol solvent molecule. The differences in intermolecular interactions are accompanied by differences in Ln···OH distances between solvates of crystal structures, which from a photophysical perspective can have an effect on the extent of multiphonon relaxation pathways.

Aside from X-ray diffraction studies, the complexes were analysed by means of IR spectroscopy and elemental analyses. The latter, in particular, revealed the presence of variable degrees of lattice solvent molecules, consistent with the structure determinations (see Chapter 8 – Experimental Section).

3.4.2 Crystal Structure Analysis

Selected distances are given in Table 3.2 for each complex, including average Ln-O distances (for raw data – see Appendix), Ln···Ln distances, and the relative distances between the Ln^{3+} and closest OH oscillator (Ln···OH).

The average Ln-O distance for all assemblies decreases from Eu^{3+} (~2.38 Å) to Yb^{3+} (~2.30 Å), consistent with considerations based on the lanthanide contraction.

The Ln···Ln distance in each of the assemblies were found to be affected by the lanthanide contraction, but also the presence (or absence) of co-crystallised solvent molecules and the identity of the alkali metal. The lanthanide contraction gives rise to a general decrease in Ln···Ln distance, within each crystal class (Table 3.2).

It is clear that this trend is only comparable within each crystal class, and thus the position of the alkali metal-bound ethanol molecule has a profound effect on the

packing of the tetranuclear assemblies and the Ln···Ln distance. Furthermore, within the systems II and IV, the presence of the K^+ or Rb^+ alkali metal presents some anomalies in the lanthanide contraction trend within each crystal class, which is not unexpected due to the larger size of the Rb^+ ion compared to the K^+ ion. Regardless, the Ln···Ln distance is always greater than 8.70 Å, which is long enough to suggest that direct energy migration between the two lanthanoid centres within the assembly should not be occurring.[110]

The position of the alkali metal coordinated ethanol (or BuOH) molecule is also of importance, as the coordinated alcohol OH oscillation can provide some outer sphere multiphonon relaxation to lanthanoid excited states. In fact, the alkali metal in the complex has a profound effect on the position of the bound ethanol. It is evident that the shortest Ln···OH distances are present in the Ln^{3+}/Na^+ complexes. Moreover, in the class II and IV species, the Ln···OH distances increase in assemblies bearing the larger Rb^+ ion compared to the K^+ ion (Table 3.2).

In each assembly there is an OH hydrogen bond (or OH···π) interaction which will intrinsically lower the frequency of the OH stretching vibration in the assemblies,[215] and thus lead to more inefficient quenching of lanthanoid excited states (compared to free OH). Analysis of the IR spectrum of each of the assemblies in the solid state, reveals a band in the 3,640-3,660 cm^{-1} region attributed to the OH stretch of the coordinated ethanol molecule. This frequency range is rather small and suggests that regardless of the structure class, lanthanoid multiphonon relaxation pathways should not be influenced by the nature of the OH interaction.

Therefore, it is evident that the major contributor to multiphonon relaxation pathways will be the distance of the vibration from the metal centre. Evidently, the class I, Ln^{3+}/Na^+, assemblies will be the most prone to vibronic deactivation due to the close proximity of the OH to the lanthanoid centre.

Table 3.2 – Selected distances (Å) between the two lanthanoid cations (Ln···Ln) within the tetranuclear assemblies, between the lanthanoid centres and the OH group of bound EtOH/BuOH (Ln···OH), and average Ln-O bond distances within the first coordination sphere. Structures are grouped by their structure class.

Class	Assembly	Ln···Ln	Ln···OH	Ave. Ln-O
1	$\{Eu_2Na_2\}^{I}$	8.980	4.355	2.383
	$\{Tb_2Na_2\}^{I}$	8.955	4.348	2.354
	$\{Er_2Na_2\}^{I}$	8.925	4.339	2.324
	$\{Yb_2Na_2\}^{I}$	8.917	4.395	2.305
2	$\{Tb_2K_2\}^{II}$	8.838	5.630	2.358
	$\{Dy_2K_2\}^{II}$	8.821	5.628	2.344
	$\{Ho_2K_2\}^{II}$	8.803	5.701	2.332
	$\{Er_2Rb_2\}^{II}$	8.813	6.062	2.325
	$\{Yb_2K_2\}^{II}$	8.804	5.720	2.306
	$\{Yb_2Rb_2\}^{II}$	8.792	6.080	2.303
3	$\{Er_2K_2\}^{III}$	9.145	6.239	2.316
	$\{Yb_2K_2\}^{III}$	9.128	6.256	2.299
	$\{Eu_2K_2\text{-BuOH}\}^{III}$	9.271	6.297	2.382
4	$\{Eu_2K_2\}^{IV}$	8.968	5.861	2.380
	$\{Eu_2Rb_2\}^{IV}$	8.949	6.096	2.380
	$\{Tb_2Rb_2\}^{IV}$	8.937	6.082	2.357
	$\{Gd_2K_2\}^{IV}$	8.966	5.868	2.369
	$\{Gd_2Rb_2\}^{IV}$	8.951	6.112	2.372
	$\{Dy_2K_2\}^{IV}$	8.946	5.832	2.344
	$\{Dy_2Rb_2\}^{IV}$	8.921	6.076	2.343
	$\{Ho_2Rb_2\}^{IV}$	8.908	6.053	2.330

3.5 Coordination Sphere Analysis

The geometry of the lanthanoid coordination sphere plays an important role in the emission spectrum of the lanthanoids. For this study the coordination sphere geometry was assessed for each of the crystallised lanthanoid species presented thus far, with the aim of obtaining a greater insight into how subtle changes in the crystallised solvate of the tetranuclear assemblies would affect the resulting coordination geometry of the metal centre.

The coordination geometry for each lanthanoid species was assessed using Shape Version 2.1 software.[216,217] The software allows a mathematical calculation of continuous shape measures (CShM) proposed by Avnir.[218] These measures present a numerical evaluation of how much a particular structure deviates from an ideal shape.

Alvarez has developed the Shape Version 2.1 software and describe the evaluation of CShM using Eqn 3.1.[217,219–223] The CShM for the problem structure (P) is evaluated in comparison to a reference polyhedron (R) for N atoms (N = 8 for our eight-coordinate structures). These N atoms are characterised by their position vectors (P_i) relative to the position vectors of the corresponding vertices in the reference polyhedron (R_i). The position vector of the centre of P is defined by P_0.

$$CShM(R) = min\frac{\sum_{i=1}^{N}|P_i - R_i|^2}{\sum_{i=1}^{N}|P_i - P_0|^2}100 \qquad \text{Eqn 3.1}$$

Using Eqn 3.1, the minimum is taken for all possible pairings of P and R, whereby only the vertex permutations which leave the metal atom in the centre of the polyhedron are considered. Therefore, when P is identical to the R, CShM(R) = 0. The Shape Version 2.1 software uses Eqn 3.1 for a given crystal structure and assesses the CShM compared to reference polyhedra of choice.

Each of the lanthanoid species were assessed against 13 reference eight-coordinate polyhedra, and it was found that each species was best described as either a square antiprism or a triangular dodecahedron (showing CShM values closest to 0).

This can be rationalised further using a Shape Map, which plots the CShM of the triangular dodecahedron (x-axis) and square antiprism (y-axis) geometries for each lanthanoid species. Thus, the shape map presents the CShM values as coordinates on an x- and y- axis (Figure 3.19), whereby on a given axis, a value of 0 corresponds to an exact match with the regular polyhedron. These coordinates for all lanthanoid structures presented in this chapter are presented in Table 3.3. The shape map also presents a black trace corresponding to the lowest energy interconversion pathway (LEIP) between the square antiprism and triangular dodecahedron geometries.

The shape map shows clearly that a variety of CShM clusters emerges. Interestingly, it was noted that the presence (or absence) and the nature of the lattice solvent molecules as well as the identity of the Ae^{+} cation have a non-negligible influence on the specific geometry of the coordination environment around the lanthanoid centre. These clusters correspond to the assemblies within the crystal classes described previously.

From an analysis of the Shape map, it becomes evident that all the class I species bearing Na^{+} have a coordination geometry that is closest to a square antiprism, irrespective of the lanthanoid cation. The deviation from the LEIP (black line in Figure 4) increases from the smaller Yb^{3+} to the larger Eu^{3+} indicating a distortion away from the regular polyhedra with increasing lanthanoid size.

From this arrangement, a slight distortion is observed for the class II structures bearing K^{+}/Rb^{+}, however this solvate is again best described by a square antiprismatic geometry. The deviation from the LEIP follows the same trend as the class I structures which increases with increasing lanthanoid size, from $\{Yb_2K_2\}^{II}$ to $\{Tb_2K_2\}^{II}$. The $\{Yb_2Rb_2\}^{II}$ assembly is an outlier in this trend, with a higher deviation from the LEIP compared to $\{Er_2Rb_2\}^{II}$. This distortion is attributed to the size differences between the smallest Yb^{3+} and largest Rb^{+} ions in the tetranuclear assembly series, causing a larger distortion in the coordination sphere.

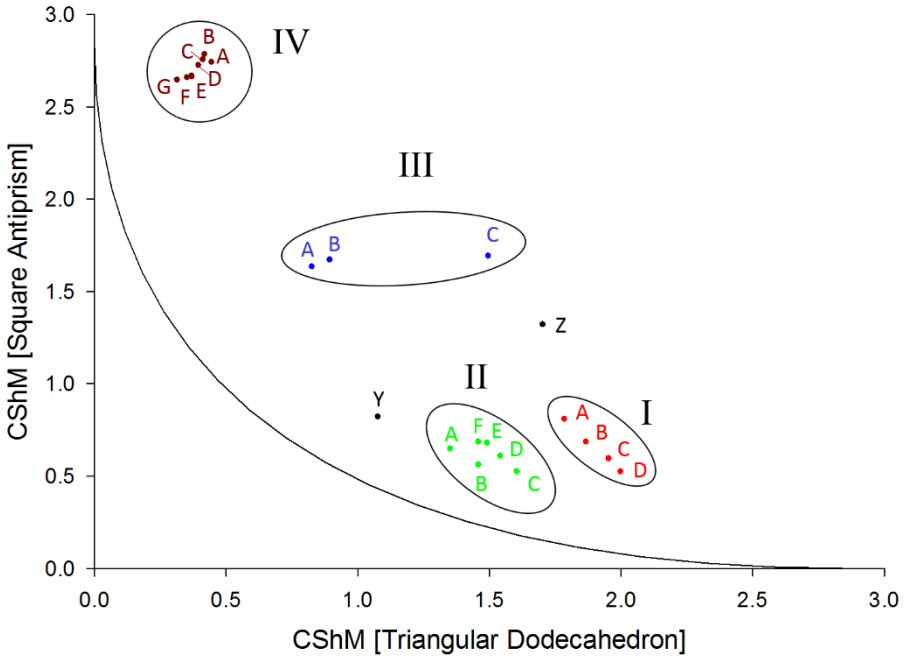

I	II	III	IV	Other
A: $\{Eu_2Na_2\}^{I}$,	A: $\{Er_2Rb_2\}^{II}$,	A:$\{Yb_2K_2\}^{III}$,	A: $\{Eu_2K_2\}^{IV}$,	Y:
B: $\{Tb_2Na_2\}^{I}$,	B: $\{Yb_2Rb_2\}^{II}$,	B: $\{Er_2K_2\}^{III}$,	B:$\{Eu_2Rb_2\}^{IV}$,	$[Ho(\mathbf{L1})_3(EtOH)(H_2O)]$
C: $\{Er_2Na_2\}^{I}$,	C: $\{Yb_2K_2\}^{II}$,	C: $\{EuK$-	$\{Gd_2K_2\}^{IV}$,	Z: $[Eu(Phen)(\mathbf{L1})_3]$
D: $\{Yb_2Na_2\}^{I}$	D: $\{Ho_2K_2\}^{II}$,	$BuOH\}^{III}$	C: $\{Gd_2Rb_2\}^{IV}$,	
	E: $\{Tb_2K_2\}^{II}$,		D: $\{Dy_2K_2\}^{IV}$,	
	F: $\{Dy_2K_2\}^{II}$		E: $\{Tb_2Rb_2\}^{IV}$,	
			F: $\{Dy_2Rb_2\}^{IV}$,	
			G: $\{Ho_2Rb_2\}^{IV}$	

Figure 3.19 – Top: Shape map presenting the CShM of the 23 lanthanoid species presented in this chapter, against the reference square antiprism and triangular dodecahedron polyhedra. The black trace represents the LEIP between the two reference polyhedra. Classes of assemblies are circled and the class number printed alongside. Bottom: The legend is shown in the table.

Further distortion is evident for the class III structures that appear solvated by two molecules of water and one of ethanol. The deviation trend is again consistent from $\{Yb_2K_2\}^{III}$ to $\{Er_2K_2\}^{III}$. As might be expected, the $\{Eu_2K_2\text{-}BuOH\}^{III}$ assembly is different from the other class III assemblies, highlighting a Eu^{3+} coordination sphere that is somewhat more distorted from both reference polyhedra

with a deviation from the LEIP of 49%. This result suggests that although the assembly is class III by solvation, the coordination geometry of the Eu^{3+} ion is somewhat more distorted by the addition of the bulkier BuOH molecule to the structure.

Lastly, better described as a triangular dodecahedron, lie the class IV assemblies with two lattice ethanol molecules. Again, the deviation from the LEIP increases with increasing lanthanoid size, from $\{Ho_2Rb_2\}^{IV}$ to $\{Eu_2K_2\}^{IV}$. In the solvate IV series, the presence of K^+ or Rb^+ appears to affect the deviation from regular polyhedra to a lesser extent. This observation is most likely due to the fact that the investigated structures now include larger lanthanoids, whose coordination geometry is less affected by the size of the alkali metal.

To summarise the data, four different geometrical arrangements have been identified through an analysis of all the crystal structures. The specific geometries vary from a slightly distorted square antiprism (class I) to a slightly distorted triangular dodecahedron (class IV), and this trend is illustrated in Figure 3.20. In general, the deviation from regular geometries is strongly influenced by the size of the lanthanoid in the assembly, and in certain cases, the size of the alkali metal.

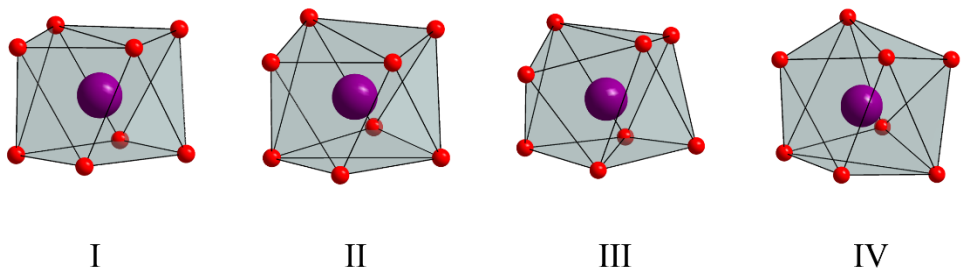

Figure 3.20 - View of the various coordination geometries from distorted square antiprism (I) towards distorted triangular dodecahedron (IV). The numerals I, II, III, and IV correspond to the lanthanoid coordination spheres in each class presented in Table 3.1.

The eight-coordinate geometries of the [Eu(Phen)(**L1**)] and [Ho(**L1**)(EtOH)(H_2O)] complexes were also evaluated against the square antiprism and triangular dodecahedron reference polyhedra, with the CShM coordinates plotted in the Shape Map in Figure 3.19. The [Ho(**L1**)(EtOH)(H_2O)] complex has

a coordination sphere that is best described as a distorted square antiprism, with a geometric shape between that observed in the solvate II and III assemblies, with a deviation from the regular geometries of ~15%. This is not surprising given the relaxation in the coordination sphere due to the presence of two monodentate ligands. On the other hand, the [Eu(Phen)(**L1**)] complex has a coordination sphere which is distorted from both regular polyhedra, with a deviation from the LEIP of ~45%. Again, this is expected given the lack of symmetry in the coordination sphere due to the *N*-donor Phen ligand.

Table 3.3 - Selected data from Shape analysis[216] of the coordination geometries for triangular dodecahedron (TDD) and square antiprism (SAPR) polyhedra. The percentage deviation (%dev.) from the lowest energy interconversion pathway (LEIP) is also shown.

Class	Complex	TDD	SAPR	%dev.
I	$\{Eu_2Na_2\}^{I}$	1.7855	0.8077	32.1
	$\{Tb_2Na_2\}^{I}$	1.8676	0.6836	29.7
	$\{Er_2Na_2\}^{I}$	1.9539	0.5938	28.2
	$\{Yb_2Na_2\}^{I}$	1.9990	0.5232	26.3
II	$\{Tb_2K_2\}^{II}$	1.4922	0.6794	20.9
	$\{Dy_2K_2\}^{II}$	1.4591	0.6851	20.3
	$\{Ho_2K_2\}^{II}$	1.5422	0.6079	19.4
	$\{Er_2Rb_2\}^{II}$	1.3518	0.6472	16.2
	$\{Yb_2K_2\}^{II}$	1.6049	0.5236	15.6
	$\{Yb_2Rb_2\}^{II}$	1.4590	0.5603	17.6
III	$\{Er_2K_2\}^{III}$	0.8263	1.6329	32.3
	$\{Yb_2K_2\}^{III}$	0.8942	1.6706	29.2
	$\{Eu_2K_2\text{-}BuOH\}^{III}$	1.4966	1.6920	49.2
IV	$\{Eu_2K_2\}^{IV}$	0.4454	2.7420	37.5
	$\{Eu_2Rb_2\}^{IV}$	0.4185	2.7839	37.0
	$\{Gd_2K_2\}^{IV}$	0.4130	2.7560	36.3
	$\{Gd_2Rb_2\}^{IV}$	0.3956	2.7248	34.9
	$\{Tb_2Rb_2\}^{IV}$	0.3698	2.6671	32.6
	$\{Dy_2K_2\}^{IV}$	0.3712	2.6633	32.6
	$\{Dy_2Rb_2\}^{IV}$	0.3521	2.6583	31.6
	$\{Ho_2Rb_2\}^{IV}$	0.3144	2.6456	29.4
Other	[Eu(Phen)(**L1**)$_3$]	1.7036	1.3203	45.1
	[Ho(**L1**)$_3$(EtOH)(OH$_2$)]	1.0775	0.8204	14.8

3.6 Conclusion

The **L1**H ligand has been synthesised using a slight modification of a literature method. After deprotonation of the α-C, the β-triketonate coordinates to the lanthanoids in a bis-chelating fashion, as identified by a single crystal X-ray structure. The β-triketonate coordinates to the lanthanoids in the familiar fashion of the classic β-diketonate counterpart, where a 3:1 ligand to metal ratio is preferred giving neutralisation of the charge. Thus, two new mononuclear lanthanoid β-triketonate complexes were crystallised, one of those binding a neutral *N*-donor ligand to reduce the impact of high frequency oscillators on the lanthanoid centre.

A straightforward change of the base in the reaction of the β-triketonate ligand with hydrated lanthanoid chloride salts yielded unprecedented discrete Ln^{3+}/Ae^{+} tetranuclear assemblies with the general formula $[Ln(Ae{\cdot}HOR)(\mathbf{L1})_4]_2$, whereby the tetranuclear metal core is preserved after changes to the lanthanoid, alkali metal, and coordinated alcohol molecules. The preservation of the tetranuclear core provides evidence of the robustness of the discrete structure, even whilst changing the lanthanoid, alkali metal, or solvent alcohol.

The library of tetranuclear assemblies crystallised in four different crystal classes, which once identified, allowed trends to be analysed in important interatomic distances such as Ln···Ln, average Ln-O, and Ln···OH. These distances might have some effect on the resulting photophysical properties of the lanthanoid complexes, which will be investigated in the next chapter.

The coordination sphere was assessed for all crystallised species, using Shape Version 2.1 software, which identified that the four crystallised classes have a direct impact on the coordination sphere being either a square antiprism or a triangular dodecahedron. Again, this subtle difference can explain discrepancies in the solid state emissions, which will be discussed in the next chapter.

The lanthanoid β-triketonate species presented in this chapter are the first structural examples of this new class of lanthanoid complex. Given the structural versatility already observed in the lanthanoid β-diketonate class, there remains extensive research opportunities in the field.

4 Solid-State Photophysical Analysis of Lanthanoid β-Triketonates

Some of the work presented in this chapter has been published in peer reviewed journals which are cited below:

B. L. Reid, S. Stagni, J. M. Malicka, M. Cocchi, G. S. Hanan, M. I. Ogden, M. Massi, *Chem. Commun.* **2014**, *50*, 11580–11582. doi: 10.1039/C4CC04961F

B. L. Reid, S. Stagni, J. M. Malicka, M. Cocchi, A. N. Sobolev, B. W. Skelton, E. G. Moore, G. S. Hanan, M. I. Ogden, M. Massi, *Chem. Eur. J.* **2015**, *21(50)*, 18354-18363. doi: 10.1002/chem.201502536

4.1 Introduction

This chapter focusses on the initial investigation of the emissive properties of the tetranuclear assemblies in the solid state, whose structures were described in Chapter 3. The triplet state energy of the **L1**H ligand was evaluated against the excited state energies of the lanthanoid cations as a method to determine which lanthanoids would be targeted for sensitised emission. The triplet state was determined to have an energy high enough to sensitise the metal-centred emission of Eu^{3+}, Er^{3+}, and Yb^{3+}. Indeed, the Ln^{3+}/Ae^{+} tetranuclear assemblies (Ln^{3+} = Eu^{3+}, Er^{3+}, Yb^{3+}; Ae^{+} = Na^{+}, K^{+}, Rb^{+}) and the [Eu(Phen)(**L1**)$_3$] complex were characterised by strong and long-lived

emissions in the solid state, with a remarkably long-lived decay in the Yb^{3+} and Er^{3+} tetranuclear assemblies. These decays were in fact among the longest-lived in the β-diketonate class for the NIR emitters in the solid state. Given the performance of these complexes in the solid state, an exemplar Yb^{3+} tetranuclear assembly was used in the fabrication of a NIR-OLED, which revealed a brightness and EL efficiency which is among the best of all previously reported NIR-OLEDs using lanthanoids as the emissive species. The Yb^{3+} emission spectrum in the NIR-OLED was characterised by a structured band which varied significantly to the solid state precursor, which prompted an investigation into the thermal stability of the tetranuclear assemblies.

4.2 Photophysical Properties of the Tribenzoylmethane Ligand

To identify the absorption potential of the antenna in the tetranuclear assemblies, the UV-Visible absorption spectrum of the **L1**H molecule and **L1**$^-$ ligand was assessed (Figure 4.1).

The UV-visible absorption spectrum of **L1**H in ethanol presents three main absorption bands at 250 nm, 290 nm, and 340 nm. These are attributed to ππ* transitions.[224] After addition of excess NaOH, KOH, and RbOH to the ethanolic solution, the **L1**H molecule is deprotonated and the **L1**$^-$ ligand will be the major species in solution. The absorption spectra, after deprotonation, are very similar with an increase in molar absorptivity of the lower energy band centred at 340 nm ($\varepsilon^{\mathbf{L1}H}$ = 2,994 $M^{-1}cm^{-1}$; $\varepsilon^{\mathbf{L1}Na}$ = ~10,452 $M^{-1}cm^{-1}$; $\varepsilon^{\mathbf{L1}K}$ = ~10,472 $M^{-1}cm^{-1}$; $\varepsilon^{\mathbf{L1}Rb}$ = ~9,845 $M^{-1}cm^{-1}$), which is consistent with the lower energy associated with increased conjugation in the deprotonated ligand. Moreover, the high energy absorption band centred at 250 nm is concordantly decreased in molar absorptivity ($\varepsilon^{\mathbf{L1}H}$ = 29,423 $M^{-1}cm^{-1}$; $\varepsilon^{\mathbf{L1}Na}$ = ~18,709 $M^{-1}cm^{-1}$; $\varepsilon^{\mathbf{L1}K}$ = ~18,930 $M^{-1}cm^{-1}$; $\varepsilon^{\mathbf{L1}Rb}$ = ~18,276 $M^{-1}cm^{-1}$).

The similarities in the absorption spectra, after deprotonation of the ligand by differing alkali metal bases, indicate that the alkali metal does not influence the antenna molar absorptivity in the UV-Visible spectral region, and thus the presence of different alkali metals in the tetranuclear assemblies should not have a large effect on the sensitisation of lanthanoids *via* the **L1**$^-$ ligand. The absorption spectra reveal that

the antenna should allow lanthanoid sensitisation by excitation of **L1**$^-$ between 250 nm and 430 nm.

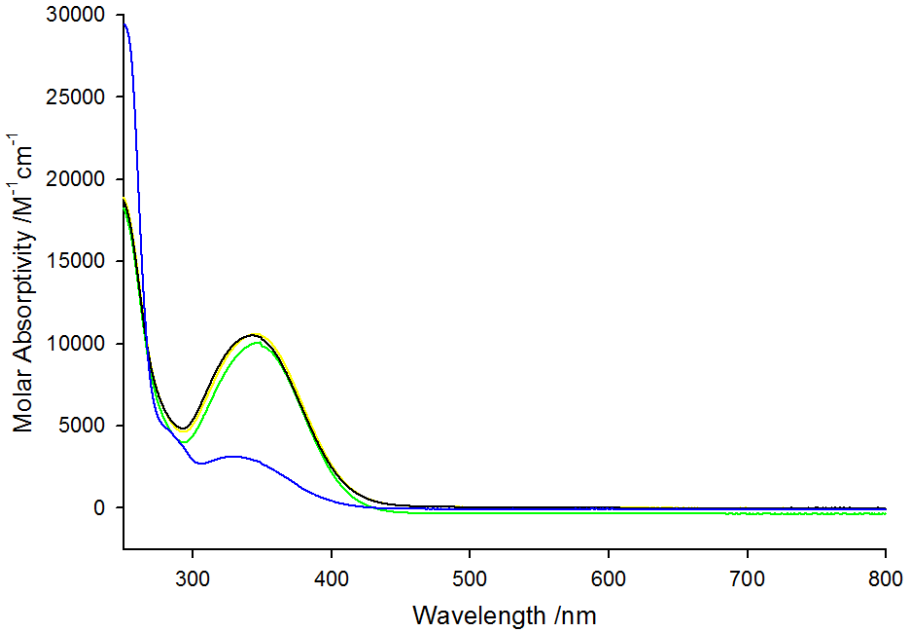

Figure 4.1 – Absorption profiles of **L1**H (blue) **L1**$^-$ (excess NaOH, black trace), **L1**$^-$ (excess KOH, yellow trace), and **L1**$^-$ (excess RbOH, green trace) at 298 K. Concentration of **L1**H/**L1**$^-$ is 2.13x10^{-5} M whilst ~10x excess base was added in each case.

To determine which lanthanoids are likely to be sensitised by the ligand, it is useful to determine the lowest singlet ($^1\pi\pi^*$) and triplet ($^3\pi\pi^*$) excited state energies of the ligand (**L1**H or **L1**$^-$). These energies were estimated from the emission spectra from the **L1**H molecule and its corresponding Gd^{3+} complex in a frozen ethanol matrix at 77 K (Figure 4.2). The emission spectrum of the **L1**H molecule in frozen ethanol presents a structured emission spanning the visible spectral region from ~390 nm to ~500 nm, with a low intensity tail which extends to ~700 nm. The main band is attributed to emission from the $^1\pi\pi^*$ state of the **L1**H ligand, whilst the low energy tail may be attributed to emission from the $^3\pi\pi^*$ state. This $^3\pi\pi^*$ state emission is enhanced due to the improvement in ISC consistent with El-Sayed's rule.[98] After addition of excess Gd^{3+} and triethylamine, the emission spectrum is changed. The structured band previously attributed to emission from the $^1\pi\pi^*$ state is again present, together with another structured band spanning the region from ~480 nm to ~700 nm, which is attributed to emission from the ligand $^3\pi\pi^*$ state, enhanced at 77 K due to the

improvement in the efficiency of ISC as a consequence of the presence of the heavy Gd^{3+} ion contributing to an external heavy atom effect.[225] The $^1\pi\pi^*$ and $^3\pi\pi^*$ state energies can be estimated at the 0-phonon transition, lying at the lowest wavelength of each emission band.

The $^1\pi\pi^*$ and $^3\pi\pi^*$ state energies for **L1**$^-$ were therefore identified to lie at ~25,575 cm^{-1} and ~20,704 cm^{-1}, respectively, as indicated in Figure 4.2. The difference in energy between the $^1\pi\pi^*$ and the $^3\pi\pi^*$ is therefore ~4,871 cm^{-1}, which is known to be at the lower limit for π-systems to undergo an efficient ISC.[90]

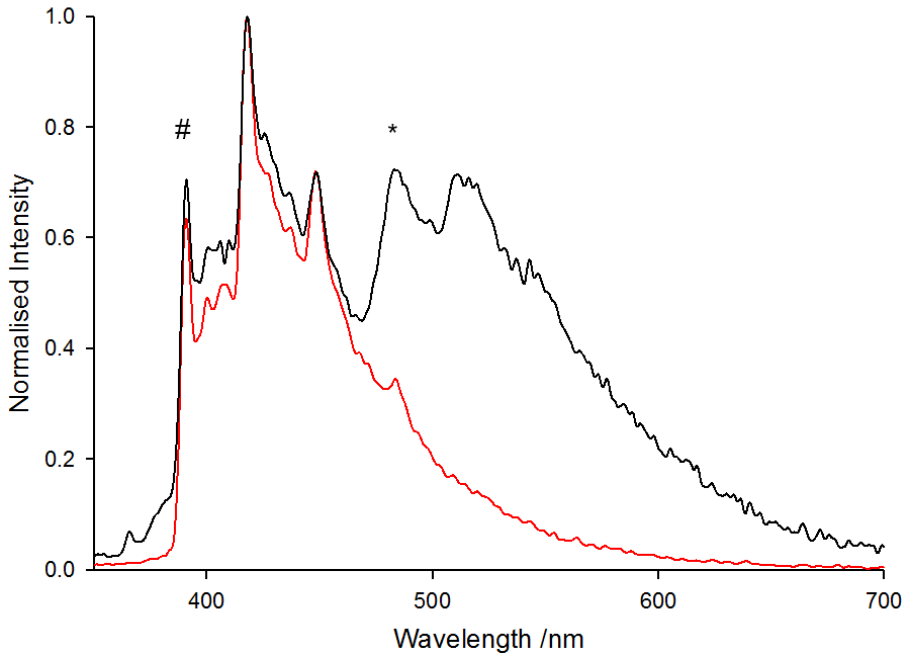

Figure 4.2 – Emission of ligand **L1**H (red trace) and **L1**$^-$ in the presence of excess Gd^{3+} and excess triethylamine (black trace) in an ethanol matrix at 77 K (λ_{ex} = 280 nm, ~10^{-5} M). The # symbol indicates the 0-phonon transition for the singlet excited state, whereas the * symbol indicates the 0-phonon transition for the triplet excited state.

The emission of **L1**$^-$ was also monitored in the solid state $\{Gd_2K_2\}^{IV}$ sample, to examine whether there is a change in the ligand excited state energies in the solid state tetranuclear assemblies (Figure 4.3). The emission spectrum presents a broad structureless band spanning the region ~480 nm to ~700 nm, and is attributed to emission from the $^3\pi\pi^*$ state. The estimated $^3\pi\pi^*$ state energy in the solid state appears to be consistent with the $^3\pi\pi^*$ emission in solution, and so it can be assumed that the

triplet state energy of **L1**$^{-}$ is more or less consistent in solution and in the solid state assemblies.

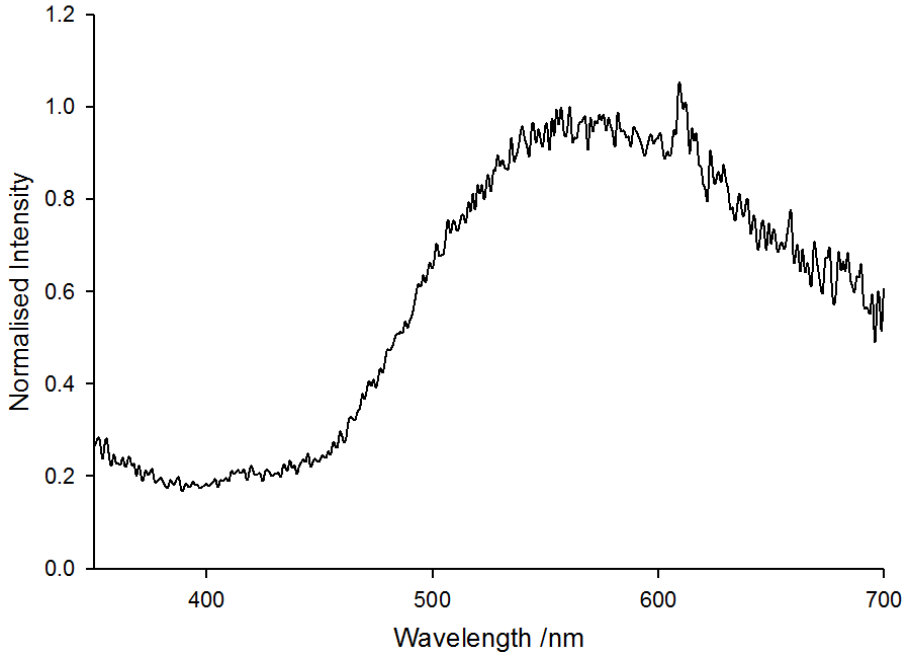

Figure 4.3 – Solid state emission spectrum (λ_{ex} = 280 nm) of the $\{Gd_2K_2\}^{IV}$ assembly at 298 K.

For an efficient energy transfer to the lanthanoids, an energy difference between the ligand $^3\pi\pi^*$ state and lanthanoid emissive state should be >3,500 cm^{-1}.[90] Given the energy of the β-triketonate $^3\pi\pi^*$ state, it is therefore assumed that the lanthanoids which will be best sensitised would be Eu^{3+} and Er^{3+} (Figure 4.4). The energy difference between the ligand $^3\pi\pi^*$ state and the lowest Yb^{3+} excited state, $^2F_{5/2}$, is 10,454 cm^{-1}. According to previously reported investigations, this value should favour an efficient sensitisation,[80] however, energy transfer to a higher energy charge-transfer (CT) state of Yb^{2+} could also be invoked.[105,108] In respect to the [Eu(Phen)(**L1**)$_3$] complex, the $^3\pi\pi^*$ state energy of the Phen ligand has been reported previously at 21,050 cm^{-1} in the presence of hydrated $GdCl_3$,[226] with an absorption spectrum which covers the region of 220 nm to 360 nm,[168] and thus will also have the potential to sensitise Eu^{3+} *via* the antenna effect.

The excited states of Tb^{3+} and Dy^{3+} lie very close in energy to the ligand $^3\pi\pi^*$ state (Tb^{3+}, $^3\pi\pi^*$-$^5D_4$ = 204 cm^{-1}; Dy^{3+}, $^3\pi\pi^*$-$^4F_{9/2}$ = -396 cm^{-1}) and thus the sensitisation of these lanthanoids should be inefficient. The excited lanthanoids are very prone to

deactivation *via* BET to ligand excited states. In fact, the solid state emission of the $\{Tb_2K_2\}^{II}$ and $\{Dy_2K_2\}^{II/IV}$ assemblies in the solid state revealed a very weak band attributed to ligand-centred emission akin to that observed from the $\{Gd_2K_2\}^{IV}$ assembly, providing evidence that an efficient sensitisation is indeed not achieved. The NIR emission from the $\{Ho_2K_2\}^{II}$ complex was also trialled and revealed only a very weak metal-centred emission band in the solid state. Although the Ho^{3+} species has excited states capable of efficient sensitisation by the β-triketonate ligand, the very weak emission suggests that the Ho^{3+} is prone to strong non-radiative decay pathways.

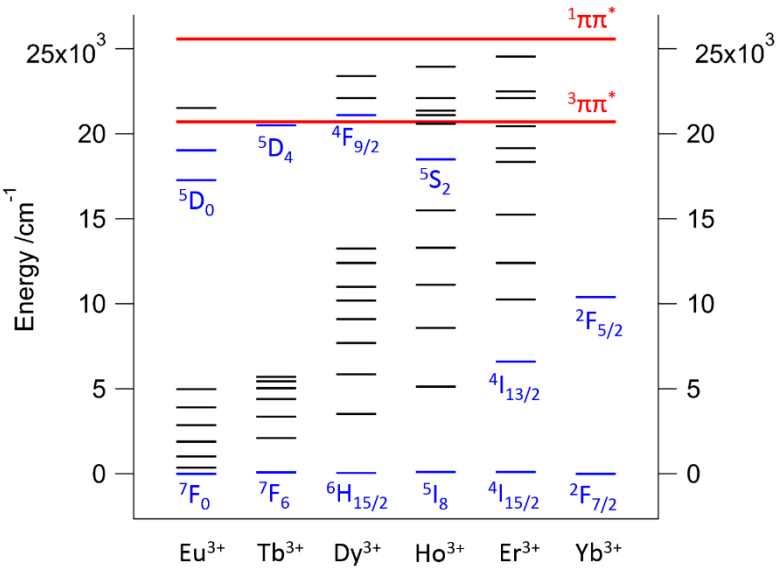

Figure 4.4 – Jabloński diagram depicting the ground and excited energy states of various lanthanoids (blue = ground and emissive states). The red lines illustrate the excited state energies of the **L1**$^-$ ligand. Lanthanoid energy values taken from Carnall *et al.*[51–54]

The strongest emitters were found to be the Eu^{3+}, Er^{3+}, and Yb^{3+} species and the investigation of the solid state emissive properties will focus on these tetranuclear assemblies.

4.3 Lanthanoid Emissions

The Eu^{3+}, Er^{3+}, and Yb^{3+} assemblies were found to be emissive, with bright red emission observed for the Eu^{3+} assemblies and NIR emissions observed for the Er^{3+} and Yb^{3+} complexes (Figure 4.5). All emission spectra presented in this section are a consequence of the antenna effect, indicated by the similarity between the broad structureless excitation spectrum in the assemblies and the absorption spectrum (Figure 4.1) of the ligand. Furthermore, all the emission spectra were found to be independent from the excitation wavelength.

The pure emissions from the Eu^{3+} species were captured using a camera with a OG550 filter, while the NIR emission from the Yb^{3+} species were captured using a camera with the same UV-Visible barrier filter with its IR filter removed to ensure that NIR light was detected by the photodevice. The emission of Er^{3+} was unable to be captured at 1550 nm by the camera. For complete camera details, see Chapter 8 - Experimental.

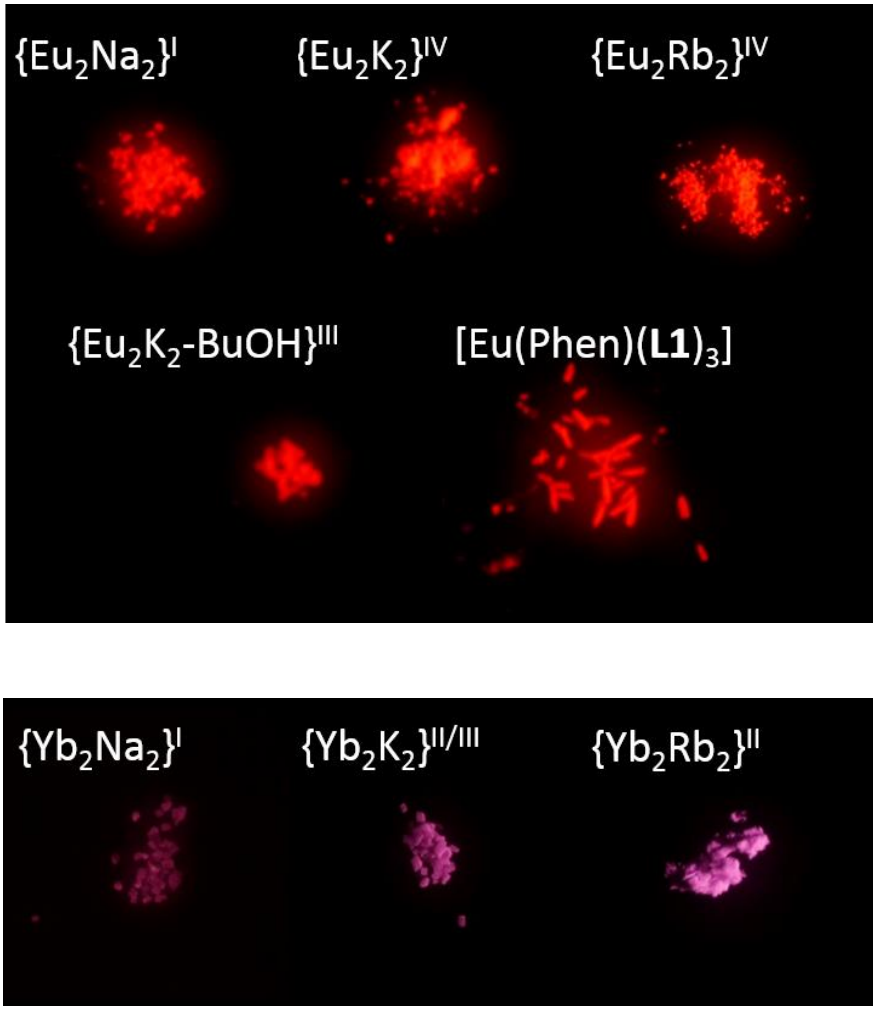

Figure 4.5 – Visual emission of crystals after excitation at 350 nm with a Polilight. Cut-on filter 550 nm for Eu^{3+} complexes, and 900 nm for Yb^{3+} complexes.

4.3.1 Emission from the NIR Emitters

Characteristic NIR fluorescent emission was observed from the $\{Yb_2Na_2\}^{I}$, $\{Yb_2K_2\}^{II/III}$, and $\{Yb_2Rb_2\}^{II}$ assemblies in the 900 nm to 1100 nm region (Figures 4.6-4.8). The emission is attributed to the $^2F_{7/2}\leftarrow{}^2F_{5/2}$ transition, which is split into four main observable bands at 978, 1005, 1015, and 1037 nm, due to ligand field effects, consistent with the doubly degenerate nature (Kramer's Doublets) of the Yb^{3+} Stark components.[49] The high energy shoulder around 950 nm in the emission spectra can be attributed to emission from "hot" excited states.[227] Slight differences in the relative intensities in the bands are ascribed to the various degree of distortion in the

coordination sphere geometries, consistent with that observed in the crystal structures. It is also noted that for each species the excitation at 350 nm resulted in no observable emission in the 400 nm to 900 nm spectral region indicating an efficient sensitisation of the Yb^{3+} cation by the β-triketonate.

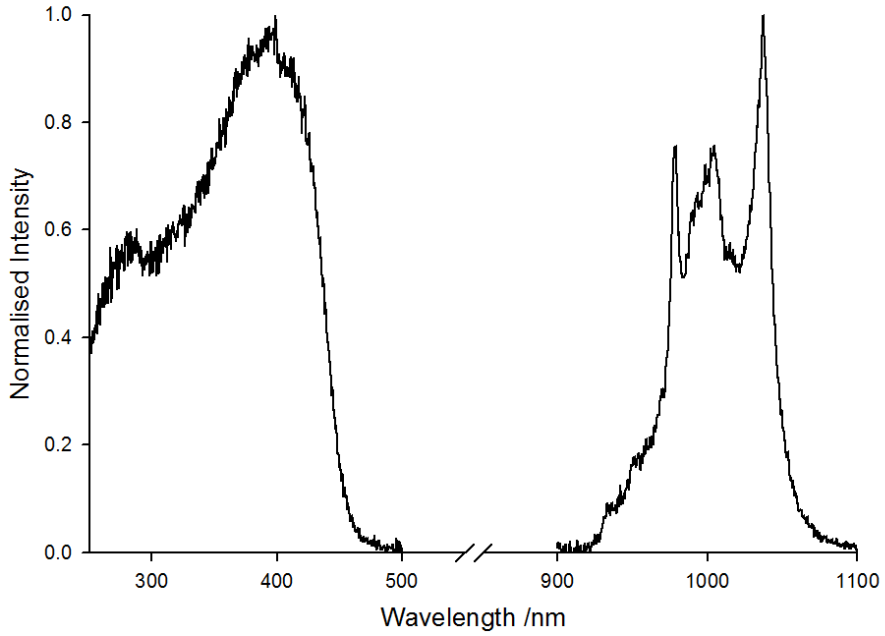

Figure 4.6 - Normalised excitation (λ_{em} = 1037 nm) and emission (λ_{ex} = 350 nm) spectra of the $\{Yb_2Na_2\}^I$ assembly in the solid state at 298 K.

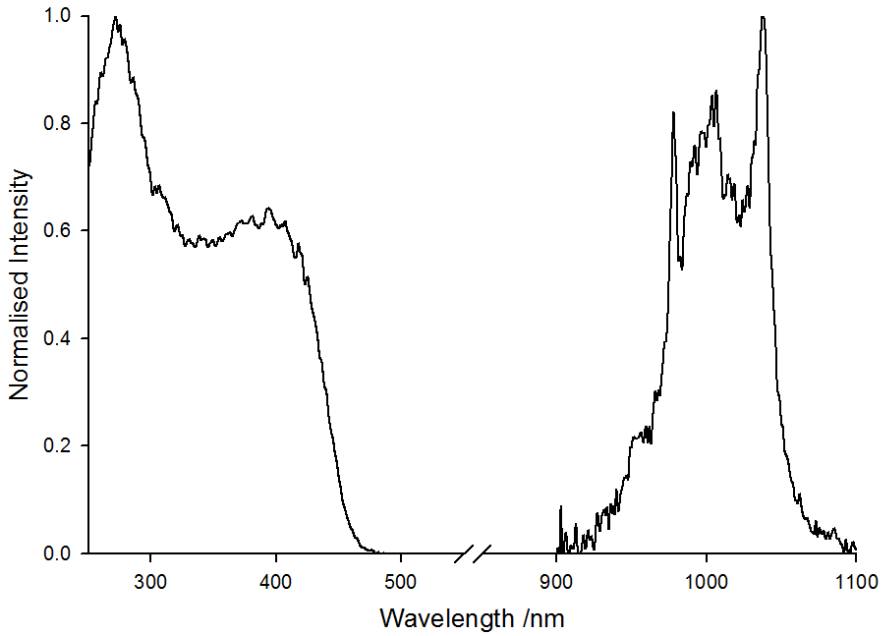

Figure 4.7 – Normalised excitation (λ_{em} = 1035 nm) and emission (λ_{ex} = 350 nm) spectra of the $\{Yb_2K_2\}^{II/III}$ assembly in the solid state at 298 K.

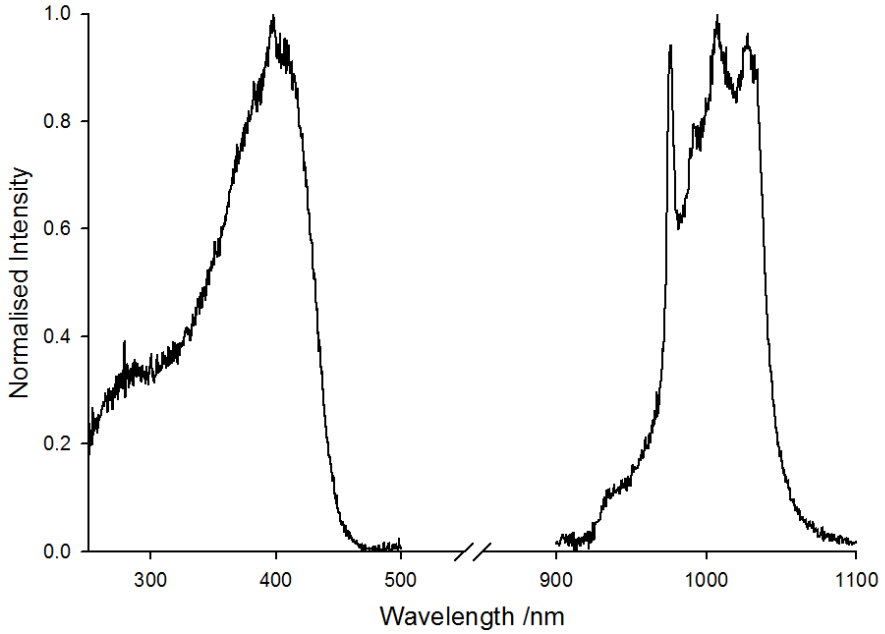

Figure 4.8 – Normalised excitation (λ_{em} = 978 nm) and emission (λ_{ex} = 350 nm) spectra of the $\{Yb_2Rb_2\}^{II}$ assembly in the solid state at 298 K.

The excited state lifetimes (τ_{obs}) for the $\{Yb_2Na_2\}^{I}$, $\{Yb_2K_2\}^{II/III}$, and $\{Yb_2Rb_2\}^{II}$ assemblies were fit to a monoexponential function, giving values of 37.0 µs, 46.7 µs,

and 44.4 μs respectively (Figure 4.9). These values (reported in Table 4.1) are significantly long-lived and among the longest recorded for solid state Yb^{3+} species with bound β-diketonate ligands (see Table 4.2 for literature values), for which typical values are ~5 μs.[183] The values of τ_{obs} for the assemblies reported herein are even longer than those of complexes where ligands were perfluorinated to reduce the extent of multiphonon relaxation caused by CH bonds (~12 μs).[122] Only complexes bearing perfluorinated *and* deuterated β-diketonate ligands appear to have values of τ_{obs} longer than the family of $[Yb(Ae{\cdot}HOEt)(\mathbf{L1})_4]_2$ assemblies (from 47 μs at 53% deuteration, to 289 μs at 96% deuteration at the α-C position).[182] Thus, the β-triketonate ligand appears to be a viable alternative to the classic β-diketonate ligand for the Yb^{3+} species, particularly due to the synthetic challenges faced for the perfluorination and deuteration of the ligand.

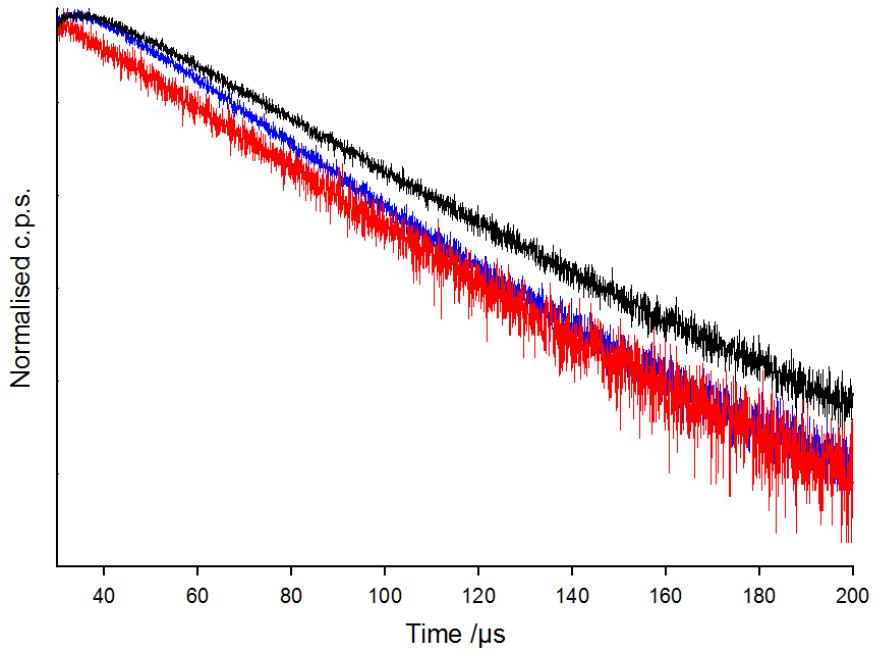

Figure 4.9 – Lifetime decays of the $\{Yb_2Na_2\}^{I}$ (blue trace; λ_{ex} = 350 nm, λ_{em} = 980 nm.), $\{Yb_2K_2\}^{II/III}$ (red trace; λ_{ex} = 350 nm, λ_{em} = 1035 nm.), and $\{Yb_2Rb_2\}^{II}$ (black trace; λ_{ex} = 350 nm, λ_{em} = 980 nm.) assemblies in the solid state at 298 K.

Assuming a radiative lifetime (τ_R) value of 1.2 ms, which is standard for Yb^{3+} β-diketonate complexes,[125,228] the intrinsic quantum yields (Φ_{Ln}^{Ln}) can be approximated to 3.1, 3.9, and 3.8% for the $\{Yb_2Na_2\}^{I}$, $\{Yb_2K_2\}^{II/III}$, and $\{Yb_2Rb_2\}^{II}$

assemblies, respectively. Following the trend reported for τ_{obs}, these values are among the highest recorded Φ_{Ln}^{Ln} values for the Yb^{3+} β-diketonate family in the solid state, indicating the efficiency of the $[Yb(Ae{\cdot}HOEt)(\mathbf{L1})_4]_2$ assemblies in preventing quenching *via* multiphonon relaxation.

Table 4.1 - Selected photophysical data of the NIR emitting $\{Ln_2Ae_2\}$ assemblies in the solid state.

Assembly	τ_{obs} **(µs)**	Φ_{Ln}^{Ln} **(%)**[a]
$\{Yb_2Na_2\}^{I}$	37.0	3.1
$\{Yb_2K_2\}^{II/III}$	46.7	3.9
$\{Yb_2Rb_2\}^{II}$	44.4	3.8
$\{Er_2Na_2\}^{I}$	4.8	0.7
$\{Er_2K_2\}^{III}$	5.0	0.8
$\{Er_2Rb_2\}^{II}$	5.8	0.9

[*a*] Intrinsic quantum yields were calculated using τ_R values of 1.2 ms for Yb^{3+}, and 0.66 ms[49] for Er^{3+}.

Table 4.2 – Literature Yb^{3+} lifetime decays bearing β-diketonate ligands in the solid state.

	Complex	τ_{obs} **(µs)**
Non-Fluorinated	$Yb(h)_3(5NO_2phen)$[183]	5.2
	$Yb(Dmh)_3(5NO_2phen)$[183]	5.0
Fluorinated	$Yb(Tfnb)_3(5NO_2phen)$[183]	7.2
	$[Yb(Btfax)]NBu_4$[122]	12.1
Deuterated + Fluorinated	$Cs[Yb(Hfa)_4]$ 53% deuteration[182]	47.4

Abbreviations in table include: h = 2,4-hexanedionate; Dmh = 2,6-dimethyl-3,5-heptanedionate; Tfnb = 4,4,4-trifluoro-1(2-naphtyl)-1,3-butandionate; $5NO_2$phen = 5-nitro-1,10-phenanthroline; Hfa = hexafluoroacetylacetone; Btfax = 1,1'-(4,4'-(2,2bis((4-(4,4,4-trifluoro-3-oxobutanoyl)phenoxy)methyl)propane-1,3-diyl)bis(oxy)bis(4,4,4-trifluorobutane-1,3-dione).

Table 4.3 - Literature Er^{3+} lifetime decays bearing β-diketonate ligands in the solid state.

	Complex	**τ_{obs} (μs)**
Non-Fluorinated	$Er(Dmh)_3(Bipy)$[229]	1.7
	$Er(Dmh)_3(Bath)$[229]	1.7
	$Er(Dmh)_3(5NO_2phen)$[229]	1.4
Fluorinated	$Er(Fod)_3(Bipy)$[181]	1.5
	$Er(Fod)_3(Bath)$[181]	1.4
Deuterated + Fluorinated	$Cs[Er(Hfa)_4]$ 99% deuteration	~11

Abbreviations in table include: Dmh = 2,6-dimethyl-3,5-heptanedionate; Bipy = 4,4'-bipyridine; Bath = bathophenanthroline; $5NO_2phen$ = 5-nitro-1,10-phenanthroline; Fod = 6,6,7,7,8,8,8-heptafluoro-2,2-dimethyl-3,5-octadionate; Hfa = hexafluoroacetylacetone;

The $[Er(Ae{\cdot}HOEt)(\mathbf{L1})_4]_2$ (Ae^+ = Na^+, K^+ and Rb^+) assemblies also display fluorescent NIR emission in the 1420 nm to 1620 nm range, which is attributed to the characteristic $^4I_{15/2} \leftarrow {}^4I_{13/2}$ transition (Figures 4.10-4.12). The band appears narrow and structured as a result of ligand field effects.[181] Again, the structure of the emission band varies slightly due to the relatively different ligand field effects present in the three assemblies. The excitation spectra (Figures 4.10-4.12), along with the typical broad antenna component, also show a sharp peak at 485 nm consistent with the spin-allowed $^4I_{15/2} \rightarrow {}^4F_{7/2}$ intraconfigurational transition.[230]

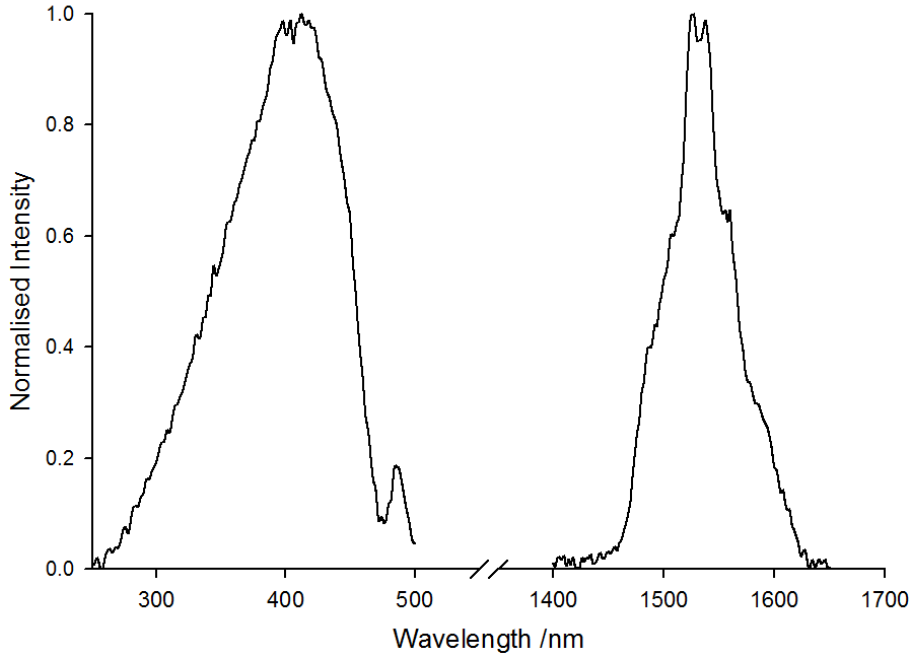

Figure 4.10 – Normalised excitation (λ_{em} = 1538 nm) and emission (λ_{ex} = 380 nm) spectra of the $\{Er_2Na_2\}^{I}$ assembly in the solid state at 298 K.

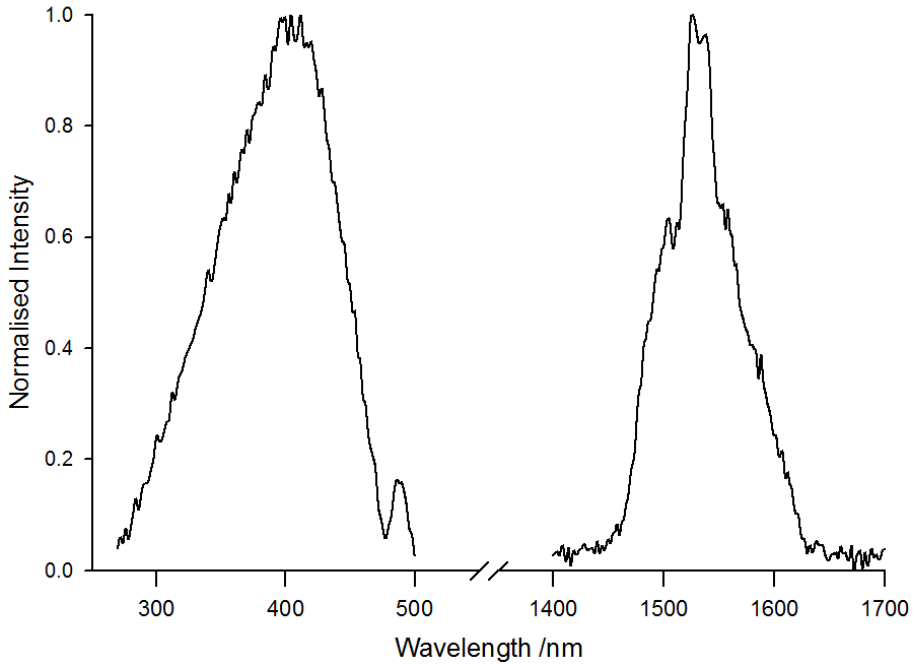

Figure 4.11 – Normalised excitation (λ_{em} = 1526 nm) and emission (λ_{ex} = 370 nm) spectra of the $\{Er_2K_2\}^{III}$ assembly in the solid state at 298 K.

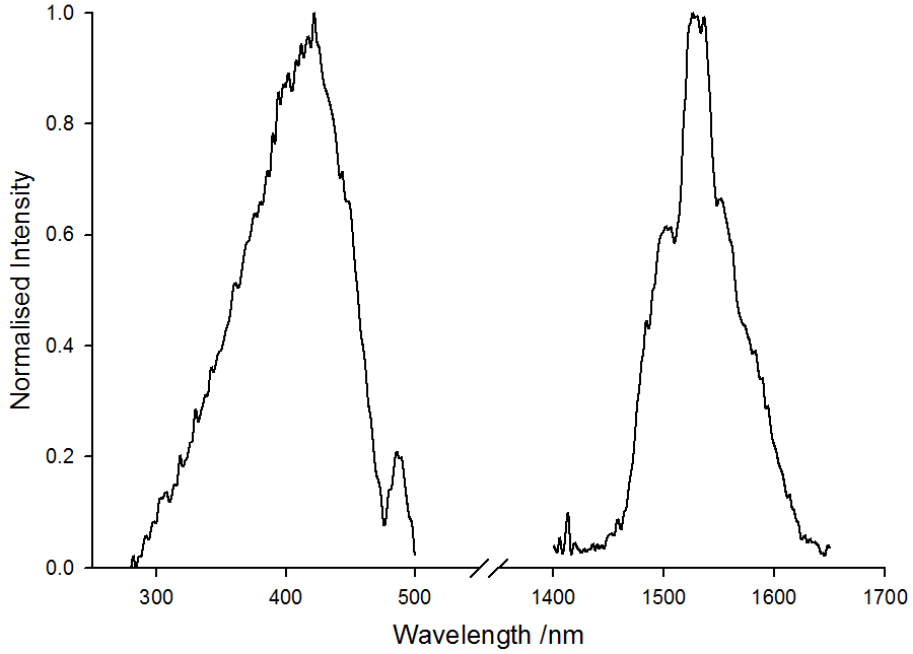

Figure 4.12 – Normalised excitation (λ_{em} = 1528 nm) and emission (λ_{ex} = 400 nm) spectra of the $\{Er_2Rb_2\}^{II}$ assembly in the solid state at 298 K.

The values of τ_{obs} were fit to a monoexponential decay of 4.8 μs, 5.0 μs, and 5.8 μs for $\{Er_2Na_2\}^{I}$, $\{Er_2K_2\}^{III}$, and $\{Er_2Rb_2\}^{II}$ respectively (Table 4.1, Figure 4.13). As per the case of the Yb^{3+} assemblies, these τ_{obs} values are longer than those found in Er^{3+} β-diketonate complexes (~1-2 μs),[229] with perfluorinated Er^{3+} β-diketonate complexes (~1-2 μs),[181] and are only outclassed in cases when the β-diketonate ligand has been both perfluorinated *and* deuterated (from ~6 μs at 58% deuteration, to ~11 μs at 98% deuteration at the α-C position).[182] Table 4.3 provides details of the literature values discussed here. Therefore, the advantageous reduction of multiphonon relaxation observed in the case of Yb^{3+} is consistently maintained for the Er^{3+} assemblies.

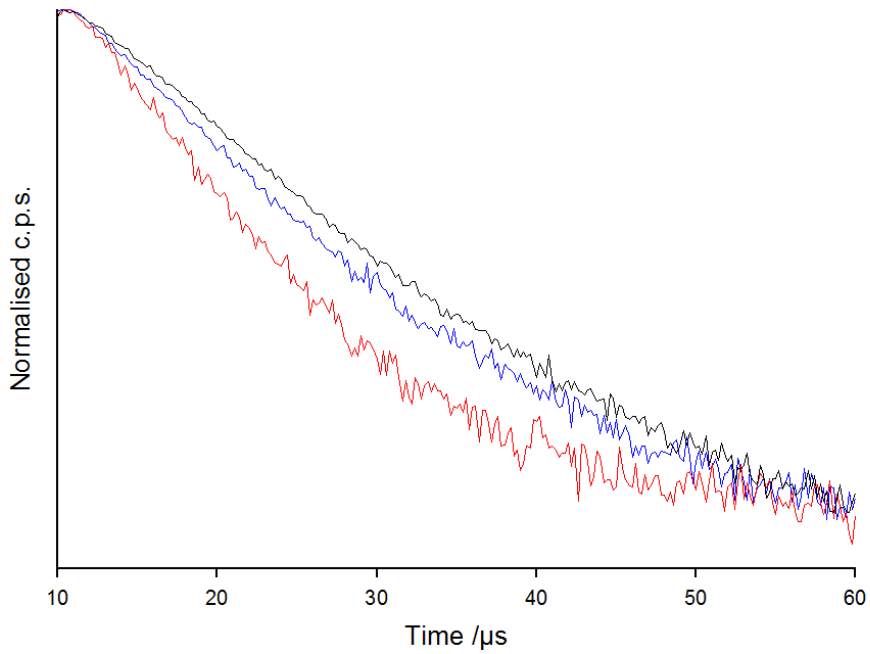

Figure 4.13 – Lifetime decays of the $\{Er_2Na_2\}^{I}$ (blue trace, λ_{ex} = 380 nm, λ_{em} = 1526 nm), $\{Er_2K_2\}^{III}$ (red trace, λ_{ex} = 370 nm, λ_{em} = 1526 nm), and $\{Er_2Rb_2\}^{II}$ (black trace, λ_{ex} = 400 nm, λ_{em} = 1530 nm) assemblies in the solid state. Each decay required deconvolution of the Instrumental Response Function (IRF) at 298 K.

The values of τ_{obs} for the Na^+-bearing assemblies of Yb^{3+} and Er^{3+} are shortened by ~20% when compared to their analogous assemblies incorporating either K^+ or Rb^+. This effect is tentatively attributed to more efficient quenching caused by the closer proximity of the ethanolic OH groups in the Na^+-containing structures, as illustrated by the X-ray diffraction studies (see Chapter 3).

Figures 4.14-4.15 illustrate the multiphonon relaxation pathways for the investigated Yb^{3+} and Er^{3+} species. The OH stretch frequency used is experimental value from the solid state IR spectra (ν ~ 3,645 cm^{-1}, see Chapter 8 – Experimental Section), and should efficiently quench both the Yb^{3+} and Er^{3+} excited states. Furthermore, the β-triketonate molecule has a CC bond in place of a CH bond in the β-diketonate molecule; and thus needs a much greater vibrational quanta to quench the Yb^{3+} and Er^{3+} excited states compared to that of CH. The improvement in the NIR emitting species presented in this chapter is attributed to the removal of this CH vibration.

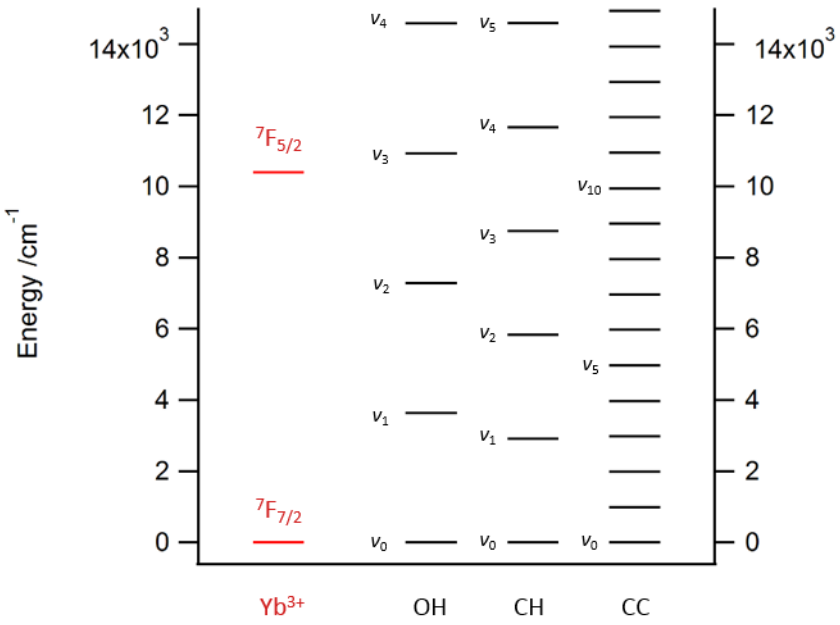

Figure 4.14 – The relative vibrational energies of OH, CH, and CC compared to the excited state of Yb^{3+}.

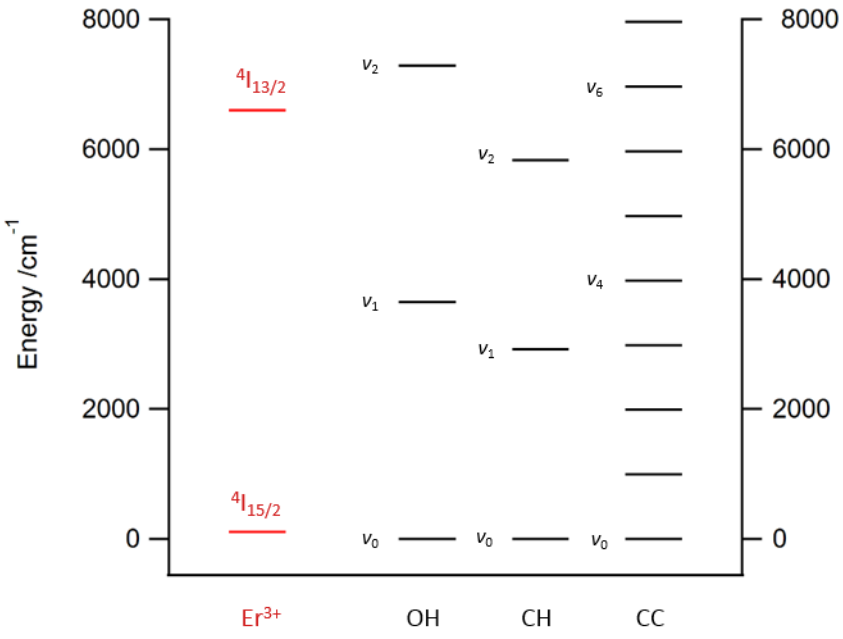

Figure 4.15 - The relative vibrational energies of OH, CH, and CC compared to the excited state of Er^{3+}.

Overall, the photophysical data demonstrate that the $[Ln(Ae{\cdot}HOEt)(\mathbf{L1})_4]_2$ assemblies represent a family of efficient and brightly NIR-emitting species in the case of Yb^{3+} and Er^{3+}. Clearly, the major observed factor for the improvement of the luminescence performance seems to be associated with the removal of quenching effects from the α-CH in the β-triketonate $\mathbf{L1}^-$ ligand. However, the close proximity of an OH vibration to the metal centre also appears to affect the Na^+ bearing assemblies. This new class of β-triketonate ligand may offer a viable and more facile synthetic approach to ligand design for lanthanoid NIR-emitting complexes, without the need to rely exclusively on perfluorination and deuteration strategies. The comparison of the observed lifetime values to the literature (Figures 4.2 and 4.3) show the clear elongation in luminescence lifetime when the β-triketonate is used.

4.3.2 Emission from Europium Species

In the solid state, the $\{Eu_2Na_2\}^{I}$, $\{Eu_2K_2\}^{IV}$, $\{Eu_2Rb_2\}^{IV}$, and $\{Eu_2K_2\text{-}BuOH\}^{III}$, assemblies display the characteristic Eu^{3+} metal-centred emission between 580 nm and 750 nm (Figures 4.16-4.19). In each excitation spectrum (Figures 4.16-4.19), together with a broad antenna component, there is a sharp band at 465 nm, consistent with an intraconfigurational $^7F_0 \rightarrow {}^5D_2$ transition.[49]

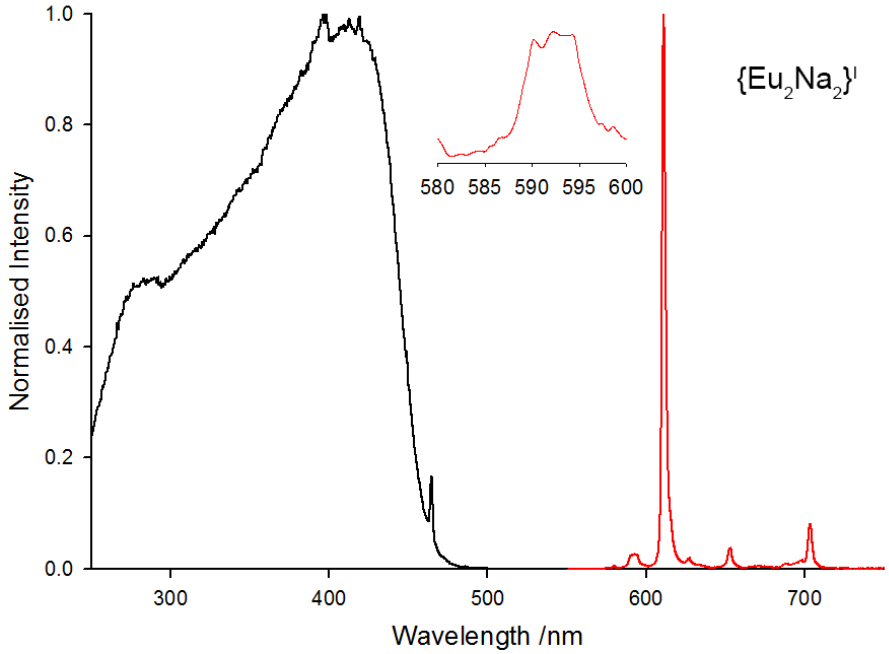

Figure 4.16 – Normalised excitation (λ_{em} = 612 nm) and emission (λ_{ex} = 350 nm) spectra of the $\{Eu_2Na_2\}^{I}$ assembly in the solid state at 298 K. Inset: A close-up region of the emission spectrum highlighting the splitting in the $^7F_1 \longleftarrow {}^5D_0$ emission band.

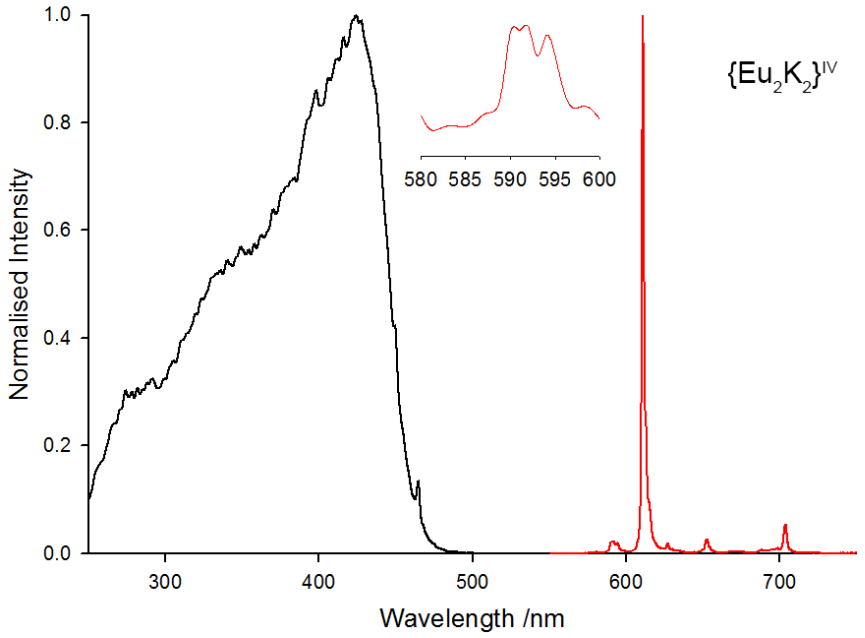

Figure 4.17 – Normalised excitation (λ_{em} = 612 nm) and emission (λ_{ex} = 350 nm) spectra of the $\{Eu_2K_2\}^{IV}$ assembly in the solid state at 298 K. Inset: A close-up region of the emission spectrum highlighting the splitting in the $^7F_1 \longleftarrow {}^5D_0$ emission band.

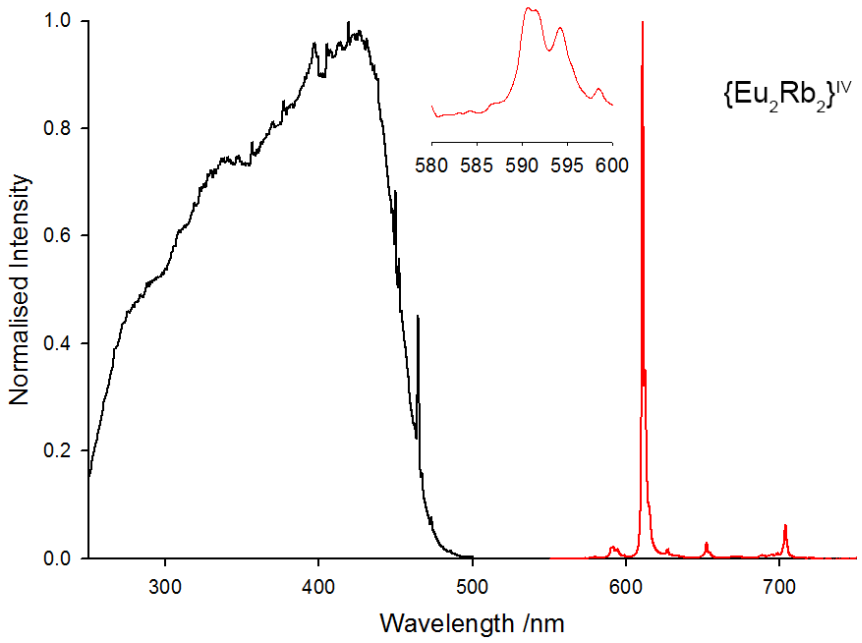

Figure 4.18 – Normalised excitation (λ_{em} = 611 nm) and emission (λ_{ex} = 350 nm) spectra of the $\{Eu_2Rb_2\}^{IV}$ assembly in the solid state at 298 K. Inset: A close-up region of the emission spectrum highlighting the splitting in the $^7F_1 \longleftarrow {}^5D_0$ emission band.

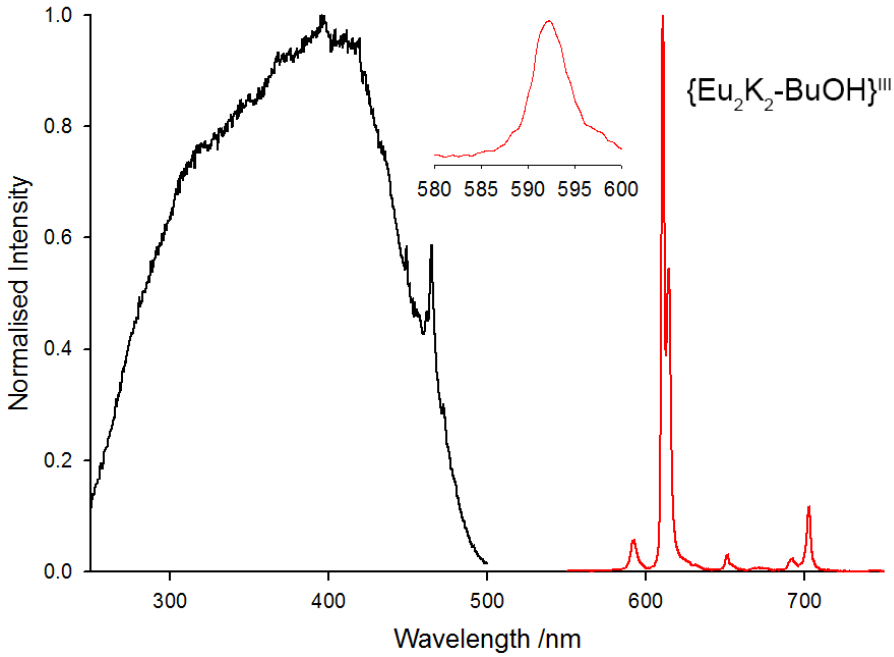

Figure 4.19 – Normalised excitation (λ_{em} = 612 nm) and emission (λ_{ex} = 350 nm) spectra of the $\{Eu_2K_2\text{-BuOH}\}^{III}$ assembly in the solid state at 298 K. Inset: A close-up region of the emission spectrum highlighting the splitting in the $^7F_1 \longleftarrow {}^5D_0$ emission band.

The triplet state energy of the **L1**$^{-}$ ligand lies ~1,704 cm^{-1} above the $^{5}D_1$ excited state energy of the Eu^{3+} ion, which is known to be an efficient energy difference to allow an amenable energy transfer to both the $^{5}D_1$ and $^{5}D_0$ energy states.[93] As evidence to support this, emission from the $^{7}F_1 \leftarrow\!\!- {}^{5}D_1$, and $^{7}F_2 \leftarrow\!\!- {}^{5}D_1$ transitions,[231] were observable in each Eu^{3+} emission spectrum at 537 nm and 545 nm respectively (Figure 4.20 for the $\{Eu_2Na_2\}^{I}$ spectrum, see Appendix for the $\{Eu_2K_2\}^{IV}$ and $\{Eu_2Rb_2\}^{IV}$ spectra). This emission is much weaker in intensity than the emission from the $^{5}D_0$ state, due to the competing fast IC from the $^{5}D_1$ state to $^{5}D_0$ state. However, it is sufficient evidence to suggest that the $^{5}D_1$ state is populated by sensitisation by the β-triketonate. Emission from the $^{5}D_1$ state has been observed with various ligands, including 1,3-substituted β-diketonates, previously.[129,132,232]

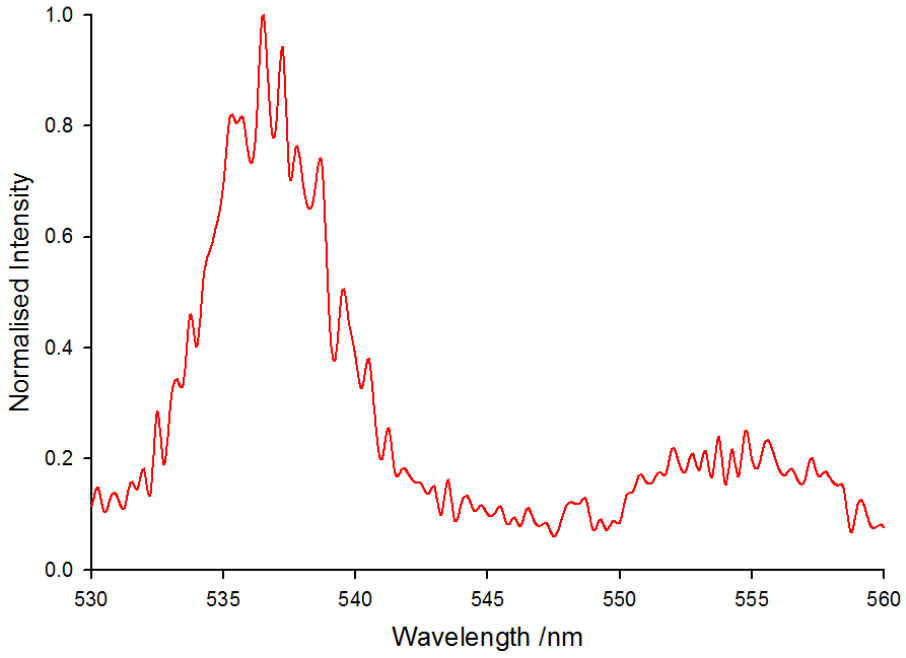

Figure 4.20 – Normalised emission (λ_{ex} = 350 nm) from the $\{Eu_2Na_2\}^{I}$ assembly in the solid state at 298 K, attributed to $^{7}F_1 \leftarrow\!\!- {}^{5}D_1$, and $^{7}F_2 \leftarrow\!\!- {}^{5}D_1$ transitions.

The characteristic Eu^{3+} $^{5}D_0$ emission spectra display five distinct bands corresponding to the $^{7}F_J \leftarrow\!\!- {}^{5}D_0$ (J = 0, 1, 2, 3, 4) transitions. The profiles of the emission spectra are very similar between all the Eu^{3+} tetranuclear assemblies, however slight

differences in the fine structure of the bands are consistent with the presence of the various degrees of distortion identified in the crystal structures.

The weak $^7F_0 \leftarrow ^5D_0$ band has a FWHM ranging between 15 cm^{-1} and 59 cm^{-1}, for the $\{Eu_2Na_2\}^I$, $\{Eu_2K_2\}^{IV}$, and $\{Eu_2Rb_2\}^{IV}$ assemblies. In contrast, a value for the $\{Eu_2K_2\text{-BuOH}\}^{III}$ assembly could not be estimated, due to the low intensity of the band. In general, this FWHM range is consistent with one unique emitting Eu^{3+} for each assembly,[137] in agreement with the fact that the two Eu^{3+} are related by an inversion centre located in the centre of the assembly and therefore have identical coordination geometries.

The MD allowed $^7F_1 \leftarrow ^5D_0$ transition is virtually superimposable for the $\{Eu_2K_2\}^{IV}$ and $\{Eu_2Rb_2\}^{IV}$ assemblies, consistent with an identical coordination geometry. The splitting pattern of three peaks, with the two lower energy ones being quasi-degenerate is consistent with the slightly distorted D_{2d} symmetry of the coordination sphere observed in the crystal structure. On the other hand, the splitting pattern of the $^7F_1 \leftarrow ^5D_0$ transition in the $\{Eu_2Na_2\}^I$ assembly is different, as it presents three peaks with the two higher energy ones being quasi-degenerate. This pattern is in agreement with a slightly distorted square antiprismatic D_{4d} symmetry.[36,37] The $\{Eu_2K_2\text{-BuOH}\}^{III}$ assembly displays a single broad peak devoid of structure, which might be an indication that the bulk sample is obtained as a mixture of differently solvated structures, and thus differing coordination geometries.

The [Eu(Phen)(**L1**)$_3$] complex also shows Eu^{3+} metal-centred emission in the solid state originating as a consequence of the antenna effect from both the **L1**$^-$ and Phen[168] ligands (Figure 4.21). The [Eu(Phen)(**L1**)$_3$] complex shows emission from the Eu^{3+} $^5D_1$ state consistent with the tetranuclear assemblies (Figure 4.22). This is expected as the triplet state of the **L1**$^-$ and Phen ligands remain above the $^5D_1$ state in the complex. An interesting note is that the $^7F_1 \leftarrow ^5D_1$ and $^7F_2 \leftarrow ^5D_1$ emission bands appear split into two observable bands in this case, possibly due to the lower symmetry in the ligand field.[71] This observation can also be tentatively attributed to the presence of "hot bands" in the $^5D_1$ excited state.

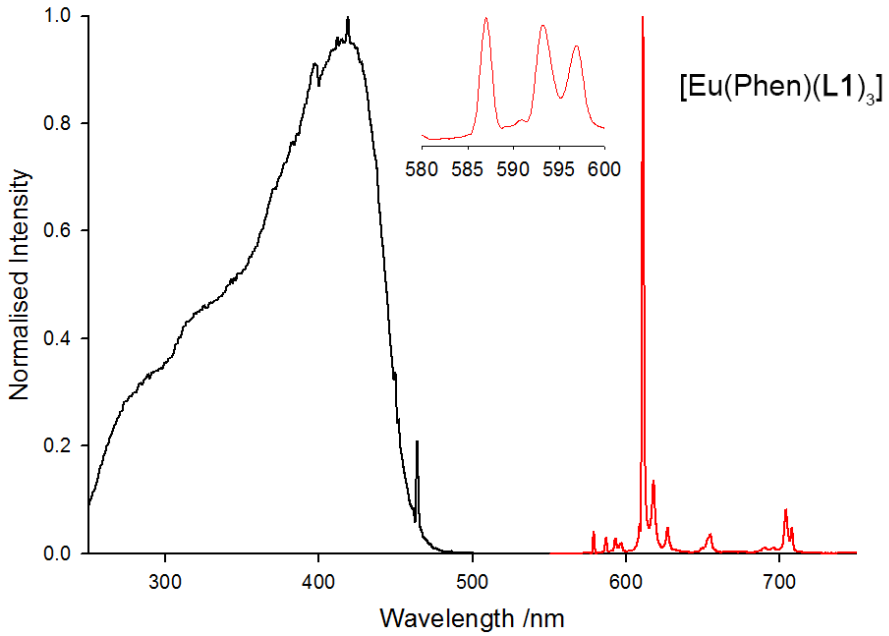

Figure 4.21 – Normalised excitation (λ_{em} = 612 nm) and emission (λ_{ex} = 350 nm) spectra of the [Eu(Phen)(**L1**)$_3$] complex in the solid state at 298 K. Inset: A close-up region of the emission spectrum highlighting the splitting in the $^7F_1 \longleftarrow {}^5D_0$ emission band.

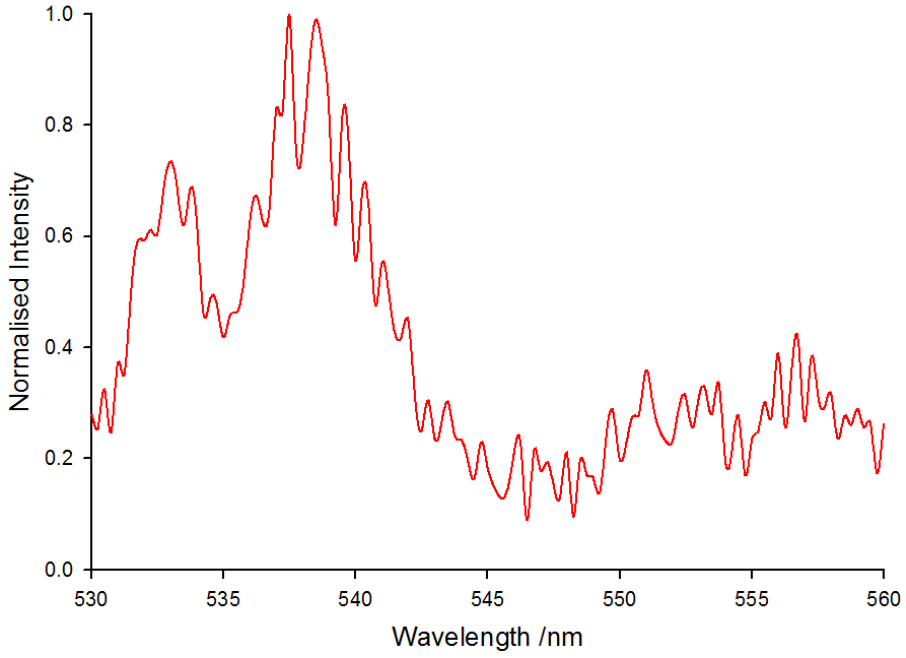

Figure 4.22 – Normalised emission (λ_{ex} = 350 nm) from the [Eu(Phen)(**L1**)$_3$] complex in the solid state at 298 K, attributed to $^7F_1 \longleftarrow {}^5D_1$, and $^7F_2 \longleftarrow {}^5D_1$ transitions.

The emission spectrum of the [Eu(Phen)(**L1**)$_3$] complex in the solid state displays the five characteristic Eu^{3+} emission bands described previously. The low intensity $^7F_0 \leftarrow ^5D_0$ band has a FWHM of 35 cm^{-1}, again indicative of one unique emitting species in the solid state.[137]

The $^7F_1 \leftarrow ^5D_0$ transition is, in this case, split into three easily distinguishable bands, two of which are very close in energy. This splitting is inherent of a local Eu^{3+} symmetry lower than D_{2d}, or coordination geometry highly distorted from regular polyhedra.[36,233] This is consistent with the observation of splitting in the $^7F_1 \leftarrow ^5D_1$ and $^7F_2 \leftarrow ^5D_1$ bands due to low symmetry, which is observed in the crystal structure where the ideal square antiprismatic geometry is distorted, with a symmetry lowered due to the *N*-donor ligand.

To further gauge the change in the Eu^{3+} emission spectra in the different Eu^{3+} coordination environments, the integration of each peak in the Eu^{3+} emission spectrum was compared to that of the $^7F_1 \leftarrow ^5D_0$ transition, whose intensity is unaffected by the ligand field (Table 4.4).

The ratio of the $^7F_2 \leftarrow ^5D_0$ band gives the best insight into subtle changes in the coordination environment as it is hypersensitive to this environment.[71,234] The ratio $I(^7F_2 \leftarrow ^5D_0)/I(^7F_1 \leftarrow ^5D_0)$ for $\{Eu_2Na_2\}^{I}$, $\{Eu_2K_2\}^{IV}$, $\{Eu_2Rb_2\}^{IV}$, $\{Eu_2K_2\text{-BuOH}\}^{III}$, and [Eu(Phen)(**L1**)$_3$] is presented in Table 4.4. This ratio is quite large in each case, which might be due to the distorted coordination geometries promoting partial relaxation of the parity-forbidden nature of the transition *via* *J*-mixing and/or ligand field mixing.[71,130] Although the $\{Eu_2Na_2\}^{I}$ (D_{4d}) has a coordination geometry which is significantly different to the $\{Eu_2K_2\}^{IV}$ and $\{Eu_2Rb_2\}^{IV}$ (D_{2d}) assemblies, there is not an appreciable discrepancy in the $I(^7F_2 \leftarrow ^5D_0)/I(^7F_1 \leftarrow ^5D_0)$ ratios.

It is interesting to note that the ratios for the $\{Eu_2K_2\text{-BuOH}\}^{III}$ and [Eu(Phen)(**L1**)$_3$] species are somewhat lower than the other assemblies. This may be an effect of these species having coordination environments which are somewhere in between both the square antiprismatic and triangular dodecahedral geometries, as identified by Shape Analysis in Chapter 3.

The $(^7F_4 \leftarrow ^5D_0)/I(^7F_1 \leftarrow ^5D_0)$ ratio is again relatively similar for all Eu^{3+} species investigated. The $\{Eu_2K_2\}^{IV}$ and $\{Eu_2Rb_2\}^{IV}$ assemblies have very similar values, consistent with the identical D_{2d} coordination geometries present. The slightly larger value for the $\{Eu_2Na_2\}^{I}$ assembly is indicative of a coordination geometry closer to that of the square antiprism, D_{4d}, whereby a centre of symmetry is absent.[71] This ratio

for the [Eu(Phen)(**L1**)$_3$] complex is slightly larger than all other investigated species. This is accompanied by a lower I($^7F_2$←$^5D_0$)/I($^7F_1$←$^5D_0$) ratio suggesting that the emission spectrum is influenced by the D_{4d} ligand field.

The $^7F_3$←$^5D_0$ transition is usually very weak, given its forbidden nature, and is generally only increased in intensity by *J*-mixing. Thus, it is not surprising that the integration of the peak is relatively small and consistent between each of the tetranuclear assemblies. The obvious deviations are for the {Eu$_2$K$_2$-BuOH}^{III} and [Eu(Phen)(**L1**)$_3$] species. The {Eu$_2$K$_2$-BuOH}^{III} has a $^7F_3$←$^5D_0$ transition which is relatively less intense that the other tetranuclear assemblies. This is likely a consequence of the low intensity $^7F_2$←$^5D_0$ transition. In contrast, the [Eu(Phen)(**L1**)$_3$] complex has a larger intensity transition which might suggest that this excited state is mixing with the $^7F_4$ excited state which is a more intense transition in the [Eu(Phen)(**L1**)$_3$] complex.

Table 4.4 – Ratios of I(^7F_J←$^5D_0$)/I($^7F_1$←$^5D_0$) for each Eu^{3+} species in the solid state, calculated from the integrated luminescence spectra.

Complex	$^7F_0$	$^7F_2$	$^7F_3$	$^7F_4$
{Eu$_2$Na$_2$}^{I}	0.07	15.49	0.83	2.15
{Eu$_2$K$_2$}^{IV}	0.05	15.68	0.75	1.73
{Eu$_2$Rb$_2$}^{IV}	0.05	16.03	0.72	1.79
{Eu$_2$K$_2$-BuOH}^{III}	0.06	12.76	0.50	1.80
[Eu(Phen)(**L1**)$_3$]	0.25	13.50	1.07	2.56

Lifetime decay (τ_{obs}) and quantum yield (Φ_{Ln}^{L}) data for the Eu^{3+} species are reported in Table 4.5. The values of τ_{obs} for the tetranuclear assemblies were found to be consistently in the 500 μs to 540 μs range (Figures 4.23-4.24), with overall quantum yields (Φ_{Ln}^{L}) measured to be in the 35-37% range. The radiative lifetimes (τ_R) could be calculated directly from the emission spectra (using Eqn 2.14), obtaining values in the 1.01 ms to 1.22 ms range. These values are all very similar, with the exception of {Eu$_2$K$_2$-BuOH}^{III}, likely due to the coordination sphere being distorted from the regular polyhedra. The intrinsic quantum yields (Φ_{Ln}^{Ln}) were determined to be ~50%, leading to sensitisation efficiencies (Φ_{sens}) of the **L1**$^-$ ligands in 68-73% range. Therefore, **L1**$^-$ is a rather efficient sensitiser for Eu^{3+} luminescence in the solid state.

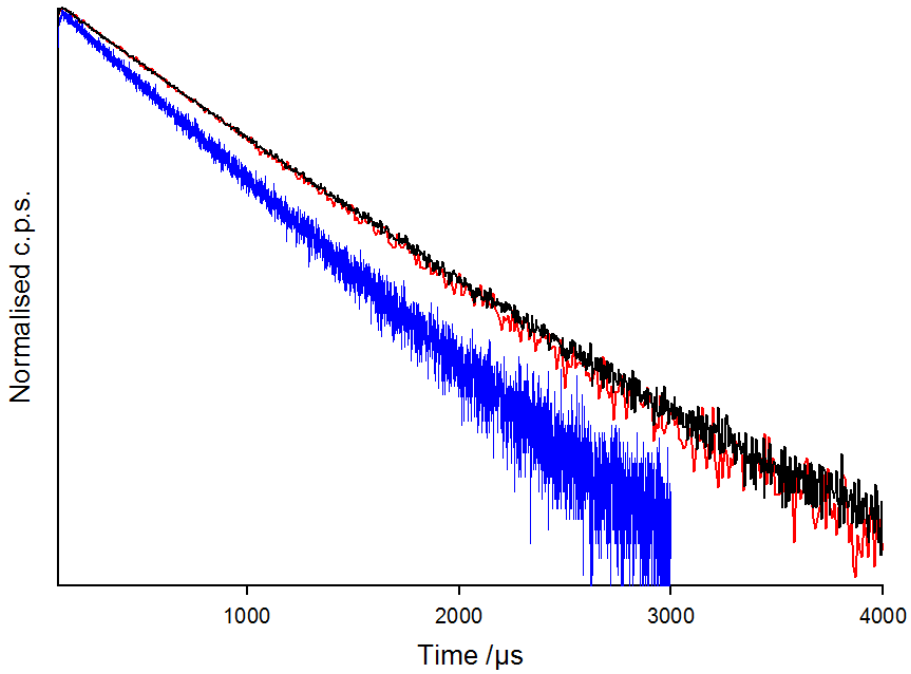

Figure 4.23 – Lifetime decays of the $\{Eu_2Na_2\}^{I}$ (blue trace, λ_{ex} = 30 nm, λ_{em} = 612 nm), $\{Eu_2K_2\}^{IV}$ (red trace, λ_{ex} = 350 nm, λ_{em} = 612 nm), and $\{Eu_2Rb_2\}^{IV}$ (black trace, λ_{ex} = 350 nm, λ_{em} = 614 nm) assemblies in the solid state at 298 K.

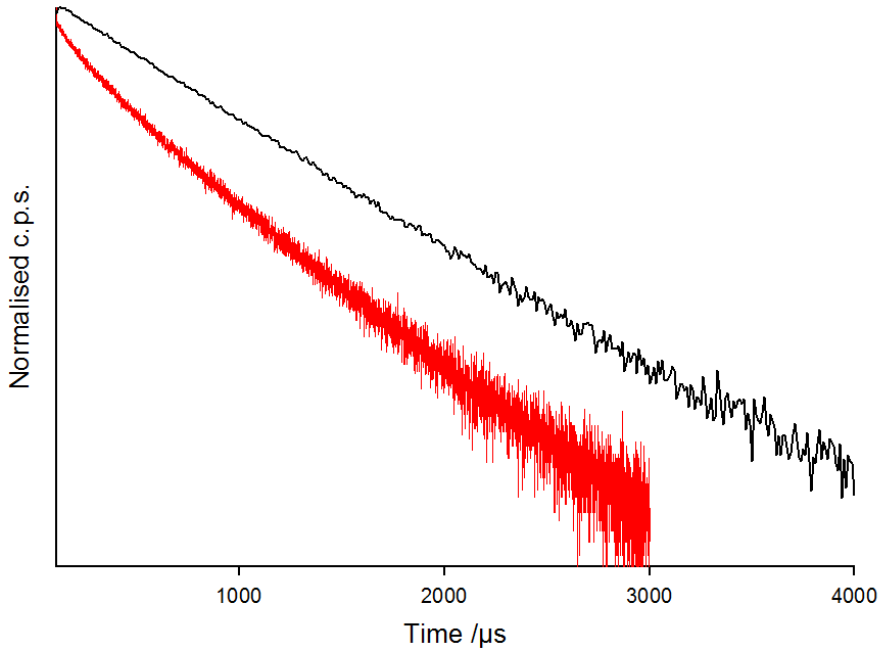

Figure 4.24 – Lifetime decays of the $\{Eu_2K_2\text{-BuOH}\}^{III}$ assembly (red trace, λ_{ex} = 350 nm, λ_{em} = 612 nm), and [Eu(Phen)(**L1**)$_3$] complex (black trace, λ_{ex} = 405 nm, λ_{em} = 612 nm) in the solid state at 298 K.

Despite the fact that the ethanolic OH group lies closer to the Eu^{3+} centres in the $\{Eu_2Na_2\}^I$ assembly, there does not appear to be a greater degree of multiphonon relaxation as observed for the case of Yb^{3+} and Er^{3+}. However, it is evident that the decay of $\{Eu_2Na_2\}^I$ is slightly shorter than the other assemblies. The lack of quenching in this case may be due to the fact that OH is a less efficient quencher of the Eu^{3+} excited state in comparison to Er^{3+} and Yb^{3+}. Figure 4.25 illustrates the OH stretching vibration frequencies, using the experimental value from the IR spectrum ($\nu \sim 3{,}645$ cm^{-1}), against the Eu^{3+} excited state.

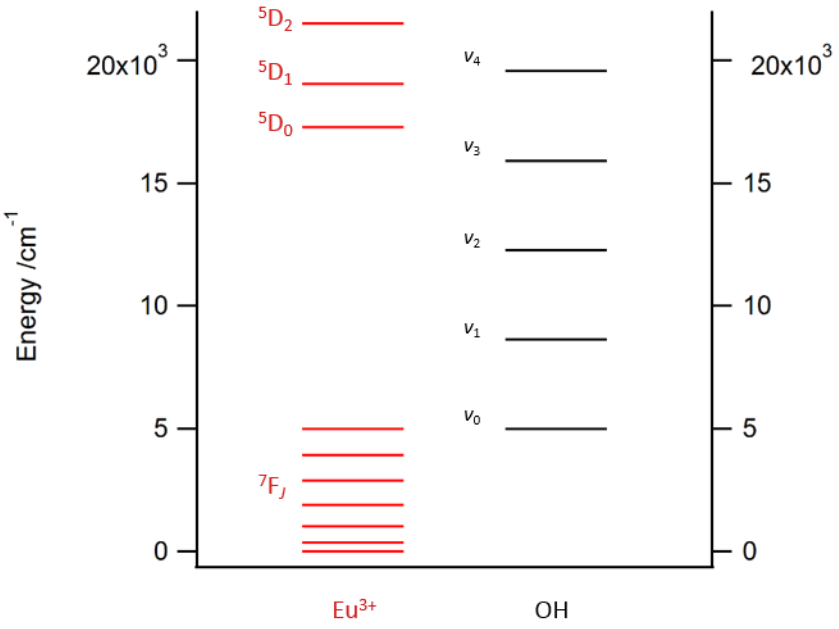

Figure 4.25 – Relative energy of the OH vibration compared to the Eu^{3+} excited state.

The [Eu(Phen)(**L1**)$_3$] complex is characterised by τ_{obs} (Figure 4.24), τ_R, and Φ_{Ln}^{Ln} values which are very similar to those observed in the tetranuclear assemblies (Table 4.5). This is not surprising as the Eu^{3+} coordination sphere is again devoid of quenching vibrations, and the Eu···Eu distance in the π-stacked pair is long enough to minimise direct Ln···Ln energy migration. However, the quantum yield (Φ_{Ln}^{L}) of the [Eu(Phen)(**L1**)$_3$] complex has improved from ~36% in the tetranuclear assemblies to 45%. This leads to a sensitisation efficiency (Φ_{sens}) of 85%, which is much improved in comparison to the tetranuclear assemblies. This may be due to more efficient sensitisation *via* the Phen ligand when exciting the complex at 350 nm.

Table 4.5 - Selected photophysical data of Eu^{3+} species in the solid state.

	τ_{obs} (ms)	τ_R (ms)[a]	Φ^{Ln}_{Ln} (%)	Φ^{L}_{Ln} (%)	Φ_{sens} (%)
$\{Eu_2Na_2\}^{I}$	0.50	1.01	50	35	70
$\{Eu_2K_2\}^{IV}$	0.52	1.03	50	37	73
$\{Eu_2Rb_2\}^{IV}$	0.54 (77%), 0.37 (23%)	1.02[b]	53[b]	36	68
$\{Eu_2K_2\text{-BuOH}\}^{III}$	0.51 (87%) 0.18 (13%)	1.22[b]	42[b]	-	-
[Eu(Phen)(**L1**)$_3$]	0.55	1.03	53	45	85

[*a*] τ_R calculated assuming a refractive index of 1.50 for the solid state.[133,134] [*b*] Calculated using the major τ_{obs} component.

The observed lifetimes in the solid state for Eu^{3+} species bearing β-diketonate ligands can vary from ~0.1 to ~1.0 ms[30] (see Table 4.6 for some literature values). Interestingly, the β-triketonate Eu^{3+} species presented here present solid state lifetime decays which are very similar to the [Eu(dbm)$_3$(phen)] complex presented by Bunzli in 1994. Thus, the Eu^{3+} species presented here do not show a clear elongation in the observed lifetime in comparison to β-diketonate analogues.

Table 4.6 – Literature Eu^{3+} observed lifetimes in the solid state with β-diketonate and phen/water ligands. Some data in table reproduced from Binnemans.[30]

Compound	τ_{obs} (ms)
[Eu(Bta)$_3$(H$_2$O)$_2$]	0.33[235]
[Eu(Mdbm)$_3$(Phen)]	0.34[178]
[Eu(Bzac)$_3$(Phen)]	0.43[236]
[Eu(Mfa)$_3$(Phen)]	0.47[178]
[Eu(Dbm)$_3$(Phen)]	0.52[178]
[Eu(Tta)$_3$(Phen)]	0.98[237]

Abbreviations in table include: Bta = benzoyltrifluoroacetone; Mdbm = 1-(4-methoxyphenyl)-3-phenyl-1,3-propanedione; Bzac = 1-phenyl-1,3-butanedione; Mfa = 1-(2-furanyl)-propandione ; Tta = thenoyltrifluoroacetonate; Phen = 1,10-phenanthroline.

Overall the photophysical data indicate that the β-triketonate assemblies of Eu^{3+} are efficient and bright red emitters, although their performance is akin to that observed for β-diketonate complexes in the solid state, rather than greatly improved as was observed for the Yb^{3+} and Er^{3+} NIR-emitters.[30]

4.4 Fabrication of a NIR-OLED

Given the remarkable photophysical properties observed for the NIR emitters in the solid state, these complexes were trialled for the fabrication of OLEDs. The $\{Yb_2K_2\}^{II/III}$ assembly was used as an exemplar for the fabrication of NIR-OLEDs.

The device was fabricated by sublimation on glass substrates precoated with indium tin oxide (ITO), semitransparent to the light generated in the emitting layer (EML). The composition of the OLED is illustrated in Figure 4.26, and was as follows: (i) ITO anode; (ii) MoO_x hole injecting layer; (iii) a 1,3-bis(*N*-carbazolyl)benzene (mCP) hole transporting layer (HTL); (iv) EML of $\{Yb_2K_2\}^{II/III}$ and mCP in a 1:1 mass ratio; (v) a 1,3,5-tris(*N*-phenyl-benzimidazol-2-yl)benzene (TPBi) electron transporting layer (ETL); (vi) LiF/Al cathode (0.5 nm of LiF, 100 nm of Al). For further details on the device fabrication, see Chapter 8 - Experimental Section.

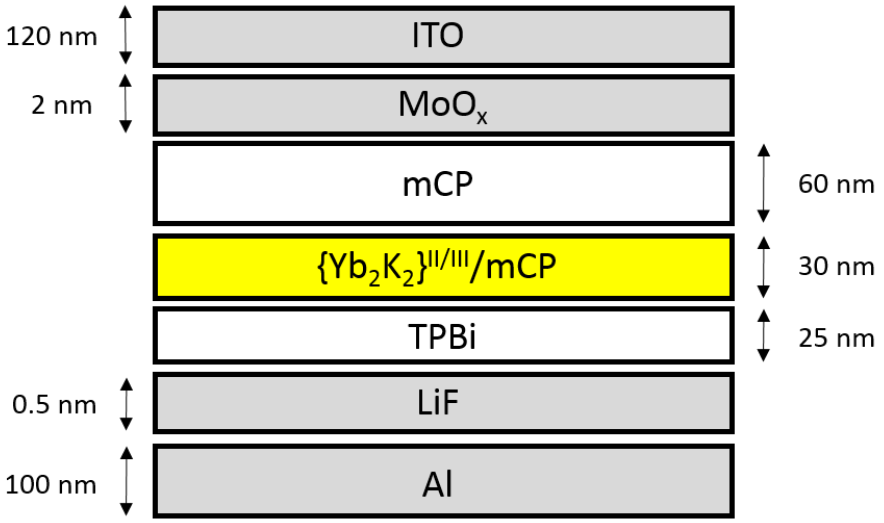

Figure 4.26 – Composition of the fabricated NIR-OLED used in this work. The Hole-Transporting Layer (HTL) was mCP, The EML was 50% $\{Yb_2K_2\}^{II/III}$ and 50% mCP. The Electron-Transporting layer (ETL) was TPBi.

The device presents an EL spectrum characteristic of the Yb^{3+} $^2F_{7/2}$←—$^2F_{5/2}$ transition, with broadening due to ligand field effects (Figure 4.27).[49] Emission bands between 900 nm and 970 nm are assigned to presence of emission from "hot" excited states,[227] consistent with the solid state precursor. It is noted that the structure in the emission band is changed in the device when compared to the solid state precursor, suggesting that the ligand field of the Yb^{3+} species in the device is different. This could be an effect of various causes, such as a possible change in composition of the sublimed material.

The performance of the device is presented in Figure 4.28. As the applied voltage is increased, the device brightness characteristically increases to a maximum EL intensity of 390 μW cm^{-2} at 12.9 V, which originates exclusively from the Yb^{3+} metal-centred NIR emission peaked at 976 nm. Furthermore, the external quantum efficiency reaches a maximum of 0.17% ph e^{-1}.

To the best of our knowledge, the performance of this device is among the best NIR-OLEDs previously reported where a rare earth has been used as the emissive species in the composition of the EML, for which typical EL intensities are ~80 μW cm^{-2}.[108,200–203] This is a remarkable result given that the β-triketonate ligand is such a straightforward extension to the classic β-diketonate ligand.

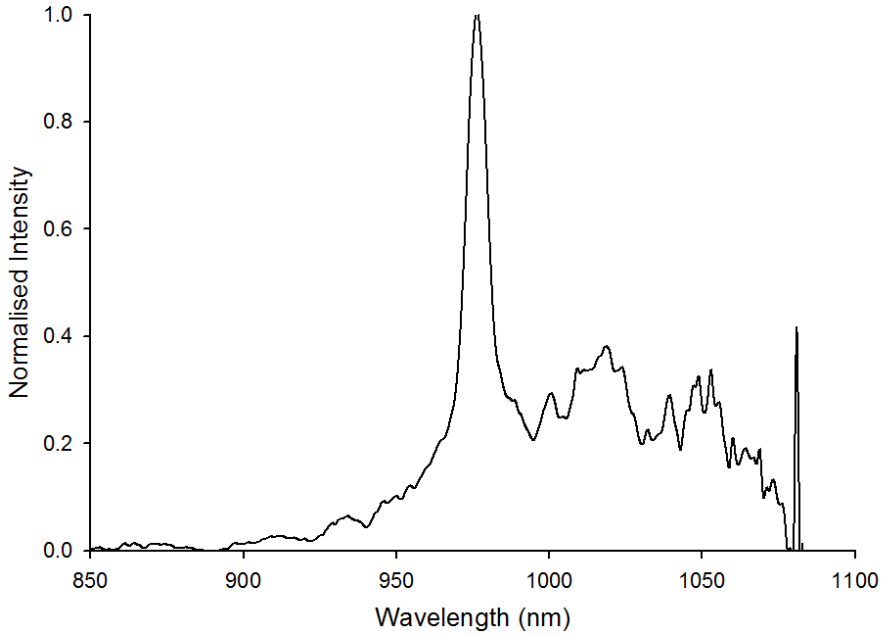

Figure 4.27 – Normalised emission spectrum of the fabricated NIR-OLED using the $\{Yb_2K_2\}^{II/III}$ assembly as the EML.

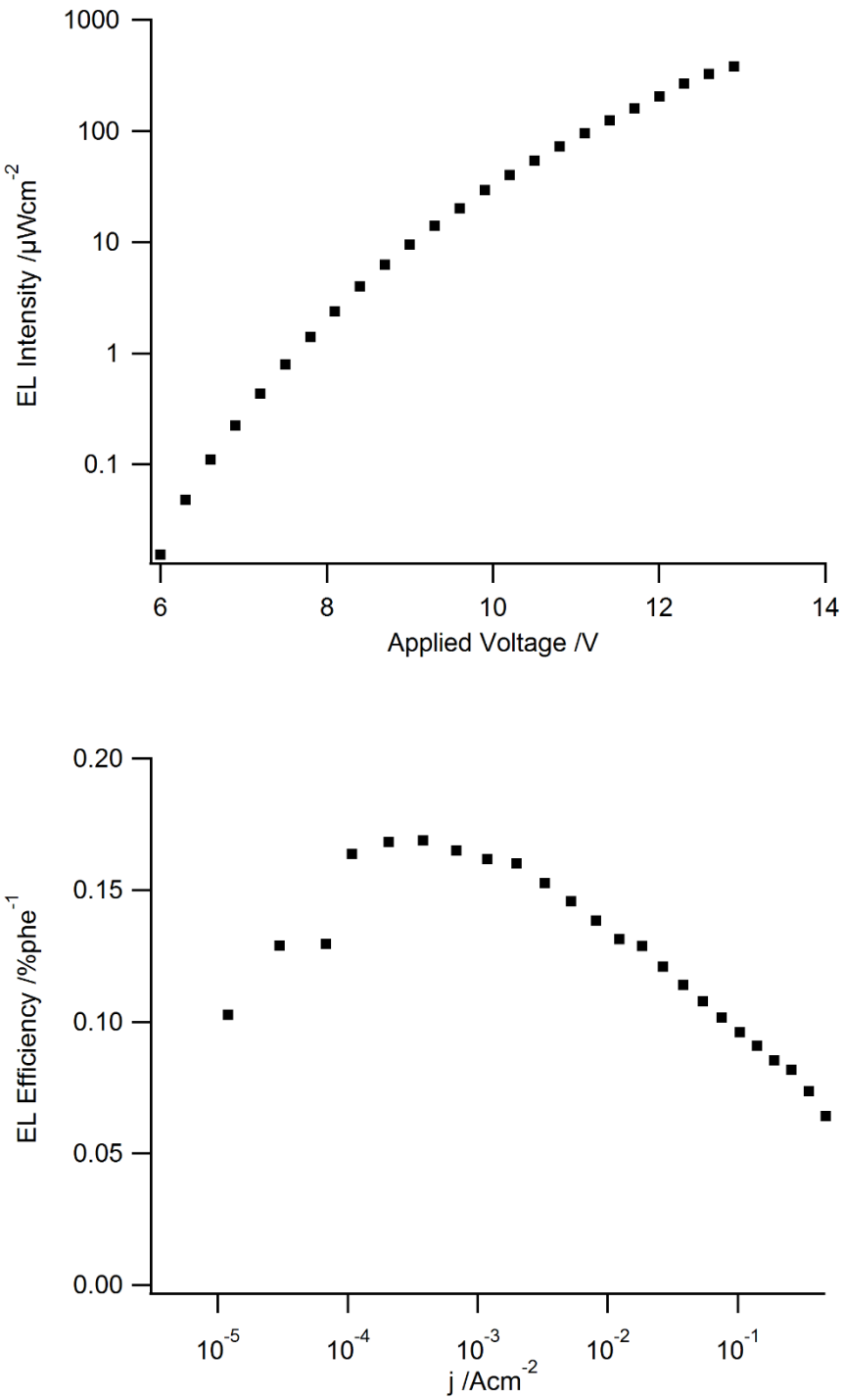

Figure 4.28 – Top: EL intensity as a function of applied voltage. Bottom: The EL efficiency vs current density.

4.5 Thermal Stability of the Tetranuclear Assemblies

Although the NIR-OLED is very efficient for this class of device, the unknown factor is whether the emissive species remains as the tetranuclear assembly precursor. The thermal stability of the tetranuclear assemblies was then investigated, to assess the likely changes in the complex after heating at temperatures above that used for sublimation (220 ºC at 10^{-6} hPa). Although the experimental conditions matching the sublimation during device fabrication (reduced pressure and argon atmosphere) were not attainable for the thermal stability studies, this approach was used as an initial investigation.

The thermal stability of the $\{Yb_2K_2\}^{II/III}$ assembly was assessed using Thermogravimetric Analysis (TGA), carried out at atmospheric pressure under N_2 (Figure 4.29).

The TGA displays an initial mass loss (~3%) between 180 °C and 210 °C, consistent with the loss of coordinated ethanol molecules in the tetranuclear assembly. The resulting complex is then thermally stable until 300 °C, which is far above the sublimation temperature during the device fabrication under reduced pressure. This would suggest that the sublimed material is not a product of complex degradation, but also gives an insight into the possible lability of the coordinated ethanol molecules upon heating the solid. Thus, at the very least, it is expected that the sublimed complex has changed in terms of solvation and/or coordination of ethanol molecules.

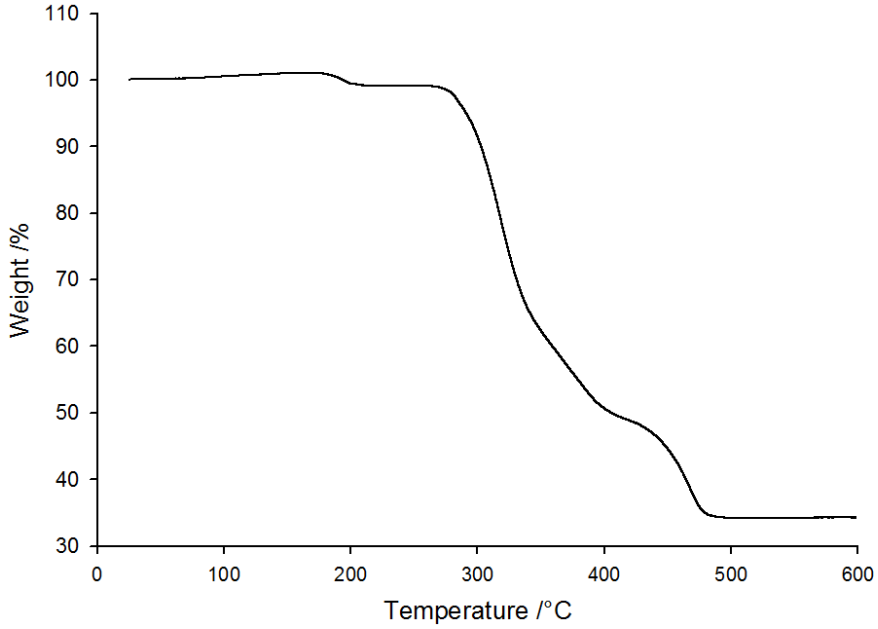

Figure 4.29 – The TGA profile of the $\{Yb_2K_2\}^{II/III}$ assembly under N_2 atmosphere.

To further investigate the thermal stability of the $\{Yb_2K_2\}^{II/III}$ assembly, the solid was heated at 280 ºC for 30 minutes in ambient conditions; a temperature at which the solid melted. Upon melting, it is expected, after analysis of the TGA, that the coordinated ethanol molecule will be evaporated and so the melted solid should undergo some chemical change.

The melted solid was characterised by its emission spectrum and by IR spectroscopy. The latter revealed a new broad band at ~3,300 cm^{-1} consistent with an OH vibration, most likely due to the melted solid attracting and holding atmospheric H_2O upon cooling. This H_2O might now be coordinated to the metal centre or held in outer sphere.

The melted $\{Yb_2K_2\}^{II/III}$ assembly displays characteristic metal-centred emission between 900 nm and 1100 nm, attributed to the $^2F_{5/2} \longleftarrow {}^2F_{7/2}$ transition (Figure 4.30). This emission originates as a consequence of the antenna effect indicated by the broad excitation spectrum (Figure 4.30), and provides evidence that the ligand does not degrade at the melting temperature. The emission spectrum resembles that of the $\{Yb_2K_2\}^{II/III}$ precursor, with more broadening in the ligand field components, most likely due to an increase in different Yb^{3+} coordination geometries as a consequence of variable hydration upon cooling. However, the similar structure in the emission

band would suggest that the coordination environment is likely to be similar to the solid state precursor. The emission spectrum is clearly still different to that observed in the NIR-OLED after sublimation, and thus the melted solid is not likely to be a good representation of the sublimed species, and in fact, the sublimed material is likely not a product resulting from only removing coordinating ethanol.

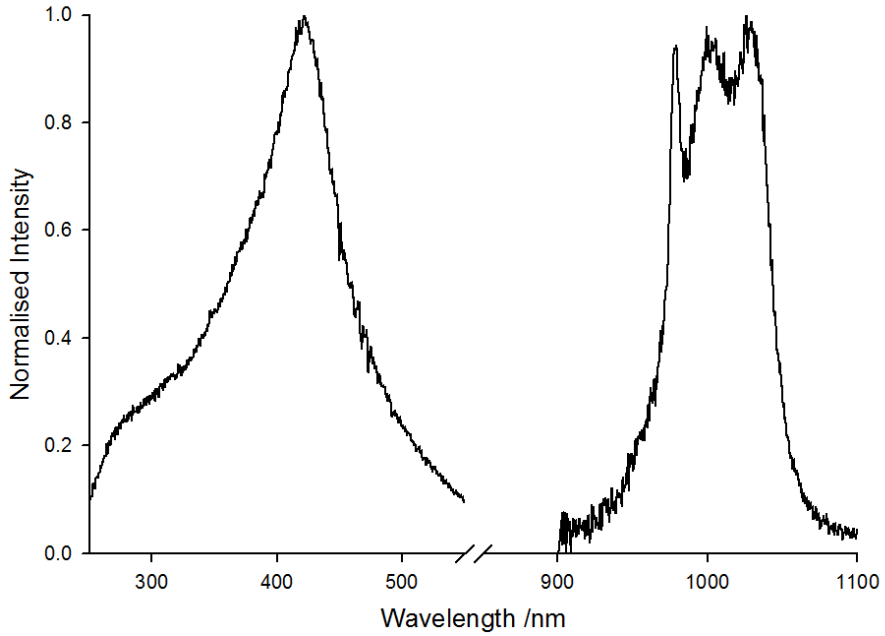

Figure 4.30 – Normalised excitation (λ_{em} = 1038 nm) and emission (λ_{ex} = 280 nm) spectra of the $\{Yb_2K_2\}^{II/III}$ assembly in the solid state after melting at 280 °C for 30 minutes.

The melted $\{Yb_2K_2\}^{II/III}$ assembly has an excited state lifetime of 19.2 μs (Figure 4.31), which is shorter than that observed in the solid state precursor (46.7 μs). This shortening is likely due to the presence of H_2O molecules in the solid, contributing to multiphonon relaxation pathways quenching the Yb^{3+} excited state.

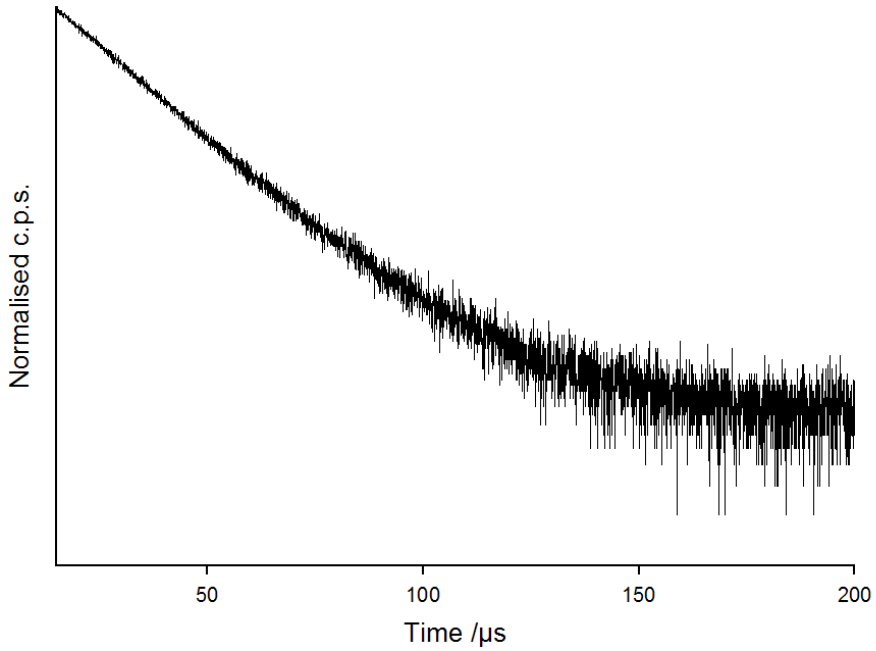

Figure 4.31 – Lifetime decay of the $\{Yb_2K_2\}^{II/III}$ assembly in the solid state after melting at 280 °C for 30 minutes. λ_{ex} = 280 nm, λ_{em} = 1038 nm.

To better gauge the structural changes after melting the tetranuclear assemblies, the $\{Eu_2K_2\}^{IV}$ assembly was also melted. Figure 4.32 shows the melted solid as well as the visible red emission from the melted $\{Eu_2K_2\}^{IV}$ assembly. This illustrates that melting the solid still results in a highly emissive Eu^{3+} species.

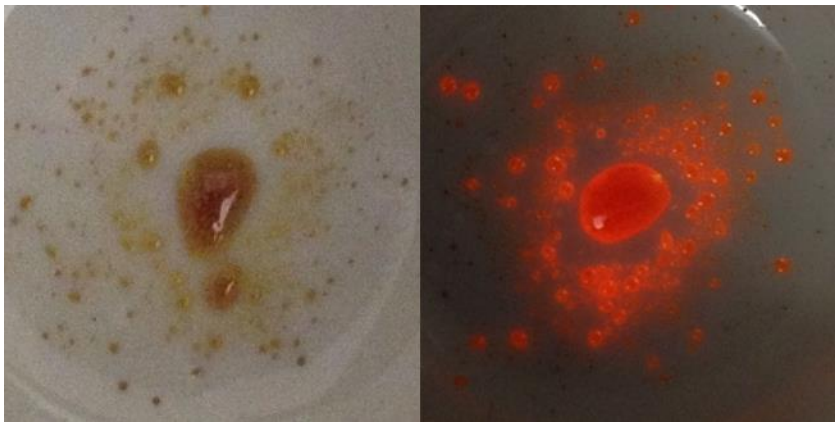

Figure 4.32 – Image of the $\{Eu_2K_2\}^{IV}$ solid after melting (left), and its emission after irradiating at 405 nm.

The emission spectrum of the melted $\{Eu_2K_2\}^{IV}$ assembly revealed the characteristic Eu^{3+} metal-centred emission, originating as a consequence of the antenna effect indicated by the similarity between the excitation spectrum of the complex after melting (Figure 4.33) and absorption spectra of the ligand (Figure 4.1). In comparison to the $\{Eu_2K_2\}^{IV}$ precursor solid, the emission spectrum of the melted solid in rather similar in terms of the relative intensities of each band, however there is an evident broadening in each peak. This broadening suggests the increase in different coordination geometries in the melted sample, which is again attributed to variable hydration upon cooling. This is supported by the increase in the FWHM of the $^7F_0 \longleftarrow {}^5D_0$ (~40 cm^{-1}) transition in comparison to the $\{Eu_2K_2\}^{IV}$ solid precursor. (~15 cm^{-1})

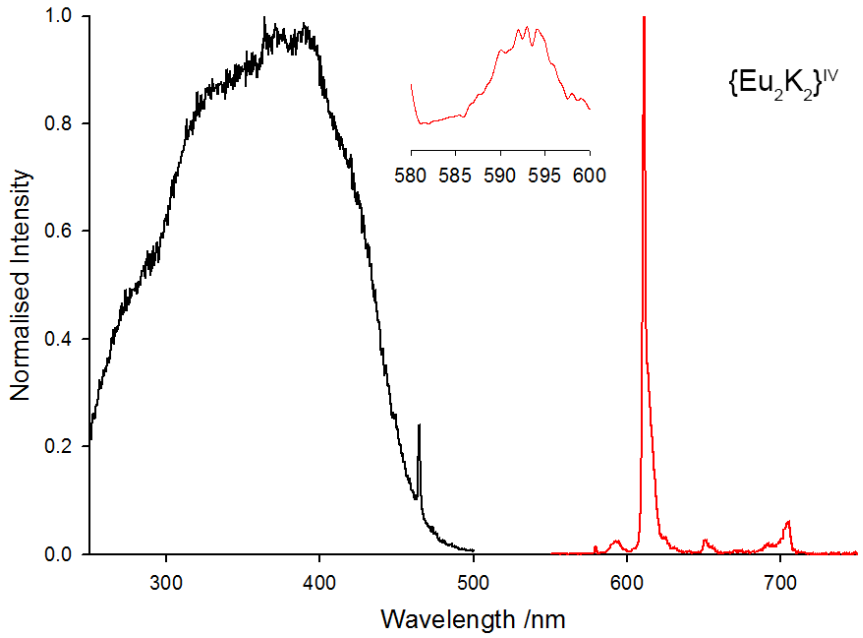

Figure 4.33 – Normalised excitation (λ_{em} = 611 nm) and emission (λ_{ex} = 350 nm) spectra of the $\{Eu_2K_2\}^{IV}$ assembly in the solid state after melting at 280 °C for 30 minutes. Inset: A close-up region of the emission spectrum highlighting the splitting in the $^7F_1 \longleftarrow {}^5D_0$ emission band.

The τ_{obs} of the melted $\{Eu_2K_2\}^{IV}$ assembly was found to be best fitted by a triexponential function (Figure 4.34) consistent with the hypothesis that there is more than one unique coordination geometry in the bulk sample. The τ_{obs} were found to be τ_1 = 0.084 ms (4%), τ_2 = 0.29 ms (54%), and τ_3 = 0.50 ms (42%). The τ_1 and τ_2 values are much shorter than the solid state precursor (0.52 ms), which is likely due to the

hygroscopic nature of the melted assemblies, enhancing quenching *via* OH vibrations close to a portion of the metal centres. The longer lived τ_3 decay is likely attributed to a Eu^{3+} environment which is still devoid of closely bound H_2O molecules, as is the case in the precursor $\{Eu_2K_2\}^{IV}$ assembly.

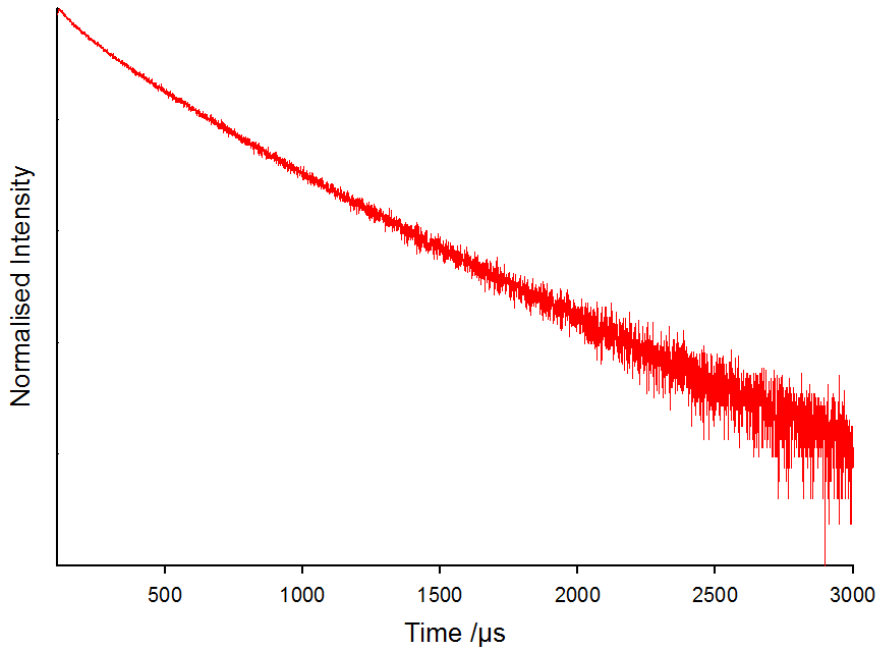

Figure 4.34 – Lifetime decay of the $\{Eu_2K_2\}^{IV}$ assembly in the solid state after melting at 280 °C for 30 minutes. λ_{ex} = 280 nm, λ_{em} = 611 nm.

The initial investigation of the thermal stability of the tetranuclear assemblies has given an insight into the coordination flexibility after heating the solids to melting point. In the fabrication of OLEDs by sublimation of the Ln^{3+} species, this type of coordination sphere flexibility is most definitely occurring. However, further investigation is still needed to identify the sublimed species present in the fabricated device.

Such further investigation should include the elemental analysis of the sublimed species in the fabricated device to investigate the relative abundance of ligand remaining. Also Atomic Absorption Spectroscopy (AAS) could be used to identify whether the K^+ ion remains in the sublimed species. These experiments would provide further evidence towards the identification of the sublimed product.

4.6 Conclusion

The **L1**$^-$ ligand was found to have $^1\pi\pi^*$ and $^3\pi\pi^*$ state energies estimated to lie at ~25,575 cm^{-1} and ~20,704 cm^{-1}, respectively. The energy of the $^3\pi\pi^*$ state lies high enough above the emissive states of Eu^{3+}, Er^{3+}, and Yb^{3+}. These tetranuclear assemblies were targeted for their respective metal-centred emissions. The tetranuclear assemblies bearing the lanthanoids Gd^{3+}, Tb^{3+}, Dy^{3+}, and Ho^{3+} were found to have emissive states which were too high to be effectively sensitised, or were found to be non-emissive.

The NIR emitting Yb^{3+} and Er^{3+} tetranuclear assemblies were evaluated and found to be characterised by metal-centred emissions, with excited state lifetimes among the longest lived for Yb^{3+} and Er^{3+} species in the solid state in the class of β-diketonate ligands. These lifetimes were, to the best of our knowledge, longer-lived than those bearing perfluorinated β-diketonate ligands, and only outclassed in cases where the β-diketonate had been perfluorinated and deuterated to reduce quenching *via* multiphonon relaxation pathways with CH vibrations in the organic antennae. This is remarkable, as the β-triketonate molecule is such a straightforward extension to the classic β-diketonate molecule, and presents a viable alternative to even the synthetically challenging perfluorinated/deuterated β-diketones. Thus, it has been found that compared to literature β-diketonate Yb^{3+}/Er^{3+} complexes, the β-triketonate provides a somewhat better antenna due to the removal of the CH vibration in β-diketonates.

The visible emitting Eu^{3+} assemblies and the [Eu(Phen)(**L1**)$_3$] complex were found to reveal a bright red metal-centred emission, with excited state lifetimes comparable to those Eu^{3+} species in the solid state bearing β-diketonate ligands. Thus, the removal of the CH vibration to a CC vibration in the β-triketonate appears to affect the resulting photophysical properties of Eu^{3+} species much less than the NIR emitting Yb^{3+} and Er^{3+} species.

The remarkable NIR emission in the Yb^{3+} solid state species was trialled in the fabrication of a NIR-OLED, by sublimation of the $\{Yb_2K_2\}^{II/III}$ assembly as the emitting layer. The resulting device possesses an EL efficiency and brightness which outclasses all previously reported NIR-OLEDs which use Ln^{3+} as the emitting species. The NIR-OLED displayed an EL emission spectrum which was evidently different to

that observed in the solid state precursor, which prompted an investigation into the thermal stability of the tetranuclear assembly.

The tetranuclear assemblies $\{Yb_2K_2\}^{II/III}$ and $\{Eu_2K_2\}^{IV}$ appear to be thermally stable and reveal metal-centred emission after melting the solids. However, the emission spectra of the melted solids are somewhat different to the solid state precursors, consistent with mixed speciation on melting the solids. The excited state lifetimes of the Yb^{3+} $^2F_{5/2}$ and the Eu^{3+} $^5D_0$ states were much shorter than the solid state precursors, and was attributed to the hygroscopic nature of the melted solids, enhancing uptake of H_2O in the solids. Analysis of the thermal stability of the $\{Yb_2K_2\}^{II/III}$ assembly by TGA illustrates that the coordinated ethanol molecule is likely to be evaporated on heating the solids.

The investigation into the photophysical properties of the melted solids provides an insight into likely changes in the coordination sphere at higher temperatures, however, further investigation into the sublimed species in the fabrication of devices is still needed. The evidence in this chapter does suggest that the emissive species in the NIR-OLED is not likely the tetranuclear assembly, but a new Yb^{3+} species. Given the harshness of the sublimation process, a more convenient method for applying the tetranuclear assembly to the EML might be *via* spin coating from solution.

5 Solution Stability of the Tetranuclear Assemblies

Some of the work presented in this chapter has been published in peer reviewed journals which are cited below:

B. L. Reid, S. Stagni, J. M. Malicka, M. Cocchi, G. S. Hanan, M. I. Ogden, M. Massi, *Chem. Commun.* **2014**, *50*, 11580–11582. doi: 10.1039/C4CC04961F

B. L. Reid, S. Stagni, J. M. Malicka, M. Cocchi, A. N. Sobolev, B. W. Skelton, E. G. Moore, G. S. Hanan, M. I. Ogden, M. Massi, *Chem. Eur. J.* **2015**, *21(50)*, 18354-18363. doi: 10.1002/chem.201502536

5.1 Introduction

The solid state emissions of the lanthanoid β-triketonates presented in the last chapter revealed that the Eu^{3+}, Er^{3+}, and Yb^{3+} species present bright and remarkably long-lived emissions in the NIR spectral. These results prompted the investigation of the assemblies as the emissive species in OLEDs, which was implemented by the sublimation of the solid under reduced pressure. The fabricated Yb^{3+} based NIR-OLED was characterised by its emission spectrum, and thermal analysis of the assembly would suggest that the species present in the OLED might not be the same as the tetranuclear assembly.

An alternate method to prepare the lanthanoid species as the EML in OLEDs is to deposit the species by spin coating from solution. Thus, it was deemed necessary to investigate the tetranuclear assemblies in solution.

This chapter will focus on the lanthanoid structures present after dissolution of the Eu^{3+} and Yb^{3+} species by means of excitation and emission spectra, as well as excited state lifetime measurements.

5.2 Dissolution of Tetranuclear Assemblies

Each of the tetranuclear assemblies, in their crystalline state, were found to be very insoluble in a range of non-polar solvents and water. On the other hand the assemblies were found to be soluble only in alcoholic solvents after sonication. Thus, ethanol was the solvent of choice for the dissolution studies. The assemblies investigated were the Eu^{3+}, Yb^{3+} species, as well as the [Eu(Phen)(**L1**)$_3$] complex. All emission profiles presented in this chapter were found to originate as a consequence of the antenna effect, as indicated by the broad excitation profiles analogous to the absorption spectrum of **L1**$^-$ in ethanol (Figure 4.1). The emission of Er^{3+} could not be observed as the ethanolic solvent is not transparent to the 1550 nm emission from the $^4I_{15/2}\leftarrow\!\!-{}^4I_{13/2}$ transition.

5.2.1 Ytterbium Assemblies

After dissolution of the $\{Yb_2Na_2\}^{I}$, $\{Yb_2K_2\}^{II/III}$, and $\{Yb_2Rb_2\}^{II}$ assemblies in ethanol, a NIR emission is still observed at 298 K between 900 nm and 1100 nm, attributed to the metal-centred $^2F_{7/2}\leftarrow\!\!-{}^2F_{5/2}$ transition of the Yb^{3+} cation (Figures 5.1-5.3). The rather featureless nature of the band may be a consequence of the non-rigid coordination sphere due to the lability of the ligands in the ethanolic solution, whereas the high energy shoulder is attributed to emission from "hot" excited states.[227] The emission spectra are almost identical for the three dissolved species indicating that the resulting Yb^{3+} coordination environments are very similar after dissolution.

In an attempt to identify structure in the emission profiles, the ethanolic solutions were frozen to provide a rigid matrix. The emission structure changes in a frozen solution at 77 K for each species. However, at 77 K it should be noted that the emissions of each of the assemblies were again almost identical. In the matrix, the emission band is visibly more structured due to the more rigid coordination environment. Also the intensity in the emission from 930 nm to 980 nm is reduced, consistent with the attribution of the emission from "hot" excited states.

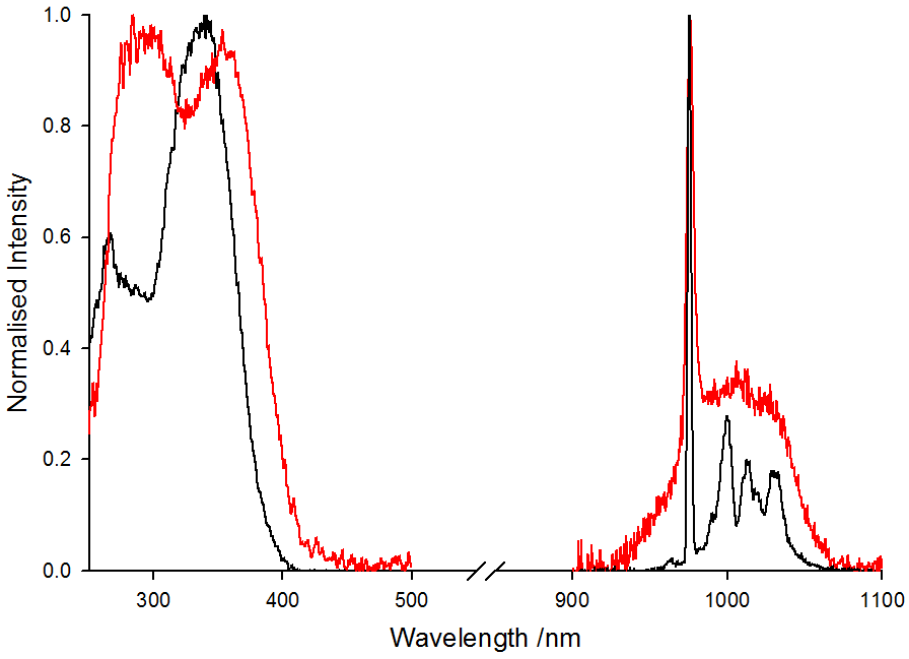

Figure 5.1 - Normalised excitation and emission (λ_{ex} = 350 nm) of the $\{Yb_2Na_2\}^I$ assembly after dissolution in ethanol at 298 K (red trace, λ_{em} = 975 nm) and 77 K (black trace, λ_{em} = 977 nm).

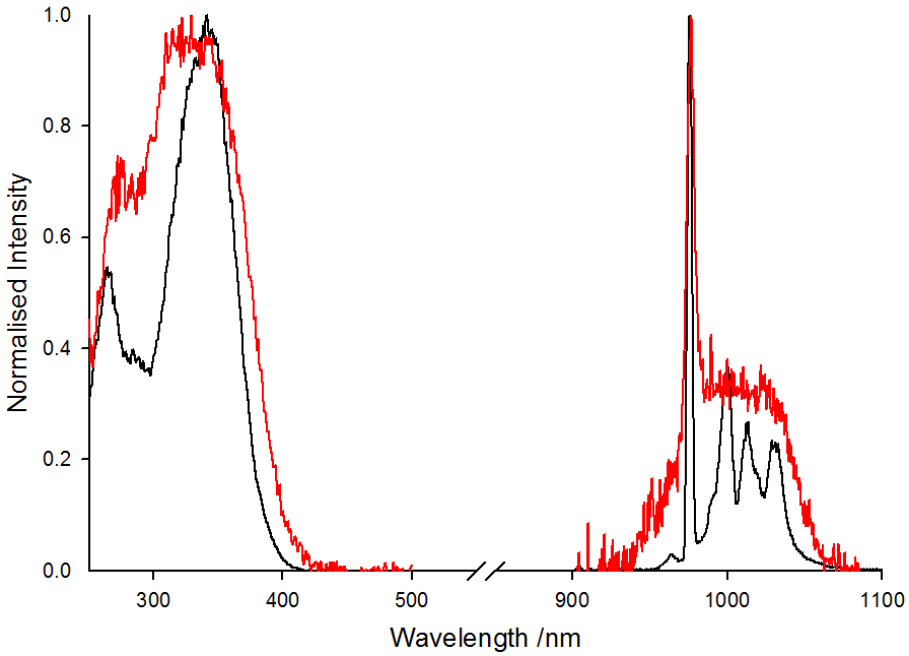

Figure 5.2 – Normalised excitation and emission (λ_{ex} = 350 nm) of the $\{Yb_2K_2\}^{II/III}$ assembly after dissolution in ethanol at 298 K (red trace, λ_{em} = 977 nm) and 77 K (black trace, λ_{em} = 976 nm).

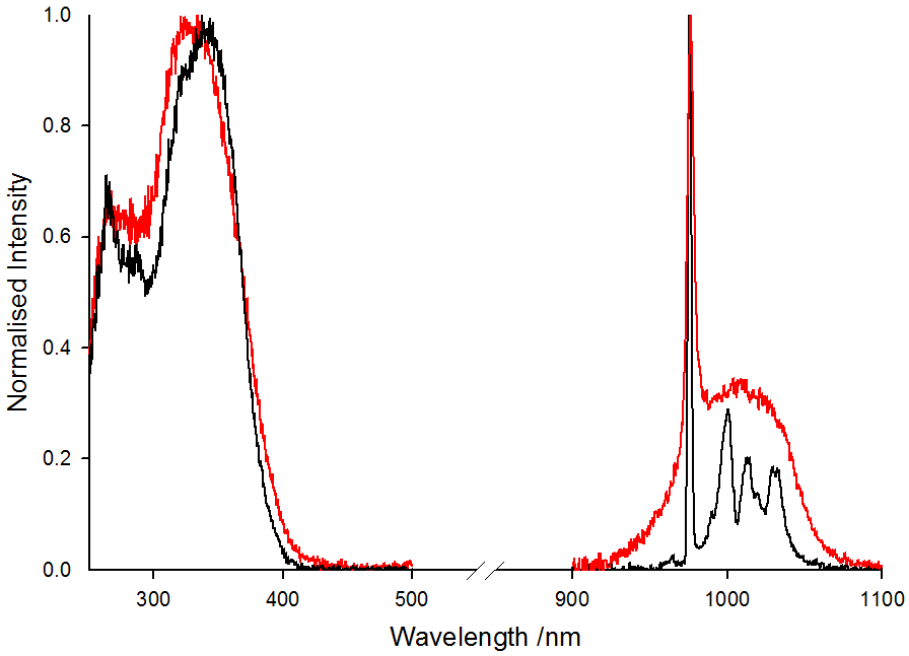

Figure 5.3 – Normalised excitation (λ_{em} = 976 nm) and emission (λ_{ex} = 350 nm) of the $\{Yb_2Rb_2\}^{II}$ assembly after dissolution in ethanol at 298 K (red trace) and 77 K (black trace).

The emission profile at 77 K can be loosely distinguished into four bands. In fact, this structure can be attributed to the four individual Stark components present in the Yb^{3+} cation, consistent with four Kramer's doublets, as well as emission from "hot" excited states. The emission spectrum of each assembly was fit to a series of overlapping Gaussians, using commercially available software (Igor, Version 6.1.2.1, Wavemetrics), to identify individual bands. There is little difference between the spectra, thus only the $\{Yb_2Na_2\}^{I}$ emission spectrum will be discussed in depth (for $\{Yb_2K_2\}^{II/III}$ and $\{Yb_2Rb_2\}^{II}$ spectra – see Appendix).

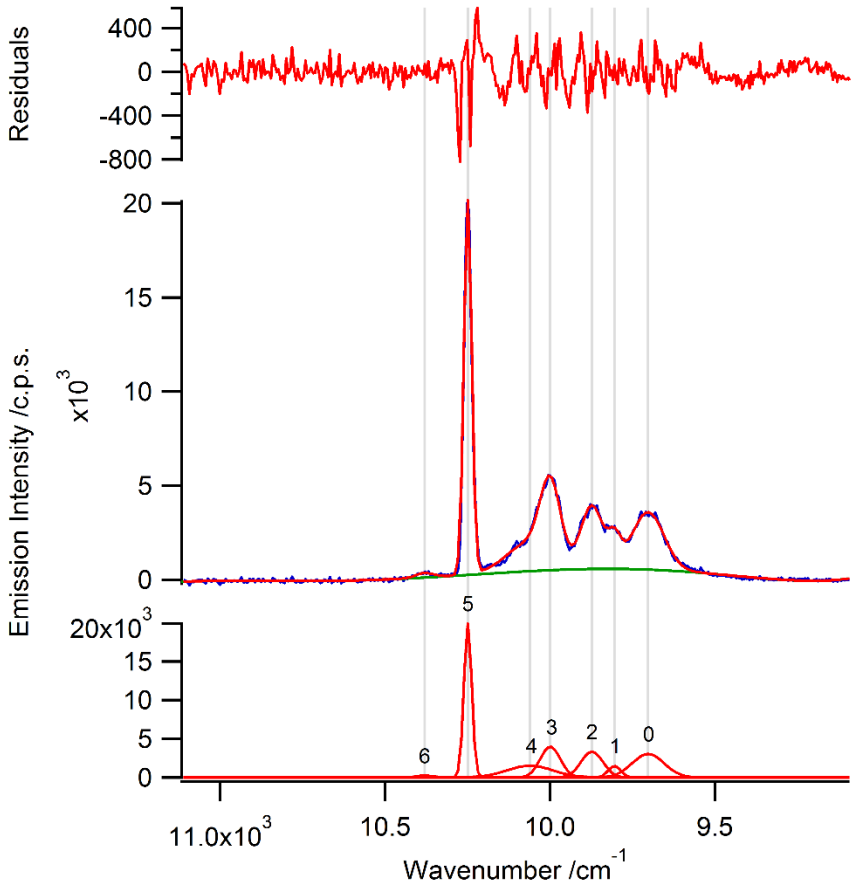

Figure 5.4 – Middle: Emission spectrum of the $\{Yb_2Na_2\}^{I}$ assembly after dissolution ethanol at 77 K. Bottom: The deconvolution of the emission spectrum. Top: Residual plot for the deconvolution fitting.

The emission spectrum can be satisfactorily fit to seven individual peaks, identified as peaks 0-6 in Figure 5.4. These peaks can be attributed to specific transitions from the Yb^{3+} metal-centred states. The Yb^{3+} ground and excited states can be defined by Kramer's doublets, for which in odd-electron systems there must be a two-fold degeneracy which cannot be lifted by the ligand field. Thus, for the Yb^{3+} ground state, $^2F_{7/2}$, the ligand field would split the J = 7/2 into, $2(J)+1 = 8$ states. However, following Kramer's rule, the Yb^{3+} ground state will be split into a maximum of four states. Similarly, the $^2F_{5/2}$ excited state will be split into three non-degenerate states. This splitting is presented in the Jabloǹski diagram in Figure 5.5.

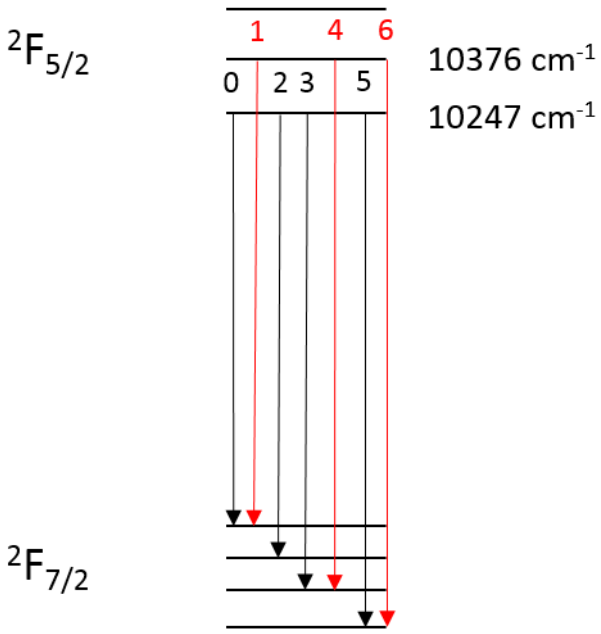

Figure 5.5 – Jabloǹski diagram showing the ground and excited states of the Yb^{3+} species after dissolution in ethanol at 77 K.

The strongest emission band, labelled 5, is attributed to the emission from the lowest energy excited state to the lowest energy ground state illustrated in Figure 5.5. This band is centred at 976 nm and thus the energy between the lowest ground state and lowest excited state can be evaluated to 10,247 cm^{-1}. Furthermore, the

other intense peaks labelled 0, 2, and 3 are attributed to emissions from the lowest energy excited state to the higher energy ground states.

The peaks labelled 6, 4, and 1 are attributed to the observable emissions from the "hot" excited state, whereby peak 6 lies 10,376 cm^{-1} above the lowest energy ground state. In the case of the β-triketonate ligand field, the energy difference in the Stark components is small enough to allow population of higher energy states even at 77 K. It is also noted that there is likely an unobservable "hot" band between the peaks 2 and 3.

Using the Boltzmann distribution (Eqn 5.1), we can estimate the percentage of the "hot" excited state populated at 77 K in this case.

$$\frac{N_2}{N_1} = e^{\frac{-(E_2-E_1)}{kT}} \qquad \text{Eqn 5.1}$$

Therefore, using Eqn 5.1, N_2/N_1 is the amount of populated higher energy state, N_2, compared to the lower energy state, N_1. E_2 and E_1 are the respective energies of these states in eV, k is the Boltzmann constant 8.617 x 10^{-5} eV/K, and T is the temperature in K.

Using this equation, with the ground and "hot" excited state energies estimated from the emission spectrum, the population of the "hot" excited state calculated to be ~9% at 77 K. This outcome provides evidence that at 77 K, the ligand field effects of the β-triketonate will allow population of the "hot" excited state. Although the ~9% population will not equate to a 100% radiative emission from this state, this provides justification to the attribution of the peaks 6, 4, and 1 to emission from the "hot" excited state.

The structured emission observed at 77 K is visibly different from that observed in the solid state, which would suggest that the tetranuclear assembly is not preserved after dissolution in ethanol. However, Yb^{3+} might not be the best probe changes in the ligand field, and so the Eu^{3+} assemblies were targeted as a way to better define structural changes.

5.2.2 Europium Assemblies

After dissolution of the $\{Eu_2Na_2\}^{I}$, $\{Eu_2K_2\}^{IV}$, and $\{Eu_2Rb_2\}^{IV}$ assemblies in ethanol, each displays characteristic Eu^{3+} metal-centred emission (Figures 5.6-5.8).

At 298 K, the emission spectra in ethanol are almost superimposable, indicating that the Eu^{3+} species may be similar between the dissolved complexes. However, compared to the solid state the fine structure of the emission bands has changed significantly.

The band structure is better observed after freezing the ethanolic solutions at 77 K. At 298 K, the low intensity $^7F_0 \leftarrow\!\!- {}^5D_0$ band has a FWHM ranging from 72 cm^{-1} to 75 cm^{-1}, in each complex, which sharpens to ~30 cm^{-1} at 77 K. This may indicate that at 298 K the ligands and/or Ae^+ are rather labile, with flexible coordination geometries. At 77 K, this flexibility is halted, resulting in a sharper and better defined $^7F_0 \leftarrow\!\!- {}^5D_0$ emission band.

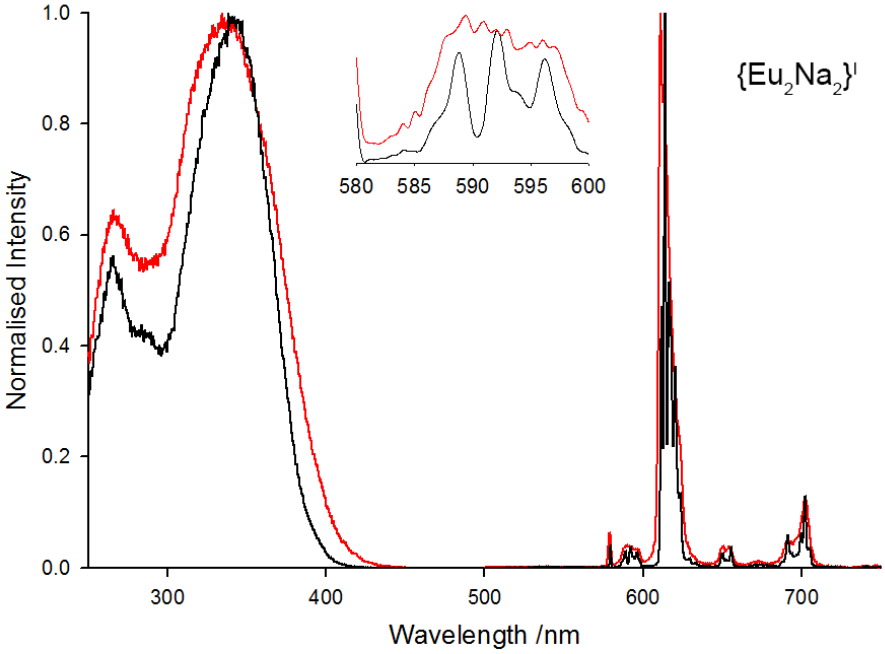

Figure 5.6 – Normalised excitation (λ_{em} = 612 nm) and emission (λ_{ex} = 350 nm) spectra of the $\{Eu_2Na_2\}^{I}$ assembly after dissolution in ethanol at 298 K (red trace) and 77 K (black trace). Inset: close-up region of the emission spectrum highlighting the splitting in the $^7F_1 \leftarrow\!\!- {}^5D_0$ emission band.

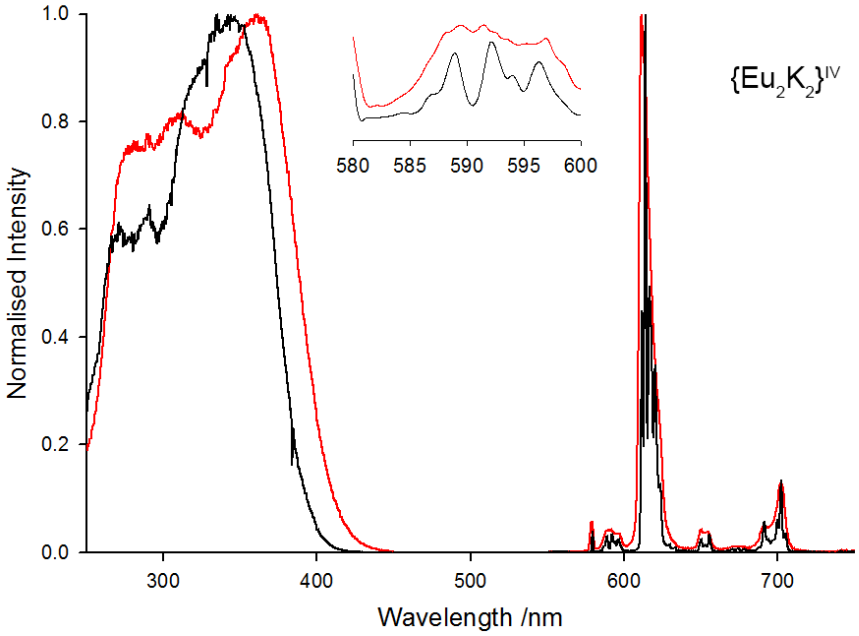

Figure 5.7 - Normalised excitation and emission (λ_{ex} = 350 nm) spectra of the $\{Eu_2K_2\}^{IV}$ assembly after dissolution in ethanol at 298 K (red trace, λ_{em} = 611 nm) and 77 K (black trace, λ_{em} = 614 nm). Inset: close-up region of the emission spectrum highlighting the splitting in the $^7F_1 \longleftarrow {}^5D_0$ emission band.

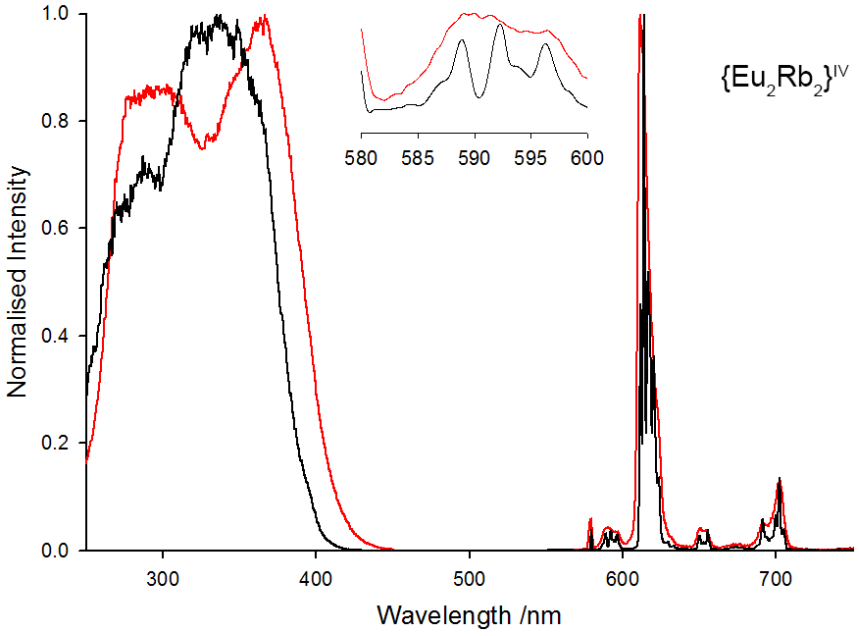

Figure 5.8 - Normalised excitation and emission (λ_{ex} = 350 nm) spectra of the $\{Eu_2Rb_2\}^{IV}$ assembly after dissolution in ethanol at 298 K (red trace, λ_{em} = 611 nm) and 77 K (black trace, λ_{em} = 614 nm). Inset: close-up region of the emission spectrum highlighting the splitting in the $^7F_1 \longleftarrow {}^5D_0$ emission band.

In the frozen medium, the structure in the $^7F_1 \leftarrow ^5D_0$ transition can be clearly identified by three bands, whilst five sharp bands appear for the $^7F_2 \leftarrow ^5D_0$ transition. Splitting in the bands of these two transitions are inherent for a Eu^{3+} local symmetry lower than C_{2v}.[36,233] Furthermore, the ratio $I(^7F_2 \leftarrow ^5D_0)/I(^7F_1 \leftarrow ^5D_0)$ = 18.24, 19.08, and 18.42 for $\{Eu_2Na_2\}^I$, $\{Eu_2K_2\}^{IV}$ and $\{Eu_2Rb_2\}^{IV}$, respectively at 77 K, and 18.05, 18.31, and 18.09, respectively at 298 K. This ratio has increased compared to the solid state precursor, providing evidence of a change in the Eu^{3+} geometry in solution.

In ethanolic solution at 298 K, the Eu^{3+} excited state lifetimes are shortened for each assembly in comparison to those at 77 K (Figures 5.7-5.9), and concordantly, the relative quantum efficiencies are lowered by ~40% as well (Table 5.1). This provides evidence that ethanol molecules may be coordinating in solution, as coordinated ethanol molecules can provide quenching OH vibrations, which are less efficient quenchers at low temperature.

Table 5.1 – Selected photophysical data for Eu^{3+} species after dissolution in ethanol.

	T (K)	τ_{obs} **(ms)**	τ_R **(ms)**	Φ_{Ln}^{Ln} **(%)**
$\{Eu_2Na_2\}^I$	298	0.15	1.15	13
	77	0.41	1.14	36
$\{Eu_2K_2\}^{IV}$	298	0.18	1.15	16
	77	0.43	1.10	39
$\{Eu_2Rb_2\}^{IV}$	298	0.18	1.14	15
	77	0.43	1.16	37
[Eu(Phen)(**L1**)$_3$]	298	0.43	1.25	34
	77	0.41 (77%), 0.60 (23%)	1.16[b]	35[*b*]

[*b*] Calculated using the major τ_{obs} component.

As well as the emission structure, the observed lifetime decays and quantum efficiencies after dissolution in ethanol for the $\{Eu_2Na_2\}^I$, $\{Eu_2K_2\}^{IV}$ and

$\{Eu_2Rb_2\}^{IV}$ assemblies are very similar to each other when compared at 298 K and also at 77 K. This is further evidence to suggest that in solution the resulting species are very similar with respect to their coordination geometry and irrespective of the specific $\{Eu_2Ae_2\}^{class}$ that was dissolved.

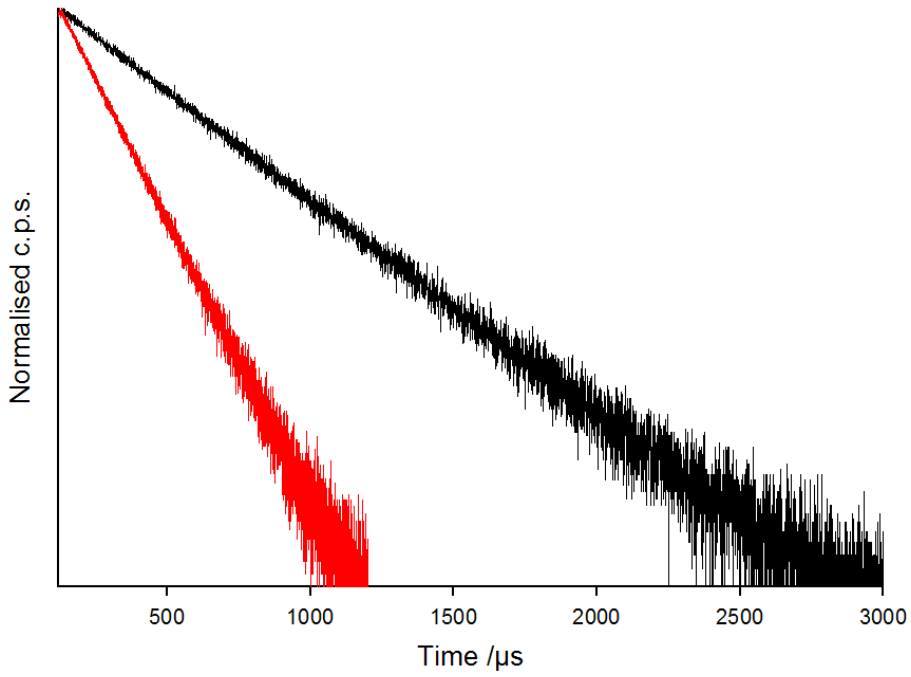

Figure 5.9 - Lifetime decays of the $\{Eu_2Na_2\}^{I}$ assembly after dissolution in ethanol at 298 K (red trace) and 77 K (black trace) (λ_{ex} = 350 nm, λ_{em} = 612 nm).

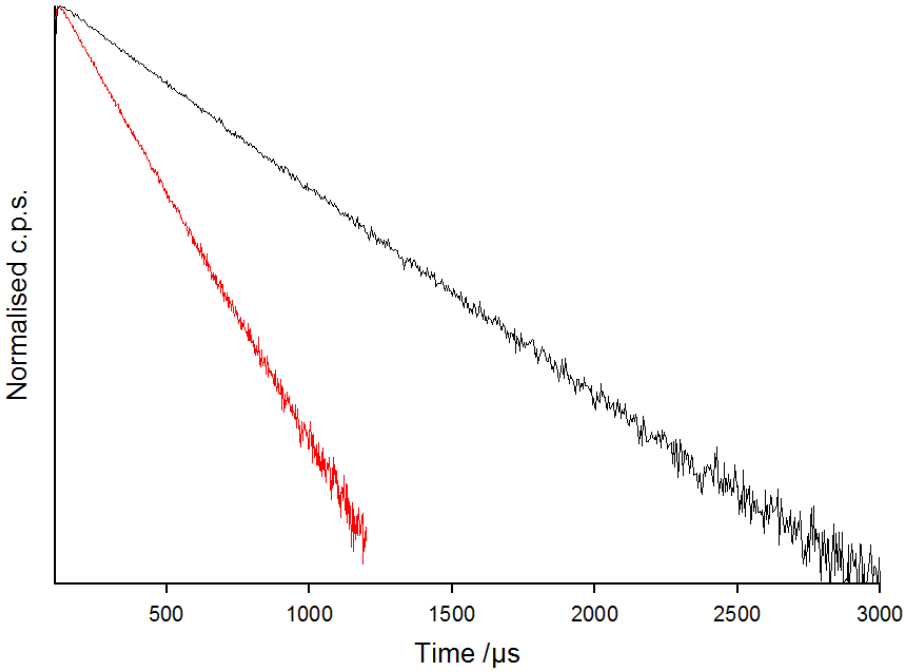

Figure 5.10 - Lifetime decays of the $\{Eu_2K_2\}^{IV}$ assembly after dissolution in ethanol (λ_{ex} = 350 nm) at 298 K (red, λ_{em} = 611 nm) and 77 K (black, λ_{em} = 614 nm).

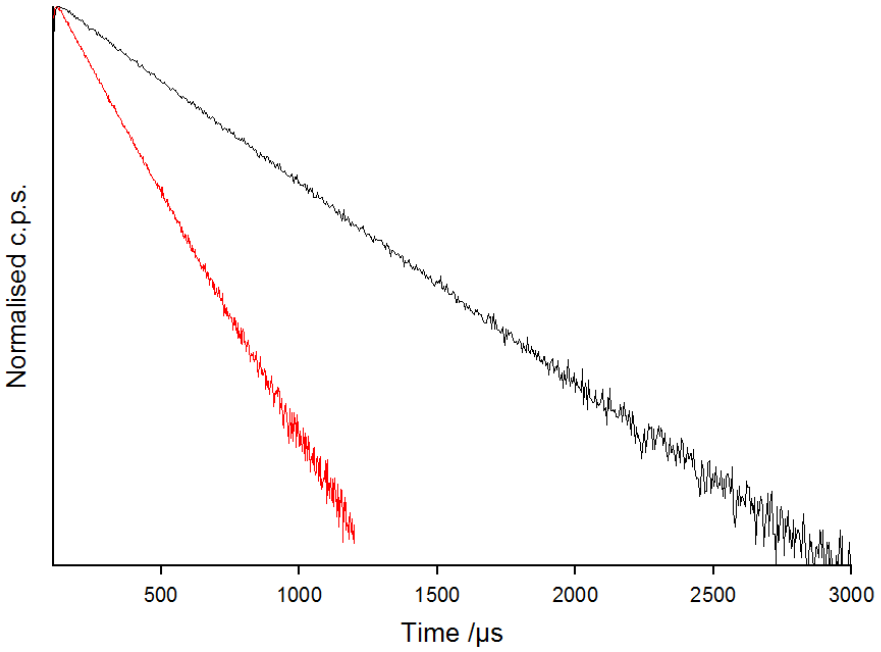

Figure 5.11 - Lifetime decays of the $\{Eu_2Rb_2\}^{IV}$ complex after dissolution in ethanol (λ_{ex} = 350 nm) at 298 K (red, λ_{em} = 611 nm) and 77 K (black, λ_{em} = 614 nm).

After dissolution of the [Eu(Phen)(**L1**)$_3$] complex in ethanol, the structure in the emission spectrum is similar at 298 K and 77K, but has changed when compared to the solid state (Figure 5.12). The $^7F_1 \leftarrow ^5D_0$ emission band is split into three unique, now equally spaced, components at 298 K and 77 K. In both temperatures, the band representing the $^7F_2 \leftarrow ^5D_0$ transition is now split into five components with a ratio $I(^7F_2 \leftarrow ^5D_0)/I(^7F_1 \leftarrow ^5D_0) = 18.34$ at 77 K, and 16.94 at 298 K.

All of the above aspects of the emission spectrum indicate that the symmetry of the metal is likely to be lower than C_{2v}.[36,233] This decrease in symmetry may be due to the flexibility of both ligands in solution.

Interestingly, the excited state lifetime and quantum efficiency are relatively unaffected by temperature (298 K vs 77 K) for the [Eu(Phen)(**L1**)$_3$] complex, which might suggest that the coordination sphere is devoid of solvent molecules, and thus the complex is rather stable after dissolution in ethanol.

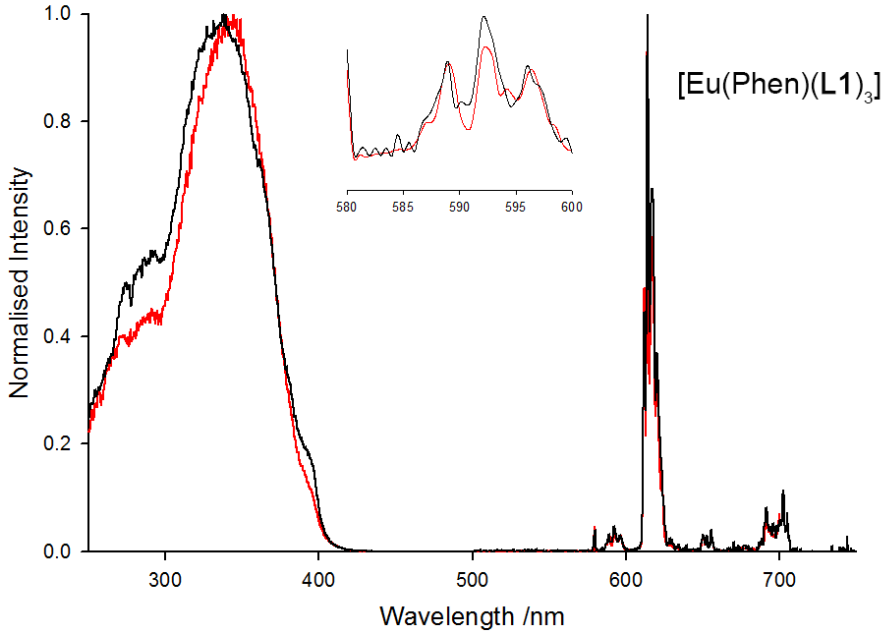

Figure 5.12 - Normalised excitation (λ_{em} = 614 nm) and emission (λ_{ex} = 350 nm) spectra of the [Eu(Phen)(**L1**)$_3$] complex after dissolution in ethanol at 298 K (red line) and 77 K (black line).

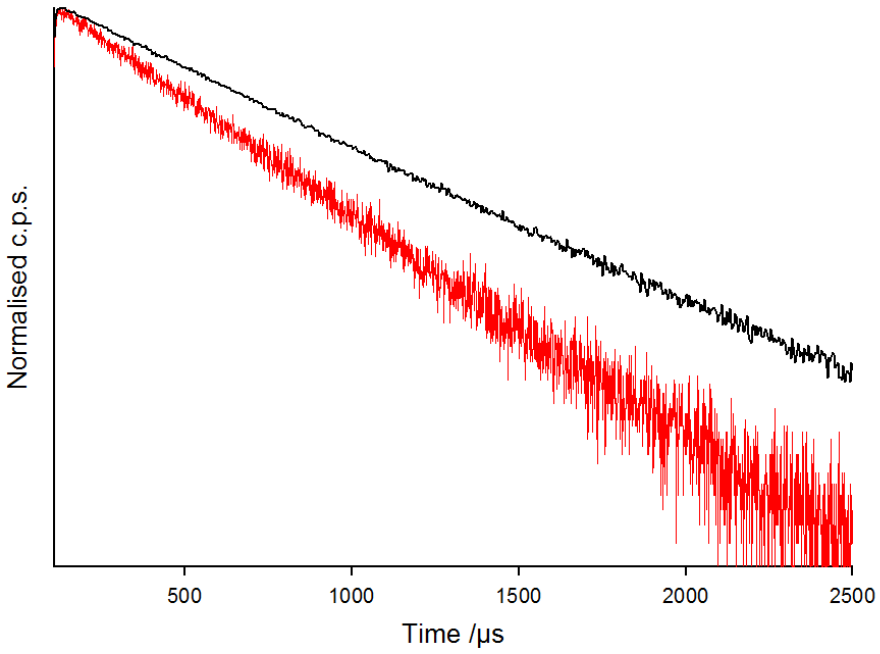

Figure 5.13 - Lifetime decays of the [Eu(Phen)(**L1**)$_3$] complex after dissolution in ethanol at 298 K (red) and 77 K (black) (λ_{ex} = 350 nm, λ_{em} = 614 nm).

5.3 Probing Coordinated Solvent

To further probe the stability of the assemblies in alcoholic solvent, the number of alcohol molecules coordinated to the Eu^{3+} centre in solution was predicted by a comparison of the Eu^{3+} excited state lifetime in methanol and deuterated methanol using the method proposed by Horrocks.[115] The $\{Eu_2K_2\}^{II}$ complex was used as a representative exemplar for the tetranuclear assemblies.

After dissolution of the $\{Eu_2K_2\}^{IV}$ assembly in CH_3OH and CD_3OD, the solution indeed exhibited observable characteristic Eu^{3+} metal-centred emission in the 570 nm to 750 nm spectral region (Figure 5.14). The emission spectra present the five line-like emission bands with a similar shape compared to the emission of $\{Eu_2K_2\}^{IV}$ in ethanol at 298 K (Figure 5.7), which provides a good indication that the coordination geometry is more or less consistent between ethanol and methanol, regardless of the methanol molecule being a more polar alcohol. It is noted that the

spectrum in CD_3OD is of overall lower intensity (by comparison of the $^7F_1 \leftarrow\!\!- {}^5D_0$ band), however the cause of this is unknown.

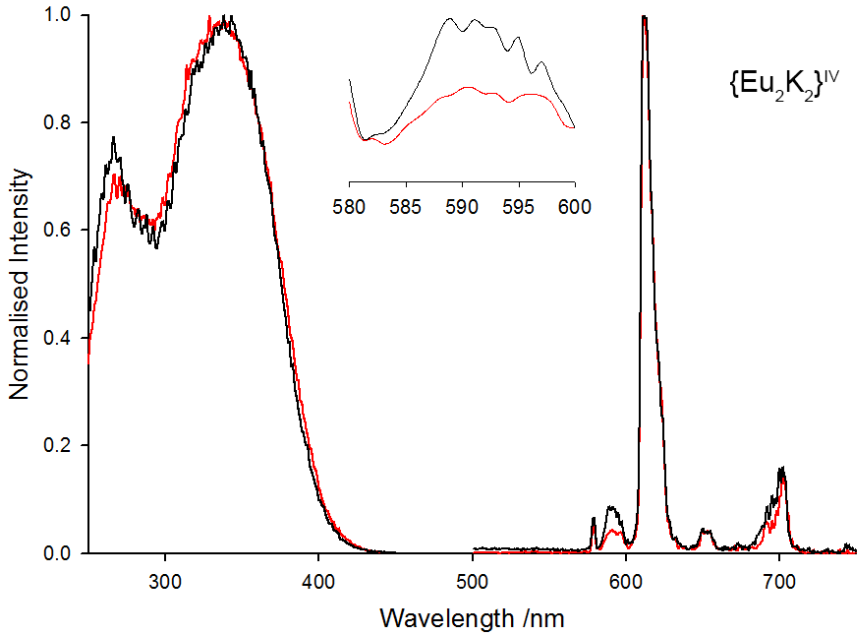

Figure 5.14 - Normalised excitation (λ_{em} = 612 nm) and emission (λ_{ex} = 387 nm) spectra of the $\{Eu_2K_2\}^{IV}$ assembly after dissolution in CH_3OH (red trace) and CD_3OD (black trace).

The measured τ_{obs} values in CH_3OH and CD_3OD were 125 µs and 153 µs, respectively. These values indicate that approximately three molecules of methanol are directly coordinated to the Eu^{3+} centre in solution (Eqn 5.2).

$$m = 2.1 \times (0.124^{-1} - 0.153^{-1})$$
$$m = 3.08 \sim 3\ molecules$$

Eqn 5.2

This observation provides strong evidence that the **L1**$^-$ is indeed labile after dissolution of the tetranuclear assembly in an alcoholic solvent, and in fact this lability results in the coordination of an average of three alcohol molecules directly to the lanthanoid centre.

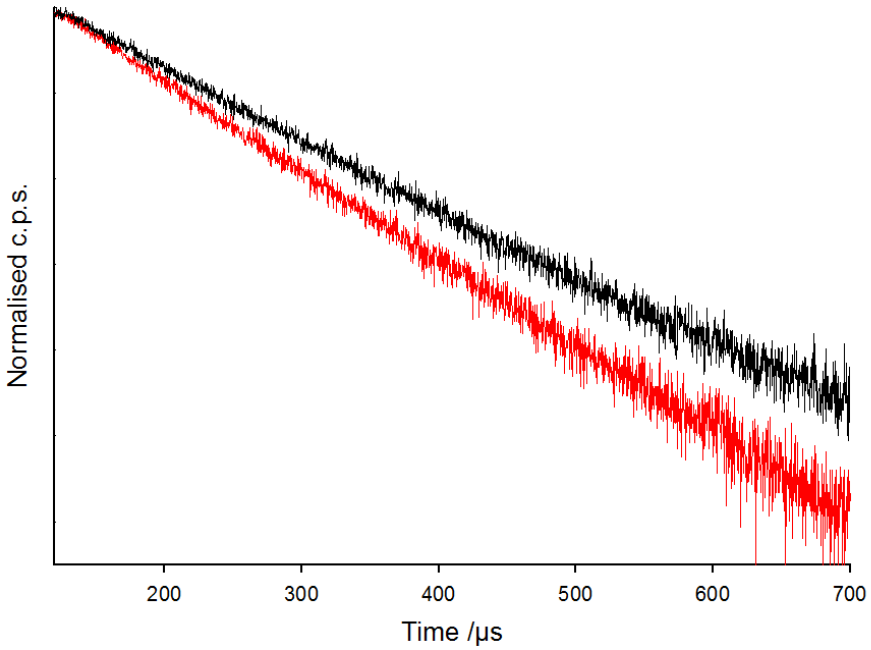

Figure 5.15 - Lifetime decays (λ_{ex} = 350 nm, λ_{em} = 612 nm) of the $\{Eu_2K_2\}^{IV}$ assembly after dissolution in CH_3OH (red trace) and CD_3OD (black trace).

In contrast to the $\{Eu_2K_2\}^{IV}$ tetranuclear assembly, the emission of the [Eu(Phen)(**L1**)$_3$] complex in ethanol suggested a flexible coordination sphere, however a coordination sphere which is less prone to ligand lability. Thus the [Eu(Phen)(**L1**)$_3$] complex was analysed using the same method, after dissolution in CH_3OH and CD_3OD.

After dissolution in methanolic solution the [Eu(Phen)(**L1**)$_3$] complex again reveals a characteristic Eu^{3+} metal-centred emission (Figure 5.16). Interestingly, the structure in the emission band has changed in comparison to the emission of [Eu(Phen)(**L1**)$_3$] in ethanol at 298 K (Figure 5.12), and after dissolution in methanol the emission spectrum resembles more the emission of the $\{Eu_2K_2\}^{IV}$ tetranuclear assembly in ethanol and methanol.

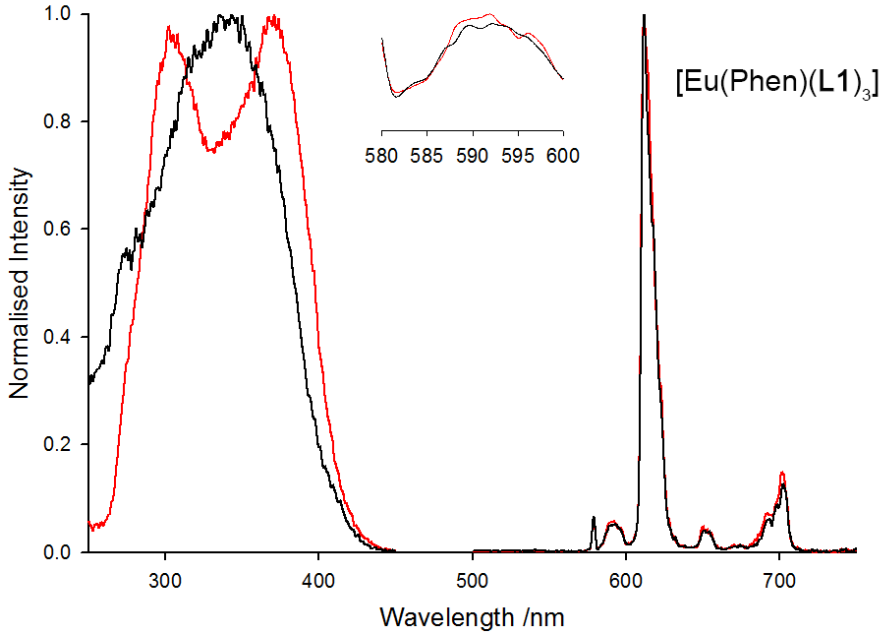

Figure 5.16 - Normalised excitation (λ_{em} = 612 nm) and emission (λ_{ex} = 350 nm) spectra of the [Eu(Phen)(**L1**)$_3$] complex after dissolution in CH_3OH (red trace) and CD_3OD (black trace).

Analysis of the excited state lifetime of [Eu(Phen)(**L1**)$_3$] complex in the CH_3OH and CD_3OD solvents revealed a biexponential decay in both solutions, τ_{CH_3OH} = 124 µs (73%), 278 µs (27%) and τ_{CD_3OD} = 150 µs (61%), 462 µs (39%) (Figure 5.17). Equating the minor and major components for number of coordinated methanol molecules *via* the Horrocks method identified again an average of three molecules for both lifetime components (Eqns 5.3-5.4).

$$m = 2.1 \times (0.124^{-1} - 0.150^{-1})$$
$$m = 2.92 \sim 3\ molecules$$

Eqn 5.3

$$m = 2.1 \times (0.278^{-1} - 0.462^{-1})$$
$$m = 2.98 \sim 3\ molecules$$

Eqn 5.4

The major component displayed lifetimes in CH_3OH/CD_3OD almost identical to that of the tetranuclear assembly, indicating that the species may be very similar in a methanolic solution, suggesting that this is likely to be the product of a labile Phen ligand. Therefore the minor component would likely be the product of **L1**$^-$ ligand lability.

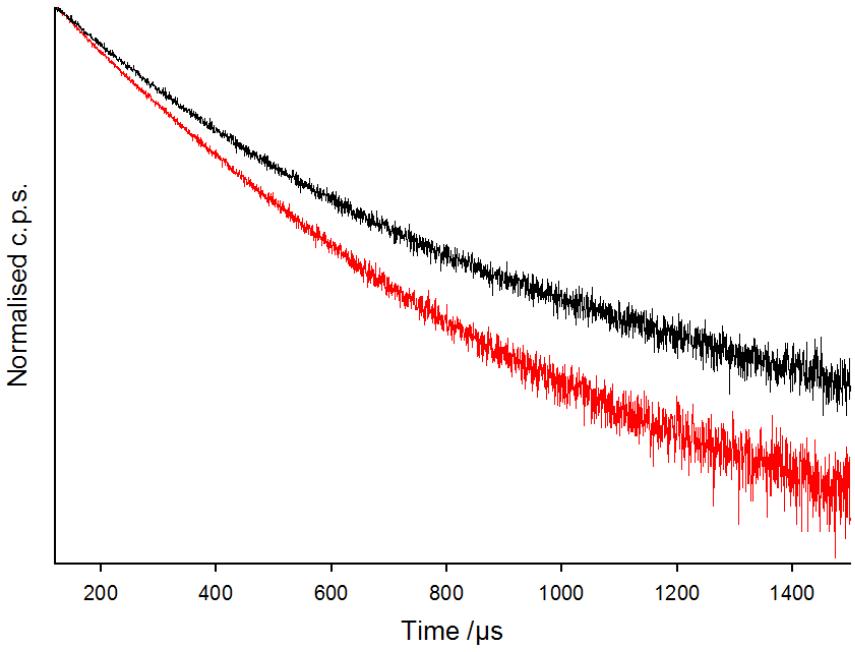

Figure 5.17 - Lifetime decays (λ_{ex} = 350 nm, λ_{em} = 612 nm) of the [Eu(Phen)(**L1**)$_3$] complex after dissolution in methanol (red trace) and methanol-d_4 (black trace).

The evidence provided from comparison of the [Eu(Phen)(**L1**)$_3$] emission spectra in solid state and in methanolic solution would suggest that the [Eu(Phen)(**L1**)$_3$] complex may not be preserved after dissolution in methanol. However, this hypothesis does not seem to hold for the dissolution of the complex in ethanol, which displays photophysical properties much different to that of the methanolic solutions.

5.4 Conclusion

In summary, ethanolic solutions of the Yb^{3+} and Eu^{3+} tetranuclear assemblies revealed characteristic metal-centred emissions at 298 K and 77 K. However, the structures in the emission spectra were very different from those observed in the solid state, even in a rigid matrix at 77 K, which suggests that the relative ligand fields are changing and perhaps the tetranuclear assembly is not preserved in solution. Furthermore, the excited state lifetimes were shortened in solution at 298 K compared to the solid state, indicative of the coordination of closely bound OH vibrations. This hypothesis is strengthened at 77 K, with an elongation in the excited state lifetime compared to the 298 K data.

Interestingly, after dissolution of the [Eu(Phen)(**L1**)$_3$] complex in ethanol the emission spectrum also changed from the solid state, however the spectra were very similar at 298 K and 77 K, which is likely due to the coordination sphere remaining saturated with the multidentate ligands, albeit with some flexibility in the solution state compared to the solid state.

To further probe the solution state stability of the assemblies, the $\{Eu_2K_2\}^{IV}$ was used as an exemplar in a deuterated methanol experiment which revealed that an average of three molecules of methanol are coordinated to the Eu^{3+} metal centre after dissolution in methanol. A comparison of the emission spectra between ethanol and methanol solvent systems indicates that the coordination sphere is likely very similar, and thus this speciation is likely to be dominant for all tetranuclear assemblies in ethanolic solvent.

In contrast, the [Eu(Phen)(**L1**)$_3$] complex reveals a biexponential decay after dissolution in methanolic solvent, with both excited state lifetimes equating to an average of three molecules of methanol bound, which could be the result of differing ligand lability in methanol, which is not observed in the ethanolic solution. This curious case for the [Eu(Phen)(**L1**)$_3$] complex, may indicate the differing coordination strengths of the ethanol and methanol molecules.

Further investigations of the solutions by NMR or Mass Spectral studies might possibly help to uncover the nature of the dissolved complex(es) hypothesised in this chapter.

6 Exploring Lanthanoid Complexes of an α-Substituted β-Diketonate

The work presented in this chapter has been published in a peer reviewed journal which is cited below:

B. L. Reid, B. W. Skelton, E. G. Moore, M. I. Ogden, M. Massi. *Aust. J. Chem.* **2015**, *68*, 1392-1398. doi: 10.1071/CH15253

6.1 Introduction

The substitution of β-diketones at the α-C position with an additional ketone group, to form β-triketones, has proved to be an interesting modification of a classic ligand, opening up new realms of lanthanoid coordination chemistry as described in the previous chapters. Substitution of β-diketonates at the α-C position has been reported as an effective way to reduce multiphonon relaxation, and hence the overall photoluminescence quantum yield in lanthanoid complexes as was observed with the β-triketonate ligands for NIR emitting materials. A common example of modification at this site is deuteration,[182] however, there are reported examples of β-diketonates substituted at the α-C position with a -CN functionality, typically with their coordination to some *d*-block metals.[238,239] As well as the potential for linear coordination through the –CN group, this functionality may also be extended to

tetrazolato units for which unique coordination modes have already been identified in alkali metal,[240] *d*-metal,[241–244] and lanthanoid[134,140,141,144,145,245] complexes.

Merkens and Englert reported the first lanthanoid complexes bearing β-diketonates substituted at the α-C position with a -CN functionality, namely the 2-cyano-1,3-methyl-1,3-propandione ligand (acacCN), with structures varying from mononuclear complexes to coordination polymers (Figure 6.1).[190] These complexes contained inner sphere H_2O molecules. If these H_2O molecules were removed, it would be expected that the resulting lanthanoid photophysical properties would be enhanced.

In fact, beyond this structural characterisation there has been no report of the photophysical properties of lanthanoid complexes bearing this type of α-CN substituted β-diketonate ligand. The ligand itself is intriguing as it removes the CH vibration at the α-C position, which would contribute to quenching of the lanthanoid excited state, but also is linearly coordinating in nature allowing the possibility of further coordination *via* the -CN substituent as reported previously.[190]

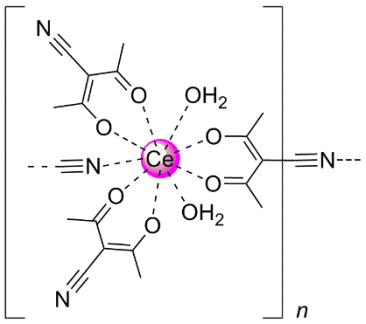

$[Ce(acacCN)_3(H_2O)_2]_n$

Figure 6.1 – Structure of a previously reported Ce^{3+} coordination polymer bearing an α-CN substituted β-diketonate ligand.

The work in this chapter aims to extend this work by investigating the photophysical properties of a Eu^{3+} complex bearing an α-CN substituted β-diketonate. The target β-diketonate in this case was the 2-cyano-1,3-phenyl-1,3-propandione ligand (**L2**H), in conjunction with a neutral Phen ligand to mitigate coordination of H_2O molecules. The **L2**H ligand can act as a better sensitiser of

lanthanoid emission *via* the antenna effect than the previously investigated acacCN ligand, whilst the Phen ligand can chelate to the lanthanoid in lieu of quenching solvent molecules, and also act as an antenna molecule itself.

The target complex was thus the neutral, mononuclear [Eu(Phen)(**L2**)$_3$] complex (Figure 6.2).

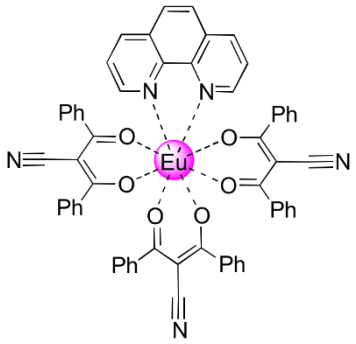

[Eu(Phen)(**L2**)$_3$]

Figure 6.2 – Proposed target [Eu(Phen)(**L2**)$_3$] complex.

6.2 Synthesis and X-ray Crystallography

The substitution of a β-diketone at the α-C position with a -CN substituent is typically achieved by the reaction of a precursor 2-chloro substituted β-diketone and an alkali metal cyanide *via* a nucleophilic substitution reaction,[246,247] although there are some alternate unique procedures.[248,249] Due to the hazards associated with these literature syntheses, herein the ligand **L2**H was prepared by a more straightforward crossed Claisen condensation reaction of 2-benzoylacetonitrile with benzoyl chloride in the presence of NaH in THF (Figure 6.3), to obtain the targeted product in a moderate yield (46%).

It should be noted that, after dissolution of **L2**H in $CDCl_3$, the ^{1}H NMR spectrum (Figure 6.4) does not reveal a signal for the α-C proton, suggesting that the enol tautomer (shown in Figure 6.3) is the major species present, consistent with previous literature.[246] The ^{1}H NMR spectrum reveals three peaks corresponding to the three unique protons on the phenyl substituent.

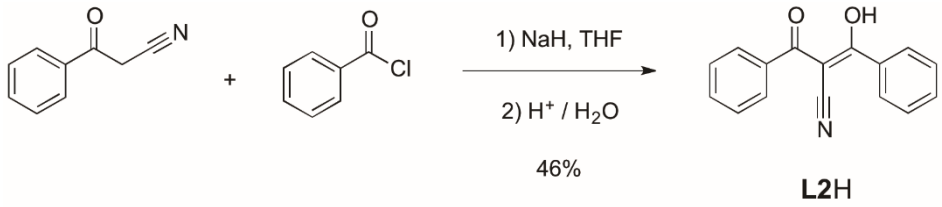

Figure 6.3 - The reaction scheme for the preparation of **L2**H.

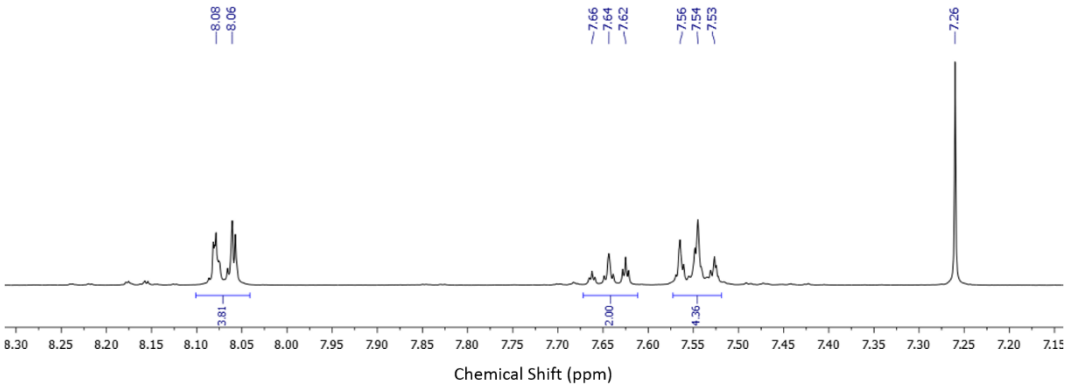

Figure 6.4 – A portion of the ^{1}H NMR spectrum of the **L2**H molecule in $CDCl_3$.

With the **L2**H ligand synthesised, the target Eu^{3+} complex could be prepared. Reaction of one equivalent of both hydrated $EuCl_3$ and Phen with three equivalents of **L2**H and triethylamine in ethanol resulted in the formation of yellow crystals after slow evaporation of the solvent over several days. The formulation of the product was determined by single crystal X-ray diffraction, revealing a coordination polymer of the formula $[Eu(Phen)(\mathbf{L2})_3]_n \cdot 0.5\ H_2O$ (Figure 6.5).

The structure observed is quite similar to the reported Ce^{3+} coordination polymer (Figure 6.1) bearing acacCN ligands, however, with the Phen ligand in this case replacing the two inner sphere water molecules observed for $[Ce(acacCN)_3(H_2O)_2]_n$.[190]

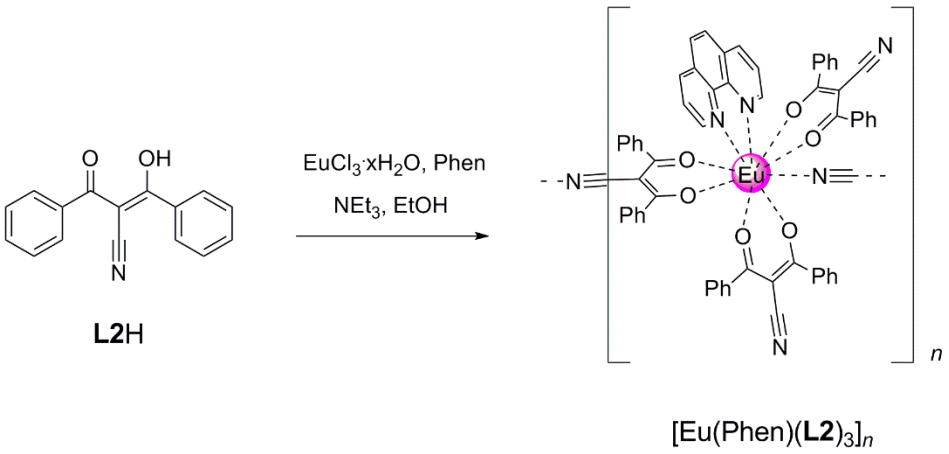

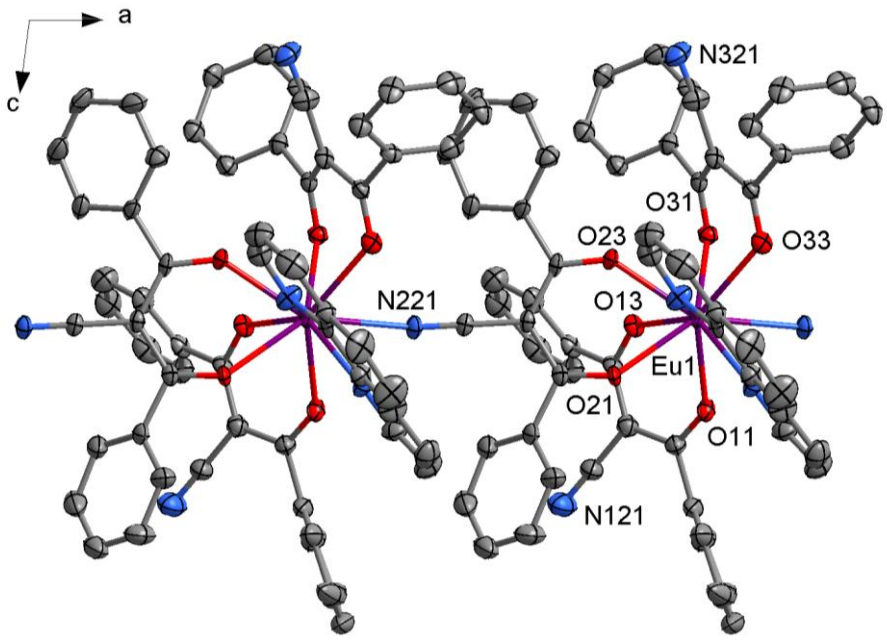

Figure 6.5 - Top: Synthetic scheme of the [Eu(Phen)(**L2**)$_3$]$_n$ coordination polymer. Bottom: Molecular plot of the coordination polymer with displacement ellipsoids drawn at the 50% probability level. Hydrogen atoms and solvent molecules have been omitted for clarity.

Each Eu^{3+} cation is nine-coordinated, with six O-donor atoms from three bis-chelating β-diketonate molecules, two N atoms from a bis-chelating Phen molecule and one N atom from a nitrile substituent of one neighbouring β-diketonate complex, thus forming a chain like structure. The Eu···Eu distance is 8.96 Å in the coordination polymer, which is a distance long enough to suggest that direct energy migration between the Eu^{3+} centres should be minimised. However,

this cross-relaxation mechanism might also be ligand mediated, which would aid energy transfer at longer Ln···Ln distances.[111]

The nine-coordinate geometry of the Eu^{3+} coordination sphere was assessed using the Shape Version 2.1 software[216] and the lowest CShM values were found for either a tricapped trigonal prism or a capped square antiprism geometry.

The CShM were plotted relative to the regular capped square antiprismatic (x-axis, C_{4v}) and tricapped trigonal prismatic (y-axis, D_{3h}) polyhedra (Figure 6.6). However, notably the CShM of Eu^{3+} in $[Eu(Phen)(\mathbf{L2})_3]_n$ does not lie along the LEIP (black trace) with a deviation of 93.1%. This indicates a distortion away from these regular polyhedra, but in fact the distortion is close to that of a reference geometry, namely, the tricapped trigonal prismatic with dissimilar edges polyhedron.[220]

Thus, the nine-coordinate geometry is best described as a tricapped trigonal prism with dissimilar edges (Figure 6.6). This type of distortion has been observed for nine-coordinate Ln^{3+} β-diketonate complexes previously.[220]

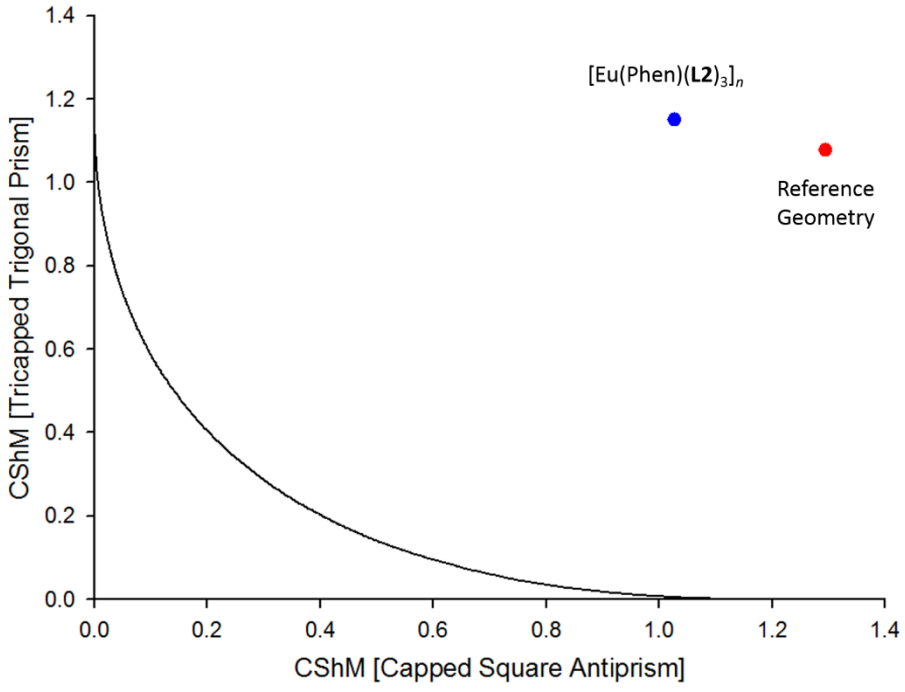

Figure 6.6 - Shape map relative to the regular capped square antiprism and tricapped trigonal prism polyhedra (LEIP - black trace). The reciprocal shape measures of $[Eu(Phen)(\mathbf{L2})_3]_n$ (1.028, 1.151 – blue spot) and the reference tricapped trigonal prism with dissimilar edges (1.295, 1.077 – red spot) are plotted.

In summary, the $[Eu(Phen)(\mathbf{L2})_3]_n$ coordination polymer was crystallised and revealed a nine-coordinate species best described as a tricapped trigonal prism with dissimilar edges. Although the targeted mononuclear complex was not obtained, the polymer achieves the same structural aspects which are ideal from a photophysical perspective such as the presence of the β-diketonate and a coordination sphere devoid of closely bound quenching oscillators.

6.3 Photophysical Properties of the Ligand

In order to identify the excitation wavelength necessary for the antenna effect, the UV-Visible absorption spectra of the **L2**H molecule and $\mathbf{L2}^-$ ligand is essential.

The UV-Visible absorption spectra of the **L2**H molecule and $\mathbf{L2}^-$ ligand (deprotonated with excess triethylamine) in acetonitrile reveal a broad band centred at ~330 nm with a tail which extends to ~400 nm. This absorption is attributed to a $^1\pi\pi^*$ absorption, however this band could also have some $^1n\pi^*$ absorption character (Figure 6.7). The maximum molar absorptivity is slightly increased and red-shifted, in the deprotonated ligand, consistent with the deprotonation enhancing the conjugation along the β-diketone backbone.

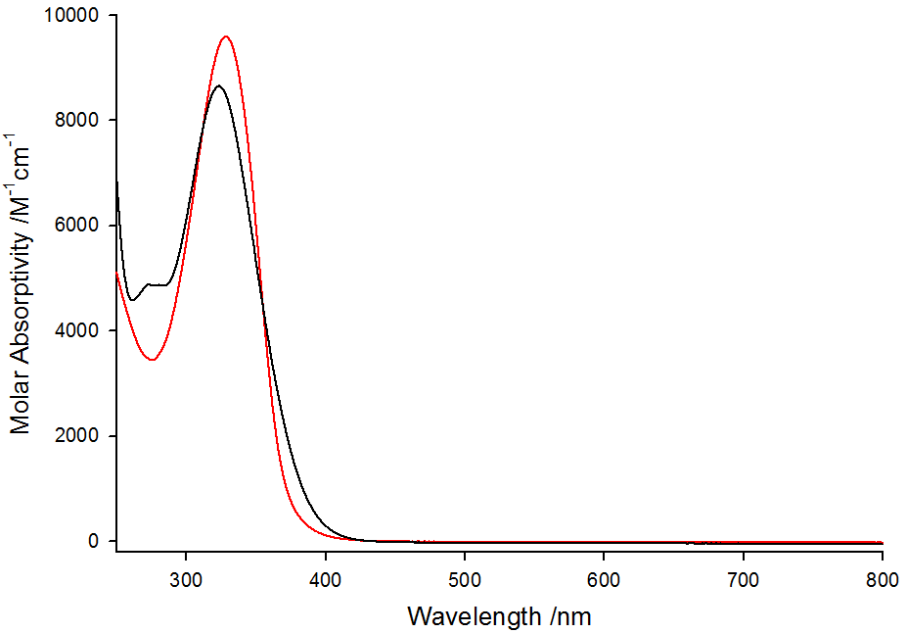

Figure 6.7 - UV-Visible absorption spectra of **L2**H (black trace), and **L2**$^{-}$ (excess triethylamine, red trace) in acetonitrile.

To estimate the energy of the singlet and triplet excited states in the **L2**H molecule and **L2**$^{-}$ ligand (after Gd^{3+} complexation), the emission spectrum of each species was analysed in acetonitrile at 77 K (Figure 6.8). The emission spectrum of the **L2**H molecule presents a broad structureless band spanning the 400 nm to 700 nm spectral region. Similarly, after deprotonation of the molecule and addition of excess Gd^{3+} to the ligand, the emission spectrum remains very similar, with the same broad structureless band spanning the 400 nm to 700 nm region. The emission in both cases is attributed to emission from the $^{1}\pi\pi^{*}$ state, with the low intensity tail between 550 nm and 700 nm perhaps containing some emission from the $^{3}\pi\pi^{*}$ state. This is an unexpected result, as after Gd^{3+} complexation the emission from the $^{3}\pi\pi^{*}$ excited state should be enhanced due to the heavy atom effect inducing the ISC mechanism.[46]

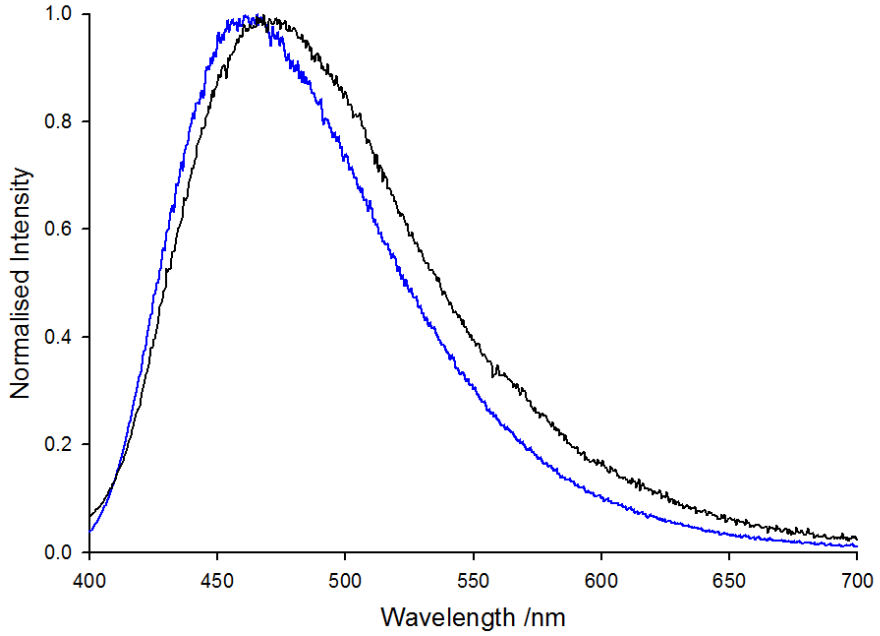

Figure 6.8 - Emission spectra of **L2**H (black trace), and **L2**$^{-}$ (blue trace) in the presence of excess Gd^{3+} and triethylamine, in acetonitrile at 77 K (λ_{ex} = 325 nm).

This result suggests that the ISC to the triplet state is very slow and/or the ligand triplet state is efficiently quenched. Therefore, the triplet state energy could not be effectively determined *via* the emission spectrum of the ligand.

The singlet state energy of the ligand could be estimated, and thus the emission spectrum was fit to a series of overlapping Gaussian functions (Figure 6.9), with the highest energy function attributed to the 0-phonon transition of the $^{1}\pi\pi^{*}$ state. The 0-phonon energy of the singlet state can be estimated from the maximum of the Gaussian labelled 4 (~24,576 cm^{-1}).

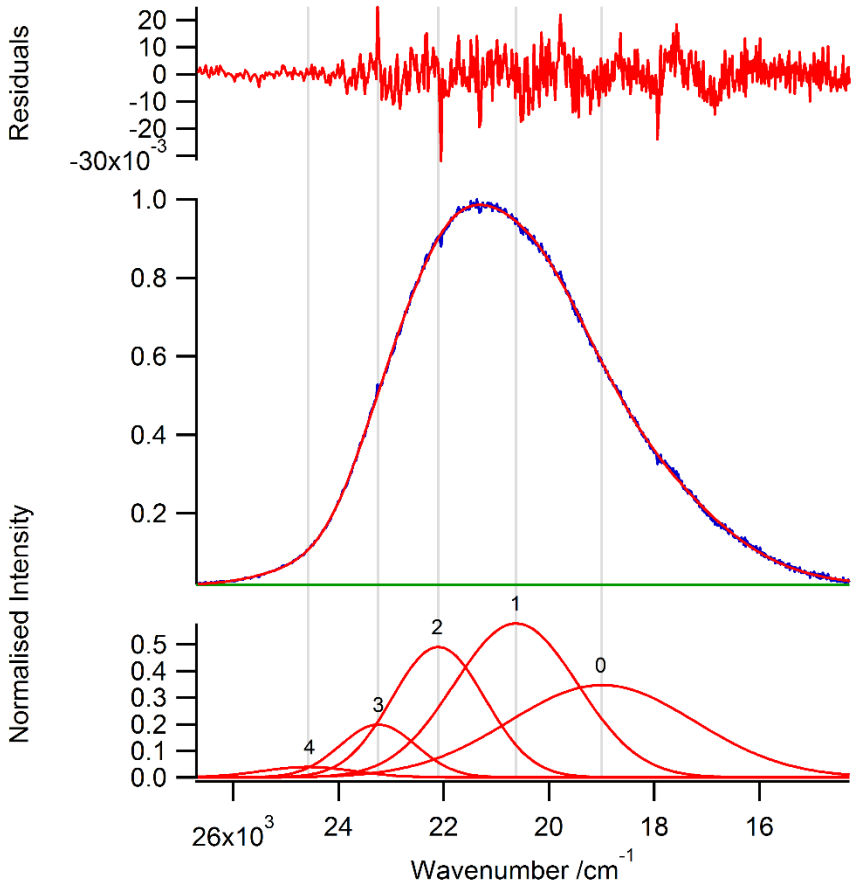

Figure 6.9 - Emission of **L2**H in acetonitrile at 77 K, fit to a series of overlapping Gaussian functions.

6.4 Photophysical Properties of the Europium Complex

The emission of the [Eu(Phen)(**L2**)]$_n$ polymer was analysed in the solid state as well as after dissolution in acetonitrile. The photophysical properties were then used to decipher whether the **L2**$^-$ ligand is an efficient antenna for Eu^{3+}.

The emission spectra presented in this chapter originate as a consequence of the antenna effect, indicated by the broad and structureless excitation spectrum which resembles the absorption of the **L2**$^-$ and Phen[168] ligands (Figure 6.7).

6.4.1 Solid State

In the solid state, the [Eu(Phen)(**L2**)$_3$]$_n$ species displays characteristic red emission after excitation at the 350 nm (Figure 6.10). The excitation spectrum presents a broad antenna component as well as several sharp peaks at 465 nm and 535 nm corresponding to the $^7F_0 \rightarrow {}^5D_2$ and $^7F_0 \rightarrow {}^5D_1$ intraconfigurational *f-f* transitions, respectively.[49] Observation of these peaks with a similar intensity compared to ligand-based absorption indicates that the ligand sensitisation pathway is rather inefficient. This inefficiency may be due the **L2** and/or Phen ligands, however, Phen is a well known sensitiser of Eu^{3+} emission[178] which suggests that the **L2** ligand may be the problem.

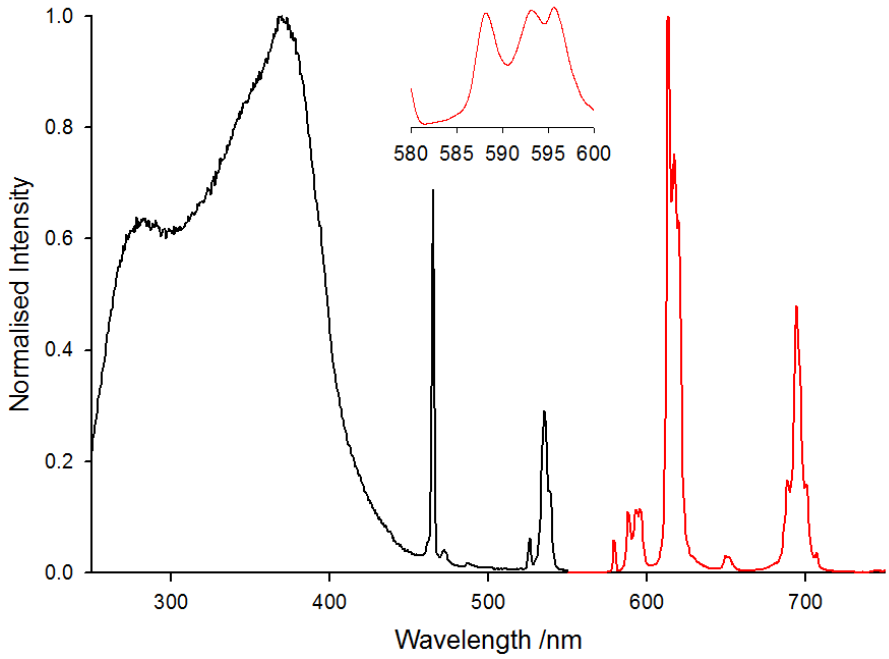

Figure 6.10 – Excitation (black trace, λ_{em} = 612 nm) and emission (red trace, λ_{ex} = 350 nm) spectra of the [Eu(Phen)(**L2**)$_3$]$_n$ coordination polymer in the solid state. Inset: A close-up region of the emission spectrum highlighting the splitting in the $^7F_1 \leftarrow {}^5D_0$ emission band.

The emission spectrum displays five line-like emission bands centred at 579, 593, 613, 650, and 694 nm, which are attributed to the Eu^{3+} metal-centred $^7F_J \leftarrow {}^5D_0$ (J = 0, 1, 2, 3, and 4) transitions, respectively. The $^7F_0 \leftarrow {}^5D_0$ transition appears as a single sharp peak of weak intensity with a FWHM of ~56 cm^{-1}, indicating a single

Eu^{3+} unique coordination sphere in the solid state. The fine structure in the $^7F_J \leftarrow ^5D_0$ (J = 1, 2) emission bands is consistent with a Eu^{3+} coordination geometry of a symmetry lower than C_{2v},[36,233] which agrees with that observed in the crystal structure.

The luminescence lifetime (τ_{obs}) of the complex was measured in the solid state, and was best fit by a biexponential function (Figure 6.11) with a major component of 572 μs (90%) and a shorter minor component of 304 μs (10%).

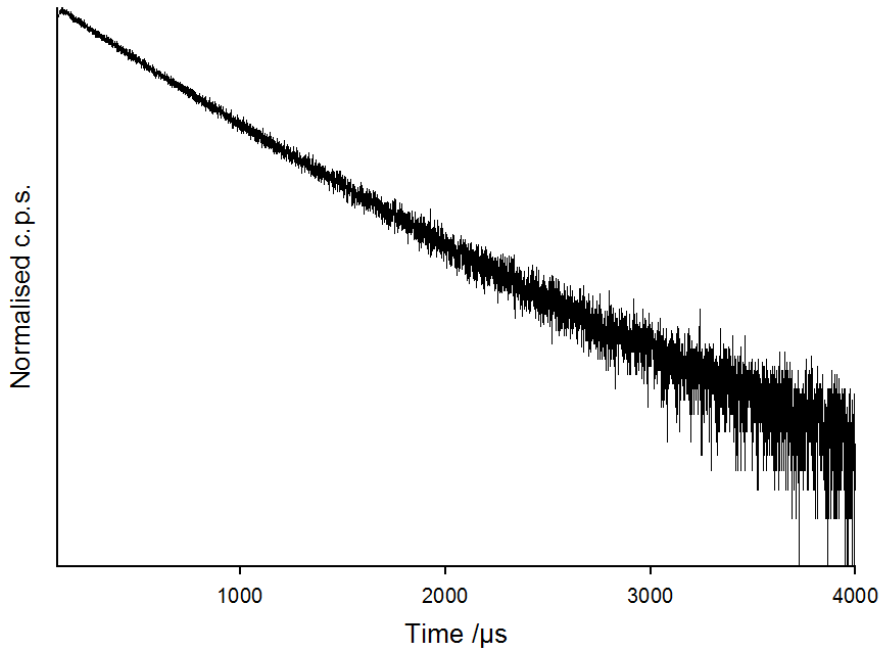

Figure 6.11 - Lifetime decay of the [Eu(Phen)(**L2**)$_3$]$_n$ coordination polymer in the solid state (λ_{ex} = 350 nm, λ_{em} = 612 nm).

The longer-lived lifetime is comparable to other β-diketonate Eu^{3+} complexes in the solid-state bearing Phen and β-diketonate ligands, for which typical values range from 350-600 μs in the solid-state .[30,178] With respect to the longer-lived τ_{obs} value, the Φ_{Ln}^{Ln} value was calculated at 35%. This value is relatively high, likely due to the Eu^{3+} coordination sphere being devoid of closely bound high energy quenching oscillators such as OH, thus mitigating any multiphonon relaxation pathways.

6.4.2 Dissolution Studies

After dissolution of the coordination polymer in acetonitrile, the emission spectrum becomes visibly different at both 298 K and 77 K (Figure 6.12), in comparison to the solid state emission. The excitation spectra in solution reveal a trace very similar to the UV-Visible absorption spectra of the **L2**$^-$ (Figure 6.7) and Phen[168] ligands, suggesting sensitisation of the Eu^{3+} *via* the antenna effect.

The $^7F_0 \leftarrow ^5D_0$ transition appears much broader in solution at 298 K, with a FWHM of ~100 cm^{-1} indicating lack of rigidity in the ligand coordination in solution, which results in a more variable coordination geometry. The FWHM is reduced to ~45 cm^{-1} at 77 K.

On freezing, the relative intensity of the emission bands changes. However, the splitting of the emission peaks do not differ significantly, which provides evidence that in a rigid matrix, the coordination geometry is different to that in the solid state and that a nine-coordinate complex may not be the major species in solution. It has been reported for the $[Ce(acacCN)_3(H_2O)_2]_n$ polymer, that after dissolution of the polymer in acetonitrile, a mononuclear eight-coordinate $[Ce(acacCN)_3(H_2O)_3]$ complex was recrystallised.[190]

Therefore, it is presumed that in an acetonitrile solution, the $[Eu(Phen)(\mathbf{L2})]_n$ coordination polymer is similarly not preserved, and rather an eight-coordinate $[Eu(Phen)(\mathbf{L2})_3]$ molecular species exists. Although not conducted here, further NMR studies of an analogous diamagnetic lanthanoid polymer in CD_3CN may provide further evidence of the structure of the dissolved species.

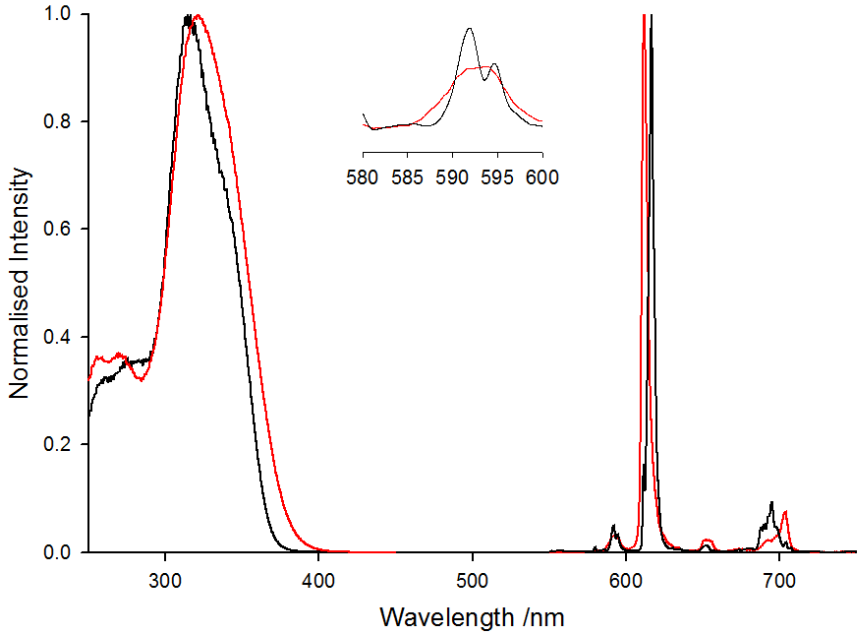

Figure 6.12 – Normalised excitation (λ_{em} = 612 nm) and emission spectra of the [Eu(Phen)(**L2**)$_3$]$_n$ coordination polymer after dissolution in acetonitrile at 298 K (red trace, λ_{ex} = 300 nm) and 77 K (black trace, λ_{ex} = 350 nm).

As further evidence for this change, the τ_{obs} in solution was satisfactorily fit using a monoexponential function at both 298 K and 77 K (Figure 6.13), and was equated to 712 µs and 707 µs, respectively. The similarity in these τ_{obs} values indicates that the Eu^{3+} emission in the acetonitrile solution is not affected strongly by multiphonon relaxation pathways.

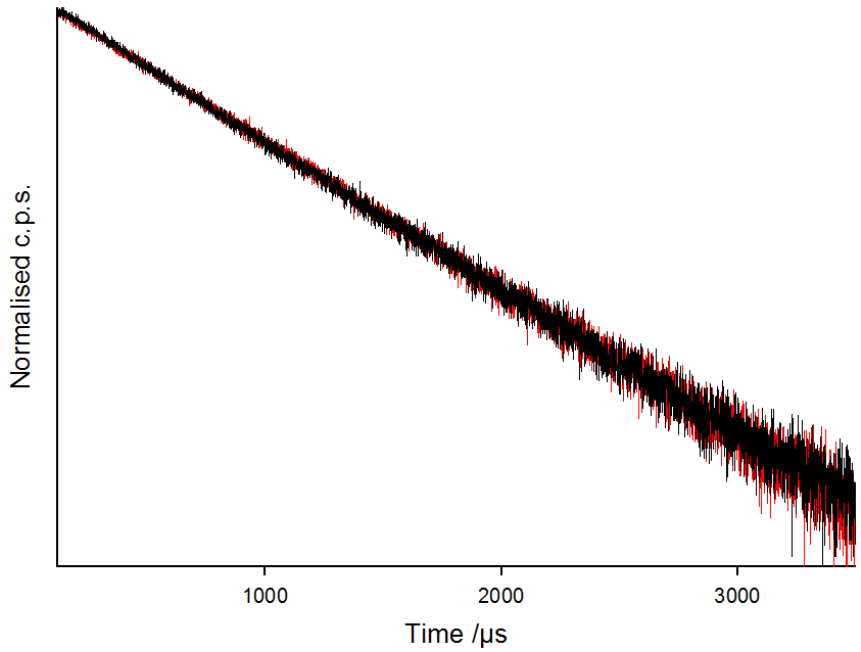

Figure 6.13 - Lifetime decays (λ_{ex} = 350 nm, λ_{em} = 612 nm) of the [Eu(Phen)(**L2**)$_3$]$_n$ coordination polymer after dissolution in acetonitrile at 298 K (red trace) and 77 K (black trace).

Elongation in the τ_{obs} value is accompanied by an increase in the Φ_{Ln}^{Ln} to 60% (298 K) and 61% (77 K). The improvement in the photophysical properties in solution suggests that there is less quenching of the $^5D_0$ state, and it is possible that the formation of the monomeric species excludes Eu···Eu cross-relaxation pathways.[111]

The quantum yield (Φ_{Ln}^{L}) of the Eu^{3+} emission in acetonitrile at 298 K was evaluated, giving a Φ_{Ln}^{L} of 2% after excitation at 300 nm, thus resulting in a rather low overall sensitisation efficiency (Φ_{sens}) of 3.4%. This outcome suggests that the sensitisation of the Eu^{3+} by the ligand **L2**$^-$ may be quite an inefficient process due to competing non-radiative deactivation pathways occurring on the singlet or triplet excited states of the ligand. A summary of excited state lifetime and photoluminescence quantum yield data are reported in Table 6.1 for solid and solution state.

Table 6.1 - Selected photophysical data for $[Eu(Phen)(\mathbf{L2})_3]_n$ in acetonitrile.

	τ_{obs} (μs)	Φ_{Ln}^{Ln} (%)	Φ_{Ln}^{L} (%)
Solid	572 (90%) 304 (10%)	35	
MeCN 298K	712	60	2.1
MeCN 77K	707	61	

A Jabloǹski diagram of the Eu^{3+} complex showing selected photophysical data is shown in Figure 6.14. The photophysical investigation of the complex has revealed some important factors in the Jabloǹski diagram. Clearly, the emission from the lanthanoid centre has a high Φ_{Ln}^{Ln} and long-lived τ_{obs}, however the Φ_{Ln}^{L} is very low suggesting that the energy transfer process is the limiting factor. This result was also alluded to in the $\mathbf{L2}^-$ emission spectrum, which indicated that the triplet state is either poorly populated or undergoes a fast non-radiative decay pathway. Furthermore, it is possible that part of the 3.4% sensitisation efficiency in solution can be from the Phen ligand, which means that the effective sensitisation from the β-diketonate might be even more inefficient.

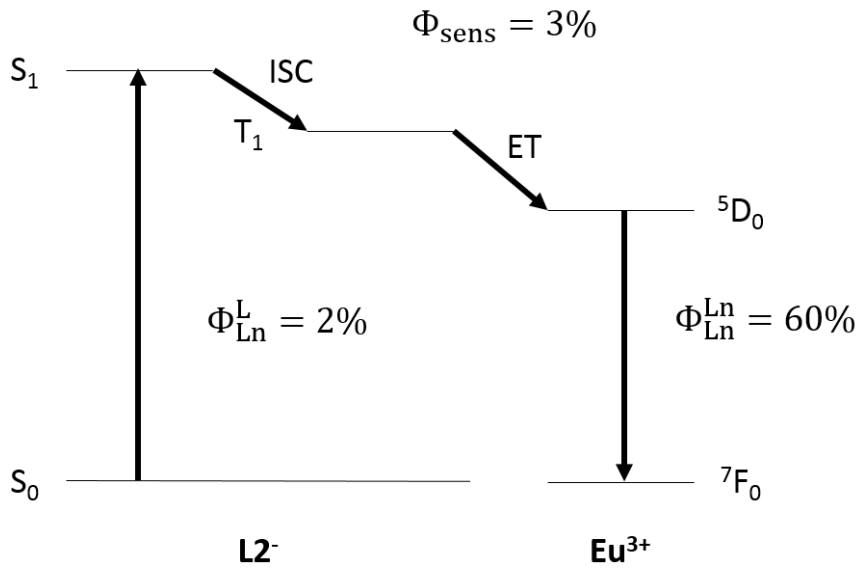

Figure 6.14 – Jabloński diagram highlighting the processes occurring in the [Eu(Phen)(**L2**)$_3$] complex.

In an effort to rationalise the low sensitisation efficiency observed in the Eu^{3+} complex with the **L2**$^-$ ligand, ultrafast transient absorption (TA) measurements were also undertaken on the femtosecond timescale in order to identify the photophysical processes occurring in the ligand and its lanthanoid complexes.

6.5 Transient Absorption

The TA of some β-diketonates has been reported in the literature, with an emphasis that β-diketonates display a variety of complex photoinduced processes upon electronic excitation.[250,251] Thus, for the **L2**$^-$ ligand it was anticipated that TA signals from both the S_2 ($^1\pi\pi^*$) and S_1 ($^1n\pi^*$) excited states, together with a longer-lived triplet state ($^3\pi\pi^*$) would be observed (Figure 6.15).[224] The lifetime of the latter can also be longer in the presence of Ln^{3+} ions, as a consequence of the increased rigidity in the molecule due to metal ion complexation. Moreover, in the presence of Gd^{3+} ions, the lifetime of the triplet state for structurally related compounds has been reported to be ~240 ns at RT.[252]

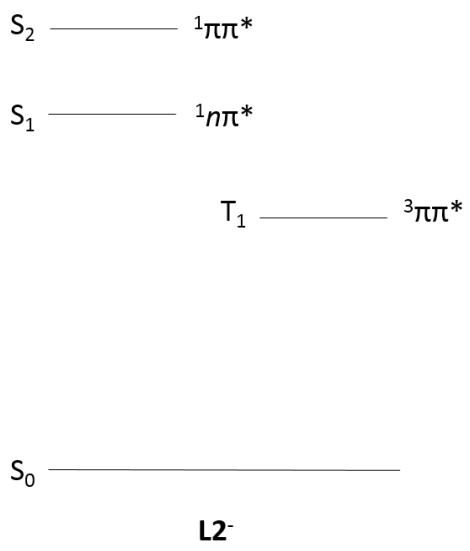

Figure 6.15 – Jabloński diagram illustrating the electronic progression anticipated for the **L2**$^-$ ligand.

The deprotonated ligand **L2**$^-$ was investigated, as well as TA measurements after addition of excess Eu^{3+} and Gd^{3+} to a solution of **L2**$^-$ in acetonitrile. The resulting TA spectra are presented with the extracted decay constants obtained from global analysis of these spectra in Figures 6.17-6.19.

The samples used for TA experiments were characterised by the absorption spectra presented in Figure 6.16. For excitation at 330 nm, the absorption values are ~0.5-0.8.

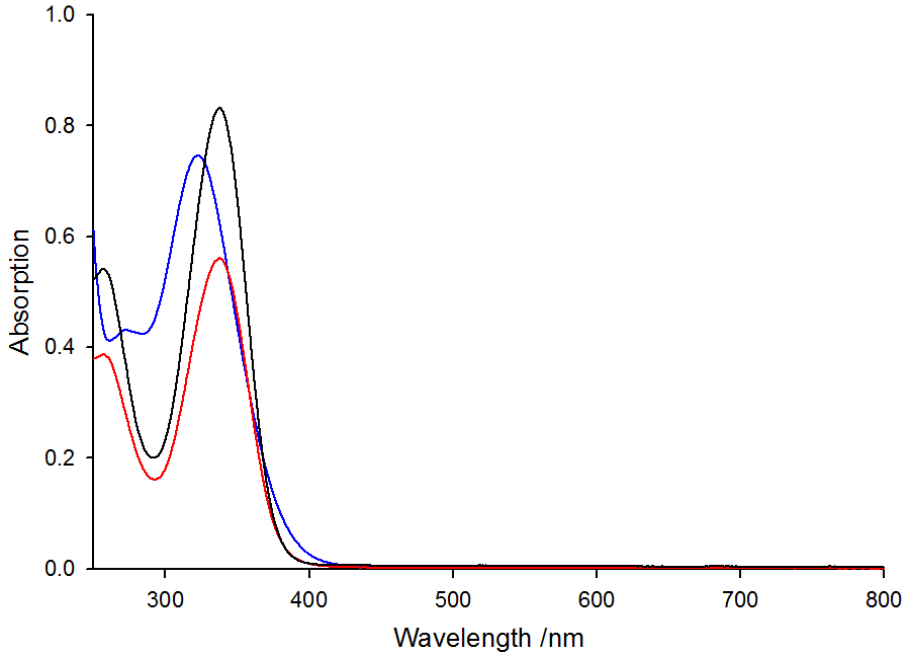

Figure 6.16 - UV-visible absorption spectra of $\mathbf{L}^-$ (blue trace), and $\mathbf{L}^-$ in presence of excess Gd^{3+} (black trace), and Eu^{3+} (red trace) in acetonitrile.

The TA spectrum of $\mathbf{L2}^-$ (Figure 6.17) reveals an initial change in optical density (ΔOD) band with a peak at ~510 nm, which decays rapidly within the first 10 ps to form a weaker broad band spanning the visible region and with maxima at ~510 nm and ~575 nm. After longer time delays, the 510 nm peak continues to disappear while the red shifted component persists at time delays >50 ps, subsequently decaying more slowly to form a long lived feature which does not completely decay to zero over the observable 2.7 ns time window.

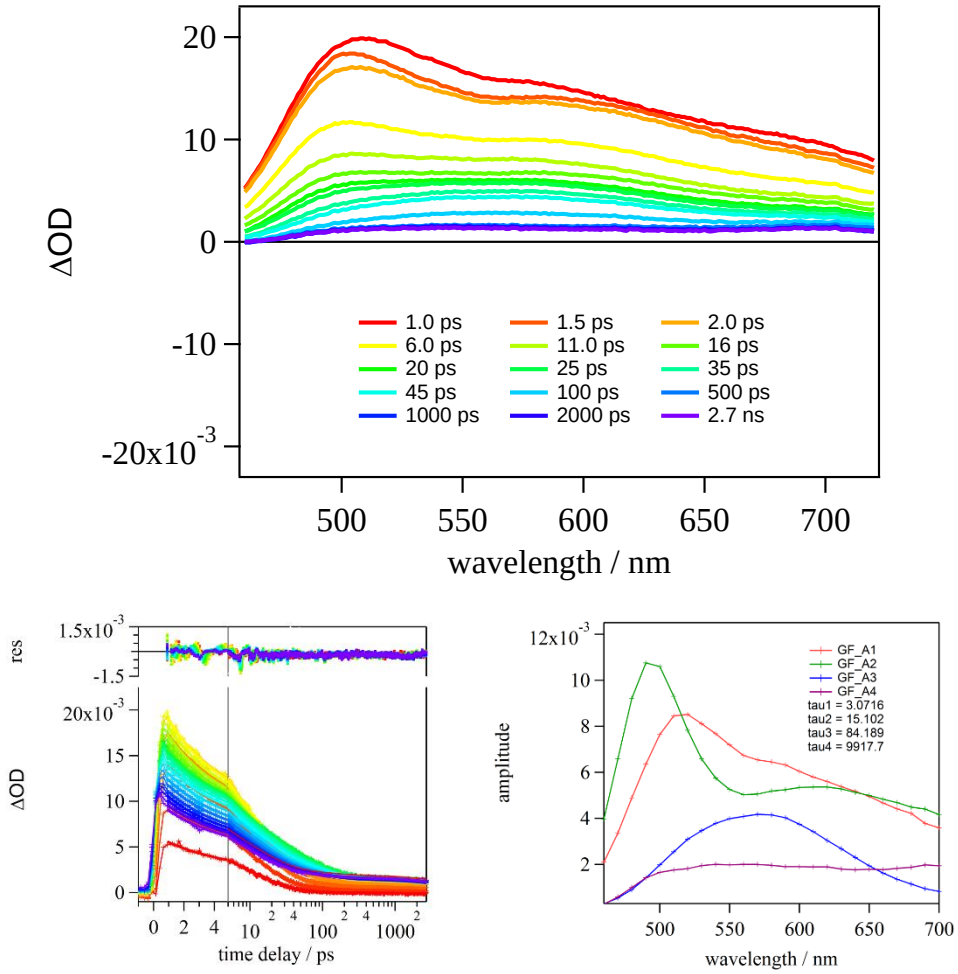

Figure 6.17 – Top: TA spectra measured at various time delays (inset) after excitation (330 nm) for **L2**$^{-}$. Bottom: Results of global fitting the observed TA data across all wavelengths for **L2**$^{-}$ in acetonitrile solution.

A four exponential decay function was required to accurately recreate the ΔOD dynamics, yielding lifetime constants of τ_1 = 3.1 ps, τ_2 = 15.1 ps, τ_3 = 84.2 ps and $\tau_4 \approx$ 9.9 ns. Such multiexponential decay behaviour is not unexpected, given the highly complex photophysical processes previously observed for similar β-diketonate derivatives studied by TA in acetonitrile solution. In these cases, similar multiexponential fitting procedures were required and yielded similar lifetime components [1.18 ps, 10.75 ps, 0.49 ns and >10 ns, for dibenzoylmethane][251] to those observed here for the **L2**$^{-}$ ligand. Hence, the observed decay kinetics in the **L2**$^{-}$ ligand is assigned to fast decay of the initially

formed S_2 excited state (τ_1 ~ 3.1 ps), followed by subsequent excited state decay (τ_2 ~ 15 ps) on the S_1 excited state potential energy surface, which is bifurcated, forming either a non-chelated enol *via* rotamerisation (τ_3 ~ 84 ps) or undergoing ISC to form a longer lived T_1 excited state (τ_4 ~ 8.1 ns). It is noted that the assigned triplet state lifetime is much shorter compared to literature values for β-diketonates, such as dibenzoylmethane, suggesting far more efficient non-radiative decay pathways for the excited T_1 state of the **L2**$^-$ ligand.

In the presence of Gd^{3+} ions, the TA spectra of **L2**$^-$ changes considerably, and is characterised by an initial ultrafast decay in the red from ~570 nm to 720 nm, accompanied by a negative ΔOD band centred at ~490 nm. These TA features rapidly evolve (<1ps) into a broad band in the ~510 nm to 580 nm spectral region, which subsequently decays and red shifts at longer time delays until essentially reaching baseline over the 2.7 ns observable time window.

In this case, a three exponential decay model was able to satisfactorily reproduce the excited state decay dynamics, with resulting time constants of τ_1 = 0.4 ps, τ_2 = 3.5 ps, and τ_3 = 468.5 ps. By analogy to the free ligand, we assign the initial fast decay to $S_2 \longrightarrow S_n$ excited state absorption, which is also accompanied in this case by strong stimulated emission (negative ΔOD) at ~490 nm. Decay of this initially populated state coincides with an increase in the TA signal at ~500 nm to 600 nm, which we attribute to $S_1 \longrightarrow S_n$ absorption, which also decays quickly with a time constant of ~2.4 ps. We assign the long lived signal to the T_1 excited state absorption, with a lifetime of $\tau_3 \approx$ 468.5 ps.

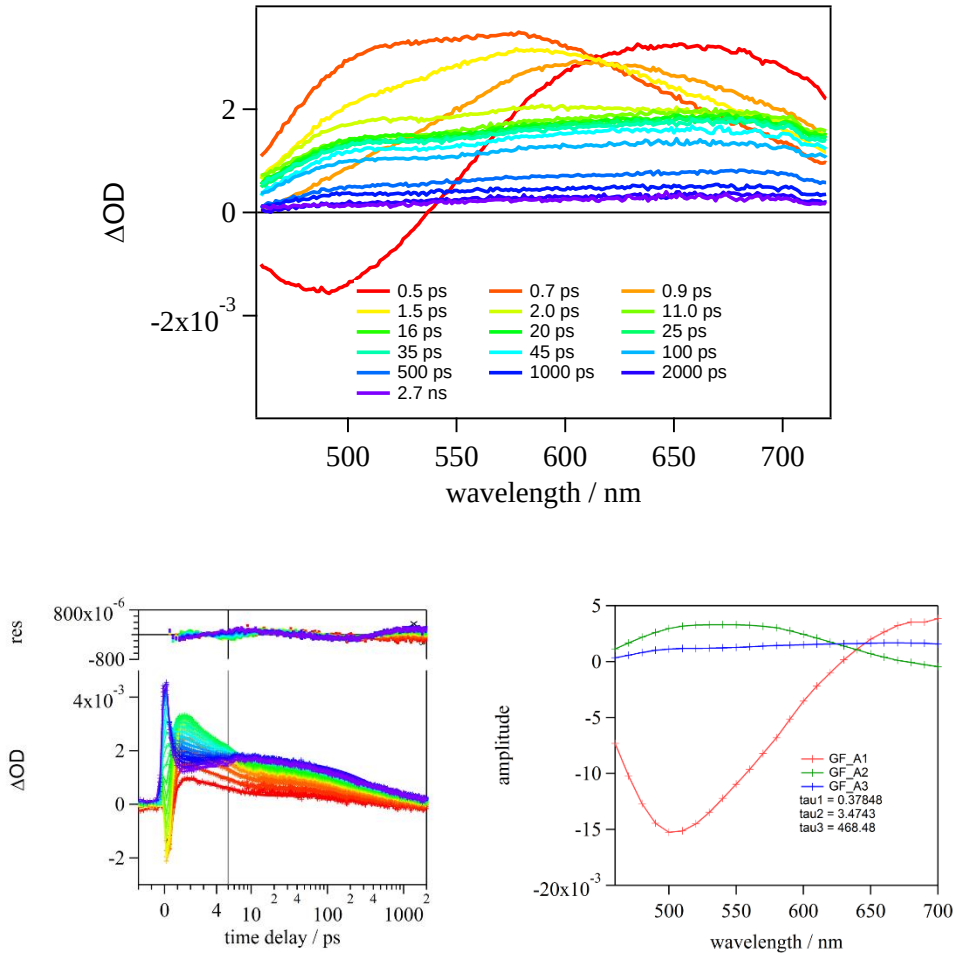

Figure 6.18 - Top: TA spectra measured at various time delays (inset) after excitation (330 nm) for **L2**$^-$ in the presence of excess Gd^{3+}. Bottom: Results of global fitting the observed TA data across all wavelengths for **L**$^-$ in the presence of excess Gd^{3+} in acetonitrile solution.

Lastly, the TA spectrum of **L2**$^-$ was investigated in the presence of Eu^{3+} ions. The spectra reveal an initial broad structureless TA signal across the entire spectral window from 460 nm to 720 nm, which decays rapidly in intensity, yielding a longer lived signal which does not fully decay over the time window investigated. Applying an identical triple exponential model, we obtain decay constants of τ_1 = 0.4 ps, τ_2 = 7.9 ps, and τ_3 = 593.3 ps which we attribute to $S_2 \longrightarrow S_n$ excited state absorption, followed by rapid internal conversion to give the $S_1 \longrightarrow S_n$ absorbing state, which undergoes ISC to form the longer lived $T_1 \longrightarrow T_n$ state with a 593.3 ps lifetime.

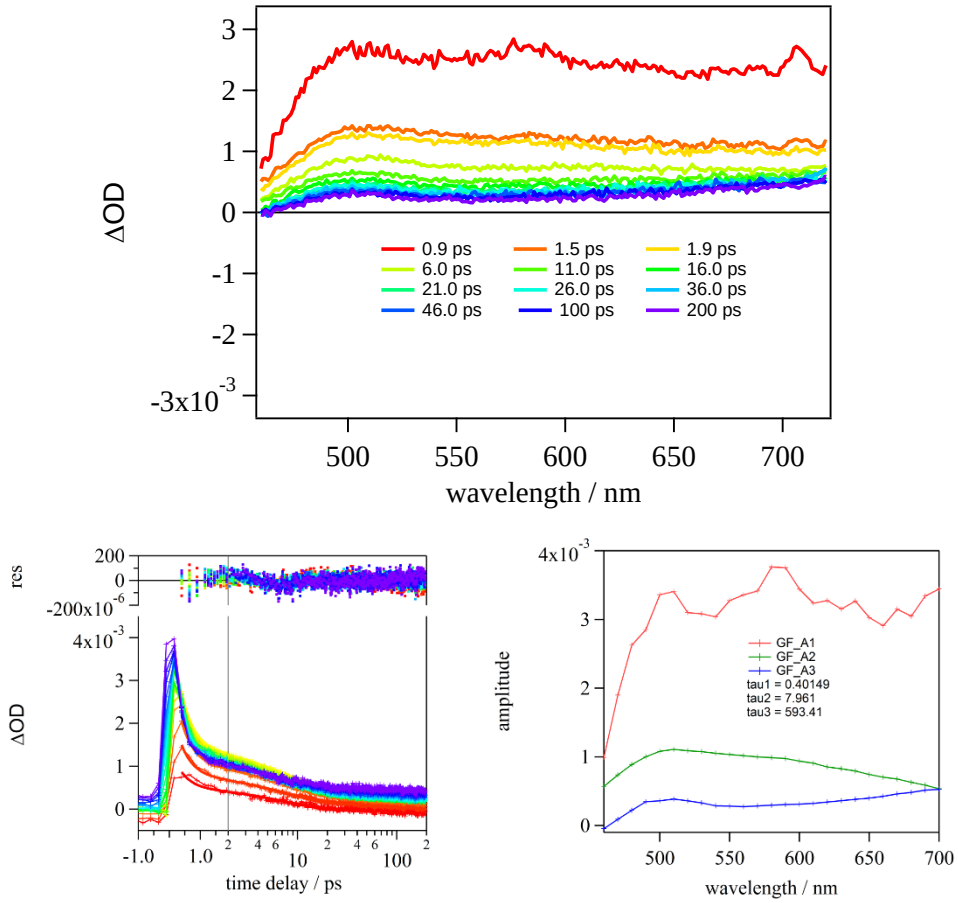

Figure 6.19 – Top: TA spectra measured at various time delays (inset) after excitation (330 nm) for **L2**$^{-}$ in the presence of excess Eu^{3+}. Bottom: Results of global fitting the observed TA data across all wavelengths for **L**$^{-}$ in the presence of excess Eu^{3+} in acetonitrile solution

A comparison with the Gd^{3+} complex reveals that the evaluated S_2 and S_1 excited state lifetimes are quite similar. For the excited T_1 state, however, the lifetime is in fact slightly longer lived for the Eu^{3+} complex, which is opposite to what we would have expected, given the T_1 state is typically recognised as an energy donor for sensitised Eu^{3+} emission. Given the similarity of the evaluated lifetimes for the Ln^{3+} complexes, in comparison to the **L2**$^{-}$ ligand, it would appear that non-radiative deactivation is a competitive deactivation pathway for the excited T_1 level, which is in agreement with the poor sensitisation properties observed for $[Eu(Phen)(\mathbf{L2})_3]_n$ complexes in acetonitrile solution.

6.6 Conclusion

The nitrile-functionalised β-diketone molecule, **L2**H, has been synthesised and used as a ligand for lanthanoid complexation. The reaction of the **L2**H molecule, Phen, and hydrated $EuCl_3$ resulted in the crystallisation of a coordination polymer of the formulation, $[Eu(Phen)(\mathbf{L2})_3]_n$. The $\mathbf{L2}^-$ ligand is characterised by an emission spectrum at 77 K attributed to the singlet state, and only a very weak component from the triplet state which suggests that the triplet state is either weakly populated or deactivated non-radiatively. In the solid state, the polymer exhibits characteristic red emission from the Eu^{3+} ion, originating as a consequence of the antenna effect.

Dissolution of the polymer in acetonitrile resulted in the formation of a species which has properties consistent with the mononuclear complex $[Eu(Phen)(\mathbf{L2})_3]$. This solution phase complex exhibits some interesting photophysical properties. The low efficiency of sensitisation from the ligand to Eu^{3+} prompted an investigation into the ultrafast processes occurring in the ligand.

Transient absorption analysis of the ligand in the presence of Ln^{3+} ions suggests that the α-CN substituted β-diketonate may not be an efficient sensitiser of Eu^{3+} emission due to efficient deactivation of its short-lived triplet state.

7 Future Directions and Conclusion

This thesis has given an account of the initial steps into the field of lanthanoid β-triketonate chemistry and photophysics, with 23 new crystal structures of this type of assembly. However, the investigation presented in this thesis has solely focussed on the tribenzoylmethanide ligand (**L1**$^-$). Given the depth of work in lanthanoid β-diketonates, it is clear that further investigation into differently functionalised β-triketonates has great potential.

The logical progression for this field of work is the extension of the β-triketonate class of ligand to a variety of functionalised ligands, which might possibly alter the resulting lanthanoid structures from the discrete lanthanoid tetranuclear assemblies reported in this work and/or directly impact their photophysical properties.

What follows are the preliminary results into the synthesis of *para* methoxy-substituted β-triketones (Figure 7.1), for a potential impact on the structural and photophysical properties of lanthanoid complexes.

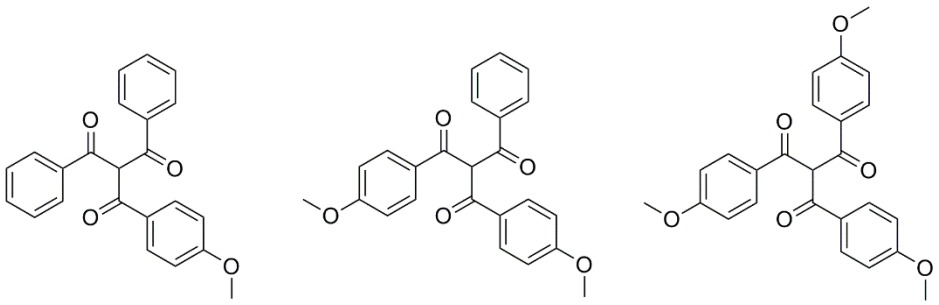

Figure 7.1 – Target molecules for the initial extension of β-triketone ligands.

7.1 Methoxy-Substituted β-Triketones

An initial aim to extend the β-triketonate ligands was the targeted synthesis of mono-, bis-, and tris-substituted β-triketones in the *para* position with a methoxy substituent.

The methoxy substituent might provide an element of steric hindrance in the formation of the discrete tetranuclear assemblies, but may also change the solubility favouring the crystallisation of different structures. A change in the *para* substituent might also affect the efficacy of the antenna effect by means of molar absorptivity and/or a change in the energy of the triplet state.

The synthesis of methoxy substituted β-triketones was achieved by the reaction of a methoxy substituted β-diketone with an acid chloride and NaH. This crossed Claisen condensation reaction is similar to that described for the synthesis of **L1**H using THF as the solvent in lieu of diethyl ether for solubility purposes. The reaction schemes are presented in Figure 7.2. Given that the β-diketonate precursor is the nucleophile in the Claisen condensation reaction; the β-diketonate was always the carrier of the methoxy substituent in the reaction.

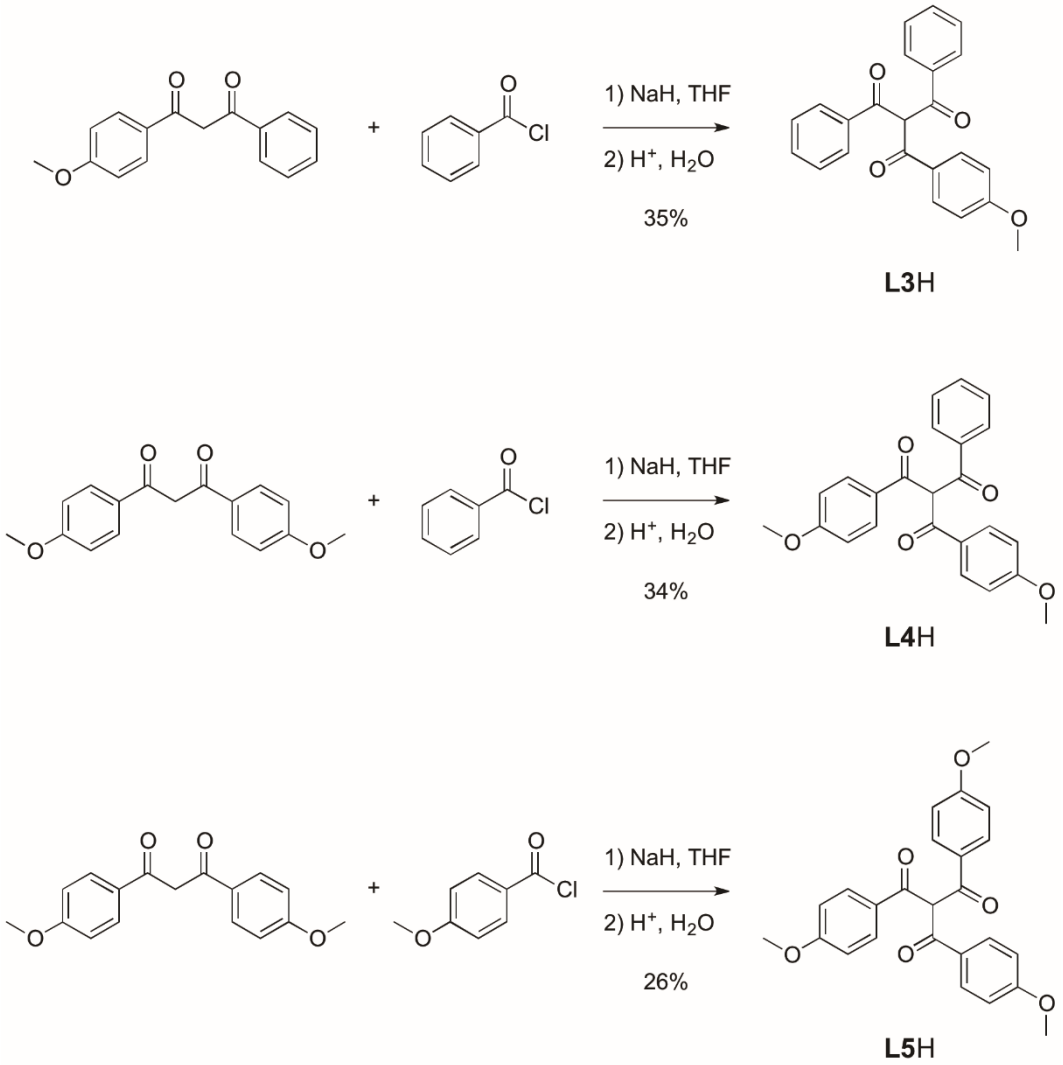

Figure 7.2 – Reaction schemes for the synthesis of mono-, bis-, and tris-substituted methoxy β-triketones.

Initial characterisation of the **L3**H, **L4**H, and **L5**H molecules by ^{1}H NMR spectroscopy in $CDCl_3$, reveals the expected changes in symmetry as the β-triketone is sequentially substituted (Figure 7.3). Each ^{1}H NMR spectrum reveals a singlet at 3.80 ppm attributed to the methoxy CH_3 protons, with a relative integration of 3, 6, and 9 for **L3**H, **L4**H, and **L5**H, respectively. The proton situated at the α-C position shifts slightly upfield as the substitution progresses, from 7.15 ppm for the mono-substituted β-triketone to 6.90 ppm for **L5**H. The shift suggests a progressive shielding effect on the proton due to the electron donating nature of the methoxy

substituent. Furthermore, the presence of this singlet provides evidence that in the $CDCl_3$ solvent, the keto tautomer is the major species present.

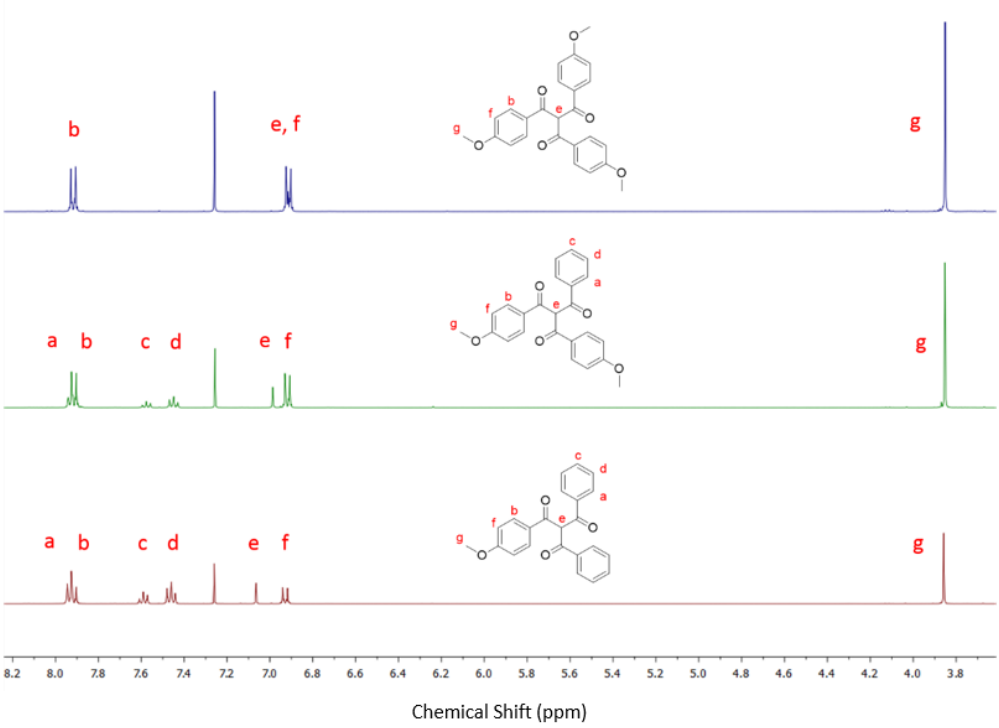

Figure 7.3 – A portion of the ^{1}H NMR spectra of **L3**H, **L4**H, and **L5**H.

The peaks labelled a, c, and d referring to the unsubstituted phenyl protons steadily decrease in integration from **L3**H through to the peaks being absent in **L5**H. Similarly, the peaks b and f, corresponding to the protons on the substituted phenyl ring, steadily increase in integration from **L3**H to **L5**H.

7.2 Triplet State Analysis

As an initial comparison to the **L1**$^-$ ligand, the triplet state of **L3**$^-$, **L4**$^-$, and **L5**$^-$ was investigated to examine the effect of ligand substitution on the relative excited state energies.

After dissolution in ethanol with excess triethylamine and Gd^{3+} at 77 K, each ligand exhibited characteristic broad ligand-centred emission (Figure 7.4). The $^{1}\pi\pi^{*}$ and $^{3}\pi\pi^{*}$ energies can be estimated at the 0-phonon transition in each spectra and are reported in Table 7.1.

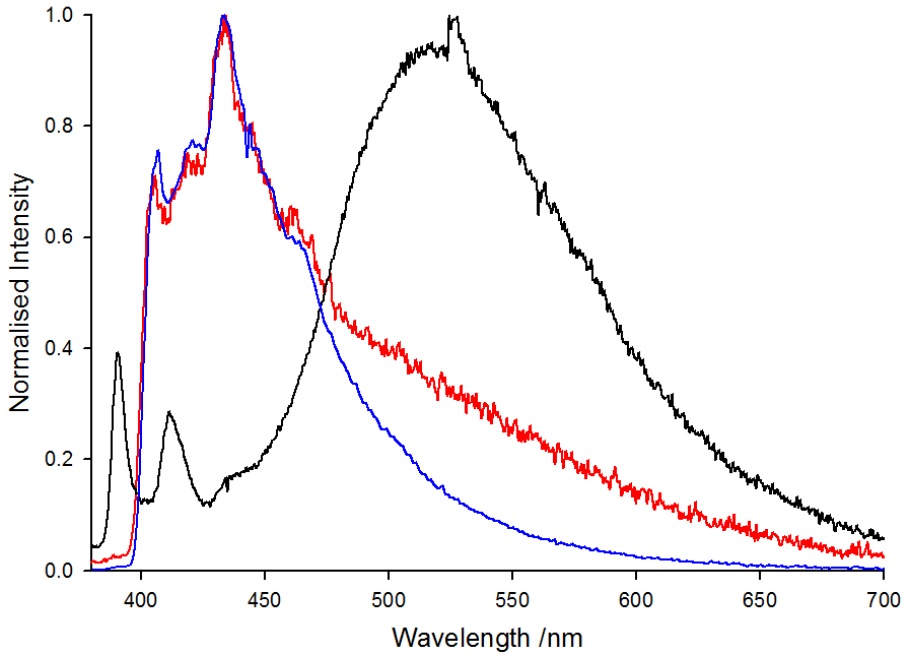

Figure 7.4 – Emission of the substituted methoxy β-triketonates in presence of excess triethylamine and Gd^{3+} at 77 K. **L2**$^{-}$ (red trace), **L3**$^{-}$ (blue trace), and **L5**$^{-}$ (black trace).

Table 7.1 – Summary of estimated excited state energies of the **L3**$^{-}$, **L4**$^{-}$, and **L5**$^{-}$ ligands.

/cm^{-1}	**L3**$^{-}$	**L4**$^{-}$	**L5**$^{-}$
$^{1}\pi\pi^{*}$	~24,570	~24,570	~25,316
$^{3}\pi\pi^{*}$	~20,700	~20,700	~20,700

In comparison to the **L1**$^{-}$ ligand, the triplet state energy is relatively similar for each of the substituted β-triketonates, however the 0-phonon transition appears to deviate for the singlet state. The **L3**$^{-}$ and **L4**$^{-}$ molecules have a singlet state energy which is red-shifted in comparison to the **L5**$^{-}$ and **L1**$^{-}$ ligands. In fact, when the emission spectra for the **L5**$^{-}$ and **L1**$^{-}$ ligands are overlaid, the 0-phonon transitions

appear to be estimated as very similar values (Figure 7.5). The red-shift in the $^{1}\pi\pi^{*}$ emission spectra of the **L3**$^{-}$ and **L4**$^{-}$ ligands may be due to an uneven electron donation in the molecule due to the asymmetric nature of its substitution. The similarity between the position of emission spectra in the **L5**$^{-}$ and **L1**$^{-}$ ligands could be due to the symmetric nature of the ligands.

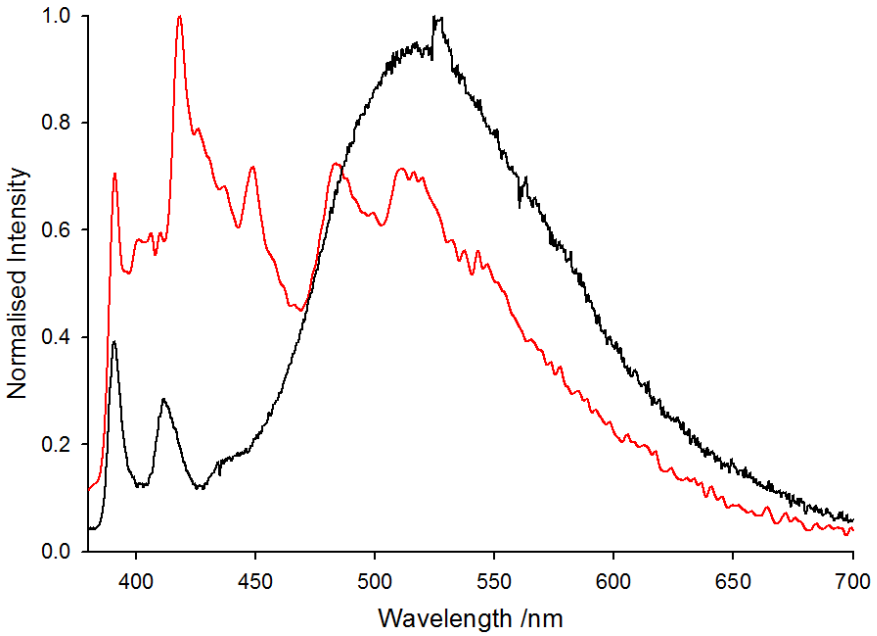

Figure 7.5 – Emission spectra of the **L1**$^{-}$ ligand (red trace) and **L5**$^{-}$ ligand (black trace) at 77 K in the presence of excess triethylamine and Gd^{3+}.

There is a noticeable difference in the emission spectra of **L5**$^{-}$ and **L1**$^{-}$ which is the relative intensities of the $^{1}\pi\pi^{*}$ emissions. The reduced intensity of this emission in **L5**$^{-}$ might hint that the ISC mechanism is much more efficient after tris-substitution.

These initial findings indicate that substitution of the β-triketone molecule may affect more than just the lanthanoid complexation. The extension to substituted β-triketones may also result in an improved antenna effect for lanthanoid sensitisation in comparison to the studied **L1**$^{-}$ ligand. This initial investigation into these substituted system gives an insight into the inherent differences in the *para* substituted β-triketonates, with many more lanthanoid structures to be discovered

as well as the extension to the synthesis of a library of substituted β-triketonate ligands.

7.3 Conclusion

Prior to the work presented in this thesis, there was a surprising lack of interest in lanthanoid β-triketonate chemistry. Whilst the depth of knowledge in lanthanoid β-diketonate chemistry grew, and continues to grow, the simple extension to β-triketonates has been seemingly overlooked.

The work in this thesis has provided a fundamental step forward in the study of lanthanoid β-triketonate chemistry. Indeed, the first structural characterisation of a metal complex bearing a β-triketonate ligand has been performed, with a total of 23 such structures determined. These studies have shown that the β-triketonate is a bis-chelating ligand, binding in a similar way to the β-diketonate, but which can also coordinate to metals using the third keto arm lying at the "back" of the molecule.

This unique coordinating mode was observed in a matrix of neutral discrete Ln^{3+}/Ae^{+} tetranuclear assemblies, where $Ln^{3+} = Eu^{3+}$, Gd^{3+}, Tb^{3+}, Dy^{3+}, Ho^{3+}, Er^{3+}, Yb^{3+}; and $Ae^{+} = Na^{+}$, K^{+}, Rb^{+}, of general formula $[Ln(Ae{\cdot}HOEt)(\mathbf{L1})_4]_2$. Thus the tetranuclear core is robust to varying size of lanthanoid and alkali metal, and can be synthesised also from BuOH rather than EtOH to crystallise an assembly of the same metal core, $[Eu(K{\cdot}HOBu)(\mathbf{L1})_4]_2$.

From a photophysical perspective, the tetranuclear assembly is intriguing, as the structure is electrically neutral with a lanthanoid coordination sphere devoid of solvent. Furthermore, the β-triketonate molecule has a low frequency CC vibration in comparison to the β-diketonate α-CH oscillator. Thus, all of the above aspects suggested that quenching of lanthanoid excited states would be minimised greatly in this type of structure. In fact, besides the phenyl CH vibrations, the lanthanoid is in an environment protected heavily from multiphonon relaxation pathways.

Curiously, the tetranuclear assemblies crystallised in four different crystal packings, which caused the lanthanoid coordination sphere to vary between a

square antiprism and a triangular dodecahedron. This progression also had a profound effect on solid state emission spectra.

The tetranuclear assemblies exhibit bright visible or NIR emission in the solid state, with the excited state lifetimes for the Yb^{3+} and Er^{3+} species being among the longest-lived for these species with β-diketonate-type ligands in the solid state. This is most likely an effect of the removal of the α-proton in the β-triketonate. The emission from Eu^{3+} species on the other hand revealed lifetimes similar to the β-diketonate class. Structured emission bands in the Eu complexes could be related to the calculated coordination geometries in each assembly.

The remarkable emission of the $\{Yb_2K_2\}^{II/III}$ assembly was applied to the fabrication of a NIR-OLED using the assembly in the EML. The assembly was deposited by sublimation under reduced pressure, and indeed the NIR-OLED revealed an Yb^{3+} metal-centred emission, with an overall device performance which is among the best reported for NIR-OLEDs where Ln^{3+} have been used in the EML. This is a remarkable result for the lanthanoid β-triketonate class of ligand, and indicates that the β-triketone molecule is a useful alternative to the classic β-diketone.

Although the device worked well, the structure in the emission band is significantly different to the solid state precursor, and thus it is believed that the assembly is not preserved in device fabrication. Thermal analysis of the solid state precursor identified that this might be the case, and therefore a cleaner method of deposition may be needed to ensure that the tetranuclear assembly is maintained as the emissive species.

As an alternative to thermal sublimation, lanthanoid complexes can be deposited in the fabrication of OLEDs by spin coating from solution. The solubility and stability of the assemblies were tested *via* dissolution in ethanol. The emission spectra and excited state lifetimes at variable temperatures presented results which were not at all consistent with the solid state precursor, and after an experiment in deuterated solvent, it was estimated that ~3 molecules of alcohol coordinate to the metal centre after dissolution. This confirmed that the tetranuclear assembly did not persist in solution.

The extension of β-triketonates to an α-substituted β-diketonate with a –CN functionality resulted in the crystallisation of a mono-dimensional coordination polymer. Although the excited state lifetime in the solid state of the polymer species was very long-lived, it was determined by a quantum yield measurement of the species in solution, that the ligand might be an inefficient sensitiser of lanthanoid emission. Transient absorption (TA) spectroscopy was used to identify the ultrafast processes occurring in the ligand, and after complexation of the **L2**$^{-}$ with lanthanoids it was determined that the ligand triplet state is likely very short lived or the ISC pathway is not efficient.

In the previous chapter, possible elaborations of the β-triketonate structure were highlighted, with a focus on how changing substituents will change the ligand electronic properties, and how such substitution might affect the lanthanoid structures crystallised. Furthermore, β-triketone variations could be extended to perfluorination and/or deuteration strategies for further enhanced photophysical aspects.

The tetranuclear assemblies described here proved the ability for the β-triketonate ligands to support cluster formation. In this work, only the alkali metals have been introduced into the crystallised structures, however there is still the possibility for new multimetallic complexes, assemblies, or coordination polymers to be isolated. Extending the metals to be incorporated to alkaline earths, and particularly *d*-metals, will extend the potential range of useful photophysical and magnetic properties. These options, combined with the ready functionalisation of the ligands, indicate that there is extensive lanthanoid β-triketonate chemistry remaining to be explored, building on the foundations reported in this thesis.

8 Experimental Section

The experimental procedures reported herein, were performed by the author, unless stated otherwise.

8.1 General Procedures

All reagents and solvents were purchased from chemical suppliers and used as received without further purification. 2-Benzoylacetonitrile was prepared according to a previously published procedure.[253] 1,3-Bis(4-methoxyphenyl)-1,3-propandione[163] and 1-(4-methoxypheny)-3-phenyl-1,3-propandione[254] were each synthesised according to literature methods. Hydrated $LnCl_3$ was prepared by the reaction of Ln_2O_3 with hydrochloric acid (5 M), followed by evaporation of the solvent under reduced pressure.[255]

Nuclear magnetic resonance (NMR) spectra were recorded using a Bruker Avance 400 spectrometer (400.1 MHz for ^1H; 100 MHz for ^{13}C) at 300 K. The data were acquired and processed by the Bruker TopSpin 3.1 software. All of the NMR spectra were calibrated to residual solvent signals. Where necessary, the assignment of the individual peaks was confirmed by 2D COSY, HSQC and HMBC experiments.

Infrared spectra (IR) were recorded on solid state samples using an attenuated total reflectance (ATR) Perkin Elmer Spectrum 100 FT-IR. IR spectra were

recorded from 4000 to 650 cm^{-1}; the intensities of the IR bands are reported as strong (s), medium (m), or weak (w), with broad (br) bands also specified. Melting points (m.p.) were determined using a BI Barnsted Electrothermal 9100 apparatus. Thermogravimetric Analysis (TGA) was recorded using a TA Instruments SDT 2960 under N_2 atmosphere. Elemental analyses were obtained at either the Université de Montreal (Canada), Curtin University (Australia), or the University of Tasmania (Australia).

Photos of the Eu^{3+} red emissions were captured using a Nikon D300 equipped with an aperture of f/9, and an OG550 EOS barrier filter. NIR emissions of Yb^{3+} species were captured using a Canon 40D with its infrared filter removed to allow wavelengths above 700 nm to be detected by the photodevice. The camera was equipped with a RM90 barrier filter, with an exposure time of five seconds.

Prof. Simon W. Lewis and Mr. Reece D. Crocker are acknowledged for help with the capture of visible and NIR photos.

8.2 Photophysical Measurements

Absorption spectra were recorded at room temperature using a Perkin Elmer Lambda 35 UV/Vis spectrometer. Uncorrected steady state emission and excitation spectra were recorded using an Edinburgh FLSP980-stm spectrometer equipped with a 450 W xenon arc lamp, double excitation and emission monochromators, a Peltier cooled Hamamatsu R928P photomultiplier tube (185–850 nm) and a Hamamatsu R5509-42 photomultiplier for detection of NIR radiation (spectral range 800-1400 nm). Emission and excitation spectra were corrected for source intensity (lamp and grating) and emission spectral response (detector and grating) by a calibration curve supplied with the instrument.

Excited state decays (τ) were recorded on the same Edinburgh FLSP980-stm spectrometer using a microsecond flashlamp. The goodness of fit was assessed by minimising the reduced goodness of fit (χ^2) function and by visual inspection of the weighted residuals.

To record the luminescence spectra at 77 K, the samples were put in quartz tubes (2 mm diameter) and inserted in a special quartz Dewar filled with liquid nitrogen. All the solvents used in the preparation of the solutions for the photophysical investigations were of spectrometric grade.

According to the approach described by Demas and Crosby,[126] the luminescence quantum yield was measured in optically dilute solutions (OD < 0.1 at excitation wavelength) obtained from absorption spectra on a wavelength scale [nm] and compared to the reference emitter by Eqn 8.1:

$$\Phi_x = \Phi_r \times \frac{A_r(\lambda_r)}{A_x(\lambda_x)} \times \frac{I_r(\lambda_r)}{I_x(\lambda_x)} \times \frac{n_x^2}{n_r^2} \times \frac{D_x}{D_r} \qquad \text{Eqn 8.1}$$

where A is the absorbance at the excitation wavelength (λ), I is the intensity of the excitation light at the excitation wavelength (λ), n is the refractive index of the solvent, D is the integrated intensity of the luminescence and Φ is the quantum yield. The subscripts r and x refer to the reference and the sample, respectively. The quantum yield determinations were performed at identical excitation wavelength for the sample and the reference, therefore cancelling the $I_r(\lambda_r)/I_x(\lambda_x)$ term in the equation. From work in Chapter 6, the $[Eu(Phen)(\mathbf{L2})_3]_n$ dissolved in acetonitrile was measured against an air-equilibrated H_2O solution of $[Ru(Bipy)_3]Cl_2$ used as reference ($\Phi_r = 0.028$).[256] Solid state quantum yields (Φ_{Ln}^{L}) were measured with the use of an integrating sphere coated with BenFlect.

For solution measurements, each species was made to ~10^{-5} M with respect to the metal, however some samples were sparingly soluble and thus are likely to be of a lower concentration.

Solid state quantum yield and Er^{3+} excitation/emission experiments, were performed by Dr. Stefano Stagni, Dr. Joanna M. Malicka, and Dr. Massimo Cocchi, at the University of Bologna, Italy.

8.3 Transient Absorption

An amplified laser system (Spitfire ACE, Spectra Physics) was used as the excitation source, delivering *ca*. 100 fs laser pulses at 800 nm with a 1 kHz repetition rate, and transient absorption measurements were undertaken using a broad-band pump-probe transient absorption spectrometer (Helios, Ultrafast Systems). Approximately 0.1 mJ of the laser output was attenuated and focussed onto a 3 mm sapphire window to generate a white light continuum probe pulse in the visible region from 460 nm to 720 nm. The remainder of the laser fundamental was coupled to an OPA system (Topas Prime, Light Conversion) delivering fs tuneable excitation pulses at 330 nm. The pump pulse polarisation was set to magic angle with respect to the probe, and samples with an absorbance of ~0.5-0.8 in a 2 mm path length (Figure 6.16) were continuously stirred mechanically. No detectable change was observed in the UV-Visible absorption spectrum of the sample at the completion of transient absorption studies, indicating no decomposition. The IRF had a FWHM of *ca*. 200 fs, measured experimentally by a Gaussian fit to the scattered laser excitation profile. All spectra were corrected for the chirp of the probe pulses, and the resulting time traces were analysed globally using commercially available software (Igor, Version 6.1.2.1, Wavemetrics). For measurements in which excess Ln^{3+} was added; lanthanoid triflates were added to a solution of **L2**H with excess triethylamine in acetonitrile.

Transient Absorption experiments were performed in my stay of research at the University of Queensland, Australia, with the supervision and help of Dr. Evan G. Moore.

8.4 OLED Device Fabrication and Characterisation

OLEDs were fabricated by growing a sequence of thin layers on clean glass substrates precoated with a layer of indium tin oxide (ITO), 120 nm thick, with a sheet resistance of 20 Ω per square. A 2 nm-thick hole-injecting layer of MoO_x was

deposited on top of the ITO by thermal evaporation under high vacuum of 10^{-6} hPa. All remaining layers were deposited in succession by thermal evaporation under high vacuum, followed by thermal evaporation of the cathode layer consisting of 0.5 nm thick LiF and a 100 nm thick aluminium cap. The HTL (1,3-bis(*N*-carbazolyl) benzene, mCP), emitting layer and the ETL (1,3,5-tris(Nphenylbenzimidazole-2-yl)benzene, TPBi) were of 60 nm, 30 nm, 25 nm thicknesses, respectively. The EML was evaporated by co-deposition of $\{Yb_2K_2\}^{II/III}$ and mCP in 1:1 mass ratio.

The current-voltage characteristics were measured with a Keithley Source-Meter unit, model 236, under continuous operation mode, while the light output power was measured with an EG&G power meter, and EL spectra recorded with a StellarNet spectroradiometer. All measurements were carried out at RT under an argon atmosphere and were reproduced for many runs, excluding chemical reaction with oxygen or moisture.

NIR-OLED fabrication and characterisation was performed by Dr. Stefano Stagni, Dr. Joanna Malicka, and Dr. Massimo Cocchi at the University of Bologna, Italy.

8.5 Synthetic Procedures

Two drops of ethanol are added in the work-up of **L1**H, **L3**H, **L4**H, and **L5**H as a method to better solubilise the remaining impurities.

8.5.1 2-Benzoyl-1,3-diphenyl-1,3-propandione (**L1**H)

The synthesis of (**L1**H) was adapted from a procedure reported by Guthrie.[193] Dibenzoylmethane (0.5 g, 2.23 mmol) was added to a suspension of NaH (0.09 g, 2.23 mmol) in diethyl ether (10 mL) and the resulting mixture stirred at RT for three hours. Benzoyl chloride (260 μL, 2.23 mmol) was added drop wise to the mixture and left to stir at RT overnight. Ethanol (2 drops), water (2 mL), and HCl (5 M, 2 mL) were added to the mixture and the solid filtered and washed with water to

afford a white solid (620 mg, 85%). M.p. 221-223 °C (lit. 226-231);[193] elemental analysis calcd (%) for $C_{22}H_{16}O_3 \cdot 0.1\ H_2O$: C, 80.03; H, 4.95; found: C, 79.87; H, 4.86; ATR-IR: ν = 3329 w, 3065 w, 2002 w, 1979 w, 1913 w, 1819 w, 1787 w, 1667 s, 1595 s, 1581 s, 1492 w, 1448 s, 1401 w, 1324 m, 1311 w, 1285 s, 1260 m, 1194 s, 1181 s, 1158 w, 1102 w, 1077 w, 1030 w, 1000 s, 975 w, 393 w, 840 m, 763 s, 691 cm^{-1} s; ^{1}H NMR (400 MHz, DMSO-d_6): δ = 7.57 (6H, t, J = 7.2 Hz, phenyl CH), 7.68-7.72 (3H, m, phenyl CH), 8.02 (6H, d, J = 7.3 Hz, phenyl CH), and 8.11 (1H, s, CH) ppm; ^{13}C NMR (100 MHz, DMSO-d_6): δ = 65.1 (CH), 128.6 (phenyl CH), 129.0 (phenyl CH), 134.1 (phenyl C), 135.4 (phenyl CH), and 193.7 (CO) ppm.

In the ^{1}H-NMR spectrum only a trace amount of the enol tautomer of the **L1**H ligand is visible; the assignment corresponds to the keto tautomer of the ligand as drawn in Figure 3.3.

8.5.2 2-Cyano-1,3-phenyl-1,3-propandione (L2H)

Benzoylacetonitrile (330 mg, 2.27 mmol) was added to a suspension of NaH (250 mg, 10.42 mmol) in THF (10 mL) and stirred at ambient temperature for 30 minutes. Benzoyl chloride (264 µL, 2.27 mmol) was added dropwise, and the mixture was stirred at RT overnight. Ethanol (2 drops) and water (10 mL) were added, and made acidic with HCl (1 M). The mixture was extracted with ethyl acetate (10 mL), dried ($MgSO_4$), and concentrated *in vacuo*. Ethyl acetate (10 mL) and HCl (1 M, 10 mL) were added to the solid, and concentrated *in vacuo* until a solid had precipitated in the water layer. The yellow/orange solid was collected at the pump (260 mg, 46%). M.p. 129-131 °C; ATR-IR: ν = 3060 w, 2924 w, 2659 m, 2556 s, 2215 s, 1785 w, 1746 m, 1684 s, 1619 m, 1599 s, 1497 s, 1412 s, 1316 m, 1291 m, 1234 m, 1178 m, 1072 w, 1045 w, 1027 w, 999 w, 969 w, 928 w, 801 w, 776 w, 757 w, 733 w, 692 m, 682 cm^{-1} m; ^{1}H NMR (400 MHz, $CDCl_3$): δ = 7.55 (2H, m, CH), 7.66 (1H, m, CH), 8.06-8.08 (2H, d, CH) ppm.

8.5.3 2-Benzoyl-1-(4-methoxyphenyl)-3-phenyl-1,3-propandione (L3H)

1-(4-methoxyphenyl)-phenyl-1,3-propandione (0.36 g, 1.44 mmol) was added to a suspension of NaH (0.09 g, 2.23 mmol) in THF (10 mL) and the resulting mixture stirred at RT for three hours. Benzoyl chloride (200 µL, 1.72 mmol) was

added dropwise to the mixture and left to stir at RT overnight. Ethanol (2 drops), water (2 mL), and HCl (5 M, 2 mL) were added to the mixture and the solid filtered and washed with water to afford a white solid (180 mg, 35%). M.p. 185-187 °C; ATR-IR: ν = 3325 w, 3062 w, 3018 w, 2941 w, 2845 w, 1681 s, 1662 s, 1597 s, 1574 s, 1513 m, 1448 m, 1421 m, 1323 m, 1287 s, 1263 s, 1196 m, 1177 s, 1120 m, 1077 m, 1027 m, 1005 m, 937 w, 901 w, 849 m, 828 w, 814 w, 797 w, 757 m, and 685 cm^{-1} w; ^{1}H NMR (400 MHz, $CDCl_3$): δ = 6.93 (2H, d, J = 8.8 Hz, 4-methoxyphenyl CH), 7.07 (1H, s, CH), 7.46 (4H, t, J = 8.0 Hz, phenyl CH), 7.59 (2H, t, J = 8.0, phenyl CH), and 7.90-7.92 (2H, d, 4-methoxyphenyl CH), and 7.92-7.94 (4H, d, phenyl CH) ppm; ^{13}C NMR (100 MHz, $CDCl_3$): δ = 55.7 (CH_3), 66.6 (*C*H), 114.4 (4-methoxyphenyl *C*H), 128.9 (phenyl *C*H), 129.1 (phenyl *C*H), 131.4 (4-methoxyphenyl *C*H), 134.0 (phenyl *C*H), 136.0 (phenyl *C*), 164.4 ($COCH_3$), 190.6 (4-methoxybenzoyl *C*O), and 192.4 (benzoyl *C*O) ppm.

8.5.4 2-Benzoyl-1,3-bis(4-methoxyphenyl)-1,3-propandione (L4H)

1,3-bis(4-methoxyphenyl)-1,3-propandione (0.20 g, 0.70 mmol) was added to a suspension of NaH (0.06 g, 1.4 mmol) in THF (10 mL) and the resulting mixture stirred at RT for three hours. Benzoyl chloride (82 µL, 0.7 mmol) was added dropwise to the mixture and left to stir at RT overnight. Ethanol (2 drops), water (2 mL), and HCl (5 M, 2 mL) were added to the mixture and the solid filtered and washed with water to afford a white solid (90 mg, 34%). M.p. 205-206 °C; ATR-IR: ν = 3313 w, 3076 w, 3010 w, 2937 w, 2842 w, 1678 s, 1661 s, 1595 s, 1575 s, 1512 m, 1447 m, 1420 m, 1326 m, 1288 s, 1258 s, 1197 m, 1169 s, 1119 m, 1081 m, 1028 m, 1014 m, 1001 m, 944 w, 903 w, 850 m, 834 w, 812 w, 795 w, 760 m, and 693 cm^{-1} w; ^{1}H NMR (400 MHz, $CDCl_3$): δ = 6.92 (4H, d, 4-methoxyphenyl CH), 6.99 (1H, s, CH), 7.45 (2H, t, phenyl CH), 7.56 (1H, t, phenyl CH), 7.89-7.90 (4H, d, 4-methoxyphenyl CH), and 7.91-7.90 (2H, d, phenyl CH) ppm.

8.5.5 2-(4-methoxybenzoyl)-1,3-bis(4-methoxyphenyl)-1,3-propandione (L5H)

1,3-bis(4-methoxyphenyl)-1,3-propandione (0.25 g, 0.90 mmol) was added to a suspension of NaH (0.07 g, 1.8 mmol) in THF (10 mL) and the resulting mixture

stirred at RT for three hours. 4-Methoxybenzoyl chloride (135 μL, 1.0 mmol) was added drop wise to the mixture and left to stir at RT overnight. Ethanol (2 drops), water (2 mL), and HCl (5 M, 2 mL) were added to the mixture and the solid filtered and washed with water to afford a white solid (96 mg, 26%). M.p. 172-173 °C; ATR-IR: ν = 3313 w, 3076 w, 3010 w, 2937 w, 2842 w, 1678 s, 1661 s, 1595 s, 1575 s, 1512 m, 1447 m, 1420 m, 1326 m, 1288 s, 1258 s, 1197 m, 1169 s, 1119 m, 1081 m, 1028 m, 1014 m, 1001 m, 944 w, 903 w, 850 m, 834 w, 812 w, 795 w, 760 m, and 693 cm^{-1} w; ^1H NMR (400 MHz, $CDCl_3$): δ = 6.91-6.93 (6H, d, 4-methoxyphenyl CH), 6.92 (1H, s, CH), and 6.93-7.91 (6H, t, 4-methoxyphenyl CH) ppm.

8.5.6 [Ho(L1)$_3$(EtOH)(H$_2$O)]

To a mixture of **L1**H (69 mg, 0.21 mmol) and hydrated $HoCl_3$ (20 mg) in ethanol (10 mL), triethylamine (88 μL, 0.61 mmol) was added. The mixture was heated at reflux for 30 minutes. The resulting mixture was filtered and the filtrate left to stand at ambient temperature. Slow evaporation of the solvent over several days afforded yellow crystals. Characterised by single crystal X-ray diffraction.

8.5.7 [Eu(Phen)(L1)$_3$]

To a mixture of **L1**H (54 mg, 0.16 mmol), Phen (10 mg, 0.05 mmol) and hydrated $EuCl_3$ (20 mg) in ethanol (10 mL), triethylamine (23 μL, 0.16 mmol) was added and the mixture was heated at reflux for 30 minutes. The resulting mixture was hot filtered and the filtrate left to stand at ambient temperature. Slow evaporation of the solvent over several days afforded yellow crystals (20 mg, 30%).

M.p. 232-233 °C; elemental analysis calcd (%) for $C_{78}H_{53}N_2O_9Eu$·EtOH: C, 70.64; H, 4.37; found: C, 70.54; H, 4.09; ATR-IR: ν = 3058 w, 3024 w, 1642 m, 1583 s, 1537 s, 1448 m, 1428 m, 1366 s, 1310 m, 1292 m, 1275 m, 1176 w, 1154 m, 1101 w, 1072 w, 1027 w, 1013 w, 1000 w, 968 w, 920 w, 895 m, 863 w, 844 w, 823 w, 810 w, 780 w, 743 m, 729 w, 721 w, 692 m, 667 cm^{-1} w.

8.5.8 [Eu(Phen)(L2)$_3$]$_n$

To a mixture of hydrated $EuCl_3$ (20 mg), Phen (10 mg, 0.05 mmol), and **L2**H (41 mg, 0.17 mmol) in ethanol (10 mL), triethylamine (23 μL, 0.17 mmol) was added. The resulting mixture was heated at reflux for 30 minutes. The solution was hot filtered, and left to crystallise by slow evaporation of the solvent. After several days, pale yellow crystals were deposited (40 mg, 86%).

M.p. 195-196 °C; elemental analysis calcd (%) for $C_{60}H_{37}N_5O_6Eu \cdot H_2O$: C, 65.88; H, 3.59; N, 6.40; found: C, 65.59; H, 3.68; N, 6.27. ATR-IR: ν = 3661 w, 3061 w, 2988 m, 2905 w, 2197 s, 1591 s, 1558 s, 1519 m, 1471 w, 1443 w, 1361 s, 1179 w, 1075 w, 999 w, 927 w, 863 w, 842 w, 808 w, 777 w, 698 cm^{-1} w.

8.5.9 General Synthesis of $[Ln(Ae \cdot HOR)(L1)_4]_2$

To a mixture of **L1**H (68-72 mg, 0.21 mmol) and hydrated $LnCl_3$ (20 mg), an aqueous AeOH solution ($Ae^+ = Na^+$, K^+, Rb^+; 1 M, 206-218 μL, 0.21 mmol) was added. Alcoholic solvent (ROH, where R = Et, Bu; 10 ml) was added and the mixture heated at reflux for 30 minutes. The resulting mixture was hot filtered and the filtrate left to stand at RT. Slow evaporation of the solvent over several days afforded yellow crystals (10-40 mg).

$[Eu(Na \cdot HOEt)(L1)_4]_2$, $\{Eu_2Na_2\}^{I}$

M.p. 268-270 °C; elemental analysis calcd (%) for $C_{180}H_{132}Eu_2Na_2O_{26} \cdot 1.5\ H_2O$: C 70.01; H 4.41; found: C 69.68; H 4.11; ATR-IR: ν = 3647 w, 3559 w, 3058 w, 3027 w, 2976 w, 1646 m, 1596 w, 1583 s, 1542 s, 1491 m, 1448 s, 1368 s, 1311 w, 1277 w, 1270 m, 1179 w, 1150 w, 1073 w, 1053 w, 1027 w, 999 w, 975 w, 898 m, 823 w, 779 w, 746 m, 694 m, 669 cm^{-1} w.

$[Eu(K \cdot HOEt)(L1)_4]_2$, $\{Eu_2K_2\}^{IV}$

M.p. 244-246 °C; elemental analysis calcd (%) for $C_{180}H_{132}Eu_2K_2O_{26} \cdot H_2O$: C 69.49; H 4.34; found: C 69.13; H 3.93; ATR-IR: ν = 3644 w, 3568 w, 3057 w, 3024 w, 1645 m, 1610 w, 1584 s, 1543 s, 1491 m, 1448 m, 1370 s, 1311 m, 1278 m, 1180 w, 1151 m, 1073 w, 1027 w, 1013 w, 999 w, 925 w, 898 m, 823 w, 780 w, 748 m, 694 m, 669 cm^{-1} w.

[Eu(K·HOBu)(L1)$_4$]$_2$, {Eu$_2$K$_2$-BuOH}^{III}

M.p. 238-240 °C; elemental analysis calcd (%) for $C_{184}H_{140}Eu_2K_2O_{26}$: C 70.18; H 4.48; found: C, 70.43; H, 4.79; ATR-IR: ν = 3405 br w, 3057 w, 3027 w, 2959 w, 2932 w, 2870 w, 1593 m, 1546 s, 1509 s, 1476 s, 1461 m, 1441 w, 1416 m, 1282 w, 1219 w, 1180 w, 1154 w, 1060 w, 1022 w, 987 w, 940 w, 811 w, 782 w, 752 w, 719 m, 690 cm^{-1} w.

[Eu(Rb·HOEt)(L1)$_4$]$_2$, {Eu$_2$Rb$_2$}^{IV}

M.p. 247-248 °C; elemental analysis calcd (%) for $C_{180}H_{132}Eu_2Rb_2O_{26}$: C 67.86; H 4.18; found: C 67.48; H 4.07; ATR-IR: ν = 3647 w, 3567 w, 3057 w, 3025 w, 1646 m, 1584 s, 1543 s, 1488 m, 1448 m, 1369 s, 1311 m, 1276 m, 1178 w, 1152 m, 1073 w, 1027 w, 1014 w, 999 w, 975 w, 927 w, 898 m, 823 w, 780 w, 749 m, 694 m, 669 cm^{-1} w.

[Gd(K·HOEt)(L1)$_4$]$_2$, {Gd$_2$K$_2$}^{IV}

M.p. 269-270 °C. elemental analysis calcd (%) for $C_{180}H_{132}Gd_2K_2O_{26}\cdot 0.5\ H_2O$: C, 69.46; H, 4.31; found: C, 69.05; H, 4.05; ATR-IR: ν = 3642 w, 3567 w, 3057 w, 3027 w, 1645 m, 1609 w, 1583 s, 1543 s, 1491 m, 1447 m, 1368 s, 1311 m, 1277 m, 1178 w, 1150 m, 1073 w, 1027 w, 1013 w, 999 w, 928 w, 897 m, 823 w, 780 w, 745 m, 694 m, 668 cm^{-1} w.

[Gd(Rb·HOEt)(L1)$_4$]$_2$, {Gd$_2$Rb$_2$}^{IV}

M.p. 263-264 °C; elemental analysis calcd (%) for $C_{180}H_{132}Gd_2Rb_2O_{26}$: C, 67.64; H, 4.16; found: C, 67.65; H, 3.51; the elemental analysis is slightly off, possibly due to the presence of multiple solvates; ATR-IR: ν = 3650 w, 3571 w, 3057 w, 3021 w, 1645 m, 1610 w, 1584 s, 1543 s, 1491 m, 1448 m, 1369 s, 1311 m, 1278 m, 1179 w, 1151 m, 1074 w, 1027 w, 1013 w, 999 w, 925 w, 898 m, 823 w, 812 w, 780 w, 747 m, 694 m, 669 cm^{-1} w.

[Tb(Na·HOEt)(L1)$_4$]$_2$, {Tb$_2$Na$_2$}^{I}

M.p. 262-263 °C. elemental analysis calcd (%) for $C_{180}H_{132}Tb_2Na_2O_{26}$: C, 70.31; H, 4.33; found: C, 69.74; H, 4.33; elemental analysis is slightly off possibly due to the presence of multiple solvates; ATR-IR: ν = 3644 w, 3557 w, 3058 w, 3032 w, 1645 m, 1584 s, 1543 s, 1491 m, 1448 m, 1369 s, 1311 m, 1278 m, 1179 w, 1150 m, 1073 w, 1027 w, 1013 w, 999 w, 974 w, 923 w, 898 m, 823 w, 780 w, 746 m, 694 m, 669 cm^{-1} w.

[Tb(K·HOEt)(L1)$_4$]$_2$, {Tb$_2$K$_2$}^{II}

M.p. 239-241 °C; elemental analysis calcd (%) for $C_{180}H_{132}Tb_2K_2O_{26}\cdot 1.5\ H_2O$: C, 68.98; H, 4.34; found: C, 68.50; H, 3.83; the elemental analysis is slightly off, possibly due to the presence of multiple solvates; ATR-IR: ν = 3648 w, 3567 w, 3057 w, 3024 w, 1645 m, 1609 w, 1584 s, 1542 s, 1491 m, 1448 m, 1368 s, 1311 m, 1277 m, 1179 w, 1151 m, 1073 w, 1027 w, 1013 w, 999 w, 975 w, 929 w, 897 m, 823 w, 780 w, 747 m, 694 m, 669 cm^{-1} w.

[Tb(Rb·HOEt)(L1)$_4$]$_2$, {Tb$_2$Rb$_2$}^{IV}

M.p. 263-264 °C; elemental analysis calcd (%) for $C_{180}H_{132}Tb_2Rb_2O_{26}\cdot 3\ H_2O$: C, 66.44; H, 4.27; found: C, 66.13; H, 3.35; the elemental analysis is slightly off, possibly due to the presence of multiple solvates; ATR-IR: ν = 3650 w, 3575 w, 3056 w, 3024 w, 1644 m, 1609 w, 1584 s, 1544 s, 1491 m, 1447 m, 1369 s, 1311 m, 1276 m, 1179 w, 1153 m, 1073 w, 1027 w, 1013 w, 999 w, 925 w, 897 m, 824 w, 780 w, 748 m, 694 m, 669 cm^{-1} w.

[Dy(K·HOEt)(L1)$_4$]$_2$, {Dy$_2$K$_2$}$^{II/IV}$

M.p. 262-263 °C; Anal. Calcd for $C_{180}H_{132}Dy_2K_2O_{26}$: C, 69.42; H, 4.27; found: C, 69.60; H, 3.78; ATR-IR: ν = 3650 w, 3563 w, 3055 w, 3019 w, 2972 w, 1645 m, 1609 w, 1584 m, 1545 s, 1490 m, 1447 m, 1371 s, 1310 m, 1279 m, 1193 w, 1177 w, 1151 m, 1072 w, 1028 w, 1010 w, 975 w, 927 w, 898 m, 824 w, 780 w, 749 m, 694 m, 668 cm^{-1} w.

[Dy(Rb·HOEt)(L1)$_4$]$_2$, {Dy$_2$Rb$_2$}^{IV}

M.p. 267-268 °C; elemental analysis calcd (%) for $C_{180}H_{132}Dy_2Rb_2O_{26}$·0.5 H_2O: C, 67.23; H, 4.17; found: C, 66.81; H, 3.59; the elemental analysis is slightly off, possibly due to the presence of multiple solvates; ATR-IR: ν = 3653 w, 3571 w, 3057 w, 1645 m, 1611 w, 1584 s, 1545 s, 1491 m, 1447 m, 1373 s, 1311 m, 1277 m, 1178 w, 1151 m, 1073 w, 1027 w, 1013 w, 999 w, 976 w, 925 w, 898 m, 823 w, 812w, 780 w, 748 m, 694 m, 668 cm^{-1} w.

[Ho(K·HOEt)(L1)$_4$]$_2$, {Ho$_2$K$_2$}^{II}

M.p. 260-261 °C; elemental analysis calcd (%) for $C_{180}H_{132}Ho_2K_2O_{26}$: C, 69.31; H, 4.27; found: C, 69.11; H, 3.87; ATR-IR: ν = 3567 w, 3059 w, 3019 w, 2968 w, 1668 m, 1644 m, 1611 w, 1584 s, 1546 s, 1490 m, 1447 m, 1389 s, 1371 s, 1310 m, 1279 m, 1195 w, 1180 w, 1179 w, 1151 m, 1074 w, 1024 w, 1012 w, 999 w, 927 w, 898 m, 840 w, 823 w, 778 w, 749 m, 749 w, 694 m, 668 cm^{-1} w.

[Ho(Rb·HOEt)(L1)$_4$]$_2$, {Ho$_2$Rb$_2$}^{IV}

M.p. 268-270 °C; elemental analysis calcd (%) for $C_{180}H_{132}Ho_2Rb_2O_{26}$: C, 67.31; H, 4.14; found: C, 66.84; H, 3.68; ATR-IR: ν = 3660 w, 3570 w, 3056 w, 1645 m, 1612 w, 1584 s, 1548 s, 1492 m, 1447 m, 1373 s, 1311 m, 1278 m, 1179 w, 1151 m, 1073 w, 1027 w, 1013 w, 999 w, 976 w, 924 w, 897 m, 824 w, 780 w, 749 m, 695 m, 669 cm^{-1} w.

[Er(Na·HOEt)(L1)$_4$]$_2$, {Er$_2$Na$_2$}^{I}

M.p. 263-264 °C; elemental analysis calcd (%) for $C_{180}H_{132}Er_2Na_2O_{26}$·2 H_2O: C 69.13; H 4.38; found: C, 69.68; H, 3.88; ATR-IR: ν = 3652 w, 3557 w, 3058 w, 2021 w, 2979 w, 1646 m, 1612 w, 1584 s, 1547 s, 1491 m, 1447 s, 1373 s, 1311 s, 1271 m, 1150 m, 1072 w, 1052w, 1027 w, 1013 w, 998 w, 978 w, 933 w, 923 w, 899 m, 823 w, 780 w, 747 m, 694 m, 669 cm^{-1} w.

[Er(K·HOEt)(L1)$_4$]$_2$, {Er$_2$K$_2$}^{III}

M.p. 244-246 °C; elemental analysis calcd (%) for $C_{180}H_{132}Er_2K_2O_{26}·H_2O$: C, 68.81; H, 4.30. Found: C, 68.29; H, 3.82; ATR-IR: ν = 3654 w, 3573 w, 3057 w, 3022 w, 1646 m, 1615 w, 1584 s, 1546 s, 1493 m, 1449 m, 1372 s, 1315 m, 1277 m, 1183 w, 1152 m, 1074 w, 1030 w, 1017 w, 998 w, 973 w, 930 w, 898 m, 827 w, 780 w, 749 m, 698 m, 670 cm^{-1} w.

[Er(Rb·HOEt)(L1)$_4$]$_2$, {Er$_2$Rb$_2$}^{II}

M.p. 242-244 °C; elemental analysis calcd (%) for $C_{180}H_{132}Er_2Rb_2O_{26}·0.5\ H_2O$: C 67.03; H 4.16; found: C, 66.70; H, 3.73; ATR-IR: ν = 3643 w, 3057 w, 1645 m, 1615 w, 1584 s, 1546 s, 1492 m, 1448 m, 1372 s, 1311 m, 1277 m, 1182 w, 1152 m, 1073 w, 1027 w, 1014 w, 1002 w, 980 w, 925 w, 897 m, 823 w, 780 w, 749 m, 694 m, 668 cm^{-1} w.

[Yb(Na·HOEt)(L1)$_4$]$_2$, {Yb$_2$Na$_2$}^{I}

M.p. 260-262 °C; elemental analysis calcd (%) for $C_{180}H_{132}Yb_2Na_2O_{26}·3\ H_2O$: C, 68.48; H, 4.41; found: C, 68.37; H, 4.09; ATR-IR: ν = 3643 w, 3555 w, 3054 w, 2921 w, 2853 w, 1645 m, 1613 w, 1590 s, 1547 s, 1490 m, 1441 s, 1397 w, 1364 s, 1328 w, 1294 w, 1270 m, 1181 w, 1154 w, 1093 w, 1073 w, 1029 w, 998 w, 932 w, 900 m, 824 w, 783 w, 754 m, 695 m, 671 cm^{-1} w.

[Yb(K·HOEt)(L1)$_4$]$_2$, {Yb$_2$K$_2$}$^{II/III}$

M.p. 240-242 °C; elemental analysis calcd (%) for $C_{180}H_{132}Yb_2K_2O_{26}·2\ H_2O$: C, 68.17; H, 4.32; found: C, 68.13; H, 3.91; ATR-IR: ν = 3655 w, 3567 w, 3057 w, 1645 m, 1613 w, 1585 s, 1548 s, 1492 m, 1448 m, 1374 s, 1311 m, 1279 m, 1180 w, 1152 m, 1073 w, 1028 w, 1014 w, 999 w, 925 w, 898 m, 824 w, 780 w, 749 m, 694 m, 669 cm^{-1} w.

[Yb(Rb·HOEt)(L1)$_4$]$_2$, {Yb$_2$Rb$_2$}^{II}

Crystals appear as pale yellow needles; m.p. 244-245 °C; elemental analysis calcd (%) for $C_{180}H_{132}Yb_2Rb_2O_{26}$: C 66.98; H 4.12; found: C 66.80; H 3.97;

ATR-IR: ν = 3635 w, 3468 w, 3057 w, 3020 w, 1643 m, 1611 w, 1585 s, 1548 s, 1492 m, 1448 m, 1374 s, 1311 m, 1277 m, 1177 w, 1153 m, 1073 w, 1027 w, 1014 w, 999 w, 975 w, 929 w, 898 m, 824 w, 780 w, 749 m, 694 m, 669 cm^{-1} w.

8.6 X-ray Crystallography

Diffraction data for the $\{Yb_2K_2\}^{II}$ assembly were collected using a Bruker Microstar equipped with a Platinum 135 charge-coupled device (CCD) detector, a Helios optics, a kappa geometry goniometer, and a rotating anode source for Cu Kα radiation at 100(2) K. Cell refinement and data reduction were achieved using APEX2. Absorption corrections were applied using SADABS. The structure was solved by direct methods using SIR2011,[257] and refined against F^2 by full-matrix least squares using Olex2.1.4.[258]

Crystallographic data for all other structures were collected at 100(2) K on an Oxford Diffraction Gemini or Xcalibur diffractometer fitted with Mo Kα or Cu Kα radiation. Following absorption corrections and solution by direct methods, the structures were refined against F^2 with full-matrix least-squares using the program SHELXL-97 or SHELX-2014.[259]

Anisotropic displacement parameters were employed for the non-hydrogen atoms. Unless stated otherwise, all hydrogen atoms were added at calculated positions and refined by use of a riding model with isotropic displacement parameters based on those of the parent atom.

CCDC-1401028 $\{Eu_2Na_2\}^{I}$, CCDC-1401029 $\{Eu_2K_2\}^{IV}$, CCDC-1401030 $\{Eu_2K_2\text{-BuOH}\}^{III}$, CCDC-1401031 $\{Eu_2Rb_2\}^{IV}$, CCDC-1401032 [Eu(Phen)(**L1**)$_3$], CCDC-1401033 $\{Er_2Na_2\}^{I}$, CCDC-1401034 $\{Er_2K_2\}^{III}$, CCDC-1401035 $\{Er_2Rb_2\}^{II}$, CCDC-1401036 $\{Yb_2Na_2\}^{I}$, CCDC-1001908 $\{Yb_2K_2\}^{II}$, CCDC-1401037 $\{Yb_2K_2\}^{III}$, CCDC-1401038 $\{Yb_2Rb_2\}^{II}$, and CCDC-1063131 [Eu(Phen)(**L2**)]$_n$ contain supplementary crystallographic data, and can be obtained free of charge via <http://www.ccdc.cam.ac.uk/conts/retrieving.html>, or from the Cambridge Crystallographic Data Centre, 12 Union Road, Cambridge CB2 1EZ, U.K.; fax: (+44) 1223-336-033; or e-mail: <deposit@ccdc.cam.ac.uk>.

The diffraction data of the $\{Yb_2K_2\}^{II}$ assembly was collected, and structure solved by myself in a stay of research at the University of Montréal, Canada, under the supervision of Mr. Thierry Maris, and Prof. Garry S. Hanan. In my X-ray diffraction training at the University of Montréal, many of the other structures presented in this thesis were formulated. However, final data collection and structure solutions for all other structures were achieved by Prof. Brian W. Skelton, or Dr. Alexandre N. Sobolev at the University of Western Australia, Australia.

8.6.1 X-ray Crystallography Data

$[Eu(Na{\cdot}HOEt)(L1)_4]_2$, $\{Eu_2Na_2\}^{I}$

Empirical formula $C_{180}H_{132}Eu_2Na_2O_{26}$; *MW* = 3060.79. λ = 0.71073 Å. Triclinic, Space group $P\bar{1}$, (No. 2), *a* = 13.8309(3), *b* = 14.6650(3), *c* = 18.1873(4) Å, α = 104.903(2)°, β = 90.612(2)°, γ = 90.238(2)°, Volume = 3564.55(13) Å^3, *Z* = 1; ρ_c = 1.426 Mg/m^3, μ = 0.955 mm^{-1}, crystal size 0.21 x 0.14 x 0.05 mm^3; $\theta_{min,\ max}$ = 3.58, 32.71°. Reflections collected = 51951, unique reflections = 23685 [*R*(int) = 0.0519]. Max. and min. transmission = 1.00/0.947. Number of parameters = 946, S = 1.005. Final *R* indices [$I>2\sigma(I)$] *R*1 = 0.0490, *wR*2 = 0.1003; *R* indices (all data) *R*1 = 0.0675, *wR*2 = 0.1084. Largest diff. peak and hole = 4.845 and -1.972 e. Å^{-3}.

$[Eu(K{\cdot}HOEt)(L1)_4]_2{\cdot}2$ EtOH, $\{Eu_2K_2\}^{IV}$

Empirical formula $C_{184}H_{144}Eu_2K_2O_{28}$; *MW* = 3185.10. λ = 1.54178 Å. Triclinic, Space group $P\bar{1}$, *a* = 13.9581(4), *b* = 14.8305(5), *c* = 19.6602(7) Å, α = 80.186(3)°, β = 72.466(3)°, γ = 90.124(3)°, Volume = 3817.7(2) Å^3, *Z* = 1; ρ_c = 1.385 Mg/m^3, μ = 6.914 mm^{-1}, crystal size 0.275 x 0.105 x 0.05 mm^3; $\theta_{min,\ max}$ = 2.40, 67.31°. Reflections collected = 36759, unique reflections = 13559 [*R*(int) = 0.0594]. Max. and min. transmission = 0.718 and 0.247. Number of parameters = 1069, S = 1.038. Final *R* indices [$I>2\sigma(I)$] *R*1 = 0.0542, *wR*2 = 0.1403; *R* indices (all data) *R*1 = 0.0621, *wR*2 = 0.1482. Largest diff. peak and hole = 2.414 and -0.905 e. Å^{-3}. One phenyl ring, and both the coordinated and uncoordinated ethanol solvent molecules were modelled as being disordered over two sets of sites with occupancies constrained to 0.5 after trail refinement.

[Eu(K·HOBu)(L1)$_4$]$_2$·2 H$_2$O BuOH, {Eu$_2$K$_2$-BuOH}^{III}

Empirical formula $C_{188}H_{154}Eu_2K_2O_{29}$; *MW* = 3259.22. λ = 0.71073 Å. Triclinic, Space group $P\bar{1}$, *a* = 14.5832(5), *b* = 16.4263(5), *c* = 18.3874(7) Å, α = 63.817(3)°, β = 89.549(3)°, γ = 82.095(3)°, Volume = 3908.2(3) Å^3, *Z* = 1; ρ_c = 1.385 Mg/m^3, μ = 0.924 mm^{-1}, crystal size 0.47 x 0.39 x 0.13 mm^3; $\theta_{min,\ max}$ = 2.08, 30.00°. Reflections collected = 59227, unique reflections = 22751 [*R*(int) = 0.0442]. Max. and min. transmission = 0.900 and 0.735. Number of parameters = 1075, S = 1.040. Final *R* indices [*I*>2σ(*I*)] *R*1 = 0.0433, *wR*2 = 0.1016; *R* indices (all data) *R*1 = 0.0584, *wR*2 = 0.1093. Largest diff. peak and hole = 2.148 and -1.008 e. Å^{-3}. Two phenyl rings were modelled as being disordered over two sets of sites with occupancies refined to 0.732(6) and its complement. The atoms of the minor components were refined with isotropic displacement parameters. The solvent was modelled as a BuOH disordered about an inversion centre and a water molecule on general positions.

[Eu(Rb·HOEt)(L1)$_4$]$_2$·2 EtOH, {Eu$_2$Rb$_2$}^{IV}

Empirical formula $C_{184}H_{144}Eu_2O_{28}Rb_2$; *MW* = 3277.84. λ = 0.71073 Å. Triclinic, Space group $P\bar{1}$, *a* = 14.0028(3), *b* = 14.7844(3), *c* = 19.7354(4) Å, α = 80.113(2)°, β = 72.448(2)°, γ = 90.143(2)°, Volume = 3831.20(14) Å^3, *Z* = 1; ρ_c = 1.421 Mg/m^3, μ = 1.517 mm^{-1}, crystal size 0.29 x 0.26 x 0.19 mm^3; $\theta_{min,\ max}$ = 2.39, 32.15°. Reflections collected = 82925, unique reflections = 25128 [*R*(int) = 0.0411]. Max. and min. transmission = 0.801 and 0.744. Number of parameters = 1087, S = 1.038. Final *R* indices [*I*>2σ(*I*)] *R*1 = 0.0343, *wR*2 = 0.0677; *R* indices (all data) *R*1 = 0.0451, *wR*2 = 0.0718. Largest diff. peak and hole = 0.932 and -0.552 e. Å^{-3}.

[Eu(Phen)(L1)$_3$]

Empirical formula $C_{78}H_{53}EuN_2O_9$; *MW* = 1314.18. λ = 0.71073 Å. Triclinic, Space group $P\bar{1}$, *a* = 10.5972(3), *b* = 13.5765(3), *c* = 21.3722(5) Å, α = 93.095(2)°, β = 102.252(2)°, γ = 95.526(2)°, Volume = 2982.11(13) Å^3, *Z* = 2; ρ_c = 1.464 Mg/m^3, μ = 1.117 mm^{-1}, crystal size 0.35 x 0.12 x 0.12 mm^3; $\theta_{min,\ max}$ = 2.35, 32.73°. Reflections collected = 64852, unique reflections = 20096 [*R*(int) = 0.0355]. Max.

and min. transmission = 0.892 and 0.768. Number of parameters = 811, S = 1.044. Final *R* indices [$I>2\sigma(I)$] *R*1 = 0.0287, *wR*2 = 0.0605; *R* indices (all data) *R*1 = 0.0356, *wR*2 = 0.0633. Largest diff. peak and hole = 0.874 and -0.516 e. Å^{-3}.

[Eu(Phen)(L2)$_3$]$_n$·0.5 H$_2$O

Empirical formula $C_{60}H_{39}EuN_5O_{6.50}$; *MW* = 1085.92. Triclinic, Space group $P\bar{1}$, *a* = 8.9578(3), *b* = 10.2101(4), *c* = 28.0127(10) Å, α = 91.280(3)°, β = 97.177(3)°, γ = 98.179(3)°, Volume = 2514.01(16) Å^3, *Z* = 2; ρ_c = 1.435 Mg/m^3, μ = 1.307 mm^{-1}, crystal size 0.34 x 0.16 x 0.07 mm^3; $\theta_{min,\ max}$ = 2.02, 27.50°. Reflections collected = 25976, unique reflections = 11531 [*R*(int) = 0.0521]. Max. and min. transmission = 0.910 and 0.691. Number of parameters = 658, S = 1.238; Final R indices [$I>2\sigma(I)$] *R*1 = 0.1034, *wR*2 = 0.2707; R indices (all data) *R*1 = 0.1090, *wR*2 = 0.2738; Largest diff. peak and hole 4.122 and -6.129 e. Å^{-3}.

[Gd(K·HOEt)(L1)$_4$]$_2$·2 EtOH, {Gd$_2$K$_2$}^{IV}

Empirical formula $C_{184}H_{144}Gd_2K_2O_{28}$; *MW* = 3195.68. Triclinic, Space group $P\bar{1}$, *a* = 13.9309(3), *b* = 14.8457(3), *c* = 19.6249(5) Å, α = 80.167(2)°, β = 72.496(2)°, γ = 90.110(2)°, Volume = 3807.77(16) Å^3, *Z* = 1; ρ_c = 1.394 Mg/m^3, μ = 0.993 mm^{-1}, crystal size 0.53 x 0.29 x 0.21 mm^3; $\theta_{min,\ max}$ = 2.044, 34.000°. Reflections collected = 120523, unique reflections = 31054 [*R*(int) = 0.0428]. Max. and min. transmission = 0.842 and 0.728. Number of parameters = 1087, S = 1.061; Final R indices [$I>2\sigma(I)$] *R*1 = 0.0345, *wR*2 = 0.0791; R indices (all data) *R*1 = 0.0419, *wR*2 = 0.0824; Largest diff. peak and hole 2.032 and -1.195 e. Å^{-3}.

[Gd(Rb·HOEt)(L1)$_4$]$_2$·2 EtOH, {Gd$_2$Rb$_2$}^{IV}

Empirical formula $C_{184}H_{144}Gd_2Rb_2O_{28}$; *MW* = 3288.42. Triclinic, Space group $P\bar{1}$, *a* = 14.0074(3), *b* = 14.8085(4), *c* = 19.7192(4) Å, α = 80.083(2)°, β = 72.374(2)°, γ = 90.044(2)°, Volume = 3833.95(16) Å^3, *Z* = 1; ρ_c = 1.424 Mg/m^3, μ = 1.563 mm^{-1}, crystal size 0.31 x 0.22 x 0.16 mm^3; $\theta_{min,\ max}$ = 2.797, 31.971°. Reflections collected = 47040, unique reflections = 24546 [*R*(int) = 0.0284]. Max. and min. transmission = 0.810 and 0.696. Number of parameters = 1093, S = 1.033;

Final R indices [$I>2\sigma(I)$] $R1$ = 0.0366, $wR2$ = 0.0829; R indices (all data) $R1$ = 0.0453, $wR2$ = 0.0873; Largest diff. peak and hole 1.828 and -1.375 e. Å^{-3}.

[Tb(Na·HOEt)(L1)$_4$]$_2$, {Tb$_2$Na$_2$}^{I}

Empirical formula $C_{180}H_{132}Tb_2Na_2O_{26}$; *MW* = 3074.68. Triclinic, Space group $P\bar{1}$, *a* = 13.8911(8), *b* = 14.6303(6), *c* = 18.0785(8) Å, α = 104.868(4)°, β = 90.597(4)°, γ = 89885(4)°, Volume = 3550.9(3) Å^3, *Z* = 1; ρ_c = 1.438 Mg/m^3, μ = 5.516 mm^{-1}, crystal size 0.25 x 0.09 x 0.07 mm^3; $\theta_{min, max}$ = 3.13, 67.34°. Reflections collected = 34110, unique reflections = 12611 [*R*(int) = 0.0645]. Max. and min. transmission = 0.728 and 0.389. Number of parameters = 946, S = 1.030; Final R indices [$I>2\sigma(I)$] $R1$ = 0.0519, $wR2$ = 0.1267; R indices (all data) $R1$ = 0.0629, $wR2$ = 0.1366; Largest diff. peak and hole 2.023 and -0.963 e. Å^{-3}.

[Tb(K·HOEt)(L1)$_4$]$_2$, {Tb$_2$K$_2$}^{II}

Empirical formula $C_{180}H_{132}K_2O_{26}Tb_2$; *MW* = 3106.89. Triclinic, Space group $P\bar{1}$, *a* = 13.9716(3), *b* = 14.5463(5), *c* = 18.1001(4) Å, α = 104.116(2)°, β = 89.996(2)°, γ = 89.797(2)°, Volume = 3582.59(17) Å^3, *Z* = 1; ρ_c = 1.440 Mg/m^3, μ = 1.114 mm^{-1}, crystal size 0.420 x 0.175 x 0.088 mm^3; $\theta_{min, max}$ = 2.043, 28.000°. Reflections collected = 30660, unique reflections = 17248 [*R*(int) = 0.0308]. Max. and min. transmission = 0.911 and 0.700. Number of parameters = 946, S = 1.052; Final R indices [$I>2\sigma(I)$] $R1$ = 0.0494, $wR2$ = 0.1056; R indices (all data) $R1$ = 0.0628, $wR2$ = 0.1115; Largest diff. peak and hole 2.749 and -1.660 e. Å^{-3}.

[Tb(Rb·HOEt)(L1)$_4$]$_2$·2 EtOH, {Tb$_2$Rb$_2$}^{IV}

Empirical formula $C_{184}H_{144}Tb_2Rb_2O_{28}$; *MW* = 3243.73. Triclinic, Space group $P\bar{1}$, *a* = 13.9918(2), *b* = 14.7907(6), *c* = 19.7441(3) Å, α = 80.1700(10)°, β = 72.3190(10)°, γ = 90.0860(10)°, Volume = 3829.65(11) Å^3, *Z* = 1; ρ_c = 1.406 Mg/m^3, μ = 1.621 mm^{-1}, crystal size 0.47 x 0.44 x 0.28 mm^3; $\theta_{min, max}$ = 2.14, 41.15°. Reflections collected = 160326, unique reflections = 49625 [*R*(int) = 0.0445]. Max. and min. transmission = 0.703 and 0.526. Number of parameters = 1081, S = 1.004;

Final R indices [I>2σ(I)] R1 = 0.0355, wR2 = 0.0693; R indices (all data) R1 = 0.0502, wR2 = 0.0742; Largest diff. peak and hole 1.880 and -1.056 e. Å^{-3}.

[Dy(K·HOEt)(L1)$_4$]$_2$, {Dy$_2$K$_2$}^{II}

Empirical formula $C_{180}H_{132}Dy_2K_2O_{26}$; *MW* = 3114.06. Triclinic, Space group $P\bar{1}$, *a* = 13.9658(4), *b* = 14.5111(4), *c* = 18.0746(5) Å, α = 103.049(2)°, β = 90.026(2)°, γ = 89.566(2)°, Volume = 3568.29(17) Å^3, *Z* = 1; ρ_c = 1.449 Mg/m^3, μ = 1.174 mm^{-1}, crystal size 0.24 x 0.21 x 0.10 mm^3; $\theta_{min,\ max}$ = 2.83, 30.00°. Reflections collected = 85194, unique reflections = 20748 [R(int) = 0.0582]. Max. and min. transmission = 0.895 and 0.823. Number of parameters = 947, S = 1.157; Final R indices [I>2σ(I)] R1 = 0.0701, wR2 = 0.1635; R indices (all data) R1 = 0.0807, wR2 = 0.1681; Largest diff. peak and hole 4.190 and -1.589 e. Å^{-3}.

[Dy(K·HOEt)(L1)$_4$]$_2$·2 EtOH, {Dy$_2$K$_2$}^{IV}

Empirical formula $C_{184}H_{144}Dy_2K_2O_{28}$; *MW* = 3206.19. Triclinic, Space group $P\bar{1}$, *a* = 13.9132(5), *b* = 14.8410(8), *c* = 19.6256(8) Å, α = 80.221(4)°, β = 72.392(4)°, γ = 89.987(4)°, Volume = 3800.8(3) Å^3, *Z* = 1; ρ_c = 1.401 Mg/m^3, μ = 1.105 mm^{-1}, crystal size 0.21 x 0.11 x 0.04 mm^3; $\theta_{min,\ max}$ = 2.79, 27.00°. Reflections collected = 27980, unique reflections = 16193 [R(int) = 0.0374]. Max. and min. transmission = 0.959 and 0.764. Number of parameters = 1081, S = 0.993; Final R indices [I>2σ(I)] R1 = 0.0417, wR2 = 0.0861; R indices (all data) R1 = 0.0529, wR2 = 0.0908; Largest diff. peak and hole 0.992 and -1.054 e. Å^{-3}.

[Dy(Rb·HOEt)(L1)$_4$]$_2$·2 EtOH, {Dy$_2$Rb$_2$}^{IV}

Empirical formula $C_{184}H_{144}Dy_2Rb_2O_{28}$; *MW* = 3298.93. Triclinic, Space group $P\bar{1}$, *a* = 13.9581(3), *b* = 14.7899(3), *c* = 19.7191(3) Å, α = 80.097(2)°, β = 72.276(2)°, γ = 90.065(2)°, Volume = 3813.58(13) Å^3, *Z* = 1; ρ_c = 1.436 Mg/m^3, μ = 1.681 mm^{-1}, crystal size 0.28 x 0.19 x 0.11 mm^3; $\theta_{min,\ max}$ = 2.80, 35.94°. Reflections collected = 113525, unique reflections = 34619 [R(int) = 0.0619]. Max. and min. transmission = 0.868 and 0.722. Number of parameters = 1081, S = 1.092;

Final R indices [I>2σ(I)] R1 = 0.0537, wR2 = 0.1071; R indices (all data) R1 = 0.0703, wR2 = 0.1136; Largest diff. peak and hole 3.134 and -1.253 e. Å^{-3}.

[Ho(L1)$_3$(EtOH)(H$_2$O)]·0.5 EtOH

Empirical formula $C_{69}H_{56}HoO_{11.50}$; MW = 1234.07. Triclinic, Space group $P\bar{1}$, a = 12.7743(4), b = 13.8632(4), c = 17.0964(4) Å, α = 100.360(2)°, β = 100.374(2)°, γ = 102.132(3)°, Volume = 2836.07(14) Å^3, Z = 2; ρ_c = 1.445 Mg/m^3, μ = 1.460 mm^{-1}, crystal size 0.40 x 0.18 x 0.15 mm^3; $\theta_{min,\ max}$ = 3.01, 33.00°. Reflections collected = 78818, unique reflections = 21339 [R(int) = 0.0354]. Max. and min. transmission = 0.832 and 0.674. Number of parameters = 763, S = 1.088; Final R indices [I>2σ(I)] R1 = 0.0503, wR2 = 0.1237; R indices (all data) R1 = 0.0603, wR2 = 0.1294; Largest diff. peak and hole 4.897 and -2.881 e. Å^{-3}.

[Ho(K·HOEt)(L1)$_4$]$_2$, {Ho$_2$K$_2$}^{II}

Empirical formula $C_{180}H_{132}Ho_2K_2O_{26}$; MW = 3118.92. Triclinic, Space group $P\bar{1}$, a = 14.0116(4), b = 14.5056(3), c = 18.0275(4) Å, α = 102.746(2)°, β = 90.006(2)°, γ = 89.190(2)°, Volume = 3573.36(15) Å^3, Z = 1; ρ_c = 1.449 Mg/m^3, μ = 1.234 mm^{-1}, crystal size 0.59 x 0.43 x 0.19 mm^3; $\theta_{min,\ max}$ = 2.84, 30.00°. Reflections collected = 96102, unique reflections = 20828 [R(int) = 0.0415]. Max. and min. transmission = 0.799 and 0.588. Number of parameters = 946, S = 1.063; Final R indices [I>2σ(I)] R1 = 0.0354, wR2 = 0.0878; R indices (all data) R1 = 0.0392, wR2 = 0.0904; Largest diff. peak and hole 2.303 and -1.233 e. Å^{-3}.

[Ho(Rb·HOEt)(L1)$_4$]$_2$·2 EtOH, {Ho$_2$Rb$_2$}^{IV}

Empirical formula $C_{184}H_{144}Ho_2Rb_2O_{28}$; MW = 3303.79. Triclinic, Space group $P\bar{1}$, a = 13.9449(8), b = 14.7815(6), c = 19.7069(11) Å, α = 80.013(4)°, β = 72.296(5)°, γ = 90.008(4)°, Volume = 3805.0(3) Å^3, Z = 1; ρ_c = 1.442 Mg/m^3, μ = 1.743 mm^{-1}, crystal size 0.21 x 0.09 x 0.045 mm^3; $\theta_{min,\ max}$ = 2.14, 28.34°. Reflections collected = 28503, unique reflections = 16616 [R(int) = 0.0493]. Max. and min. transmission = 0.963 and 0.855. Number of parameters = 1021, S = 1.023;

Final R indices [$I>2\sigma(I)$] $R1$ = 0.0528, $wR2$ = 0.0811; R indices (all data) $R1$ = 0.0767, $wR2$ = 0.0891; Largest diff. peak and hole 1.027 and -0.924 e. Å^{-3}.

[Er(Na·HOEt)(L1)$_4$]$_2$, {Er$_2$Na$_2$}^{I}

Empirical formula $C_{180}H_{132}Er_2Na_2O_{26}$; *MW* = 3091.35. λ = 1.54178 Å. Triclinic, Space group $P\bar{1}$, *a* = 13.9483(4), *b* = 14.5978(5), *c* = 18.0419(4) Å, α = 104.810(2)°, β = 90.329(2)°, γ = 89.553(2)°, Volume = 3551.42(18) Å^3, *Z* = 1; ρ_c = 1.445 Mg/m^3, μ = 2.812 mm^{-1}, crystal size 0.22 x 0.15 x 0.07 mm^3; $\theta_{min,\ max}$ = 2.53, 67.26°. Reflections collected = 35217, unique reflections = 12613 [*R*(int) = 0.0352]. Max. and min. transmission = 0.829 and 0.670. Number of parameters = 951, S = 1.033. Final *R* indices [$I>2\sigma(I)$] $R1$ = 0.0363, $wR2$ = 0.0899; *R* indices (all data) $R1$ = 0.0408, $wR2$ = 0.0936. Largest diff. peak and hole = 1.639 and -0.573 e. Å^{-3}.

[Er(K·HOEt)(L1)$_4$]$_2$·2 H$_2$O EtOH, {Er$_2$K$_2$}^{III}

Empirical formula $C_{182}H_{142}Er_2K_2O_{29}$; *MW* = 3205.68. λ = 0.71073 Å. Triclinic, Space group $P\bar{1}$, *a* = 14.9371(5), *b* = 15.5737(6), *c* = 18.1585(7) Å, α = 114.504(4)°, β = 91.285(3)°, γ = 98.795(3)°, Volume = 3781.1(2) Å^3, *Z* = 1; ρ_c = 1.408 Mg/m^3, μ = 1.233 mm^{-1}, crystal size 0.46 x 0.07 x 0.04 mm^3; $\theta_{min,\ max}$ = 2.28, 30.33°. Reflections collected = 36741, unique reflections = 20185 [*R*(int) = 0.0383]. Max. and min. transmission = 0.954 and 0.745. Number of parameters = 990, S = 1.041. Final R indices [$I>2\sigma(I)$] $R1$ = 0.0427, $wR2$ = 0.0883; R indices (all data) $R1$ = 0.0544, $wR2$ = 0.0926. Largest diff. peak and hole = 1.076 and -0.653 e. Å^{-3}. The solvent molecules were modelled as an ethanol molecule disordered about a crystallographic inversion centre and a water disordered over two sites with occupancies refined to 0.67(2) and its complement.

[Er(Rb·HOEt)(L1)$_4$]$_2$, {Er$_2$Rb$_2$}^{II}

Empirical formula $C_{180}H_{132}Er_2O_{26}Rb_2$; *MW* = 3216.31. λ = 0.71073 Å. Triclinic, Space group $P\bar{1}$, *a* = 14.2006(3), *b* = 14.4538(4), *c* = 18.0067(4) Å, α = 102.245(2)°, β = 89.699(2)°, γ = 88.888(2)°, Volume = 3610.99(15) Å^3, *Z* = 1; ρ_c = 1.479 Mg/m^3, μ = 1.900 mm^{-1}, crystal size 0.31 x 0.19 x 0.06 mm^3; $\theta_{min,\ max}$ = 2.20, 29.00°.

Reflections collected = 37245, unique reflections = 19183 [*R*(int) = 0.0298]. Max. and min. transmission = 0.897 and 0.680. Number of parameters = 946, S = 1.092. Final *R* indices [$I>2\sigma(I)$] *R*1 = 0.0530, *wR*2 = 0.1226; *R* indices (all data) *R*1 = 0.0631, *wR*2 = 0.1270. Largest diff. peak and hole = 2.651 and -2.067 e. $Å^{-3}$.

$[Yb(Na{\cdot}HOEt)(L1)_4]_2$, $\{Yb_2Na_2\}^{I}$

Empirical formula $C_{180}H_{132}Na_2O_{26}Yb_2$; *MW* = 3102.91. λ = 0.71073 Å. Triclinic, Space group $P\bar{1}$. *a* = 14.0236(5), *b* = 14.5560(6), *c* = 18.0333(6) Å, α = 104.724(3)°, β = 90.128(3)°, γ = 89.234(3)°, Volume = 3559.9(2) $Å^3$, *Z* = 1; ρ_c = 1.447 Mg/m^3, μ = 1.389 mm^{-1}, crystal size 0.42 x 0.30 x 0.075 mm^3; $\theta_{min,\ max}$ = 2.749, 27.00°. Reflections collected = 58235, unique reflections = 15529 [*R*(int) = 0.0642]. Max. and min. transmission = 0.901 and 0.643. Number of parameters = 951, S = 1.109. Final *R* indices [$I>2\sigma(I)$] *R*1 = 0.0531, *wR*2 = 0.1380; *R* indices (all data) *R*1 = 0.0582, *wR*2 = 0.1415. Largest diff. peak and hole = 4.980 and -2.350 e. $Å^{-3}$.

$[Yb(K{\cdot}HOEt)(L1)_4]_2$, $\{Yb_2K_2\}^{II}$

Empirical formula $C_{180}H_{132}K_2O_{26}Yb_2$; MW = 3135.13. Triclinic, Space group $P\bar{1}$. *a* = 14.1075(12), *b* = 14.4693(12), *c* = 17.9695(14) Å, α = 102.772(4)°, β = 90.083(4)°, γ = 91.038(4)°, Volume = 3576.6(5) $Å^3$, *Z* = 1; ρ_c = 1.456 Mg/m^3, μ = 3.494 mm^{-1}, crystal size 0.286 x 0.091 x 0.078 mm^3; $\theta_{min,\ max}$ = 2.52, 70.38°. Reflections collected = 254230, unique reflections = 13465 [R(int) = 0.0685]. Max. and min. transmission = 0.753 and 0.479. Number of parameters = 950, S = 1.062; Final *R* indices [$I>2\sigma(I)$] *R*1 = 0.0589, *wR*2 = 0.1549; *R* indices (all data) *R*1 = 0.0634, *wR*2 = 0.1622; Largest diff. peak and hole 2.638 and -1.931 e. $Å^{-3}$. The hydrogen atom of the ethanol molecule (OH) was determined using residual electron density.

$[Yb(K{\cdot}HOEt)(L1)_4]_2{\cdot}2\ H_2O\ EtOH$, $\{Yb_2K_2\}^{III}$

Empirical formula $C_{182}H_{142}K_2O_{29}Yb_2$; *MW* = 3217.24. λ = 1.54178 Å. Triclinic, Space group $P\bar{1}$, *a* = 14.9691(6), *b* = 15.5713(7), *c* = 18.1646(8) Å, α = 114.386(4)°,

β = 91.488(4)°, γ = 98.946(4)°, Volume = 3790.1(3) Å^3, *Z* = 1; ρ_c = 1.410 Mg/m^3, μ = 3.326 mm^{-1}, crystal size 0.12 x 0.04 x 0.02 mm^3; $\theta_{min,\ max}$ = 3.00, 67.05°. Reflections collected = 40531, unique reflections = 13400 [*R*(int) = 0.0742]. Max. and min. transmission = 1.00 and 0.89. Number of parameters = 991, S = 1.01. Final *R* indices [*I*>2σ(*I*)] *R*1 = 0.0442, *wR*2 = 0.0925; *R* indices (all data) *R*1 = 0.0624, *wR*2 = 0.0987. Largest diff. peak and hole = 0.898 and -0.757 e. Å^{-3}. The solvent molecules were modelled as an ethanol molecule disordered about a crystallographic inversion center and a water disordered over two sites with occupancies refined to 0.69(3) and its complement.

[Yb(Rb·HOEt)(L1)$_4$]$_2$, {Yb$_2$Rb$_2$}^{II}

Empirical formula $C_{180}H_{132}O_{26}Rb_2Yb_2$; MW = 3227.87. λ = 0.71073 Å. Triclinic, Space group $P\bar{1}$, *a* = 14.2183(4), *b* = 14.4303(3), *c* = 17.9542(5) Å, α = 102.094(2)°, β = 89.682(2)°, γ = 88.527(2)°, Volume = 3600.56(16) Å^3, Z = 1; ρ_c = 1.489 Mg/m^3, μ = 2.038 mm^{-1}, crystal size 0.33 x 0.15 x 0.09 mm^3; $\theta_{min,\ max}$ = 2.84, 31.97°. Reflections collected = 77555, unique reflections = 23506 [*R*(int) = 0.0470]. Max. and min. transmission = 0.841 and 0.661. Number of parameters = 946, S = 1.064. Final *R* indices [I>2σ(I)] *R*1 = 0.0535, w*R*2 = 0.1246; *R* indices (all data) *R*1 = 0.0695, w*R*2 = 0.1331. Largest diff. peak and hole = 3.188 and -3.241 e. Å^{-3}.

8.6.2 Shape Version 2.1 Data

Shape data was attained using the Shape Version 2.1 software available from <http://www.ee.ub.es/index.php/news-ee/575-shape-available>. The coordination geometries were assessed against all eight-coordinate geometries for the tetranuclear assemblies, (nine-coordinate geometries for the [Eu(Phen)(**L2**)$_3$]$_n$ coordination polymer), and CShM plotted on a shape map against the two closest fitting geometries for each species. These were square antiprism and triangular dodecahedron (capped square antiprism and tricapped trigonal prism for the [Eu(Phen)(**L2**)$_3$]$_n$ coordination polymer).

9 References

[1] S. I. Weissman, *J. Chem. Phys.* **1942**, *10*, 214–217.

[2] N. Sabbatini, S. Perathoner, V. Balzani, B. Alpha, J.-M. Lehn, in *Supramol. Photochem.* (Ed.: V. Balzani), Springer Netherlands, Dordrecht, **1987**, pp. 187–206.

[3] J.-M. Lehn, *Angew. Chem. Int. Ed.* **1990**, *29*, 1304–1319.

[4] J.-C. G. Bünzli, S. Comby, A.-S. Chauvin, C. D. B. Vandevyver, *J. Rare Earth.* **2007**, *25*, 257–274.

[5] A. de Bettencourt-Dias, *Dalton Trans.* **2007**, 2229–2241.

[6] S. Faulkner, S. J. A. Pope, B. P. Burton-Pye, *Appl. Spectrosc. Rev.* **2005**, *40*, 1–31.

[7] J.-C. G. Bünzli, S. V. Eliseeva, *J. Rare Earth.* **2010**, *28*, 824–842.

[8] M. A. Katkova, M. N. Bochkarev, *Dalton Trans.* **2010**, *39*, 6599–6612.

[9] J.-C. G. Bünzli, *Coord. Chem. Rev.* **2015**, *293-294*, 19–47.

[10] J.-C. G. Bünzli, in *Lumin. Lanthan. Ions Coord. Compd. Nanomater.* (Ed.: A. de Bettencourt-Dias), John Wiley & Sons Ltd, Chichester, United Kingdom, **2014**, pp. 125–196.

[11] J.-C. G. Bünzli, in *Spectrosc. Prop. Rare Earths Opt. Mater.* (Eds.: R. Hull, J. Parisi, R.M. Osgood, H. Warlimont, G. Liu, B. Jacquier), Springer-Verlag, Berlin/Heidelberg, **2005**, pp. 462–499.

[12] A. J. Amoroso, S. J. A. Pope, *Chem. Soc. Rev.* **2015**, *44*, 4723–4742.

[13] J.-C. G. Bünzli, *J. Lumin.* **2015**, 1–13.

[14] B. M. van der Ende, L. Aarts, A. Meijerink, *Phys. Chem. Chem. Phys.* **2009**, *11*, 11081–11095.

[15] J.-C. G. Bünzli, A.-S. Chauvin, in *Handb. Phys. Chem. Rare Earths*, Elsevier, **2014**, pp. 169–281.

[16] J. Andres, R. D. Hersch, J.-E. Moser, A.-S. Chauvin, *Adv. Funct. Mater.* **2014**, *24*, 5029–5036.

[17] J. M. Stanley, B. J. Holliday, *Coord. Chem. Rev.* **2012**, *256*, 1520–1530.

[18] J. Feng, H. Zhang, *Chem. Soc. Rev.* **2013**, *42*, 387–410.

[19] K. Binnemans, *Chem. Rev.* **2009**, *109*, 4283–4374.

[20] B. W. Ennis, S. Muzzioli, B. L. Reid, D. M. D'Alessio, S. Stagni, D. H. Brown, M. I. Ogden, M. Massi, *Dalton Trans.* **2013**, *42*, 6894–6901.

[21] C. R. Driscoll, B. L. Reid, M. J. McIldowie, S. Muzzioli, G. L. Nealon, B. W. Skelton, S. Stagni, D. H. Brown, M. Massi, M. I. Ogden, *Chem. Commun.* **2011**, *47*, 3876–3878.

[22] S. V. Eliseeva, J.-C. G. Bünzli, *Chem. Soc. Rev.* **2010**, *39*, 189–227.

[23] J. Frangioni, *Curr. Opin. Chem. Biol.* **2003**, *7*, 626–634.

[24] S. V. Eliseeva, J.-C. G. Bünzli, *New J. Chem.* **2011**, *35*, 1165–1176.

[25] G. A. Crosby, R. E. Whan, R. M. Alire, *J. Chem. Phys.* **1961**, *34*, 743–748.

[26] G. A. Crosby, R. E. Whan, *J. Chem. Phys.* **1960**, *32*, 614–615.

[27] L. R. Melby, N. J. Rose, E. Abramson, J. C. Caris, *J. Am. Chem. Soc.* **1964**, *86*, 5117–5125.

[28] H. Bauer, J. Blanc, D. Ross, *J. Am. Chem. Soc.* **1964**, *86*, 5125–5131.

[29] K. Wang, in *Encycl. Inorg. Bioinorg. Chem.* (Ed.: R.A. Scott), John Wiley & Sons, Ltd, Chichester, UK, **2012**.

[30] K. Binnemans, in *Handb. Phys. Chem. Rare Earths* (Eds.: K.A. Gschneidner, J.-C.G. Bunzli, V.J. Pecharsky), Elsevier B.V., Amsterdam, The Netherlands, **2005**, pp. 107–272.

[31] L. G. Hubert-Pfalzgraf, N. Miele-Pajot, R. Papiernik, J. Vaissermann, *J. Chem. Soc. Dalton Trans.* **1999**, *9*, 4127–4130.

[32] P. W. Roesky, G. Canseco-Melchor, A. Zulys, *Chem. Commun.* **2004**, 738–739.

[33] P. C. Andrews, W. J. Gee, P. C. Junk, M. Massi, *New J. Chem.* **2013**, *37*, 35–

48.

[34] D. T. Thielemann, A. T. Wagner, Y. Lan, P. Oña-Burgos, I. Fernández, E. S. Rösch, D. K. Kölmel, A. K. Powell, S. Bräse, P. W. Roesky, *Chem. Eur. J.* **2015**, *21*, 2813–2820.

[35] D. T. Thielemann, A. T. Wagner, E. Rösch, D. K. Kölmel, J. G. Heck, B. Rudat, M. Neumaier, C. Feldmann, U. Schepers, S. Bräse, et al., *J. Am. Chem. Soc.* **2013**, *135*, 7454–7457.

[36] S. Cotton, *Lanthanide and Actinide Chemistry*, John Wiley & Sons, Ltd, Chichester, UK, **2006**.

[37] A. de Bettencourt-Dias, in *Lumin. Lanthan. Ions Coord. Compd. Nanomater.* (Ed.: A. de Bettencourt-Dias), John Wiley & Sons Ltd, Chichester, United Kingdom, **2014**, pp. 1–48.

[38] J. Andrez, G. Bozoklu, G. Nocton, J. Pécaut, R. Scopelliti, L. Dubois, M. Mazzanti, *Chem. Eur. J.***2015**, *21*, 15188–15200.

[39] W. J. Evans, *Coord. Chem. Rev.* **2000**, *206-207*, 263–283.

[40] I. V. Basalov, V. Dorcet, G. K. Fukin, J.-F. Carpentier, Y. Sarazin, A. A. Trifonov, *Chem. Eur. J.* **2015**, *21*, 6033–6036.

[41] G. Nocton, W. W. Lukens, C. H. Booth, S. S. Rozenel, S. A. Medling, L. Maron, R. A. Andersen, *J. Am. Chem. Soc.* **2014**, *136*, 8626–8641.

[42] V. S. Sastri, J.-C. Bünzli, V. R. Rao, G. V. S. Rayudu, J. R. Perumareddi, in *Mod. Asp. Rare Earths Their Complexes*, Elsevier, **2003**, pp. 73–125.

[43] H. B. Kagan, J. L. Namy, *Tetrahedron* **1986**, *42*, 6573–6614.

[44] Z. Dan, C. Ji, L. Deqian, *J. Rare Earth.* **2014**, *32*, 681–685.

[45] N. Kaltsoyannis, P. Scott, *The F-Elements*, Oxford University Press, Oxford, **1999**.

[46] P. Atkins, T. Overton, J. Rourke, M. Weller, F. Armstrong, *Shriver and Atkins' Inorganic Chemistry*, OUP Oxford, **2010**.

[47] J.-C. G. Bünzli, S. V Eliseeva, in *Lanthan. Lumin.* (Eds.: P. Hänninen, H. Härmä), Springer Berlin Heidelberg, Berlin, Heidelberg, **2010**, pp. 1–45.

[48] N. Sabbatini, M. Guardigli, J.-M. Lehn, *Coord. Chem. Rev.* **1993**, *123*, 201–228.

[49] J.-C. G. Bünzli, S. V. Eliseeva, in *Compr. Inorg. Chem. II* (Eds.: J. Reedijk,

K. Poeppelmeier), Elsevier, Amsterdam, Netherlands, **2013**, pp. 339–398.

[50] W. T. Carnall, *J. Chem. Phys.* **1968**, *49*, 4412–4423.

[51] W. T. Carnall, *J. Chem. Phys.* **1968**, *49*, 4450–4455.

[52] W. T. Carnall, *J. Chem. Phys.* **1968**, *49*, 4447–4449.

[53] W. T. Carnall, *J. Chem. Phys.* **1968**, *49*, 4424–4442.

[54] W. T. Carnall, *J. Chem. Phys.* **1968**, *49*, 4443–4446.

[55] W. T. Carnall, G. L. Goodman, K. Rajnak, R. S. Rana, *J. Chem. Phys.* **1989**, *90*, 3443–3457.

[56] D. L. Pavia, G. M. Lampman, G. S. Kriz, *Introduction to Spectroscopy*, Thomson Learning Inc., **2001**.

[57] M. Born, R. Oppenheimer, *Ann. Phys.* **1927**, *389*, 457–484.

[58] J. Franck, E. G. Dymond, *Trans. Faraday Soc.* **1926**, *21*, 536–542.

[59] E. Condon, *Phys. Rev.* **1926**, *28*, 1182–1201.

[60] M. Kasha, *Discuss. Faraday Soc.* **1950**, *9*, 14–19.

[61] E. N. Harvey, *A History of Luminescence from the Earliest Times until 1900*, American Philosophical Society, Philadelphia, **1957**.

[62] B. Valeur, M. N. Berberan-Santos, *J. Chem. Educ.* **2011**, *88*, 731–738.

[63] A. Jabłoński, *Nature* **1933**, *131*, 839–840.

[64] H. Kautsky, *Trans. Faraday Soc.* **1939**, *35*, 216–219.

[65] G. N. Lewis, M. Kasha, *J. Am. Chem. Soc.* **1944**, *66*, 2100–2116.

[66] W. H. Melhuish, *Pure Appl. Chem.* **1984**, *56*, 231–245.

[67] G. G. Stokes, *Phil. Trans. R. Soc. Lond.* **1852**, *142*, 463–562.

[68] G. G. Stokes, *Phil. Trans. R. Soc. Lond.* **1853**, *143*, 385–396.

[69] C. E. Schäffer, C. K. Jørgensen, *J. Inorg. Nucl. Chem.* **1958**, *8*, 143–148.

[70] R. Reisfeld, C. K. Jørgensen, in *Lasers Excit. States Rare Earths* (Eds.: M. Becke, M.F. Lappert, J.L. Margrave, R.W. Parry, C.K. Jørgensen, S.J. Lippard, K. Niedenzu, H. Yamateru), Springer-Verlag, Berlin, Heidelberg, New York, **1977**, pp. 123–156.

[71] K. Binnemans, *Coord. Chem. Rev.* **2015**, *295*, 1–45.

[72] B. R. Judd, *Phys. Rev.* **1962**, *127*, 750–761.

[73] G. S. Ofelt, *J. Chem. Phys.* **1962**, *37*, 511–520.

[74] B. M. Walsh, in *Adv. Spectrosc. Lasers Sens.* (Eds.: B. Di Bartolo, O. Forte),

Springer Netherlands, Dordrecht, **2006**, pp. 403–433.

[75] G. A. Crosby, *Mol. Cryst.* **1966**, *1*, 37–81.

[76] A. de Bettencourt-Dias, P. S. Barber, S. Viswanathan, *Coord. Chem. Rev.* **2014**, *273-274*, 165–200.

[77] G. F. de Sá, O. L. Malta, C. de Mello Donegá, A. M. Simas, R. L. Longo, P. A. Santa-Cruz, E. F. da Silva, *Coord. Chem. Rev.* **2000**, *196*, 165–195.

[78] J. P. Leonard, C. B. Nolan, F. Stomeo, T. Gunnlaugsson, in *Photochem. Photophysics Coord. Compd. II* (Eds.: V. Balzani, S. Campagna), Springer Berlin Heidelberg, Berlin, Heidelberg, **2007**, pp. 1–43.

[79] J. Lehr, P. D. Beer, S. Faulkner, J. J. Davis, *Chem. Commun.* **2014**, *50*, 5678–5687.

[80] M. Mehlstäubl, G. S. Kottas, S. Colella, L. De Cola, *Dalton Trans.* **2008**, *2*, 2385–2388.

[81] A. Baschieri, S. Muzzioli, E. Matteucci, S. Stagni, M. Massi, L. Sambri, *Dalton Trans.* **2015**, *44*, 37–40.

[82] L. J. Charbonnière, S. Faulkner, C. Platas-Iglesias, M. Regueiro-Figueroa, A. Nonat, T. Rodríguez-Blas, A. de Blas, W. S. Perry, M. Tropiano, *Dalton Trans.* **2013**, *42*, 3667–3681.

[83] W. S. Perry, S. J. A. Pope, C. Allain, B. J. Coe, A. M. Kenwright, S. Faulkner, *Dalton Trans.* **2010**, *39*, 10974–10983.

[84] T. A. Miller, J. C. Jeffery, M. D. Ward, H. Adams, S. J. A. Pope, S. Faulkner, *Dalton Trans.* **2004**, 1524–1526.

[85] S. Faulkner, D. Sykes, in *Springer Ser. Fluoresc.* (Eds.: P. Hänninen, H. Härmä), Springer-Verlag, Berlin, Heidelberg, **2010**, pp. 161–182.

[86] D. Sykes, A. J. Cankut, N. M. Ali, A. Stephenson, S. J. P. Spall, S. C. Parker, J. A. Weinstein, M. D. Ward, *Dalton Trans.* **2014**, *43*, 6414–6428.

[87] X. Rao, T. Song, J. Gao, Y. Cui, Y. Yang, C. Wu, B. Chen, G. Qian, *J. Am. Chem. Soc.* **2013**, *135*, 15559–15564.

[88] L. Song, Q. Wang, D. Tang, X. Liu, Z. Zhen, *New J. Chem.* **2007**, *31*, 506–511.

[89] Y. Shimizu, T. Azumi, *J. Phys. Chem.* **1982**, *86*, 22–26.

[90] F. J. Steemers, W. Verboom, D. N. Reinhoudt, E. B. van der Tol, J. W.

Verhoeven, *J. Am. Chem. Soc.* **1995**, *117*, 9408–9414.

[91] M. Kleinerman, *J. Chem. Phys.* **1969**, *51*, 2370–2381.

[92] T. Lazarides, M. A. H. Alamiry, H. Adams, S. J. A. Pope, S. Faulkner, J. A. Weinstein, M. D. Ward, *Dalton Trans.* **2007**, 1484–1491.

[93] S. Sato, M. Wada, *Bull. Chem. Soc. Jpn.* **1970**, *43*, 1955–1962.

[94] A. Watkis, R. Hueting, T. J. Sørensen, M. Tropiano, S. Faulkner, *Chem. Commun.* **2015**, *51*, 15633–15636.

[95] G.-L. Law, R. Pal, L. O. Palsson, D. Parker, K.-L. Wong, *Chem. Commun.* **2009**, 7321–7323.

[96] X. Wang, O. S. Wolfbeis, *Chem. Soc. Rev.* **2014**, *43*, 3666–3761.

[97] T. J. Sørensen, A. M. Kenwright, S. Faulkner, *Chem. Sci.* **2015**, *6*, 2054–2059.

[98] M. A. El-Sayed, *J. Chem. Phys.* **1963**, *38*, 2834–2838.

[99] T. Förster, *Ann. Phys.* **1948**, *437*, 55–75.

[100] D. L. Dexter, *J. Chem. Phys.* **1953**, *21*, 836–850.

[101] C. Lincheneau, E. Quinlan, J. a. Kitchen, T. McCabe, S. E. Matthews, T. Gunnlaugsson, *Supramol. Chem.* **2013**, *25*, 869–880.

[102] F. J. Steemers, H. G. Meuris, W. Verboom, D. N. Reinhoudt, E. B. van der Tol, J. W. Verhoeven, *J. Org. Chem.* **1997**, *62*, 4229–4235.

[103] N. Sabbatini, S. Perathoner, G. Lattanzi, S. Dellonte, V. Balzani, *J. Phys. Chem.* **1987**, *91*, 6136–6139.

[104] L. Prodi, M. Maestri, R. Ziessel, V. Balzani, *Inorg. Chem.* **1991**, *30*, 3798–3802.

[105] W. D. Horrocks, J. P. Bolender, W. D. Smith, R. M. Supkowski, *J. Am. Chem. Soc.* **1997**, *119*, 5972–5973.

[106] T. Ala-Kleme, K. Haapakka, M. Latva, *Anal. Chim. Acta* **1999**, *395*, 205–211.

[107] Y. Zhong, L. Si, H. He, A. G. Sykes, *Dalton Trans.* **2011**, *40*, 11389–11395.

[108] A. P. Pushkarev, V. A. Ilichev, T. V. Balashova, D. L. Vorozhtsov, M. E. Burin, D. M. Kuzyaev, G. K. Fukin, B. A. Andreev, D. I. Kryzhkov, A. N. Yablonskiy, et al., *Russ. Chem. Bull.* **2013**, *62*, 392–397.

[109] S. Comby, J.-C. G. Bünzli, in *Handb. Phys. Chem. Rare Earths* (Eds.: K.A.

Gschneidner, J.-C.G. Bünzli, V.K. Pecharsky), Elsevier B.V., Amsterdam, The Netherlands, **2007**, pp. 217–470.

[110] N. M. Shavaleev, R. Scopelliti, F. Gumy, J.-C. G. Bünzli, *Inorg. Chem.* **2009**, *48*, 7937–7946.

[111] A. Zaïm, S. V. Eliseeva, L. Guénée, H. Nozary, S. Petoud, C. Piguet, *Chem. Eur. J.* **2014**, *20*, 12172–12182.

[112] G. Stein, E. Würzberg, *J. Chem. Phys.* **1975**, *62*, 208–213.

[113] T. Shimanouchi, H. Matsuura, Y. Ogawa, I. Harada, *J. Phys. Chem. Ref. Data* **1978**, *7*, 1323–1444.

[114] W. D. Horrocks, D. R. Sudnick, *J. Am. Chem. Soc.* **1979**, *101*, 334–340.

[115] W. D. Horrocks, D. R. Sudnick, *Acc. Chem. Res.* **1981**, *14*, 384–392.

[116] R. S. Dickins, D. Parker, A. S. de Sousa, J. A. G. Williams, *Chem. Commun.* **1996**, 697–698.

[117] A. Beeby, I. M. Clarkson, R. S. Dickins, S. Faulkner, D. Parker, L. Royle, A. S. de Sousa, J. A. G. Williams, M. Woods, *J. Chem. Soc. Perkin Trans. 2* **1999**, *2*, 493–504.

[118] G. R. Choppin, D. R. Peterman, *Coord. Chem. Rev.* **1998**, *174*, 283–299.

[119] R. C. Holz, C. A. Chang, W. D. Horrocks, *Inorg. Chem.* **1991**, *30*, 3270–3275.

[120] M. P. Oude Wolbers, F. C. J. M. van Veggel, B. H. M. Snellink-Ruël, J. W. Hofstraat, F. A. J. Geurts, D. N. Reinhoudt, *J. Am. Chem. Soc.* **1997**, *119*, 138–144.

[121] I. Hemmilä, V.-M. Mukkala, H. Takalo, *J. Fluoresc.* **1995**, *5*, 159–163.

[122] S. Biju, Y. K. Eom, J.-C. G. Bünzli, H. K. Kim, *J. Mater. Chem. C* **2013**, *1*, 6935–6944.

[123] A. Beeby, R. S. Dickins, S. Faulkner, D. Parker, J. A. Gareth Williams, *Chem. Commun.* **1997**, 1401–1402.

[124] S. Faulkner, A. Beeby, M.-C. Carrié, A. Dadabhoy, A. M. Kenwright, P. G. Sammes, *Inorg. Chem. Commun.* **2001**, *4*, 187–190.

[125] M. H. V. Werts, R. T. F. Jukes, J. W. Verhoeven, *Phys. Chem. Chem. Phys.* **2002**, *4*, 1542–1548.

[126] G. A. Crosby, J. N. Demas, *J. Phys. Chem.* **1971**, *75*, 991–1024.

[127] J.-C. G. Bünzli, *Nat. Chem.* **2010**, *2*, 696–696.

[128] M. G. Urbain, *C. R. Acad. Sci.* **1906**, *142*, 205–207.

[129] A. I. Voloshin, N. M. Shavaleev, V. P. Kazakov, *J. Lumin.* **2001**, *93*, 191–197.

[130] S. Petit, F. Baril-Robert, G. Pilet, C. Reber, D. Luneau, *Dalton Trans.* **2009**, 6809–6815.

[131] A. F. Kirby, D. Foster, F. S. Richardson, *Chem. Phys. Lett.* **1983**, *95*, 507–512.

[132] S. I. Klink, G. A. Hebbink, L. Grave, P. G. B. Oude Alink, F. C. J. M. van Veggel, M. H. V. Werts, *J. Phys. Chem. A* **2002**, *106*, 3681–3689.

[133] N. M. Shavaleev, S. V. Eliseeva, R. Scopelliti, J.-C. G. Bünzli, *Chem. Eur. J.* **2009**, *15*, 10790–10802.

[134] N. M. Shavaleev, S. V Eliseeva, R. Scopelliti, J.-C. G. Bünzli, *Inorg. Chem.* **2014**, *53*, 5171–5178.

[135] M. Hilder, Photophysical Properties of Europium and Terbium Benzoate Complexes in Solid State, Monash University, **2004**.

[136] M. Bettinelli, A. Speghini, F. Piccinelli, A. N. C. Neto, O. L. Malta, *J. Lumin.* **2011**, *131*, 1026–1028.

[137] A. de Bettencourt-Dias, P. S. Barber, S. Bauer, *J. Am. Chem. Soc.* **2012**, *134*, 6987–6994.

[138] E. Deiters, B. Song, A.-S. Chauvin, C. D. B. Vandevyver, F. Gumy, J.-C. G. Bünzli, *Chem. Eur. J.* **2009**, *15*, 885–900.

[139] P. Mohanty, S. Ram, *Philos. Mag. Lett.* **2006**, *86*, 375–384.

[140] M. Giraud, E. S. Andreiadis, A. S. Fisyuk, R. Demadrille, D. Imbert, M. Mazzanti, *Inorg. Chem.* **2008**, *47*, 3952–3954.

[141] E. S. Andreiadis, D. Imbert, J. Pécaut, R. Demadrille, M. Mazzanti, *Dalton Trans.* **2012**, *41*, 1268–1277.

[142] D. Parker, J. A. G. Williams, *J. Chem. Soc. Dalton Trans.* **1996**, 3613–3628.

[143] L. J. Charbonnière, C. Balsiger, K. J. Schenk, J. G. Bünzli, *J. Chem. Soc. Dalton Trans.* **1998**, *91*, 505–510.

[144] D. D'Alessio, S. Muzzioli, B. W. Skelton, S. Stagni, M. Massi, M. I. Ogden, *Dalton Trans.* **2012**, *41*, 4736–4739.

[145] D. D'Alessio, A. N. Sobolev, B. W. Skelton, R. O. Fuller, R. C. Woodward, N. A. Lengkeek, B. H. Fraser, M. Massi, M. I. Ogden, *J. Am. Chem. Soc.* **2014**, *136*, 15122–15125.

[146] Z. Asfari, J. M. Harrowfield, M. I. Ogden, J. Vicens, A. H. White, *Angew. Chem. Int. Ed.* **1991**, *30*, 854–856.

[147] R. Wang, M. D. Carducci, Z. Zheng, *Inorg. Chem.* **2000**, *39*, 1836–1837.

[148] C. G. Pernin, J. A. Ibers, *J. Clust. Sci.* **1999**, *10*, 71–90.

[149] X.-J. Kong, Y. Wu, L.-S. Long, L.-S. Zheng, Z. Zheng, *J. Am. Chem. Soc.* **2009**, *131*, 6918–6919.

[150] X.-J. Kong, L.-S. Long, L.-S. Zheng, R. Wang, Z. Zheng, *Inorg. Chem.* **2009**, *48*, 3268–3273.

[151] B. Zhang, T. Xiao, C. Liu, Q. Li, Y. Zhu, M. Tang, C. Du, M. Song, *Inorg. Chem.* **2013**, *52*, 13332–13340.

[152] M. R. Bürgstein, M. T. Gamer, P. W. Roesky, *J. Am. Chem. Soc.* **2004**, *126*, 5213–5218.

[153] X. Yang, D. Schipper, R. A. Jones, L. A. Lytwak, B. J. Holliday, S. Huang, *J. Am. Chem. Soc.* **2013**, *135*, 8468–8471.

[154] P. Martín-Ramos, J. T. Coutinho, M. R. Silva, L. C. J. Pereira, A. M. Matos Beja, J. Martín-Gil, *J. Chem. Crystallogr.* **2014**, *44*, 255–260.

[155] D. T. Thielemann, M. Klinger, T. J. A. Wolf, Y. Lan, W. Wernsdorfer, M. Busse, P. W. Roesky, A.-N. Unterreiner, A. K. Powell, P. C. Junk, et al., *Inorg. Chem.* **2011**, *50*, 11990–12000.

[156] G. M. Sequeira, W. Y. Tan, E. G. Moore, *Dalton Trans.* **2015**, *44*, 13378–13383.

[157] Y. Hasegawa, T. Nakanishi, *RSC Adv.* **2015**, *5*, 338–353.

[158] W. J. Gee, J. G. MacLellan, C. M. Forsyth, B. Moubaraki, K. S. Murray, P. C. Andrews, P. C. Junk, *Inorg. Chem.* **2012**, *51*, 8661–8663.

[159] M. T. Gamer, Y. Lan, P. W. Roesky, A. K. Powell, R. Clérac, *Inorg. Chem.* **2008**, *47*, 6581–6583.

[160] S. Datta, V. Baskar, H. Li, P. W. Roesky, *Eur. J. Inorg. Chem.* **2007**, 4216–4220.

[161] P. C. Andrews, T. Beck, C. M. Forsyth, B. H. Fraser, P. C. Junk, M. Massi, P.

W. Roesky, *Dalton Trans.* **2007**, 5651–5654.

[162] V. Baskar, P. W. Roesky, *Z. Anorg. Allg. Chem.* **2005**, *631*, 2782–2785.

[163] P. C. Andrews, T. Beck, B. H. Fraser, P. C. Junk, M. Massi, B. Moubaraki, K. S. Murray, M. Silberstein, *Polyhedron* **2009**, *28*, 2123–2130.

[164] P. C. Andrews, G. B. Deacon, R. Frank, B. H. Fraser, P. C. Junk, J. G. MacLellan, M. Massi, B. Moubaraki, K. S. Murray, M. Silberstein, *Eur. J. Inorg. Chem.* **2009**, 744–751.

[165] P. C. Andrews, W. J. Gee, P. C. Junk, J. G. Maclellan, *Inorg. Chem.* **2004**, *49*, 1568–1573.

[166] P. C. Andrews, D. H. Brown, B. H. Fraser, N. T. Gorham, P. C. Junk, M. Massi, T. G. St Pierre, B. W. Skelton, R. C. Woodward, *Dalton Trans.* **2010**, *39*, 11227–11234.

[167] J.-C. G. Bünzil, J.-M. Pfefferlé, B. Ammann, G. Chapuis, F.-J. Zuniga, *Helv. Chim. Acta* **1984**, *67*, 1121–1127.

[168] N. Armaroli, L. De Cola, V. Balzani, J.-P. Sauvage, C. O. Dietrich-Buchecker, J.-M. Kern, *J. Chem. Soc. Faraday Trans.* **1992**, *88*, 553–556.

[169] L. Claisen, *Liebigs Ann.* **1896**, *291*, 25–137.

[170] G. Aromí, P. Gamez, J. Reedijk, *Coord. Chem. Rev.* **2008**, *252*, 964–989.

[171] D. Aguilà, L. A. Barrios, V. Velasco, O. Roubeau, A. Repollés, P. J. Alonso, J. Sesé, S. J. Teat, F. Luis, G. Aromí, *J. Am. Chem. Soc.* **2014**, *136*, 14215–14222.

[172] C. P. Hauser, D. T. Thielemann, M. Adlung, C. Wickleder, P. W. Roesky, C. K. Weiss, K. Landfester, *Macromol. Chem. Phys.* **2011**, *212*, 286–296.

[173] J. G. White, *Inorganica Chim. Acta* **1976**, *16*, 159–162.

[174] H. Wang, P. He, S. Liu, J. Shi, M. Gong, *Appl. Phys. B* **2009**, *97*, 481–487.

[175] S. Akerboom, M. S. Meijer, M. A. Siegler, W. T. Fu, E. Bouwman, *J. Lumin.* **2014**, *145*, 278–282.

[176] A. Mech, M. Karbowiak, C. Görller-Walrand, R. Van Deun, *J. Alloys Compd.* **2008**, *451*, 215–219.

[177] L. Armelao, S. Quici, F. Barigelletti, G. Accorsi, G. Bottaro, M. Cavazzini, E. Tondello, *Coord. Chem. Rev.* **2010**, *254*, 487–505.

[178] J.-C. G. Bünzli, E. Moret, V. Foiret, K. J. Schenk, Wang Mingzhao, Jin

Linpei, *J. Alloys Compd.* **1994**, *207-208*, 107–111.

[179] D. N. Woodruff, R. E. P. Winpenny, R. A. Layfield, *Chem. Rev.* **2013**, *113*, 5110–5148.

[180] S. Yajima, Y. Hasegawa, *Bull. Chem. Soc. Jpn.* **1998**, *71*, 2825–2829.

[181] P. Martín-Ramos, M. Ramos Silva, F. Lahoz, I. R. Martín, P. Chamorro-Posada, M. E. S. Eusebio, V. Lavín, J. Martín-Gil, *J. Photochem. Photobiol. A* **2014**, *292*, 16–25.

[182] R. H. C. Tan, M. Motevalli, I. Abrahams, P. B. Wyatt, W. P. Gillin, *J. Phys. Chem. B* **2006**, *110*, 24476–24479.

[183] P. Martín-Ramos, P. S. Pereira da Silva, V. Lavín, I. R. Martín, F. Lahoz, P. Chamorro-Posada, M. Ramos Silva, J. Martín-Gil, *Dalton Trans.* **2013**, *42*, 13516–13526.

[184] A.-S. Chauvin, F. Gumy, I. Matsubayashi, Y. Hasegawa, J.-C. G. Bünzli, *Eur. J. Inorg. Chem.* **2006**, *2006*, 473–480.

[185] P. B. Glover, A. P. Bassett, P. Nockemann, B. M. Kariuki, R. Van Deun, Z. Pikramenou, *Chem. Eur. J.* **2007**, *13*, 6308–6320.

[186] A. P. Bassett, R. Van Deun, P. Nockemann, P. B. Glover, B. M. Kariuki, K. Van Hecke, L. Van Meervelt, Z. Pikramenou, *Inorg. Chem.* **2005**, *44*, 6140–6142.

[187] J.-H. Kim, Y.-P. Park, *J. Korean Phys. Soc.* **2003**, *43*, 277–281.

[188] N. V. Pashchevskaya, S. N. Bolotin, M. E. Sokolov, A. A. Sklyar, V. T. Panyushkin, *Russ. J. Gen. Chem.* **2006**, *76*, 1011–1014.

[189] A. O. Ribeiro, P. S. Calefi, A. M. Pires, O. A. Serra, *J. Alloys Compd.* **2004**, *374*, 151–153.

[190] C. Merkens, U. Englert, *Dalton Trans.* **2012**, *41*, 4664–4673.

[191] S. Sitran, D. Fregona, G. Faraglia, *J. Coord. Chem.* **1991**, *24*, 127–135.

[192] P. C. Andrews, W. J. Gee, P. C. Junk, J. G. MacLellan, *Dalton Trans.* **2011**, *40*, 12169–12179.

[193] J. L. Guthrie, N. Rabjohn, *J. Org. Chem.* **1957**, *22*, 176–179.

[194] I. Halasz, N. Cindro, R. E. Dinnebier, H. Vančik, *Croat. Chem. Acta* **2013**, *86*, 187–192.

[195] F. H. Allen, *Acta Crystallogr. Sect. B-Struct. Sci.* **2002**, *58*, 380–388.

[196] M. Ismail, S. J. Lyle, J. E. Newbery, *J. Inorg. Nucl. Chem.* **1969**, *31*, 2091–2093.

[197] W. G. Quirino, C. Legnani, M. Cremona, P. P. Lima, S. A. Junior, O. L. Malta, *Thin Solid Films* **2006**, *494*, 23–27.

[198] G.-L. Law, K.-L. Wong, H.-L. Tam, K.-W. Cheah, W.-T. Wong, *Inorg. Chem.* **2009**, *48*, 10492–10494.

[199] P. A. Tanner, in *Springer Ser. Fluoresc.*, **2010**, pp. 183–233.

[200] E. V Baranov, G. K. Fukin, T. V Balashova, A. P. Pushkarev, I. D. Grishin, M. N. Bochkarev, *Dalton Trans.* **2013**, *42*, 15699–15705.

[201] T.-S. Kang, B. S. Harrison, M. Bouguettaya, T. J. Foley, J. M. Boncella, K. S. Schanze, J. R. Reynolds, *Adv. Funct. Mater.* **2003**, *13*, 205–210.

[202] M. A. Katkova, A. P. Pushkarev, T. V. Balashova, A. N. Konev, G. K. Fukin, S. Y. Ketkov, M. N. Bochkarev, *J. Mater. Chem.* **2011**, *21*, 16611–16620.

[203] H. Wei, G. Yu, Z. Zhao, Z. Liu, Z. Bian, C. Huang, *Dalton Trans.* **2013**, *42*, 8951–8960.

[204] J. P. Martins, P. Martín-Ramos, C. Coya, A. L. Álvarez, L. C. Pereira, R. Díaz, J. Martín-Gil, M. Ramos Silva, *Mater. Chem. Phys.* **2014**, *147*, 1157–1164.

[205] P. Martín-Ramos, C. Coya, Á. L. Álvarez, M. Ramos Silva, C. Zaldo, J. A. Paixão, P. Chamorro-Posada, J. Martín-Gil, *J. Phys. Chem. C* **2013**, *117*, 10020–10030.

[206] P. Martín-Ramos, C. Coya, V. Lavín, I. R. Martín, M. R. Silva, P. S. P. Silva, M. García-Vélez, A. L. Álvarez, J. Martín-Gil, *Dalton Trans.* **2014**, *43*, 18087–18096.

[207] J. C. Reid, M. Calvin, *J. Am. Chem. Soc.* **1950**, *72*, 2948–2952.

[208] L. B. Barkley, R. Levine, *J. Am. Chem. Soc.* **1953**, *75*, 2059–2063.

[209] J. Barbera, C. Cativiela, J. L. Serrano, M. M. Zurbano, *Liq. Cryst.* **1992**, *11*, 887–897.

[210] S. J. Lyle, M. Tamizi, *Anal. Chim. Acta* **1979**, *108*, 437–440.

[211] R. S. Rasmussen, D. D. Tunnicliff, R. R. Brattain, *J. Am. Chem. Soc.* **1949**, *71*, 1068–1072.

[212] C. Freund, W. Porzio, U. Giovanella, F. Vignali, M. Pasini, S. Destri, A.

Mech, S. Di Pietro, L. Di Bari, P. Mineo, *Inorg. Chem.* **2011**, *50*, 5417–5429.

[213] C. Janiak, *J. Chem. Soc. Dalton Trans.* **2000**, 3885–3896.

[214] M. A. Spackman, D. Jayatilaka, *CrystEngComm* **2009**, *11*, 19–32.

[215] D. P. Schofield, J. R. Lane, H. G. Kjaergaard, *J. Phys. Chem. A* **2007**, *111*, 567–572.

[216] M. Llunell, D. Casanova, J. Cirera, P. Alemany, S. Alvarez, "Shape version 2.1," can be found under <http://www.ee.ub.es/index.php/news-ee/575-shape-available>, **2013**.

[217] D. Casanova, M. Llunell, P. Alemany, S. Alvarez, *Chem. Eur. J.* **2005**, *11*, 1479–1494.

[218] M. Pinsky, D. Avnir, *Inorg. Chem.* **1998**, *37*, 5575–5582.

[219] S. Alvarez, D. Avnir, M. Llunell, M. Pinsky, *New J. Chem.* **2002**, *26*, 996–1009.

[220] A. Ruiz-Martínez, D. Casanova, S. Alvarez, *Chem. Eur. J.* **2008**, *14*, 1291–1303.

[221] J. Cirera, E. Ruiz, S. Alvarez, *Chem. Eur. J.* **2006**, *12*, 3162–3167.

[222] A. Ruiz-Martínez, D. Casanova, S. Alvarez, *Chem. Eur. J.* **2010**, *16*, 6567–6581.

[223] D. Casanova, J. Cirera, M. Llunell, P. Alemany, D. Avnir, S. Alvarez, *J. Am. Chem. Soc.* **2004**, *126*, 1755–1763.

[224] C. Paris, V. Lhiaubet-Vallet, O. Jiménez, C. Trullas, M. Á. Miranda, *Photochem. Photobiol.* **2009**, *85*, 178–184.

[225] M. L. Bhaumik, M. A. El-Sayed, *J. Phys. Chem.* **1965**, *69*, 275–280.

[226] K. Zhuravlev, V. Tsaryuk, V. Kudryashova, I. Pekareva, J. Sokolnicki, Y. Yakovlev, *J. Lumin.* **2010**, *130*, 1489–1496.

[227] M. Asano-Someda, Y. Kaizu, *J. Photochem. Photobiol. A* **2001**, *139*, 161–165.

[228] N. M. Shavaleev, R. Scopelliti, F. Gumy, J.-C. G. Bünzli, *Inorg. Chem.* **2009**, *48*, 2908–2918.

[229] P. Martín-Ramos, V. Lavín, M. Ramos Silva, I. R. Martín, F. Lahoz, P. Chamorro-Posada, J. A. Paixão, J. Martín-Gil, *J. Mater. Chem. C* **2013**, *1*, 5701–5710.

[230] H. Q. Ye, Z. Li, Y. Peng, C. C. Wang, T. Y. Li, Y. X. Zheng, A. Sapelkin, G. Adamopoulos, I. Hernández, P. B. Wyatt, et al., *Nat. Mater.* **2014**, *13*, 382–386.

[231] M. D. Marcantonatos, M. Deschaux, J.-J. Vuilleumier, *J. Chem. Soc. Faraday Trans. 2* **1984**, *80*, 1569–1598.

[232] Y. Zheng, Y. Zhou, J. Yu, Y. Yu, H. Zhang, W. P. Gillin, *J. Phys. D. Appl. Phys.* **2004**, *37*, 531–534.

[233] A. de Bettencourt-Dias, *Luminescence of Lanthanide Ions in Coordination Compounds and Nanomaterials*, John Wiley & Sons Ltd, Chichester, United Kingdom, **2014**.

[234] P. A. Tanner, *Chem. Soc. Rev.* **2013**, *42*, 5090–5101.

[235] G. Qian, M. Wang, Z. Yang, *J. Non. Cryst. Solids* **2001**, *286*, 235–239.

[236] S. Alves Junior, F. V. de Almeida, G. F. de Sá, C. de Mello Donegá, *J. Lumin.* **1997**, *72-74*, 478–480.

[237] F. R. Gonçalves e Silva, J. F. S. Menezes, G. B. Rocha, S. Alves, H. F. Brito, R. L. Longo, O. L. Malta, *J. Alloys Compd.* **2000**, *303-304*, 364–370.

[238] A. D. Burrows, K. Cassar, M. F. Mahon, J. E. Warren, *Dalton Trans.* **2007**, *4*, 2499–2509.

[239] M. Kondracka, U. Englert, *Inorg. Chem.* **2008**, *47*, 10246–10257.

[240] D. D'Alessio, B. W. Skelton, N. A. Lengkeek, B. H. Fraser, A. M. Krause-Heuer, S. Muzzioli, S. Stagni, M. Massi, M. I. Ogden, *Supramol. Chem.* **2015**, *27*, 787–791.

[241] P. J. Wright, S. Muzzioli, B. W. Skelton, P. Raiteri, J. Lee, G. Koutsantonis, D. S. Silvester, S. Stagni, M. Massi, *Dalton Trans.* **2013**, *42*, 8188.

[242] P. J. Wright, S. Muzzioli, M. V Werrett, P. Raiteri, B. W. Skelton, D. S. Silvester, S. Stagni, M. Massi, *Organometallics* **2012**, *31*, 7566–7578.

[243] P. J. Wright, M. G. Affleck, S. Muzzioli, B. W. Skelton, P. Raiteri, D. S. Silvester, S. Stagni, M. Massi, *Organometallics* **2013**, *32*, 3728–3737.

[244] M. V Werrett, G. S. Huff, S. Muzzioli, V. Fiorini, S. Zacchini, B. W. Skelton, A. Maggiore, J. M. Malicka, M. Cocchi, K. C. Gordon, et al., *Dalton Trans.* **2015**, *44*, 8379–8393.

[245] D. D'Alessio, L. E. Karagiannidis, B. W. Skelton, M. Massi, M. I. Ogden,

Aust. J. Chem. **2012**, *65*, 819.

[246] G. I. Roshchupkina, Y. V. Gatilov, T. V. Rybalova, V. A. Reznikov, *Eur. J. Org. Chem.* **2004**, *2004*, 1765–1773.

[247] A. B. Burdukov, G. I. Roschupkina, Y. V. Gatilov, S. A. Gromilov, V. A. Reznikov, *J. Supramol. Chem.* **2002**, *2*, 359–363.

[248] M. Okimoto, K. Numata, Y. Takahashi, M. Hoshi, K. Tomozawa, T. Shigemoto, *Synlett* **2005**, 2507–2509.

[249] C. M. Silvernail, G. Yap, R. D. Sommer, A. L. Rheingold, V. W. Day, J. A. Belot, *Polyhedron* **2001**, *20*, 3113–3117.

[250] L. Poisson, P. Roubin, S. Coussan, B. Soep, J.-M. Mestdagh, *J. Am. Chem. Soc.* **2008**, *130*, 2974–2983.

[251] P. K. Verma, A. Steinbacher, F. Koch, P. Nuernberger, T. Brixner, *Phys. Chem. Chem. Phys.* **2015**, *17*, 8459–8466.

[252] S. Tobita, M. Arakawa, I. Tanaka, *J. Phys. Chem.* **1984**, *88*, 2697–2702.

[253] L. Ma, L. Yuan, C. Xu, G. Li, M. Tao, W. Zhang, *Synthesis (Stuttg).* **2012**, *45*, 45–52.

[254] H. Zhang, D. Feng, H. Sheng, X. Ma, J. Wan, Q. Tang, *RSC Adv.* **2014**, *4*, 6417–6423.

[255] V. S. Sastri, J.-C. G. Bünzli, V. R. Rao, G. V. S. Rayudu, J. R. Perumareddi, in *Mod. Asp. Rare Earths Their Complexes*, Elsevier, **2003**, pp. 259–374.

[256] K. Nakamaru, *Bull. Chem. Soc. Jpn.* **1982**, *55*, 2697–2705.

[257] M. C. Burla, R. Caliandro, M. Camalli, B. Carrozzini, G. L. Cascarano, C. Giacovazzo, M. Mallamo, A. Mazzone, G. Polidori, R. Spagna, *J. Appl. Crystallogr.* **2012**, *45*, 357–361.

[258] O. V. Dolomanov, L. J. Bourhis, R. J. Gildea, J. a. K. Howard, H. Puschmann, *J. Appl. Crystallogr.* **2009**, *42*, 339–341.

[259] G. M. Sheldrick, *Acta Crystallogr. Sect. C-Struct. Chem.* **2015**, *71*, 3–8.

Appendix

A1 2D NMR

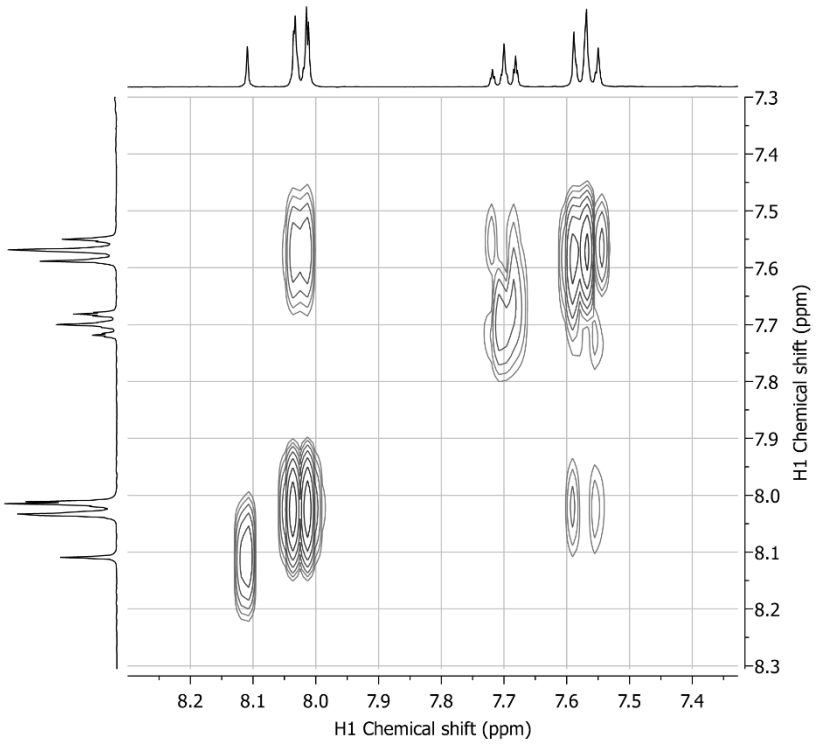

Figure A1 – 2D COSY NMR spectrum of the **L1**H molecule.

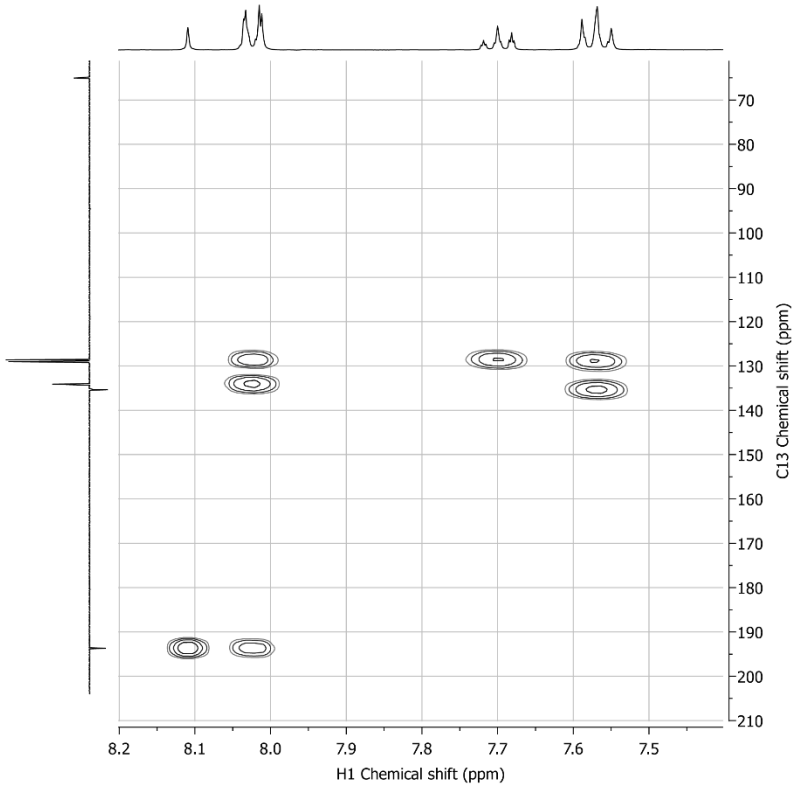

Figure A2 – 2D HMBC spectrum of the **L1**H molecule.

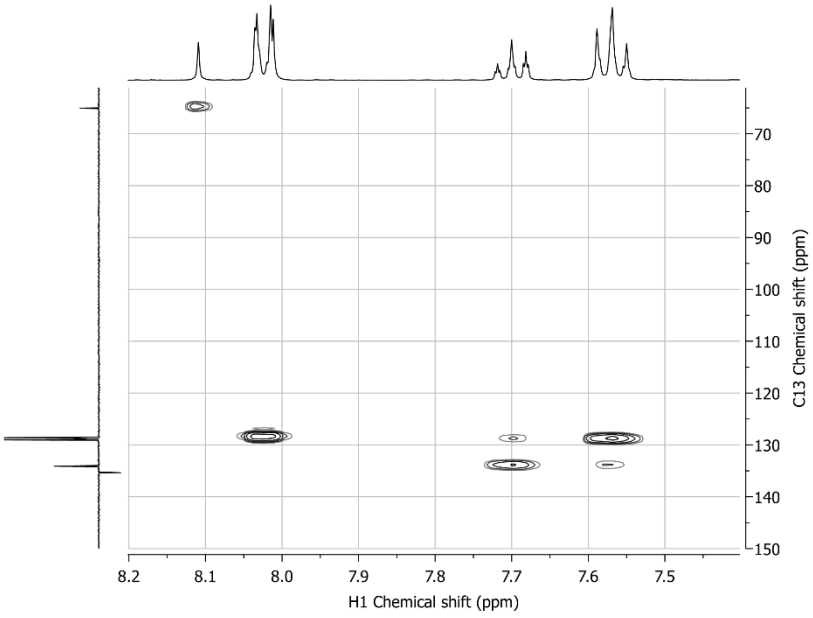

Figure A3 – 2D HSQC spectrum of the **L1**H molecule.

A2 Molecular Displacement Plots

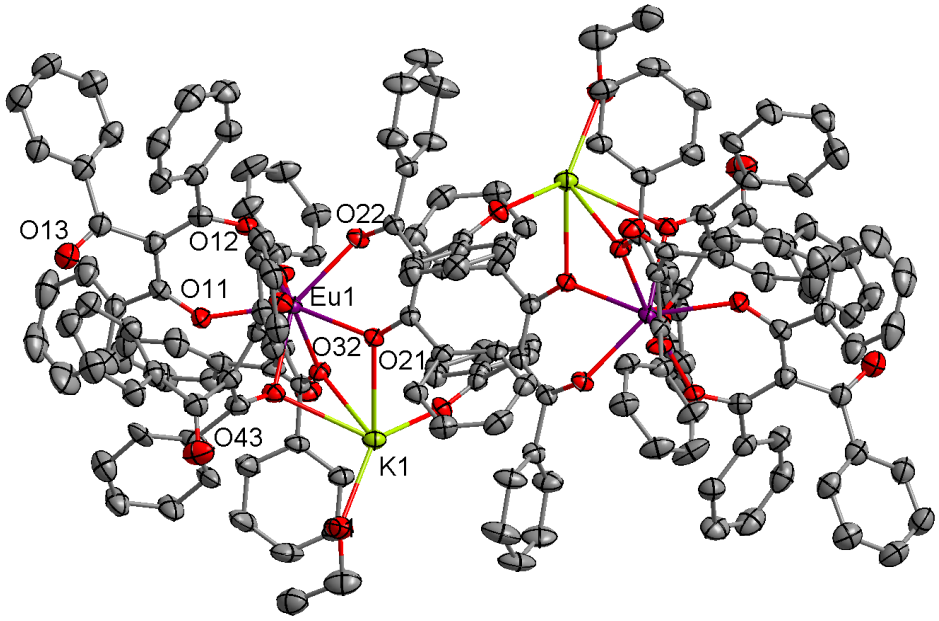

Figure A4 - Molecular plot of the $\{Eu_2K_2\}^{IV}$ assembly with displacement ellipsoids at the 50% probability level. Hydrogen atoms and solvent molecules are omitted for clarity.

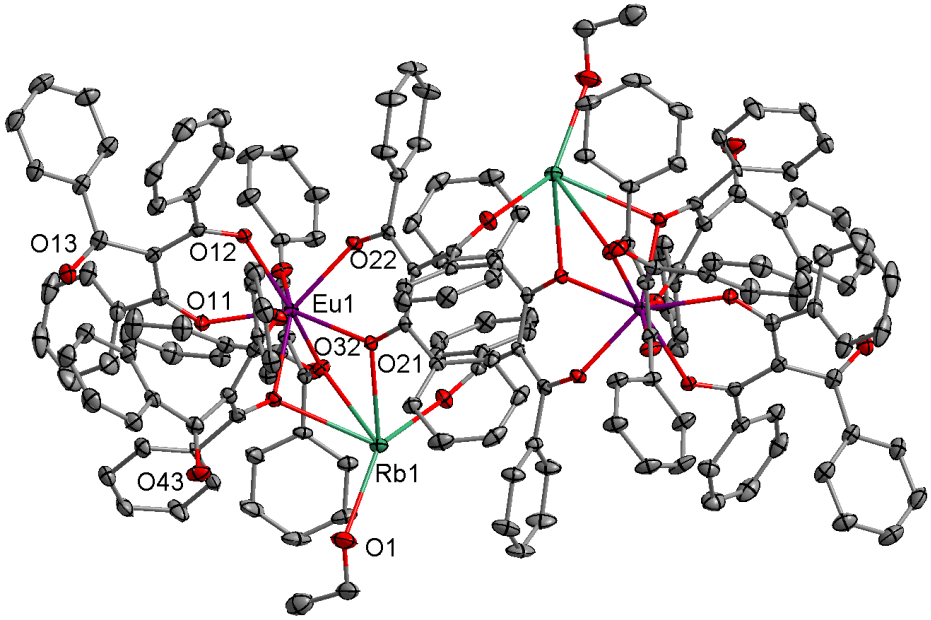

Figure A5 - Molecular plot of the $\{Eu_2Rb_2\}^{IV}$ assembly with displacement ellipsoids at the 50% probability level. Hydrogen atoms and solvent molecules are omitted for clarity.

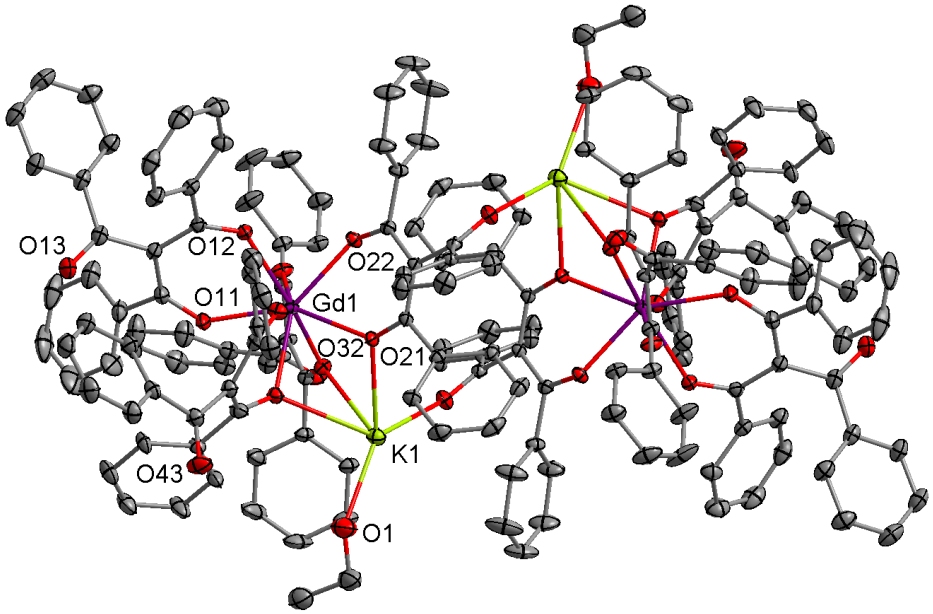

Figure A6 - Molecular plot of the $\{Gd_2K_2\}^{IV}$ assembly with displacement ellipsoids shown at the 50% probability level. Hydrogen atoms and solvent molecules are omitted for clarity.

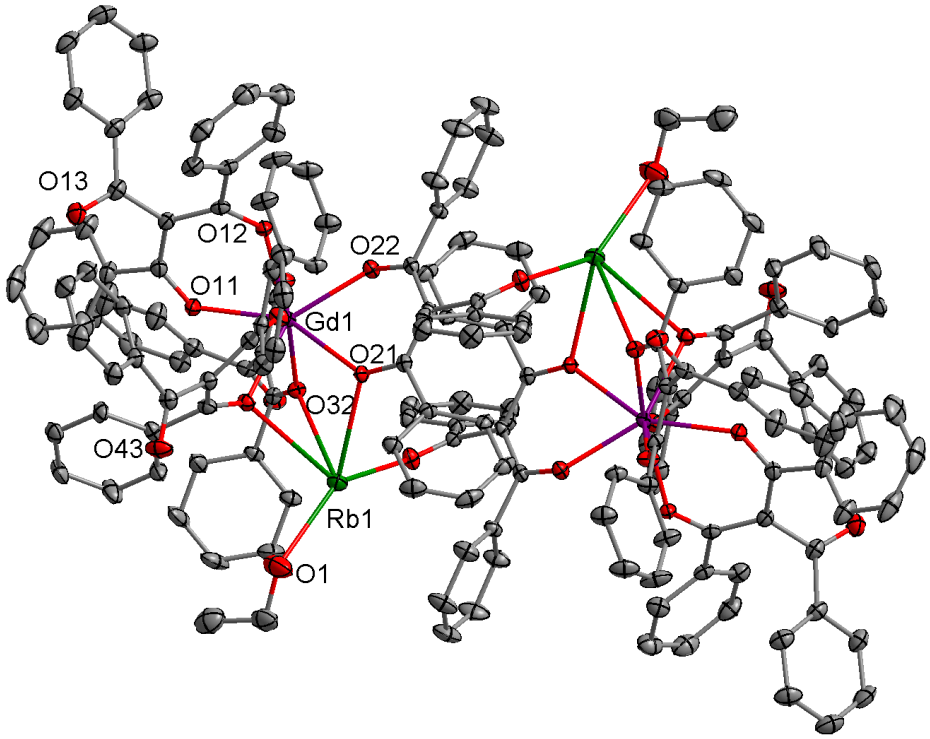

Figure A7 – Molecular plot of the $\{Gd_2Rb_2\}^{IV}$ assembly with displacement ellipsoids shown at the 50% probability level. Hydrogen atoms and solvent molecules are omitted for clarity.

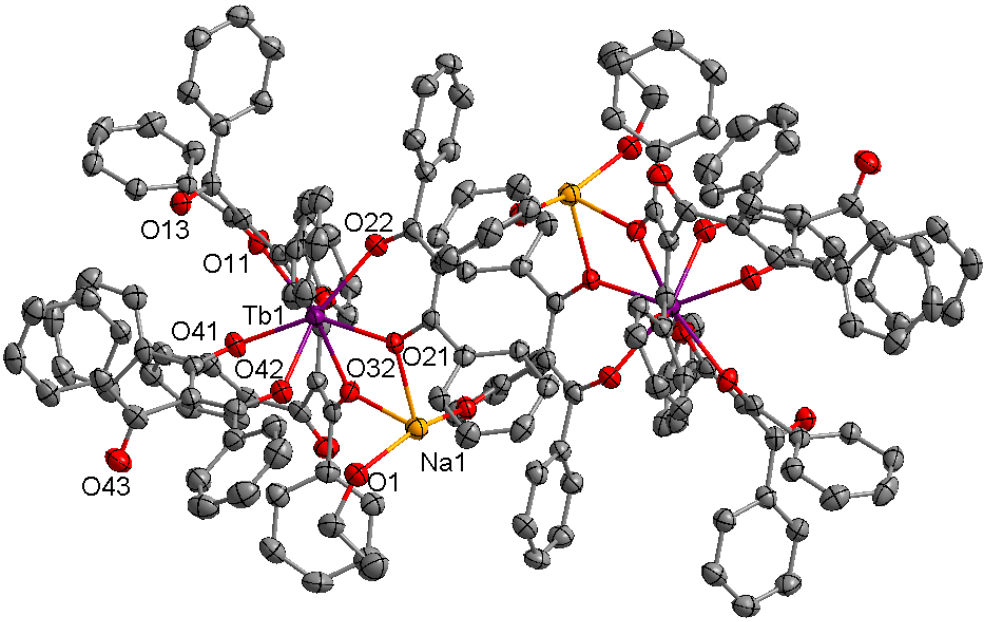

Figure A8 - Molecular plot of the $\{Tb_2Na_2\}^{I}$ assembly with displacement ellipsoids shown at the 50% probability level. Hydrogen atoms are omitted for clarity.

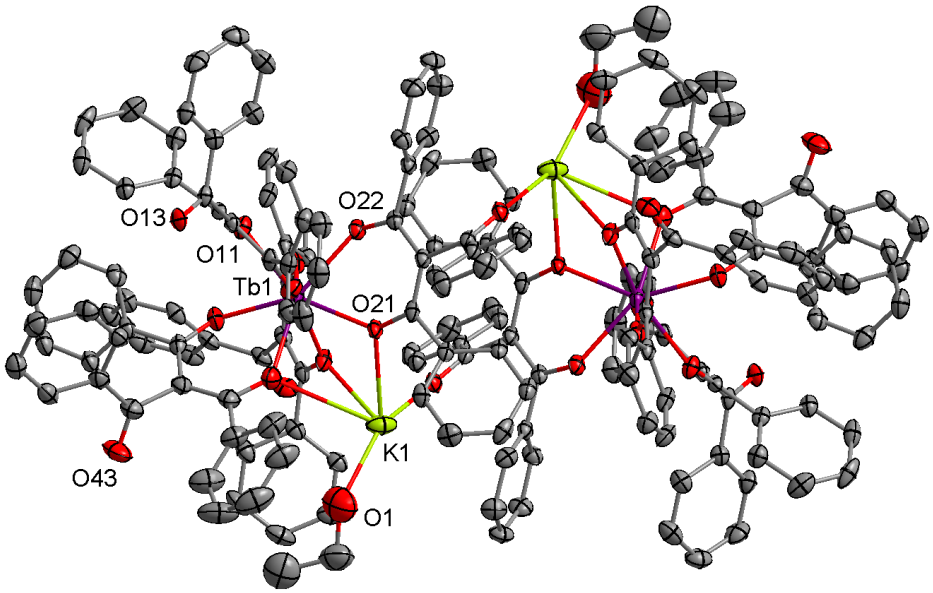

Figure A9 - Molecular plot of the $\{Tb_2K_2\}^{II}$ assembly with displacement ellipsoids shown at the 50% probability level. Hydrogen atoms are omitted for clarity.

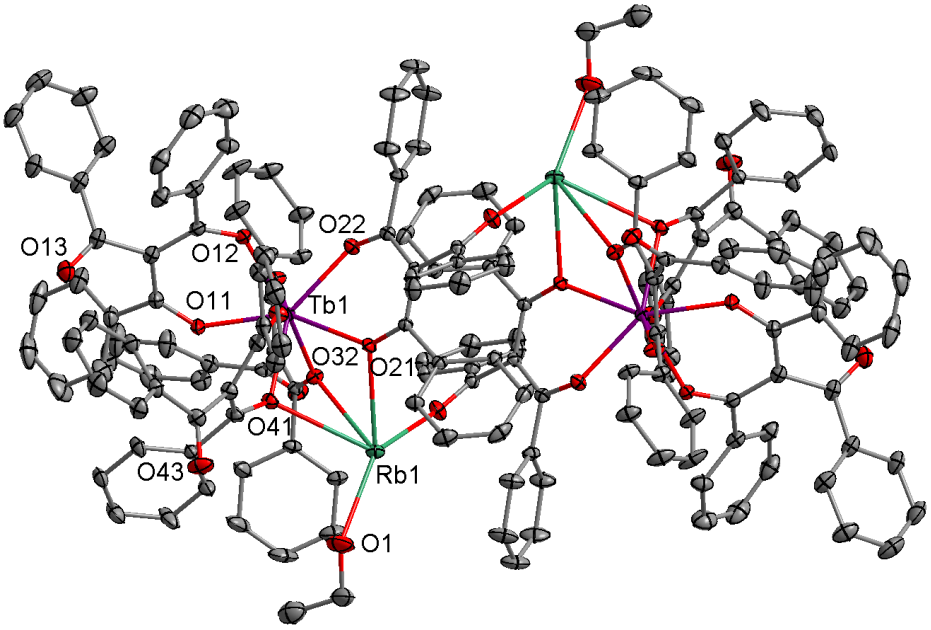

Figure A10 - Molecular plot of the $\{Tb_2Rb_2\}^{IV}$ assembly with displacement ellipsoids shown at the 50% probability level. Hydrogen atoms and solvent molecules are omitted for clarity.

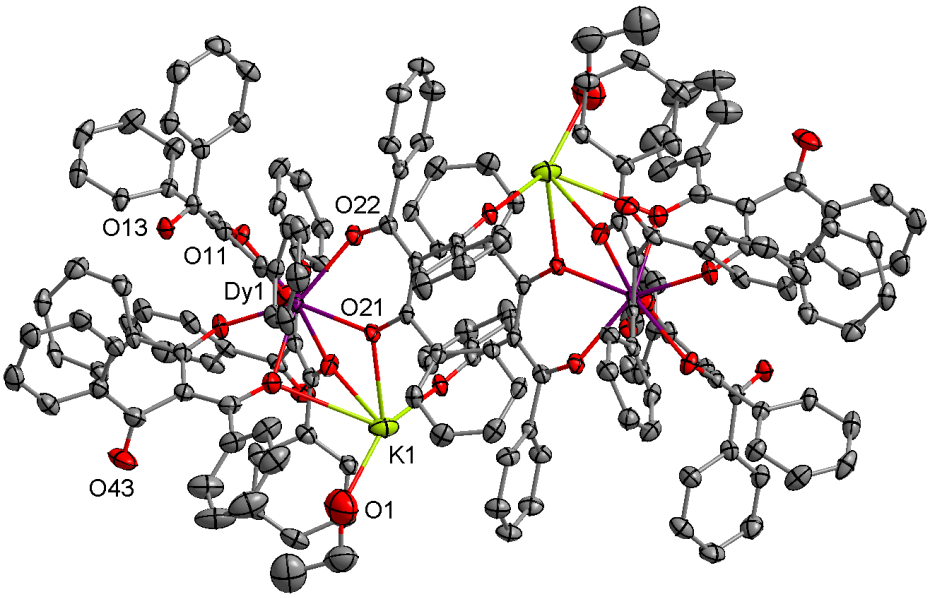

Figure A11 - Molecular plot of the $\{Dy_2K_2\}^{II}$ assembly with displacement ellipsoids shown at the 50% probability level.

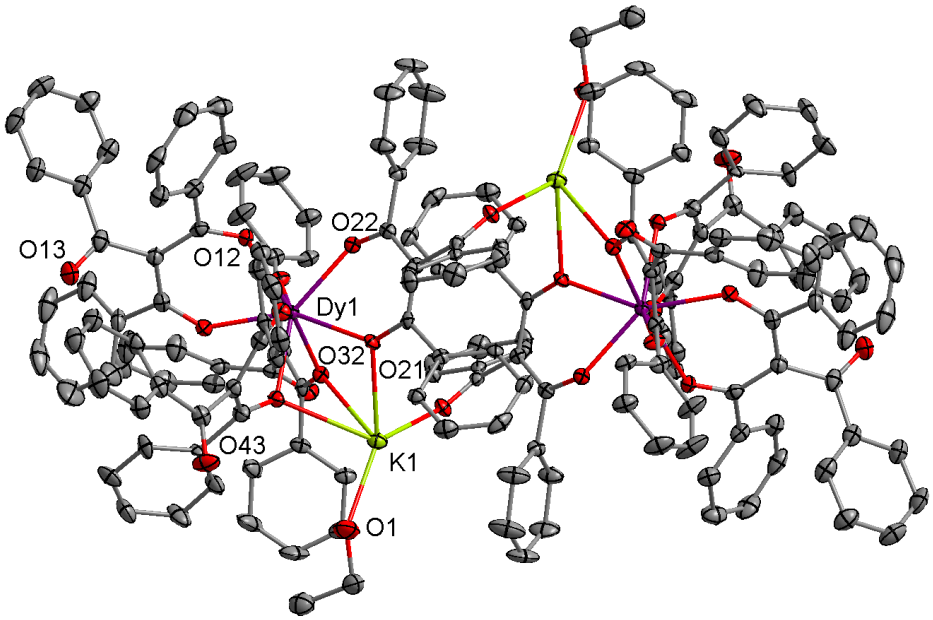

Figure A12 - Molecular plot of the $\{Dy_2K_2\}^{IV}$ assembly with displacement ellipsoids shown at the 50% probability level. Hydrogen atoms and solvent molecules are omitted for clarity.

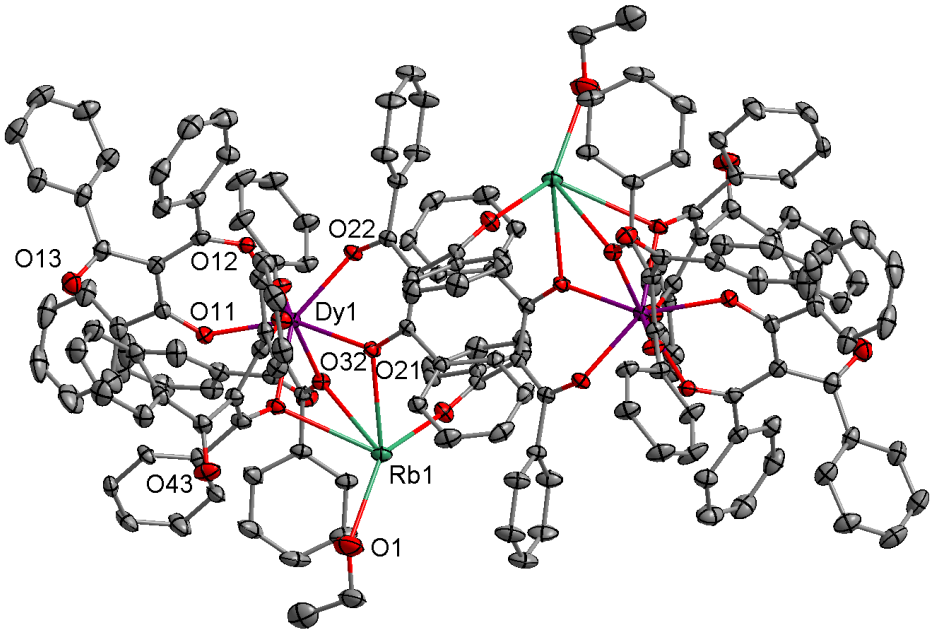

Figure A13 - Molecular plot of the $\{Dy_2Rb_2\}^{IV}$ assembly with displacement ellipsoids shown at the 50% probability level. Hydrogen atoms and solvent molecules are omitted for clarity.

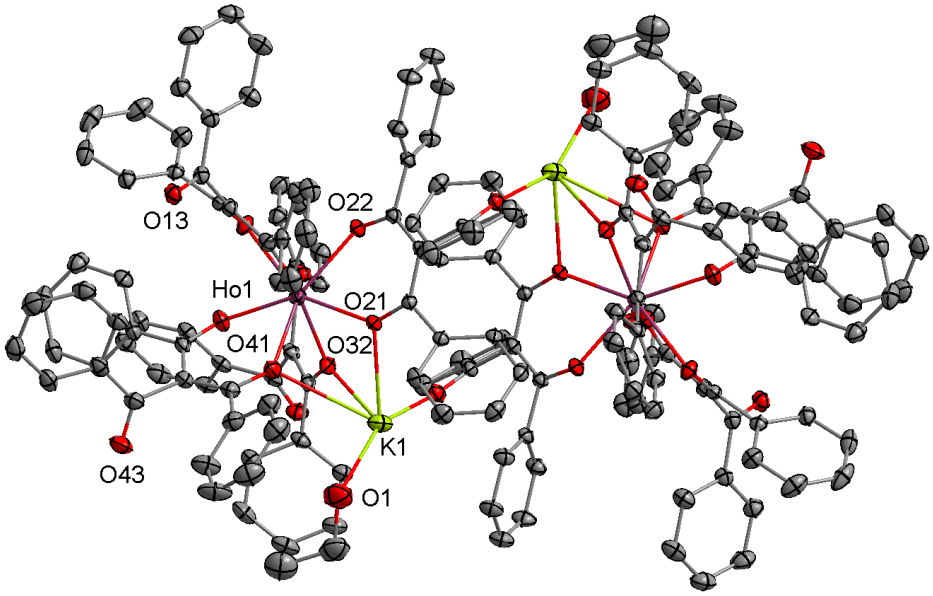

Figure A14 - Molecular plot of the $\{Ho_2K_2\}^{II}$ assembly with displacement ellipsoids shown at the 50% probability level. Hydrogen atoms have been omitted for clarity.

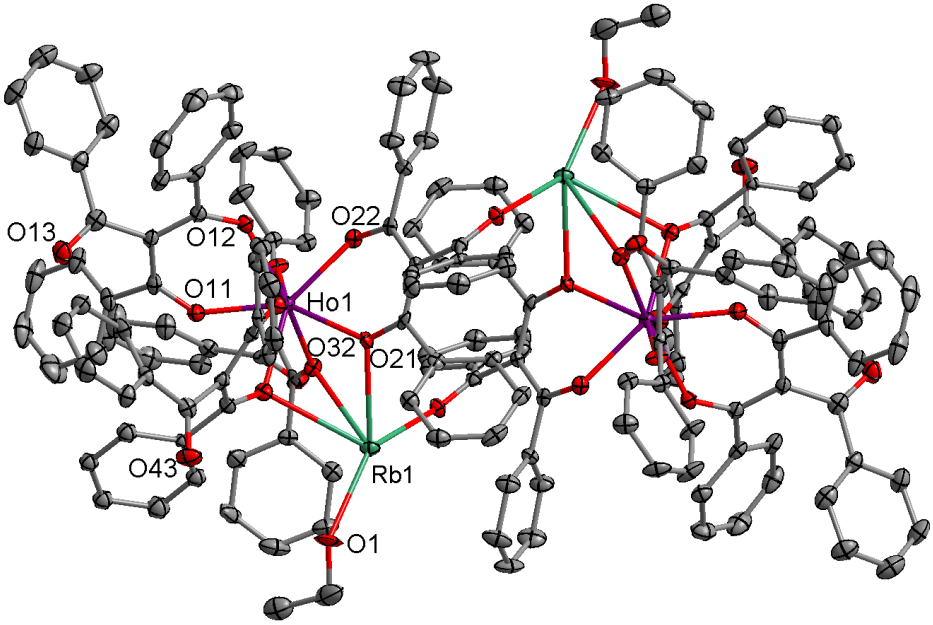

Figure A15 - Molecular plot of the $\{Ho_2Rb_2\}^{IV}$ assembly with displacement ellipsoids shown at the 50% probability level. Hydrogen atoms and solvent molecules are omitted for clarity.

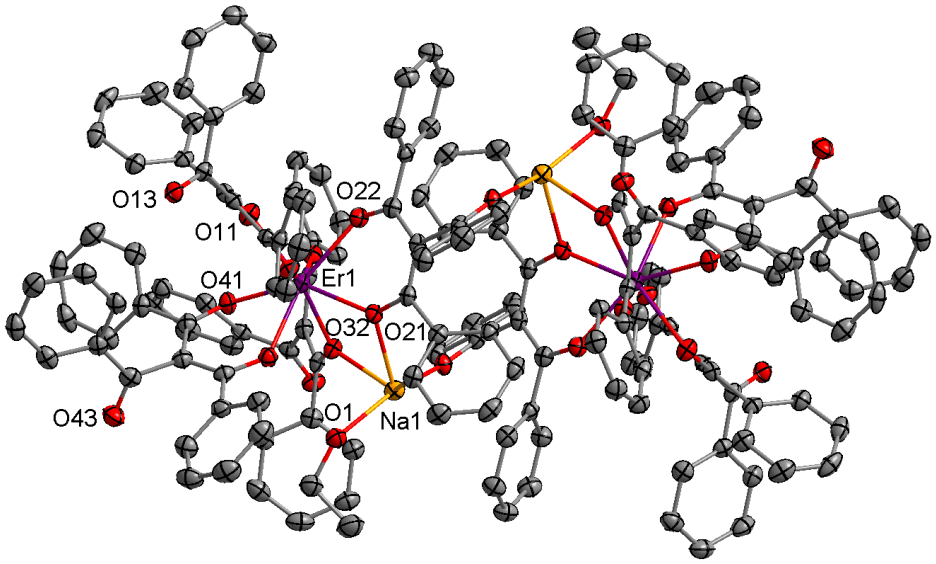

Figure A16 - Molecular plot of the $\{Er_2Na_2\}^{I}$ assembly with displacement ellipsoids shown at the 50% probability level. Hydrogen atoms have been omitted for clarity.

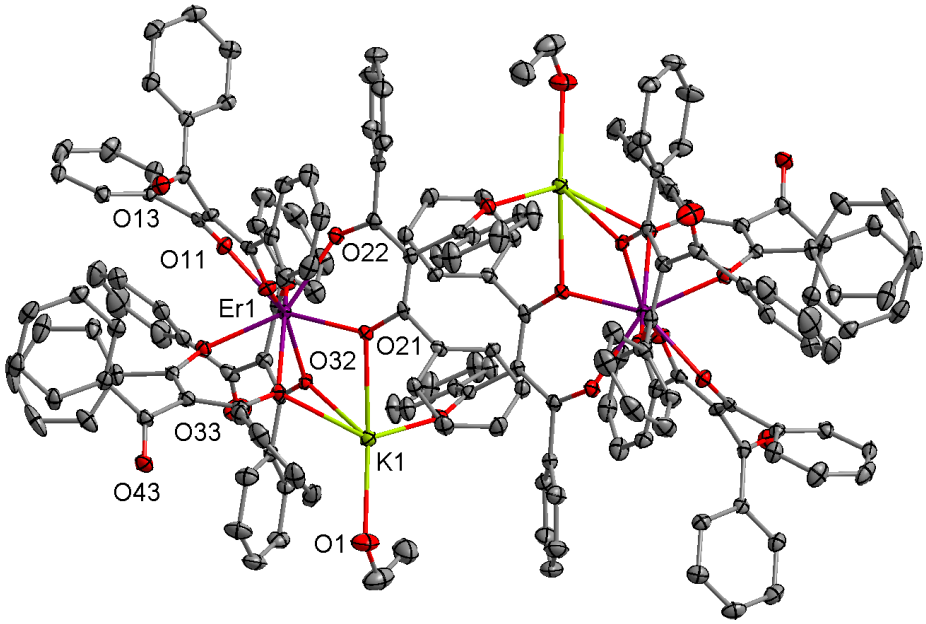

Figure A17 - Molecular plot of the $\{Er_2K_2\}^{III}$ assembly with displacement ellipsoids shown at the 50% probability level. Hydrogen atoms and solvent molecules are omitted for clarity.

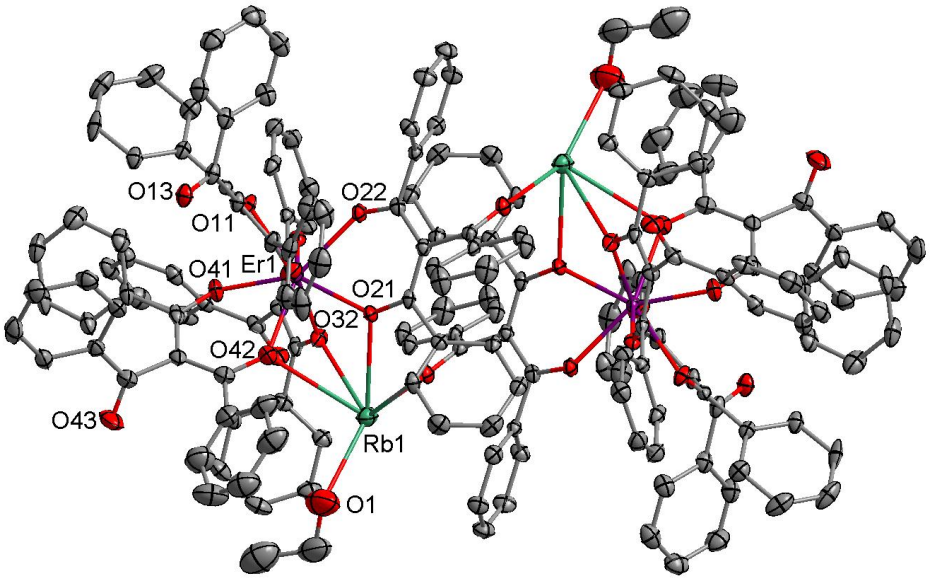

Figure A18 - Molecular plot of the $\{Er_2Rb_2\}^{II}$ assembly with displacement ellipsoids shown at the 50% probability level. Hydrogen atoms have been omitted for clarity.

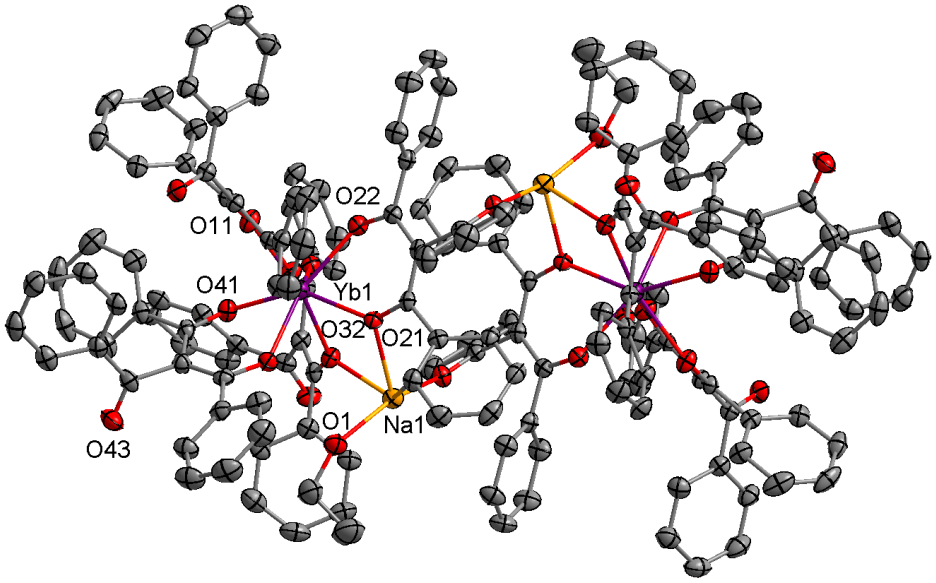

Figure A19 - Molecular plot of the $\{Yb_2Na_2\}^{I}$ assembly with displacement ellipsoids shown at the 50% probability level. Hydrogen atoms have been omitted for clarity.

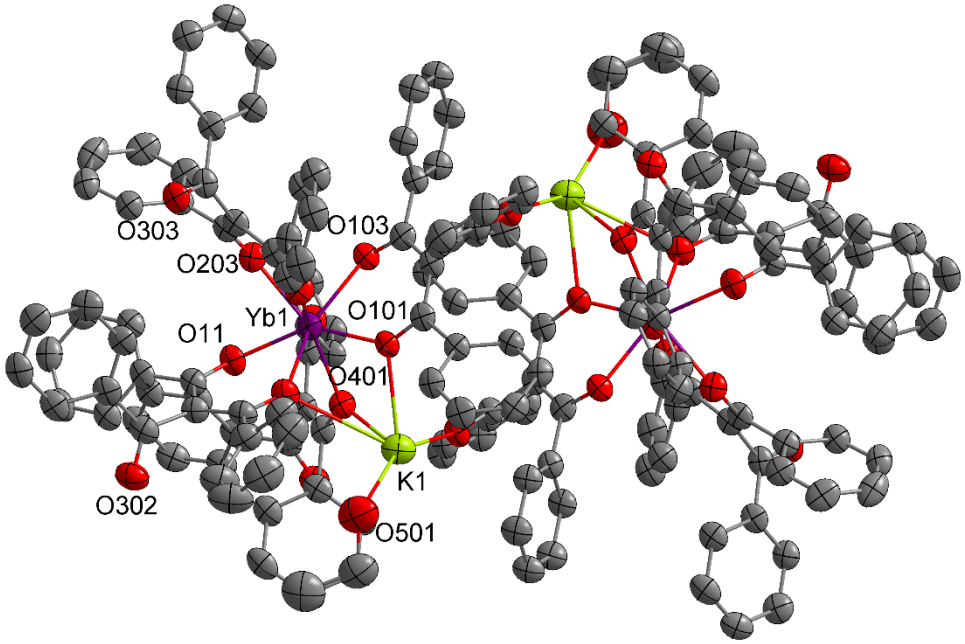

Figure A20 - Molecular plot of the $\{Yb_2K_2\}^{II}$ assembly with displacement ellipsoids shown at the 50% probability level. Hydrogen atoms have been omitted for clarity.

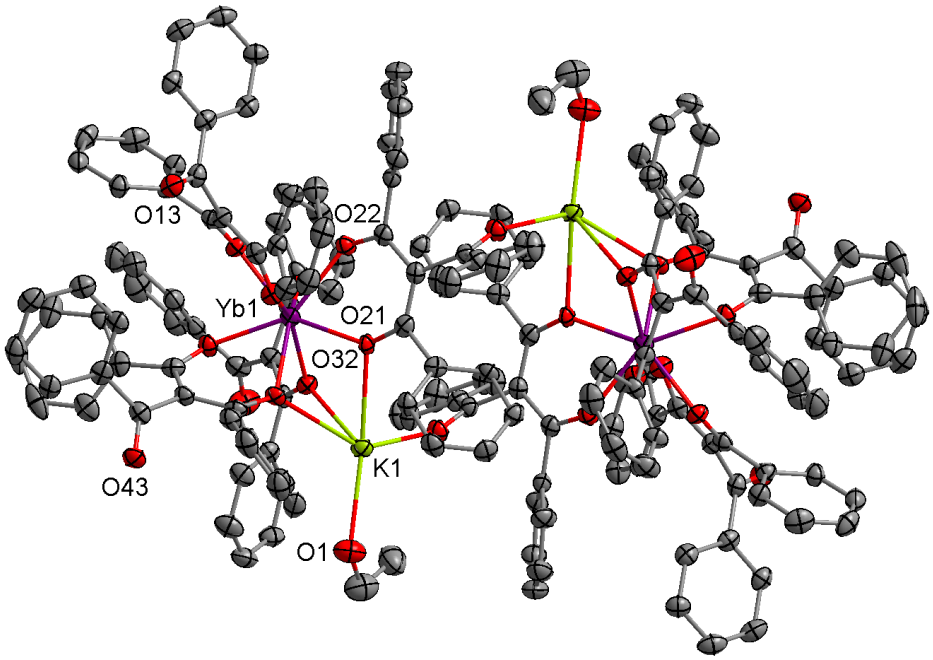

Figure A21 - Molecular plot of the $\{Yb_2K_2\}^{III}$ assembly with displacement ellipsoids shown at the 50% probability level. Hydrogen atoms and solvent molecules are omitted for clarity.

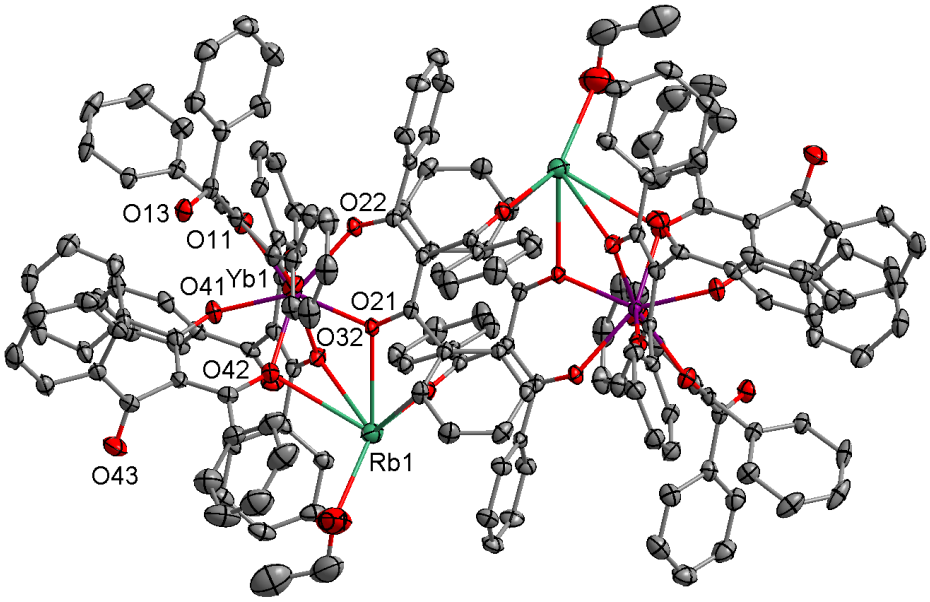

Figure A22 - Molecular plot of the $\{Yb_2Rb_2\}^{II}$ assembly with displacement ellipsoids shown at the 50% probability level. Hydrogen atoms have been omitted for clarity.

A3 Cesium Coordination Network

Three equivalents of **L1**H and Cs_2CO_3 was made to react with one equivalent of $LnCl_3 \cdot xH_2O$ in ethanol. Regardless of the Ln^{3+} used in this reaction, a two-dimensional Cs^+ coordination network was consistently crystallised (Figure A23), with the formulation $[Cs(\mathbf{L1})]_n$ identified by single crystal X-ray diffraction studies (Figure A24).

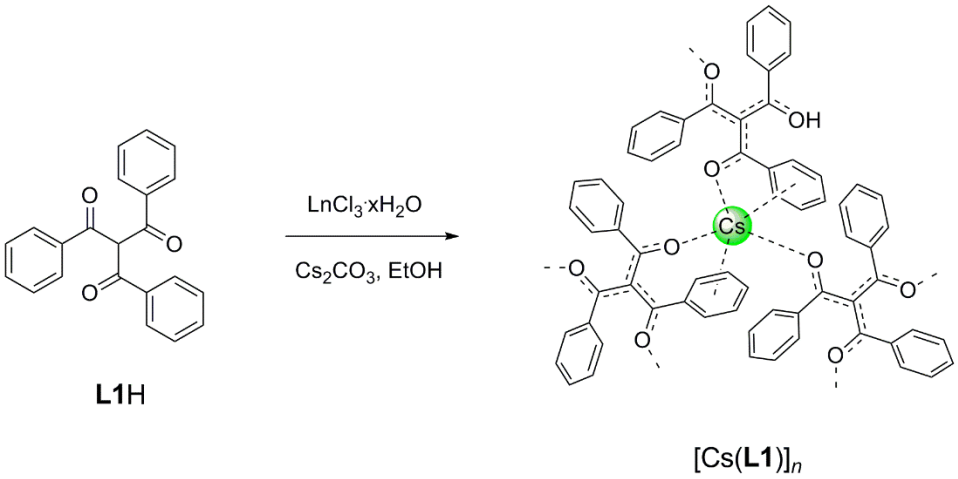

Figure A23 – Synthetic scheme for the synthesis of the Cs^+ coordination network $[Cs(\mathbf{L1})]_n$. The network is drawn to illustrate the Cs^+ coordination sphere rather than stoichiometry.

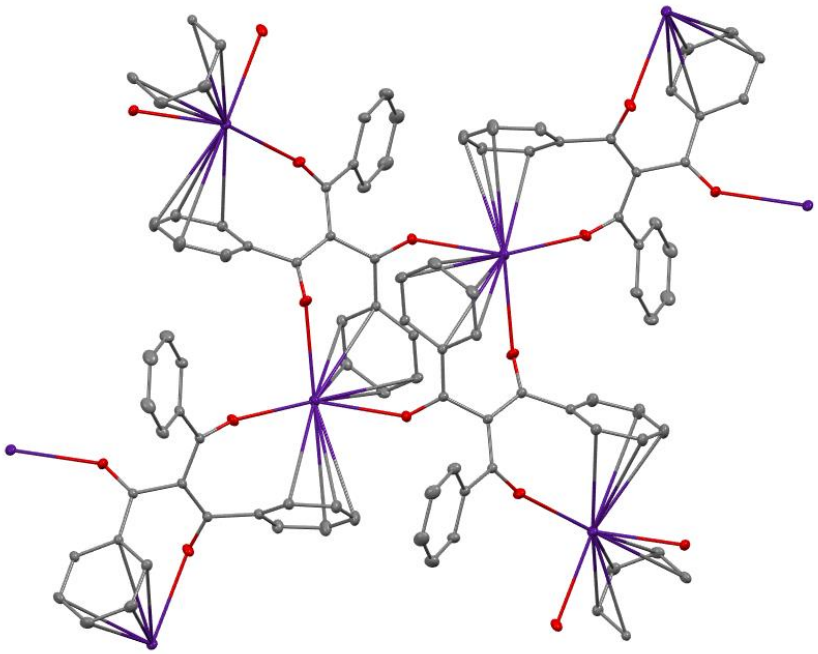

Figure A24 – Molecular plot of the $[Cs(\mathbf{L1})]_n$ coordination network with displacement ellipsoids shown at the 50% probability level. Hydrogen atoms have been omitted for clarity.

The $[Cs(\mathbf{L1})]_n$ consists of a two-dimensional network, whereby each Cs^+ cation is five-coordinate, to the three carbonyl O atoms from three different $\mathbf{L1}^-$ ligands,

and the two phenyl rings of two of the bound ligands. The distances from the Cs^+ cation to the centroids of the coordinating phenyl rings are 3.420 Å and 3.343 Å. Furthermore, the phenyl ring which does not contribute to coordination in the two-dimensional polymer in fact has a weaker Cs^+-π interaction in the third-dimension with a distance from Cs^+ to phenyl ring centroid of 4.009 Å. Including this interaction, the polymer would be best described as a three-dimensional extended coordination network.

A4 Selected Crystal Structure Interatomic Distances

Table A0.1 – Selected bond lengths [Å] for $\{Eu_2Na_2\}^{I}$.

Eu(1)-O(11)	2.366(18)
Eu(1)-O(31)	2.378(18)
Eu(1)-O(22)	2.391(18)
Eu(1)-O(21)	2.379(17)
Eu(1)-O(12)	2.387(18)
Eu(1)-O(32)	2.406(18)
Eu(1)-O(42)	2.397(19)
Eu(1)-O(41)	2.362(17)

Table A0.2 - Selected bond lengths [Å] for $\{Eu_2K_2\}^{IV}$.

Eu(1)-O(11)	2.343(3)
Eu(1)-O(31)	2.355(3)
Eu(1)-O(22)	2.360(3)
Eu(1)-O(21)	2.375(3)
Eu(1)-O(12)	2.382(3)
Eu(1)-O(32)	2.394(3)
Eu(1)-O(42)	2.407(3)
Eu(1)-O(41)	2.427(3)

Table A0.3 - Selected bond lengths [Å] for $\{Eu_2K_2\text{-}BuOH\}^{III}$

Eu(1)-O(12)	2.3444(17)
Eu(1)-O(21)	2.3484(17)
Eu(1)-O(41)	2.3512(17)
Eu(1)-O(11)	2.3760(18)
Eu(1)-O(22)	2.3810(17)
Eu(1)-O(32)	2.3861(17)
Eu(1)-O(31)	2.3951(17)
Eu(1)-O(42)	2.4726(18)

Table A0.4 - Selected bond lengths [Å] for $\{Eu_2Rb_2\}^{IV}$.

Eu(1)-O(11)	2.3485(13)
Eu(1)-O(22)	2.3606(12)
Eu(1)-O(31)	2.3657(12)
Eu(1)-O(21)	2.3735(12)
Eu(1)-O(12)	2.3788(12)
Eu(1)-O(32)	2.3876(12)
Eu(1)-O(41)	2.4130(13)
Eu(1)-O(42)	2.4155(12)

Table A0.5 - Selected bond lengths [Å] for $\{Gd_2K_2\}^{IV}$.

Gd(1)-O(11)	2.3348(11)
Gd(1)-O(22)	2.3443(11)
Gd(1)-O(31)	2.3510(11)
Gd(1)-O(21)	2.3693(10)
Gd(1)-O(12)	2.3711(11)
Gd(1)-O(32)	2.3800(10)
Gd(1)-O(42)	2.3960(11)
Gd(1)-O(41)	2.4069(11)

Table A0.6 - Selected bond lengths [Å] for $\{Gd_2Rb_2\}^{IV}$

Gd(1)-O(11)	2.3375(15)
Gd(1)-O(22)	2.3509(14)
Gd(1)-O(31)	2.3567(15)
Gd(1)-O(21)	2.3662(15)
Gd(1)-O(12)	2.3751(14)
Gd(1)-O(32)	2.3813(14)
Gd(1)-O(42)	2.4020(15)
Gd(1)-O(41)	2.4058(14)

Table A0.7 - Selected bond lengths [Å] for $\{Tb_2Na_2\}^{I}$.

Tb(1)-O(41)	2.330(3)
Tb(1)-O(11)	2.345(3)
Tb(1)-O(31)	2.346(3)
Tb(1)-O(12)	2.350(3)
Tb(1)-O(22)	2.359(3)
Tb(1)-O(21)	2.363(3)
Tb(1)-O(42)	2.366(3)
Tb(1)-O(32)	2.376(3)

Table A0.8 - Selected bond lengths [Å] for $\{Tb_2K_2\}^{II}$

Tb(1)-O(41)	2.331(2)
Tb(1)-O(21)	2.347(2)
Tb(1)-O(11)	2.349(2)
Tb(1)-O(22)	2.353(2)
Tb(1)-O(42)	2.358(3)
Tb(1)-O(31)	2.361(2)
Tb(1)-O(32)	2.370(2)
Tb(1)-O(12)	2.392(3)

Table A0.9 - Selected bond lengths [Å] for $\{Tb_2Rb_2\}^{IV}$.

Tb(1)-O(11)	2.3277(9)
Tb(1)-O(22)	2.3401(8)
Tb(1)-O(31)	2.3402(8)
Tb(1)-O(21)	2.3512(8)
Tb(1)-O(12)	2.3555(9)
Tb(1)-O(32)	2.3636(8)
Tb(1)-O(42)	2.3884(9)
Tb(1)-O(41)	2.3939(8)

Table A0.10 - Selected bond lengths [Å] for $\{Dy_2K_2\}^{II}$.

Dy(1)-O(41)	2.313(4)
Dy(1)-O(21)	2.325(4)
Dy(1)-O(22)	2.335(4)
Dy(1)-O(11)	2.340(4)
Dy(1)-O(31)	2.341(4)
Dy(1)-O(42)	2.348(4)
Dy(1)-O(32)	2.364(4)
Dy(1)-O(12)	2.389(4)

Table A0.11 - Selected bond lengths [Å] for $\{Dy_2K_2\}^{IV}$.

Dy(1)-O(11)	2.303(2)
Dy(1)-O(22)	2.318(2)
Dy(1)-O(31)	2.328(2)
Dy(1)-O(21)	2.340(2)
Dy(1)-O(12)	2.346(2)
Dy(1)-O(32)	2.3541(19)
Dy(1)-O(42)	2.374(2)
Dy(1)-O(41)	2.390(2)

Table A0.12 - Selected bond lengths [Å] for $\{Dy_2Rb_2\}^{II}$.

Dy(1)-O(11)	2.3084(16)
Dy(1)-O(22)	2.3213(15)
Dy(1)-O(31)	2.3304(15)
Dy(1)-O(21)	2.3363(15)
Dy(1)-O(12)	2.3434(16)
Dy(1)-O(32)	2.3474(15)
Dy(1)-O(42)	2.3759(15)
Dy(1)-O(41)	2.3843(15)

Table A0.13 - Selected bond lengths [Å] for $\{Ho_2K_2\}^{II}$.

Ho(1)-O(41)	2.3038(15)
Ho(1)-O(21)	2.3140(14)
Ho(1)-O(11)	2.3227(15)
Ho(1)-O(31)	2.3261(15)
Ho(1)-O(42)	2.3307(16)
Ho(1)-O(22)	2.3346(15)
Ho(1)-O(32)	2.3561(15)
Ho(1)-O(12)	2.3745(16)

Table A0.14 - Selected bond lengths [Å] for $\{Ho_2Rb_2\}^{IV}$.

Ho(1)-O(11)	2.291(3)
Ho(1)-O(22)	2.308(3)
Ho(1)-O(31)	2.319(3)
Ho(1)-O(21)	2.324(2)
Ho(1)-O(12)	2.331(3)
Ho(1)-O(32)	2.331(3)
Ho(1)-O(42)	2.365(3)
Ho(1)-O(41)	2.370(3)

Table A0.15 - Selected bond lengths [Å] for $\{Er_2Na_2\}^{I}$.

Er(1)-O(41)	2.2996(18)
Er(1)-O(11)	2.3098(18)
Er(1)-O(31)	2.3164(17)
Er(1)-O(21)	2.3191(17)
Er(1)-O(12)	2.3253(17)
Er(1)-O(22)	2.3383(18)
Er(1)-O(42)	2.3370(18)
Er(1)-O(32)	2.3471(17)

Table A0.16 - Selected bond lengths [Å] for $\{Er_2K_2\}^{III}$.

Er(1)-O(21)	2.2595(19)
Er(1)-O(12)	2.273(2)
Er(1)-O(41)	2.2961(19)
Er(1)-O(11)	2.298(2)
Er(1)-O(32)	2.3175(19)
Er(1)-O(31)	2.3282(19)
Er(1)-O(22)	2.3525(19)
Er(1)-O(42)	2.4050(19)

Table A0.17 - Selected bond lengths [Å] for $\{Er_2Rb_2\}^{II}$.

Er(1)-O(41)	2.296(3)
Er(1)-O(21)	2.300(3)
Er(1)-O(31)	2.318(3)
Er(1)-O(11)	2.318(3)
Er(1)-O(22)	2.321(3)
Er(1)-O(42)	2.330(3)
Er(1)-O(32)	2.348(3)
Er(1)-O(12)	2.365(3)

Table A0.18 - Selected bond lengths [Å] for $\{Yb_2Na_2\}^{I}$.

Yb(1)-O(41)	2.275(3)
Yb(1)-O(11)	2.295(3)
Yb(1)-O(21)	2.303(3)
Yb(1)-O(12)	2.306(3)
Yb(1)-O(31)	2.306(3)
Yb(1)-O(22)	2.308(3)
Yb(1)-O(42)	2.317(3)
Yb(1)-O(32)	2.333(3)

Table A0.19 - Selected bond lengths [Å] for $\{Yb_2K_2\}^{II}$.

Yb(1)-O(11)	2.266(3)
Yb(1)-O(101)	2.302(3)
Yb(1)-O(201)	2.340(3)
Yb(1)-O(203)	2.292(3)
Yb(1)-O(301)	2.305(3)
Yb(1)-O(401)	2.333(3)
Yb(1)-O(403)	2.304(3)
Yb(1)-O(103)	2.302(3)

Table A0.20 - Selected bond lengths [Å] for $\{Yb_2K_2\}^{III}$.

Yb(1)-O(21)	2.244(2)
Yb(1)-O(12)	2.259(2)
Yb(1)-O(11)	2.273(3)
Yb(1)-O(41)	2.278(3)
Yb(1)-O(32)	2.291(3)
Yb(1)-O(31)	2.311(2)
Yb(1)-O(22)	2.335(3)
Yb(1)-O(42)	2.399(3)

Table A0.21 - Selected bond lengths [Å] for $\{Yb_2Rb_2\}^{II}$.

Yb(1)-O(41)	2.272(3)
Yb(1)-O(21)	2.275(2)
Yb(1)-O(11)	2.297(3)
Yb(1)-O(31)	2.298(3)
Yb(1)-O(22)	2.301(3)
Yb(1)-O(42)	2.305(3)
Yb(1)-O(32)	2.328(3)
Yb(1)-O(12)	2.348(3)

A5 Emission Spectra

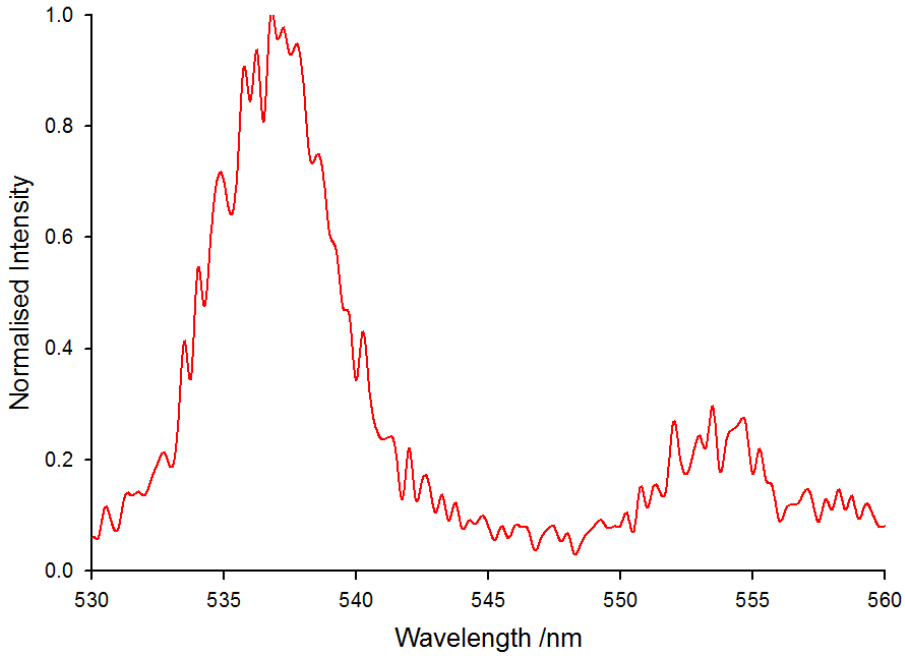

Figure A25 – Normalised emission (λ_{ex} = 350 nm) from the $\{Eu_2K_2\}^{IV}$ assembly in the solid state, attributed to $^7F_1 \longleftarrow {}^5D_1$, and $^7F_2 \longleftarrow {}^5D_1$ transitions.

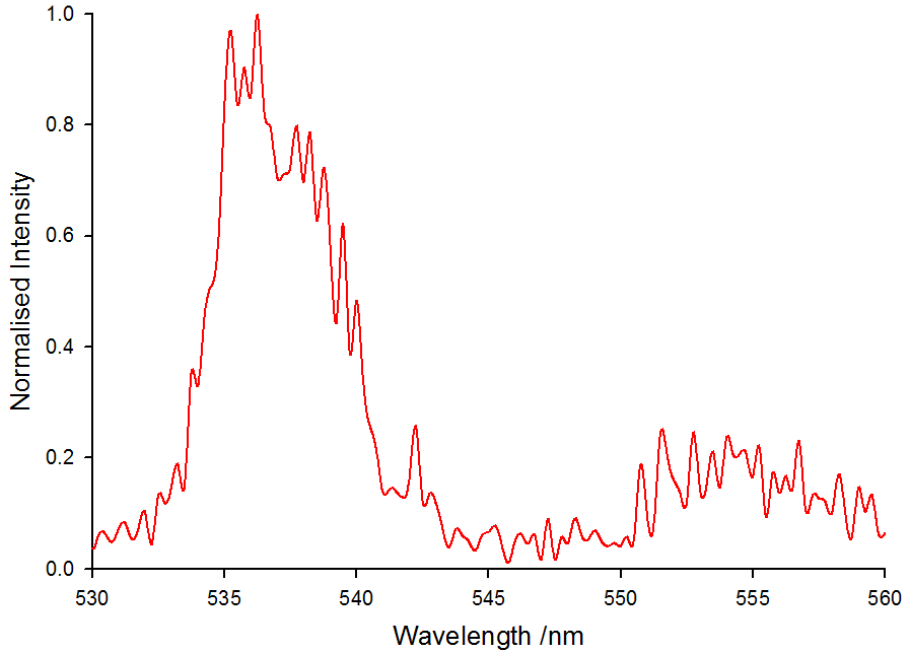

Figure A26 – Normalised emission (λ_{ex} = 350 nm) from the $\{Eu_2Rb_2\}^{IV}$ assembly in the solid state, attributed to $^7F_1 \longleftarrow {}^5D_1$, and $^7F_2 \longleftarrow {}^5D_1$ transitions.

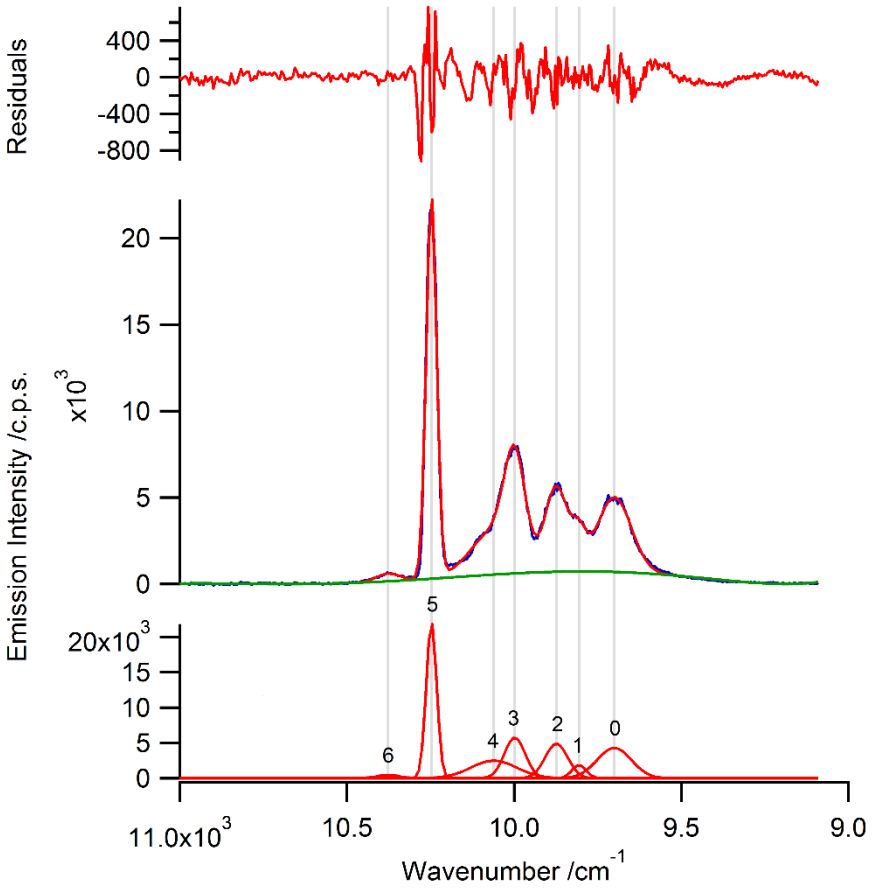

Figure A27 – Middle: Emission spectrum of the $\{Yb_2K_2\}^{II/III}$ assembly after dissolution ethanol at 77 K. Bottom: The deconvolution of the emission spectrum. Top: Residual plot for the deconvolution fitting.

Table A0.22 – Peak energies evaluated from deconvolution of the emission spectrum in Figure A27.

Peak	Energy (cm^{-1})
6	10,376
5	10,247
4	10,061
3	9,998
2	9,873
1	9,806
0	9,700

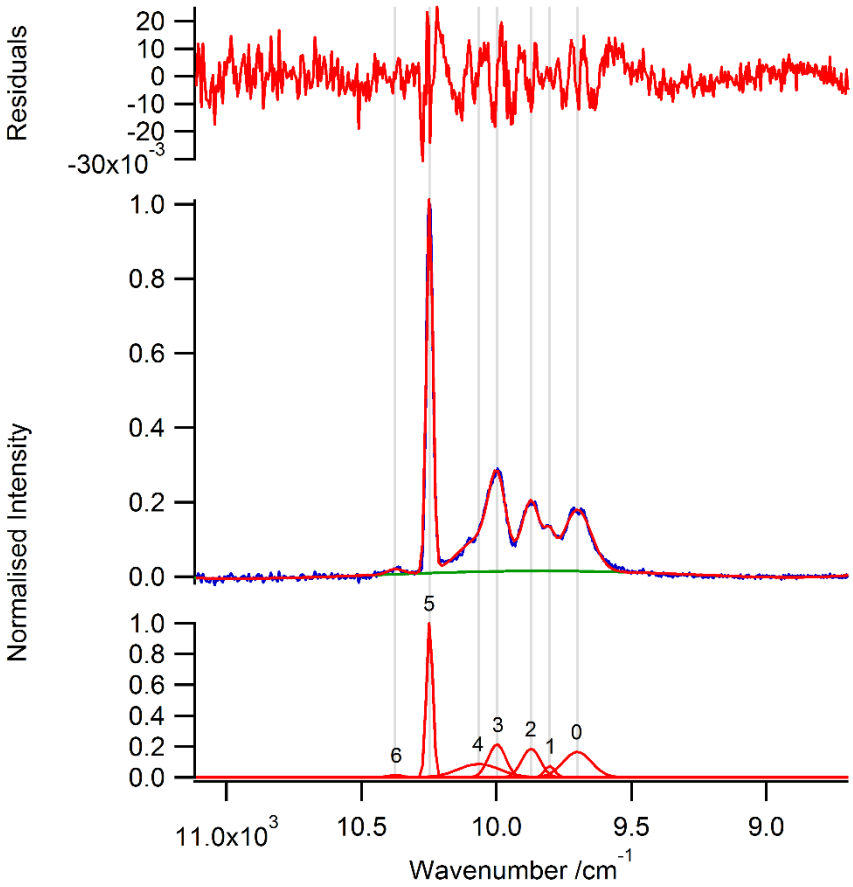

Figure A28 – Middle: Normalised Emission spectrum of the $\{Yb_2Rb_2\}^{II}$ assembly after dissolution ethanol at 77 K. Bottom: The deconvolution of the emission spectrum. Top: Residual plot for the deconvolution fitting.

Table A0.23 - Peak energies evaluated from deconvolution of the emission spectrum in Figure A28.

Peak	Energy (cm^{-1})
6	10,374
5	10,247
4	10,065
3	9,998
2	9,871
1	9,802
0	9,700